Dissertation

submitted to the

Combined Faculty of Mathematics, Engineering and Natural Sciences
of Heidelberg University, Germany

for the degree of

Doctor of Natural Sciences

Put forward by

Florian Kroh

born in: Bad Berleburg, Germany

Oral examination: April 29th, 2024

Data-driven extraction of a physically interpretable model describing amide proton transfer-weighted imaging in the human brain

Referees: Prof. Dr. Mark E. Ladd

Prof. Dr. Leif Schröder

Data-driven extraction of a physically interpretable model describing amide proton transfer-weighted imaging in the human brain

Chemical exchange saturation transfer (CEST) magnetic resonance imaging (MRI) is an emerging, non-invasive molecular imaging technique. Particularly, the CEST-based amide proton transfer-weighted (APTw) contrast represents a valuable imaging biomarker for clinical assessment of brain cancers. However, the underlying molecular origin of the APTw contrast in vivo is still under debate. This thesis aims to expand the current knowledge about the APTw contrast mechanisms in the human brain at $B_0 = 3$ T by developing a physically interpretable model (PIM) based on previously unexplored CEST signal features extracted by various machine learning methods.

This PIM enabled the successful translation of interpretable CEST signals into their respective APTw contrast contributions not only as a black-box model but by explicitly exploiting physically relevant information. This novel approach allowed not merely (i) the identification of the isolated amide and exchange-relayed nuclear Overhauser effect (rNOE) contrasts as the dominating influences on the APTw contrast, in coherence with literature. But, more interestingly, (ii) this PIM also revealed significant dependencies of amide and rNOE contributions on changes in the controllable B_1 and tissue-specific T_1.

Ultimately, the PIM allowed the identification of amide- and rNOE-driven sensitivity regimes of the APTw contrast, enabling an enhanced biophysical understanding of the CEST phenomenon in vivo, thus potentially improving the clinical assessment of brain cancers.

Datengestützte Extraktion eines physikalisch interpretierbaren Modells zur Beschreibung der Amid-Protonen-Transfer-gewichteten Bildgebung im menschlichen Gehirn

Die Chemical Exchange Saturation Transfer (CEST) Magnetresonanztomographie (MRI) ist eine aufstrebende, nicht-invasive molekulare Bildgebungstechnik. Insbesondere der CEST-basierte Amid-Protonen-Transfer-gewichtete (APTw) Kontrast stellt einen wertvollen bildgebenden Biomarker für die klinische Beurteilung von Hirntumoren dar. Der zugrunde liegende molekulare Ursprung des APTw-Kontrasts in vivo ist jedoch noch umstritten. Ziel dieser Arbeit ist es, das derzeitige Wissen über die Mechanismen des APTw-Kontrasts im menschlichen Gehirn bei $B_0 = 3$ T zu erweitern, indem ein physikalisch interpretierbares Modell (PIM) entwickelt wird, das auf bisher unerforschten CEST-Signalmerkmalen basiert, welche durch verschiedene maschinelle Lernmethoden extrahiert wurden.

Dieses PIM ermöglichte die erfolgreiche Übersetzung interpretierbarer CEST-Signale in ihre jeweiligen APTw-Kontrastbeiträge nicht nur als Black-Box-Modell, sondern durch explizite Nutzung physikalisch relevanter Informationen. Dieser neuartige Ansatz ermöglichte nicht nur (i) die Identifizierung der isolierten Amid- und exchange-relayed nuclear Overhauser effect (rNOE)-Kontraste als die dominierenden Einflüsse auf den APTw-Kontrast in Übereinstimmung mit der Literatur. Interessanter ist jedoch, dass (ii) durch das PIM auch signifikante Abhängigkeiten der Amid- und rNOE-Beiträge von Änderungen des kontrollierbaren B_1 und des gewebespezifischen T_1 aufgezeigt werden.

Letztendlich ermöglichte das PIM die Identifizierung von Amid- und rNOE-gesteuerten Sensitivitätsregimen des APTw-Kontrasts, was ein verbessertes biophysikalisches Verständnis des CEST-Phänomens in vivo ermöglicht und somit die klinische Beurteilung von Hirntumoren verbessern könnte.

Contents

List of abbreviations

AI	artificial intelligence
APTw	amide proton transfer-weighted
BW	bandwidth
CE	contrast-enhanced
CEST	chemical exchange saturation transfer
CNR	contrast to noise ratio
CSF	cerebral spinal fluid
CT	computed tomography
cw	continuous-wave
DART	dropouts meet multiple additive regression trees
DC	duty cycle
DFG	German Research Foundation
DICOM	digital imaging and communications in medicine (standard data format)
DL	deep-learning
DS	direct saturation
DWI	diffusion-weighted imaging
FID	free induction decay
FISTA	fast iterative shrinkage-thresholding algorithm
fMRI	functional magnetic resonance imaging
FWHM	full-width-at-half-maximum
GB	gradient boosting
GRE	gradient echo, or gradient-recalled echo
IDH	Isocitratdehydrogenase
LASSO	least absolute shrinkage and selection operator
LD	linear difference
LR	linear regression
MAD	mean absolute deviation
MAE	mean absolute error
MGMT	O(6)-Methylguanine-DNA-methyltransferase
MITK	medical imaging interaction toolkit
ML	machine learning
MR	magnetic resonance
MRI	magnetic resonance imaging
MRS	magnetic resonance spectroscopy

MRSI	magnetic resonance spectroscopic imaging
NAGM	normal-appearing grey matter
NAWM	normal-appearing white matter
NCT	national center for tumor diseases
NMR	nuclear magnetic resonance
NOE	nuclear Overhauser effect
PCA	principle component analysis
PET	positron emission tomography
PIM	physically interpretable model
ppm	parts per million
PTE	proton transfer enhancement
RF	radio frequency
rNOE	exchange-relayed nuclear Overhauser effect
ROI	region of interest
RT	radiotherapy
SAR	specific absorption rate
SD	standard deviation
SHAP	Shapley additive explanations
SNR	signal-to-noise ratio
SPM	statistical parametric mapping
ssMT	semi-solid magnetization transfer
TMS	tetramethylsilan
TR	repetition time
WASABI	water shift and B_1
WT	whole tumor

Chapter 1

Introduction

The foundation for nuclear magnetic resonance (NMR) was set in the 1920s with the postulation and discovery of the nuclear spin. In 1938, the discovery of this quantum mechanical phenomenon was followed up by Isidor I. Rabi et al. [1], who were the first to describe transitions between discrete energy levels in the gaseous phase induced by oscillating magnetic fields. This was the first description of the NMR phenomenon. Following this description, it took until 1946 for the phenomenon of NMR to be discovered in condensed matter simultaneously but independently by Felix Bloch [2] and E.M. Purcell [3]. Since then, it has been used in multiple scientific fields, with many applications, such as the structural analysis of molecules.

The spin dynamics in an NMR experiment conducted in liquids can be explained using the empirically discovered Bloch equations. These equations introduce two essential concepts - the longitudinal relaxation time T_1 and the transversal relaxation time T_2. These relaxation times are the foundation for many of the clinically used contrasts and are the basis for describing the relaxation of nuclear spins towards the thermal equilibrium after radio frequency (RF) irradiation.

The value of NMR was further advanced by the discovery of the chemical shift [4, 5], which describes the shift of the resonance frequency depending on the chemical environment of a nucleus. This discovery laid the basis for magnetic resonance spectroscopy (MRS), which is a crucial method in analytical biochemistry because it provides access to biochemical information such as relative metabolite concentration and metabolic turnover.

27 years after the discovery of the NMR phenomenon in condensed matter, in 1973, magnetic resonance imaging (MRI) was first realized by Lauterbur [6] and Mansfield [7], who used magnetic field gradients to enable the encoding of the spatial distribution of the nuclear spins within the MR signal. Ever since, MRI has been seen as an essential non-invasive medical diagnostic tool that provides excellent soft-tissue contrast due to the substantial differences in T_1 and T_2 relaxation times in biological tissue. Furthermore, over the past few decades, other contrast mechanisms such as magnetic resonance spectroscopic imaging (MRSI), functional magnetic resonance imaging (fMRI), diffusion-weighted imaging (DWI), perfusion imaging, and susceptibility weighted imaging have been developed, providing deeper insights into the physiology of the human body. These advancements established MRI in everyday

clinical routine as a non-invasive technique that does not rely on ionizing radiation like computed tomography (CT) or positron emission tomography (PET) imaging.

Chemical exchange saturation transfer (CEST) [8, 9, 10, 11, 12, 13] is a novel MRI technique that enables the non-invasive detection of low-concentrated metabolites and proteins, with a resolution comparable to that of conventional MRI. This enormous upside originates in the RF preparation of labile protons from low-concentrated bio-molecules performed before the conventional acquisition of the water signal. This RF preparation, also called RF saturation, is performed to magnetically label the labile protons, which continuously exchange with the bulk water protons, reducing the measurable water signal. The indirect detection via the modified water signal after the continuous exchange of magnetic labels, therefore, leads to a powerful amplification of the solute signal, allowing a high spatial resolution ≈ 1 mm^3. In summary, CEST imaging enables the extraction of information about biochemical processes of the exchanging protons by directly measuring the reduction of the water signal.

Two highly significant and well-studied CEST signals in vivo are the amide [14] signal and the exchange-relayed nuclear Overhauser effect (rNOE) [15, 16] signal. These signals indicate the presence of proteins and peptides within cells [17] and can also provide valuable information about the pH level [14, 18, 19, 20] and average molecular size [21, 22]. For this reason, they are considered to be highly promising in diagnosing various diseases such as cancer, stroke, and neurodegenerative disorders.

To isolate the amide and rNOE signals and calculate interpretable contrasts, a multi-pool Lorentzian-fit analysis [23] can be used in combination with the relaxation-compensated contrast $\mathrm{MTR}_{\mathrm{Rex}}$ [24, 25, 26]. The $\mathrm{MTR}_{\mathrm{Rex}}$ contrast is calculated by inversely subtracting the normalized CEST spectrum (i.e., the Z-spectrum) of a label scan from a reference Z-spectrum, which in turn leads to the isolation of one pool combined with the compensation of competing signals originating from the direct water saturation or macromolecular structures. This approach has been shown to be effective for imaging individual signal contributions in CEST-MRI for various clinical questions in the human brain, especially at a magnetic field strength of $B_0 = 7$ T [27, 28, 29, 30, 31, 32]. However, it should be noted that this method requires complete Z-spectra to be acquired, leading to an extensive acquisition time, and requiring the use of advanced post-processing techniques, which hamper the clinical applicability of the method.

To tackle the problem of long measurement times and complicated post-processing procedures, amide proton transfer-weighted (APTw) CEST imaging [14, 33, 34] was developed for applications of CEST in brain tumors. The amide proton transfer-weighted (APTw) contrast is extracted based on the asymmetry analysis $\mathrm{MTR}_{\mathrm{asym}}$ (i.e. the difference between the two Z-values $\mathrm{Z}(\Delta\omega = -3.5$ ppm) and $\mathrm{Z}(\Delta\omega = 3.5$ ppm) at the two frequency offsets $\Delta\omega = -3.5$ and 3.5 ppm, respectively, relative to the water signal), which decreases the amount of acquired frequency offsets and the complexity of the post-processing. Since the first publication of the APTw contrast in 2003 [14] and its first application to brain tumor patients three years later [33], many applications of the APTw contrast in neuro-imaging have proven

to be helpful in investigating clinical questions, like tumor grading [35, 36] and differentiation between tumor progression and stable disease [37, 38, 39]. This made the APTw contrast the most prominent approach for extraction of the amide signal. However, due to the simplistic calculation of the APTw contrast and the multiple contributors that cannot be distinguished, an isolated interpretation of the acquired APTw images using only the APTw contrast is not feasible. The lack of knowledge about the APTw contrast's origin and the limitations in the interpretation of clinical findings, therefore, decrease the applicability to new pathologies.

To this end, many efforts have been made to create a more stable comparable APTw contrast, while maintaining the clinically feasible measurement time. All of these advancements lead towards a consensus effort [40] to generalize the saturation schemes and highlight the possibilities regarding contrast origins. However, a caveat was that, despite the many successes, it is still impossible to interpret the APTw contrast due to its many dependencies, and therefore, easy misinterpretation is possible, and more investigation into its contributors is needed. To this day, only very limited additional information about the contributors to the APTw contrast has been uncovered, which is mainly because extensive studies of these dependencies are inherently difficult. The difficulties originate from the fact that simulation studies are limited in their ability to represent the entire range of possible spectra in vivo due to the absence of several necessary parameters and because data-driven approaches are constrained by the lack of large datasets required for such analyses.

In this thesis, a physically interpretable model (PIM) of the APTw contrast was developed that enables the investigation of the underlying mechanisms and interactions between the contributors to the APTw contrast in vivo. The PIM was developed based on an extensive clinical study, where low-power fully-sampled Z-spectra and APTw imaging data was collected for 125 different glioma patients, which enabled the usage of data-driven techniques. Combining the extensive dataset with more specific low-power CEST contrast aided in the development of the PIM, enabling the extraction of previously unexplored features of the APTw contrast. The data-driven approach, which has been made feasible for the first time (due to the previous lack of data), helped to bypass the original modeling limitations imposed by the lack of knowledge about necessary simulation parameters.

For the development of this PIM, six steps were necessary. First (i), a matching level for the evaluation of the models by investigation of the APTw contrast features and variations in vivo was calculated (Section 5.1). Secondly (ii), best-case models using fully-sampled Z-spectra (B_1 = 0.6 µT and 0.9 µT), rel. ΔB_1, T_1, and ΔB_0 as input features were created to prove that a prediction of the high-power APTw contrast from low-power data is feasible, and with that, a transfer between the saturation schemes (Section 5.2.1). Consequently (iii), the crucial features exploited by the best-case models were extracted to show that the models use physically relevant information and to identify suitable interpretable input features for the PIM (Section 5.2.2). In the next step (iv), it was evaluated whether a prediction of the APTw contrast is possible using the identified interpretable contrasts (i.e. MTR_{Rex} AMIDE, MTR_{Rex} rNOE, MTR_{Rex} semi-solid magnetization transfer (ssMT), B_1, and T_1) as input features for a gradient boosting (GB) and linear regression (LR)

model (Section 5.3.1). This was followed by (v) the in-depth analysis of the same two models using interpretable machine learning (ML) methods (Dependence plots, Shapley additive explanations (SHAP)) to understand the prediction process of the models and to extract the differences that distinguish the models (non-linearities of the GB model) (Section 5.3.2). Lastly (vi), the GB model's nonlinearities and LR model's interpretability were combined by the creation of a PIM that is based on a grid covering the relevant B_1 and T_1 range and followed by the creation of an LR model for each uniform-sized bin generated by the grid (Section 5.3.3).

In conclusion, the PIM enabled the successful translation of interpretable CEST signals into their respective APTw contrast contributions not only as a black-box model but by explicitly exploiting actual physically relevant information. This novel approach allowed not merely (i) the identification of the isolated amide and rNOE contrasts as the dominating influences on the APTw contrast, in coherence with the literature but, more interestingly, (ii) highlighted a significant dependency of the amide and rNOE contributions on changes in the B_1 and T_1 value. Furthermore, it is now possible to decompose the APTw contrast for the used dataset and analyze the composition of the APTw contrast in different brain regions. Ultimately, the PIM led to the identification of amide- and rNOE-driven sensitivity regimes of the APTw contrast, enabling a better biophysical understanding of the CEST phenomenon in vivo, thus potentially improving the clinical assessment of brain cancers.

Chapter 2

Theoretical Background

This chapter provides the theoretical background for the rest of this work. First, a brief description of the theory of nuclear magnetic resonance (NMR) is presented (Section 2.1), as well as a section on the principles used in magnetic resonance imaging (MRI) (Section 2.2). Subsequently, the observed magnetization transfer pathways are described (Section 2.3), followed by an overview of the chemical exchange saturation transfer (CEST)-phenomenon (Section 2.4), and the theory behind CEST (Section 2.5). Lastly, the theoretical foundations of the used machine learning algorithms (Section 2.6) and the corresponding methods for interpretable machine learning (ML) are outlined (Section 2.7).

2.1 Nuclear magnetic resonance

Detailed information on all topics regarding nuclear magnetic resonance (NMR), described in the following section, is provided by the books [41, 42, 43, 44, 45].

2.1.1 Nuclear spin and Zeeman effect

Since all nucleons (i.e., protons and neutrons) are fermions with half-integer spins, every atomic nucleus with an odd number of protons and/or neutrons has a non-zero total nuclear spin, represented by $\vec{I} \neq 0$. The hydrogen (^{1}H) nucleus, consisting of a single proton, has a spin of $\vec{I} = \frac{1}{2}$, hereafter simply referred to as spin I. This spin complies with the quantum-mechanical commutator relations for angular momentum:

$$[\hat{I}_i, \hat{I}_j] = i\hbar\epsilon_{ijk}\hat{I}_k \tag{2.1}$$

$$[\hat{I}^2, \hat{I}_i] = 0 \tag{2.2}$$

with $i, j, k \in [x, y, z]$. By applying the commonly used operators $\hat{I}_z$ and $\hat{I}^2$ onto the spin eigenstates $\mid I, m\rangle$, the corresponding eigenvalues result as follows:

$$\hat{I}^2 \mid I, m\rangle = \hbar^2 I(I+1) \mid I, m\rangle \tag{2.3}$$

$$\hat{I}_z \mid I, m\rangle = \hbar m \mid I, m\rangle \tag{2.4}$$

where m is the magnetic quantum number that can only attain the $(2I+1)$ values $-I, -I+1, ..., I-1, I$ and $\hbar$ is the reduced Planck constant. The non-zero spin $\hat{\vec{I}}$

leads to a magnetic moment $\hat{\vec{\mu}}$ in the following way:

$$\hat{\vec{\mu}} = \gamma \hat{\vec{I}} \tag{2.5}$$

with γ being a nucleus-specific constant called the gyro-magnetic ratio, which is $\gamma = 2.68 \cdot 10^8 \text{ rad} \cdot \text{T}^{-1} \cdot \text{s}^{-1}$ in the case of the hydrogen atom. If a nucleus with a magnetic moment $\hat{\vec{\mu}} \neq 0$ is located in an external static magnetic field $\vec{B} = (0, 0, B_0)^T$ aligned in the z-direction, an interaction occurs that can be described by the following Hamiltonian $\hat{\mathcal{H}}$:

$$\hat{\mathcal{H}} = -\hat{\vec{\mu}}\vec{B} = -\hat{\mu}_z B_0 = -\gamma \hat{I}_z B_0. \tag{2.6}$$

Due to the Hamiltonian being a scalar multiple of $\hat{I}_z$, the Schrödinger equation $\hat{\mathcal{H}} \mid I, m\rangle = E_m \mid I, m\rangle$ holds and the energy eigenvalues E_m can be calculated as:

$$E_m = -\gamma \hbar m B_0. \tag{2.7}$$

This results in the splitting into $(2I + 1)$ equidistant energy levels known as the Zeeman effect. The energy difference between two consecutive levels is given by:

$$\Delta E = \gamma \hbar B_0. \tag{2.8}$$

In spin $\frac{1}{2}\hbar$ systems there are only two possible eigenstates, $|\uparrow\rangle = |\, \frac{1}{2}, +\frac{1}{2}\rangle$ and $|\downarrow\rangle = |\, \frac{1}{2}, -\frac{1}{2}\rangle$.

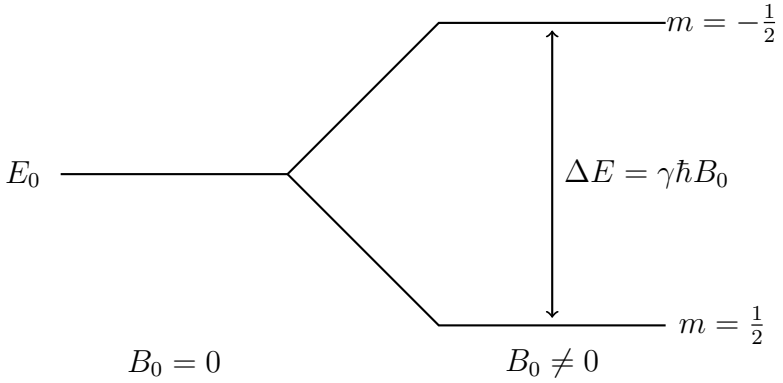

Figure 2.1: Zeeman-levels of the hydrogen atom in an external magnetic field $\vec{B}_0$. The energy difference between the two states is denoted as ΔE.

By introducing an additional magnetic field, known as radio frequency (RF) field, it is possible to induce a transition between two eigenstates. For this to happen, the frequency of the time-dependent RF field has to be ω_{RF} and it needs to be perpendicular to the magnetic field $\vec{B}_0$. The energy of the RF quantum must be equal to the energy difference $\Delta E = \gamma \hbar B_0$ between the two Zeeman levels:

$$E_{\text{RF}} = \Delta E$$

$$\omega_{\text{RF}} = \gamma B_0 = \omega_0. \tag{2.9}$$

This equation describes the resonance requirement and ω_0 is the so-called Larmor-frequency.

2.1.2 Macroscopic magnetization

In Section 2.1.1, we only considered a single ^{1}H nucleus. However, a macroscopic object is a vast ensemble of N nuclei, each with spin $\vec{I}$, following the relations described in Section 2.1.1. With an external static magnetic field along the z-axis $\vec{B} = (0, 0, B_0)$, and while in thermal equilibrium, the energy levels are occupied according to the Boltzmann statistics, resulting in the following occupation probability:

$$p_m = \frac{1}{Z} \cdot e^{-E_m/(k_\mathrm{B}T)} \tag{2.10}$$

where $Z = \Sigma_{m=-I}^{I} e^{-E_m/(k_\mathrm{B}T)}$ is the partition function, T is the temperature, and k_B is the Boltzman constant. In an ensemble of N hydrogen atoms, the expectation value for the z-component of the macroscopic magnetic moment $\langle\hat{\mu_z}\rangle$ can be calculated:

$$\langle\hat{\mu_z}\rangle = \gamma\langle\hat{I_z}\rangle = \gamma[p_{-\frac{1}{2}}\langle\downarrow|\ \hat{I}_z\ |\downarrow\rangle + p_{+\frac{1}{2}}\langle\uparrow|\ \hat{I}_z\ |\uparrow\rangle] = \gamma\frac{\hbar}{2}[p_{+\frac{1}{2}} - p_{-\frac{1}{2}}] = \gamma\frac{\hbar}{2}P \tag{2.11}$$

where the polarization P of the ensemble is defined as the occupation difference of the energy levels divided by the total amount of nuclei:

$$P = \frac{\Delta N}{N} = p_{+\frac{1}{2}} - p_{-\frac{1}{2}}. \tag{2.12}$$

Using the energy eigenvalues from equation 2.7, the polarization can be calculated by:

$$P = \frac{e^{\frac{\gamma B_0\hbar}{2k_\mathrm{B}T}} - e^{-\frac{\gamma B_0\hbar}{2k_\mathrm{B}T}}}{e^{\frac{\gamma B_0\hbar}{2k_\mathrm{B}T}} + e^{-\frac{\gamma B_0\hbar}{2k_\mathrm{B}T}}} = \tanh\left(\frac{\gamma B_0\hbar}{2k_\mathrm{B}T}\right). \tag{2.13}$$

In magnetic resonance (MR) experiments conducted at room temperature, it can be assumed that $\gamma\hbar B_0 \ll k_\mathrm{B}T$. This allows for a Taylor expansion of the hyperbolic tangent around $x = 0$:

$$P \approx \frac{\gamma B_0\hbar}{2k_\mathrm{B}T}. \tag{2.14}$$

Considering the settings used in this thesis, the resulting polarization is approximately $P \approx 10^{-6}$. The equilibrium macroscopic magnetization $\vec{M}_0$ can thus be expressed by the following equation known as the Curie law:

$$\vec{M}_0 = \frac{N}{V}\langle\hat{\vec{\mu}}\rangle = \gamma\frac{\hbar}{2}\frac{N}{V}\vec{P} \approx \frac{N}{V}\frac{\gamma^2\hbar^2}{4k_\mathrm{B}T}\vec{B}. \tag{2.15}$$

The Curie law describes temperature dependency as proportional to $1/T$. Despite the low polarization of 10^{-6}, a measurable signal can be acquired due to the high density of ^{1}H in biological tissue.

2.1.3 RF excitation

The macroscopic magnetization dynamics $\vec{M}$ in a time-dependent magnetic field $\vec{B}(t)$ can be described by the classical time evolution of the macroscopic magnetization:

$$\frac{\mathrm{d}\vec{M}(t)}{\mathrm{d}t} = \vec{M}(t) \times \gamma\vec{B}(t). \tag{2.16}$$

By applying a magnetic field $\vec{B}_1(t)$ in the x-y plane that rotates around the static magnetic field $\vec{B}_0 = (0, 0, B_0)$ the magnetization is forced into a motion around the superposition of the two fields $\vec{B} = \vec{B}_1 + \vec{B}_0$. If $\vec{B}_1(t)$ has the following form:

$$\vec{B}_1(t) = B_1 \begin{pmatrix} cos(\omega_{\mathrm{RF}} \cdot t) \\ sin(\omega_{\mathrm{RF}} \cdot t) \\ 0 \end{pmatrix}. \tag{2.17}$$

one can then superimpose $\vec{B}_1$ onto $\vec{B}_0$ an insert the superposition $\vec{B}$ into equation 2.16 and perform a coordinate transformation into a system (x', y', z') which rotates about the z-axis with the frequency ω_{RF}, thus obtaining:

$$\frac{\mathrm{d}\vec{M}'(t)}{\mathrm{d}t} = \vec{M}'(t) \times \gamma \vec{B}_{\mathrm{eff}}(t) \quad \text{with} \quad \vec{B}_{\mathrm{eff}}(t) = \begin{pmatrix} B_1 \\ 0 \\ B_0 - \frac{\omega_{\mathrm{RF}}}{\gamma} \end{pmatrix}. \tag{2.18}$$

If the resonance condition $w_{\mathrm{RF}} = \omega_0 = \gamma B_0$ is met, only the x-component of $\vec{B}_{\mathrm{eff}}$ remains, leading to a precession of the magnetization around $\vec{B}_{\mathrm{eff}}$ in the $y' - z$ plane with the frequency $\omega_1 = \gamma B_1$. The angle α between the magnetization and the z-axis can be calculated using:

$$\alpha = \int_0^{t_{\mathrm{p}}} \gamma B_1(\tau) \mathrm{d}\tau = \gamma B_1 t_{\mathrm{p}}. \tag{2.19}$$

Thus, α can be modified by a change of the field strength B_1 or the pulse duration t_{p}.

2.1.4 Relaxation process and Bloch equations

During and after excitation, the magnetization precesses around the z-axis and is driven back to its thermal equilibrium state. This phenomenon is known as relaxation and can be associated with two relaxation processes. During relaxation, the longitudinal magnetization M_z increases exponentially until it reaches the equilibrium state $M_z = M_0$, while the transversal magnetization $M_\perp$ decreases exponentially until $M_\perp = 0$. This phenomenon takes place due to the interaction of spins with their surroundings and with each other. Felix Bloch was the first person to describe this interaction. He expanded the classic magnetization equation 2.16, resulting in the Bloch-equations [46] that include the aforementioned relaxation processes:

$$\begin{aligned} \frac{\mathrm{d}M_x}{\mathrm{d}t} &= \gamma(\vec{M} \times \vec{B})_x - \frac{M_x}{T_2} \\ \frac{\mathrm{d}M_y}{\mathrm{d}t} &= \gamma(\vec{M} \times \vec{B})_y - \frac{M_y}{T_2} \\ \frac{\mathrm{d}M_z}{\mathrm{d}t} &= \gamma(\vec{M} \times \vec{B})_z - \frac{M_z - M_0}{T_1} \end{aligned} \tag{2.20}$$

The relaxation times are highly dependent on the chemical environment. The reason for the transversal relaxation time T_2 is the spin-spin interaction that leads to a loss in phase coherence. Therefore, the T_2 relaxation time is called the spin-spin relaxation time and describes the relaxation of the transversal magnetization. This

is caused by an energy exchange between the spins that leads to a loss in phase coherence. The T_1 time used in the formulas leads to the recovery of the longitudinal magnetization. It occurs due to the energy transfer to the surrounding lattice, which is why it is called the spin-lattice relaxation time. B_0 inhomogeneities, however, lead to faster dephasing of spin packages and result in a shorter T_2^* relaxation time. The temperature and degrees of freedom of the molecule are other factors influencing the relaxation process. To quantify the relaxation process, relaxation rates $R_1 = \frac{1}{T_1}$ and $R_2 = \frac{1}{T_2}$, which are the inverse relaxation times, are often used.

2.1.5 The NMR signal

By solving the Bloch-equations (eq. 2.20) for the static magnetic field in z-direction $\vec{B_0}$ the time-dependent evolution of the magnetization can be calculated:

$$M_\perp(t) = M_\perp(0) \cdot e^{i\omega_0 t} e^{-t/T_2} \tag{2.21}$$

$$M_z(t) = M_0 - (M_0 - M_z(0)) \cdot e^{-t/T_1} \tag{2.22}$$

with $M_\perp = M_x + iM_y$ and $M_z(0)$ or $M_\perp(0)$ being the magnetization component right after the irradiation.

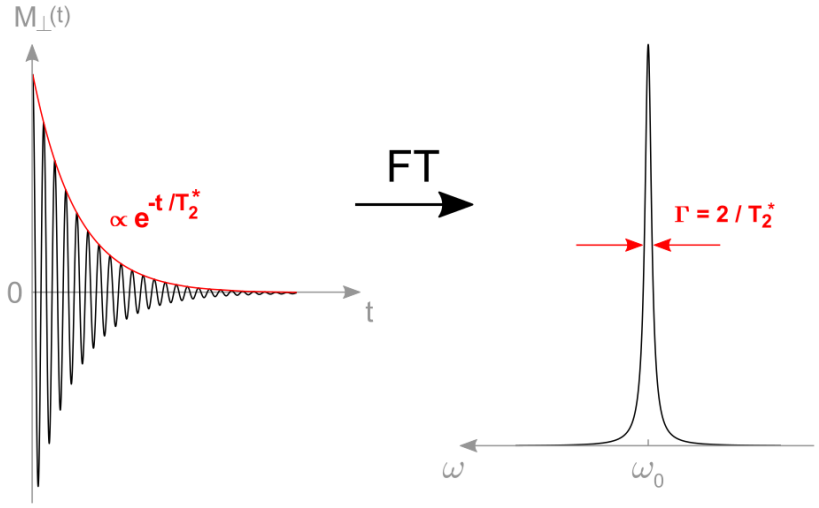

Figure 2.2: Left: display of a free induction decay (FID). Right: Fourier-transformation of the FID with the peak at ω_0 and full-width-at-half-maximum (FWHM) of $\Gamma = 2/T_2^*$. Reprinted from [47].

In NMR experiments, the received signal is an induced voltage in the receiver coil caused by a temporal change in the transverse magnetization component $M_\perp(t)$ (Figure 2.2). The MR signal in a volume V can be described as:

$$S(t) = U_{\text{ind}} \propto \int_V \rho(\vec{r}) e^{i\omega_0 t} \mathrm{d}\vec{r} \tag{2.23}$$

where $\rho(\vec{r})$ is the spatial spin distribution. The MR signal decays exponentially towards zero due to the relaxation towards the thermal equilibrium.

$$S(t) = S_0 e^{i\omega_0 t} e^{-t/T_2^*}. \tag{2.24}$$

The process of Fourier transforming the time-dependent FID in eq. 2.24 produces a frequency spectrum, as illustrated in Figure 2.2. The resulting spectrum has a Lorentzian line shape, with a FWHM Γ equal to $2/T_2^*$. The center frequency of the Lorentzian peak is the Larmor-frequency ω_0, which indicates the resonance frequency of the spin population.

2.1.6 Chemical shift

When hydrogen atoms are bound in a molecule, the protons get screened by the molecular environment. This causes a local change in the B_0 field as follows:

$$\vec{B}_{\text{local}} = \vec{B}_0 + \delta\vec{B} = \vec{B}_0(1-\sigma) \tag{2.25}$$

where σ is the shielding constant that depends on its chemical environment. The change of the resonance frequency caused by the extra shielding constant is given by:

$$\omega = \omega_0 + \delta\omega = \gamma B_0(1-\sigma). \tag{2.26}$$

The shift $\delta\omega$ of the resonance frequency is called the chemical shift and is typically given in a B_0-independent frequency ratio relative to a reference frequency ω_{ref}:

$$\delta = \frac{\omega - \omega_{\text{ref}}}{\omega_{\text{ref}}} \cdot 10^6\,[\text{ppm}]. \tag{2.27}$$

The magnitude of the chemical shift is typically expressed in parts per million (ppm). Although the reference frequency can be chosen arbitrarily, in most ^{1}H spectroscopy cases, it is set as the Larmor-frequency of the methyl groups of tetramethylsilan (TMS) [42]. For magnetization transfer experiments, the water signal is used as a reference for the CEST-spectrum. In NMR spectra, it is customary to label the frequency axis from higher to lower frequencies.

2.2 Magnetic resonance imaging

To localize the signal origin within the measurement volume, the volume has to be spatially encoded, as described below.

2.2.1 Spatial encoding

Spatial encoding is achieved by adding a magnetic field gradient $\vec{G} = (G_x, G_y, G_z)$, resulting in a spatially dependent magnetic field strength:

$$\vec{B}(\vec{r}) = \vec{B}_0 + (\vec{G}\cdot\vec{r}) \tag{2.28}$$

where $\vec{r}$ is the spatial position. By using a gradient field aligned parallel to the static magnetic field ($\vec{G}||\vec{B}_0$), the original quantization axis of the nuclear spins is preserved, and the position of the spins is now encoded by their resonance frequency:

$$\omega_0(\vec{r}) = \gamma(B_0 + \vec{G}\cdot\vec{r}). \tag{2.29}$$

In MRI, three techniques, all based on this principle, are used consecutively to encode all three spatial dimensions.

Slice selection

A linear gradient $\vec{G}(z)$ in z-direction is applied during excitation and yields the following Larmor frequency dependent on z:

$$\omega_0(z) = \gamma(B_0 + G_z \cdot z). \tag{2.30}$$

This gradient enables the selection of a single image slice by using a sinc-shaped RF excitation pulse. The position of the slice is determined by the pulse's center-frequency ω_{RF} and the slice width can be adjusted by varying the pulse bandwidth $\Delta\omega_{\mathrm{RF}}$ or the gradient strength:

$$\Delta z = \frac{\Delta\omega_{\mathrm{RF}}}{2\pi\gamma G_z}. \tag{2.31}$$

Frequency encoding

After slice selection, only the x- and y-direction are left to encode. The x-direction can be encoded by application of a gradient G_x in the x-direction during readout. This gradient results in the following x-dependent Larmor frequency:

$$\omega_0(x) = \gamma(B_0 + G_x \cdot x). \tag{2.32}$$

Following the equation, the acquired signal contains the sum of all frequencies. A Fourier transform of this frequency spectrum along the x-direction leads to a signal distribution as a function of x. However, at this point, the MR signal in each point x still consists of the sum of signal intensities across each line in y-direction.

Phase encoding

The encoding in the y-direction can be performed by manipulating the phase of the excited spin packages. The third gradient G_y is applied in the y-direction and encodes the y-direction after the excitation and prior to the signal acquisition. The magnetization accumulates a phase during the phase encoding period t_{PE}, which depends on the location y of the spin packages:

$$\Phi(y) = \frac{\gamma}{2\pi}\int_{t_0}^{t_{\mathrm{PE}}} G_y(t) \cdot y \mathrm{d}t. \tag{2.33}$$

Due to the accumulated phase remaining unchanged during the readout, N_y phase-encoding steps with different gradient strengths G_y are necessary to acquire an image with N_y data points along the y-axis. After acquiring the N_y phase-encoding steps, the final 2D image can be calculated by applying a second Fourier transform in the y-direction.

k-space

The signal obtained from MRI is represented in the k-space, which is the spatial frequency domain of an image. The central region of k-space holds information regarding basic contrasts, while the periphery of k-space encompasses sharp edges and finer details. To generate the final MR image in the spatial domain, a two-dimensional Fourier transform is applied to convert the k-space representation into an image.

2.2.2 Gradient echo imaging

The spatial encoding method described in Subsection 2.2.1 can be employed to create an imaging pulse sequence for actual acquisition. In this thesis, the gradient-echo sequence was utilized for measurements due to its ability to enable fast imaging with low repetition times.

The underlying principle of the sequence is the manipulation of the FID (see Fig. 2.3). To generate an echo, every gradient echo sequence consists of three main parts. First, an RF pulse with flip-angle α is applied, followed by a dephasing gradient along the readout direction. During the gradient application, the spin packages at different locations have different resonance frequencies, which leads to an accelerated dephasing. Finally, a rephasing gradient with opposite polarity and the same strength is applied at $\frac{TE}{2}$. This leads to gradient echoes after an echo time $t = TE$. Spoiling gradients are then used to dephase any residual magnetization in the xy-plane, enabling a short repetition time (TR). After TR elapses, the process is repeated with a different phase-encoding gradient strength until the whole k-space is filled. Since the TR can be very short, there is not enough time for a complete recovery of the magnetization towards the z-direction. The optimal flip angle α yielding maximal transversal magnetization for a given TR is much smaller than 90° and is known as the Ernst-angle α_{E}. Using this angle maximizes the residual magnetization in the z-direction and enables an imaging steady-state that is reached after several repetitions:

$$\alpha_{\mathrm{E}} = \arccos\left(e^{-TR/T_1}\right) \tag{2.34}$$

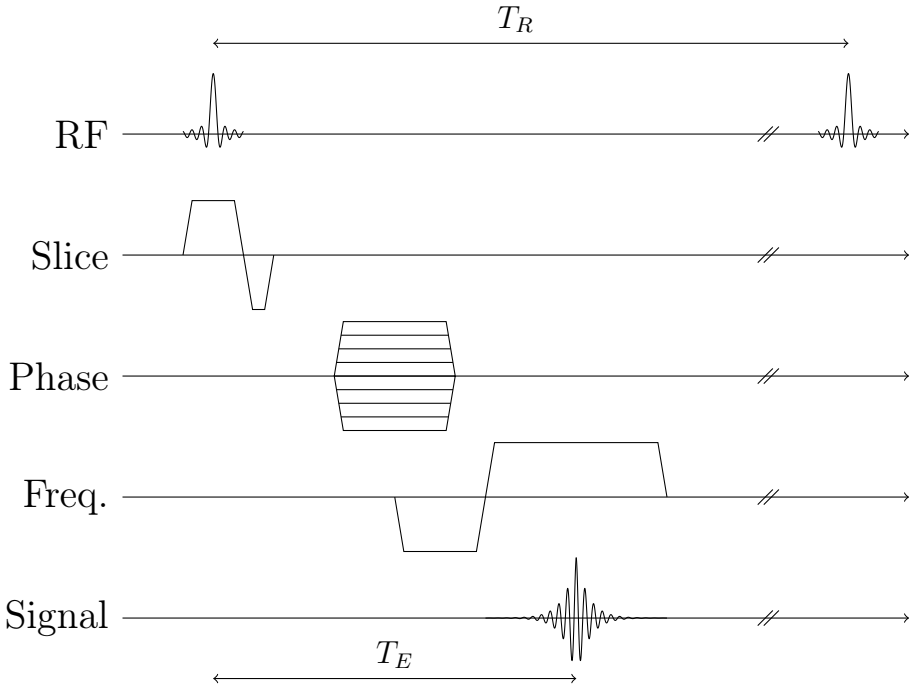

Figure 2.3: Design of a 2 dimensional gradient echo, or gradient-recalled echo (GRE)-Sequence, starting with a slice selective RF pulse, followed by two gradients used for phase and frequency encoding. After time T_E, the gradient echo occurs. Finally, after T_R elapses, the measurement is repeated for the next phase encoding step.

2.3 Magnetization transfer

The underlying concept for the chemical exchange saturation transfer (CEST) phenomenon is the detectable magnetization transfer from one compartment in biological tissue to another. For this purpose, one defines a pool i of protons with an identical chemical shift δ_i, uniform relaxation times T_{1i} and T_{2i} that exchanges magnetization with a second pool j with an exchange rate k_{ij}. All cases presented in this thesis are based on the following three fundamental exchange mechanisms that lead to magnetization transfer.

Chemical exchange

The chemical exchange process involves physically swapping chemically bound protons with protons from other molecules. This leads to the transfer of magnetization by detaching a proton from pool i and the consequent binding of the proton to a molecule in pool j. It is worth noting that the quantum mechanical state of the nuclear spin does not change during the exchange. This results in the transfer of magnetization from pool i to pool j.

Dipolar interaction

Spin systems can be coupled through dipolar interactions. This coupling enables cross-relaxation pathways between different pools that allow magnetization transfer. This effect is commonly referred to as nuclear Overhauser effect (NOE), and it largely depends on the type of spins involved, the distance between them, and their relative motion to one another.

Molecular exchange

The state of certain molecules can be either free or bound, depending on the structure of the surrounding macromolecules. These states are in constant exchange due to diffusion, which causes a variation in chemical shift and relaxation rate. As a result, there is a transfer of magnetization from one pool of molecules to another.

In the following subsections, the main magnetization pathways between water protons and protons connected to organic compounds are discussed in depth.

2.3.1 Chemical exchange

An acid-base reaction initiates the physical exchange of water protons and protons of specific functional groups in proteins, peptides, metabolites, etc. This exchange can be characterized by the exchange rate k_{sw}, representing the proton exchange rate from a solute proton pool s in a water pool w. More information about this concept can be found in references [48] and [49].

$$k_{sw} = k_{\text{base}}[OH^-] + k_{\text{acid}}[H_3O^+] + k_{\text{buffer}} \tag{2.35}$$

with $[OH^-]$ = hydroxide concentration, $[H_3O^+]$ = hydronium concentration, and the constants of proportionality k_{base} and k_{acid} which are the reaction rate constants

of the acid and base-catalyzed chemical reaction. The temperature dependency of the reaction rates k_{base}, k_{acid}, and k_{buffer} is given by the Arrhenius-equation [50]. Additional acid-base reactions are catalyzed by buffer systems covered by the constant k_{buffer}. By using the definition of pH and pOH as well as the logarithmic ion product of water $pk_w(T) = pH + pOH$ the exchange rate can be described by the pH-value and the temperature T:

$$k_{sw}(pH, T) = k_{\text{base}}(T)10^{pH-pk_w(T)} + k_{\text{acid}}(T)10^{-pH} + k_{\text{buffer}}(pH, T). \tag{2.36}$$

As the pH value increases, acid-catalyzed exchange processes are suppressed while base-catalyzed processes are enhanced. The dominance of acid-catalyzed or base-catalyzed proton transfer depends on the functional group involved, resulting in a varying exchange rate that may differ by several magnitudes.

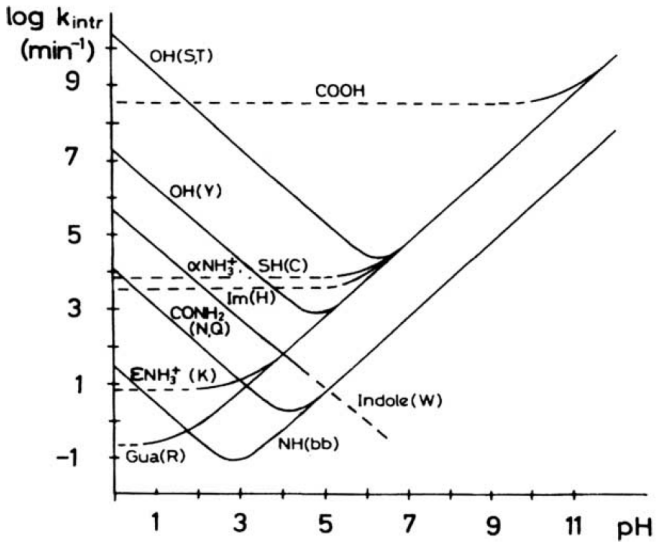

Figure 2.4: Logarithmic application of k_{sw} for various functional groups as a function of the pH value at a temperature of 25°C. (bb) refers to the backbone of the amino acid chain and the amino acids are noted by their one letter code. Reprinted from [51].

2.3.2 Dipolar interaction

Not all ^{1}H in molecules can physically exchange. The dipolar interaction solely leads to an exchange of spin states without any physical exchange. Time-varying magnetic fields oscillating at the Larmor-frequency can induce transitions between spin states. Molecular tumbling causes fluctuations in the local magnetic field and, with that, induces transitions between states. This mechanism is called the NOE. In this thesis, only the homonuclear NOE is relevant, which involves exchanges between the same nuclei type or, in this case, between two protons.

The dipolar cross-relaxation in coupled spin systems is described by the Bloch-Solomon equations [52]. In a system with two dipolar interacting spins, $\vec{I}_s$ and $\vec{I}_w$, from proton pool s and w, respectively, and an additional external magnetic field, transitions can occur between the four different coupled spin states $\mid sw\rangle$. The probability of each transition, denoted by W, depends on the interaction distance

r and the correlation time τ_c of molecular motion. The magnetization transfer is characterized by the cross-relaxation rate σ and the longitudinal relaxation rate ρ:

$$\sigma = W_{2ws} - W_{0ws} \tag{2.37}$$

$$\rho = W_{0ws} + 2W_{1ws} + W_{2ws} \tag{2.38}$$

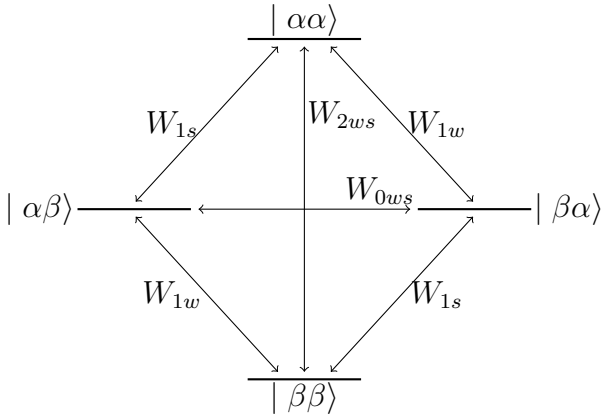

Figure 2.5: Depiction of energy levels of a dipolar coupled 2-spin system in an external magnetic field with the transition probabilities W_{ij}.

Equilibrium conditions for the cross-relaxation are given as :

$$\sigma_{sw} = f_w \sigma_{ws} \tag{2.39}$$

$$\rho_{sw} = f_w \rho_{ws}. \tag{2.40}$$

The cross-relaxation rate σ is given by:

$$\sigma(\tau_c, r) = \frac{\mu_0^2 \hbar^2 \gamma^4}{160\pi^2} \left(\frac{6}{1 + 4\omega_R^2 \tau_c^2} - 1 \right) \frac{\tau_c}{r^6} \tag{2.41}$$

with ω_R as the Larmor frequency. The negative cross-relaxation can be seen as a rate for the dipolar interaction.

2.3.3 Exchange-relayed nuclear Overhauser effect

The primary exchange of magnetization between non-exchanging covalently bound protons in macromolecules and water protons occurs through a mechanism called exchange-relayed nuclear Overhauser effect (rNOE). A schematic depiction of the process can be observed in Figure 2.6. Due to the short correlation time of unbound water and macromolecules, there is only a slow exchange possible via intermolecular dipolar coupling. Therefore, the more efficient combination of intramolecular spin diffusion continued by the intermolecular chemical exchange between protons bound in the macromolecule and the unbound water is favored [10, 16, 53].

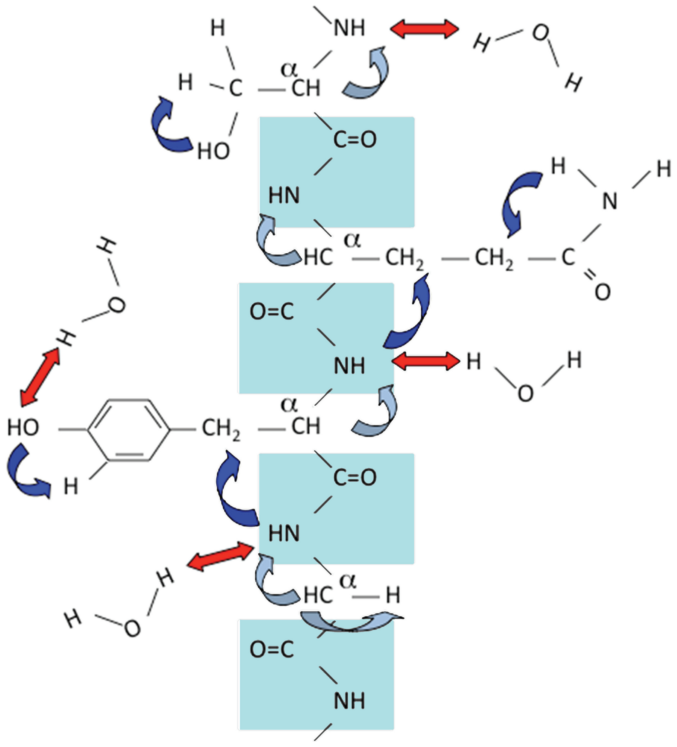

Figure 2.6: A schematic depiction of the two-step magnetization transfer process describing the rNOE. Intra-molecular magnetization transfer via spin-diffusion inside of the macromolecule is visualized with light blue and dark blue arrows. The following inter-molecular magnetization into the water pool via chemical exchange is depicted with red arrows. Reprinted from from [10].

The combined magnetization transfer rate is heavily restricted by the intra-molecular spin-diffusion, with a range of only 2-5 Hz [54]. Furthermore, changes in parameters such as pH value have almost no impact on the overall magnetization transfer rate [55, 15].

2.3.4 Semi-solid magnetization transfer

The semi-solid magnetization transfer (ssMT) refers to the magnetization exchange between water molecules and a macromolecular matrix. The protons in the macromolecular matrix have a T_2 relaxation time in the microsecond range, which is caused by the solid-like nature of the matrix. This short relaxation time results in a broad FWHM of the resonance in the order of kHz. As a result, the ssMT signal can only be utilized as an imaging contrast if measured indirectly through the water signal. The ssMT relies on magnetization transfer mechanisms that include [10]:

- inside the macromolecular matrix:
  - intra-molecular spin-diffusion
- between macromolecular matrix and free water molecules
  - inter-molecular dipolar coupling
  - inter-molecular chemical exchange
  - molecular exchange of water molecules

The exchange of molecules is possible because water can exist in both a free and bound state near the macromolecular matrix. When water is in the bound state, its mobility is heavily reduced, which leads to a longer correlation time of the water molecule, allowing inter-molecular coupling. This effect is supported by the continuous exchange of molecules through diffusion, which allows the transfer of magnetization into the free water. A schematic depiction of the process can be observed in Figure 2.7.

In summary, the intra-molecular spin-diffusion allows magnetization transfer inside the macromolecular structure, which is followed by magnetization transfer onto the free water by the inter-molecular NOE and chemical exchange. This process results in a magnetization rate of approximately 40 Hz [56].

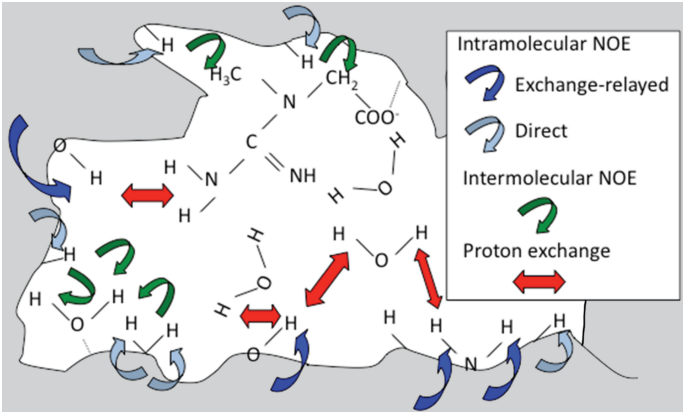

Figure 2.7: The process of semi-solid magnetization transfer enables the magnetization transfer between the macromolecular matrix (gray) and the water pool. First the intra-molecular magnetization transfer inside the matrix via rNOE (blue arrows) or spin-diffusion (gray arrows) occurs followed by the transfer into the water by inter-molecular NOE (green arrows) or chemical exchange (red arrows). Reprinted from [10].

2.4 Chemical exchange saturation transfer

With the help of the chemical exchange saturation transfer (CEST) experiment [8, 9, 10, 11, 12, 13], it is possible to indirectly detect a low-concentrated solute pool with a concentration in the millimolar range. This can be achieved by exploiting the magnetization transfer pathways from a solute pool s into the free water pool w. The introduction of these pathways can be found in Section 2.3. In general, the CEST process can be split into two phases:

- The frequency selective saturation of the solute pool
- The following acquisition of the modified water signal after magnetization was repeatedly transferred to the abundant water pool.

The indirect detection of the low-concentrated biomolecules via the water signal leads to a signal amplification called proton transfer enhancement (PTE). The PTE depends on the longitudinal relaxation times of the protons in the free water (T_{1w})

and the exchange rate between the pools and can be approximated as follows when a low-concentrated solute pool relative to the free water is assumed:

$$PTE \approx \frac{k_{\text{ex}}}{R_{1w}} \tag{2.42}$$

Due to this relationship, the CEST phenomenon enables the visualization of low-concentrated biomolecules with a spatial resolution of around 1 mm^3. The formula 2.42 suggests that an increased transfer of the magnetization between the pools (k_{ex}) and a longer storage of the magnetization within the water (R_{1w}) lead to an increase of the CEST effect. However, too fast exchange rates cannot be resolved.

2.4.1 Saturation transfer

As the name suggests, the CEST-pool s is saturated for a time t_{sat} during the saturation phase. This means that RF irradiation is used to induce an equal occupation of nuclear spin states $|I, m\rangle$ in the solute pool, which leads to a reduction of the overall magnetization to zero for a completely saturated two-state spin system. The process of presaturation consists of the saturation of a solute pool s using a frequency selective RF irradiation with a duration t_{sat} and an RF amplitude B_1. While this process is ongoing, the saturation of pool s is repeatedly transferred to pool w, resulting in an accumulation of the saturation in the water signal. This process is the basis for the signal amplification provided by the CEST experiment, as due to the transfer, the water magnetization is reduced. The reduced signal is immediately acquired/detected after the completion of the presaturation.

2.4.2 The Z-spectrum

Each frequency offset ($\Delta\omega$) in the Z-spectrum shows the remaining water magnetization M_Z^{sat} relative to the equilibrium value M_Z^0 depending on the frequency offset of the RF-irradiation:

$$Z(\Delta\omega) = \frac{M_Z^{\text{sat}}(\Delta\omega)}{M_Z^0}. \tag{2.43}$$

where $\Delta\omega = \omega_{\text{RF}} - \omega_w$ is the frequency offset of the presaturation pulse ω_{RF} with respect to the water resonance ω_w. By repeating the procedure of presaturation and subsequent water signal acquisition for different frequency offsets, one obtains a so-called Z-spectrum (Figure 2.8).

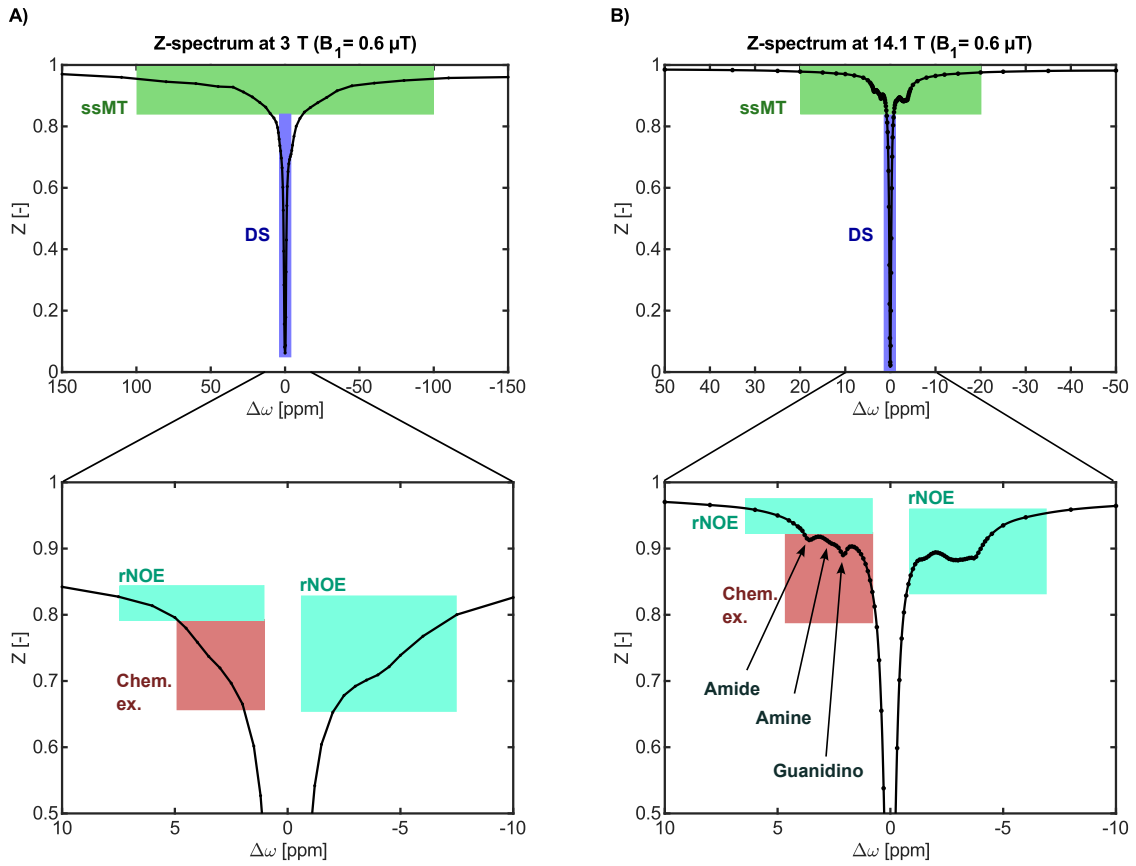

Figure 2.8: Example of an in vivo Z-spectrum at 3 T (A) and 14.1 T (B). The complete acquired frequency range (top) and zoom-in into the frequency range of the selective CEST-signals are provided (bottom). The ssMT (green), direct saturation (DS) (blue), rNOE (cyan), and chemical exchanging (red) region of the Z-spectra are marked. The increased spectral resolution at 14.1 T (B) allows the identification of the amide, amine, and guanidino resonances, which cannot be identified at 3 T (A).

Within an in vivo CEST measurement, multiple concomitant magnetization transfer effects occur, as listed below:

- The direct saturation of the water pool dominates the overall shape of the Z-spectrum (Figure 2.8, blue box). The minimum induced by this effect is at 0 ppm as it defines the reference frequency (Section 2.1.6) and reaches between ±1 ppm.

- The resonance of chemically exchanging protons can be observed in the downfield region of the Z-spectrum (positive ppm range) as dips right next to the signal of the direct saturation between 0.5 to 5 ppm (Figure 2.8, red box). The most prominent effect at the field strength of 3 T is due to the exchanging protons of amides (-NH), that exchange with a rate of 30 to 280 Hz [11, 57, 14, 25, 53, 58, 59, 60] at the frequency offset $\Delta\omega_{amide} \approx 3.5$ ppm. Additionally, the faster exchanging hydroxyl (-OH), guanidino ($-(NH_2)_2^+$) and amine protons ($-NH_2$) contribute at $\Delta\omega_{hydrox.} \approx 1.3$ ppm , $\Delta\omega_{gua} \approx 2$ ppm and $\Delta\omega_{amine} \approx 2.7$ ppm respectively. However, all three pools cannot be re-

solved well at 3 T because the fast exchange rates (2000 - 3500 Hz for hydroxyl [61, 62], 600 - 1600 Hz for guanidino [63, 57, 49, 58] and 700 - 10000 Hz for amine [64, 49]) lead to excessive peak broadening, and because their resonance frequencies are close to the water frequency.

- The rNOE effects, originating from covalently bound aliphatic protons, can be detected upfield (negative ppm range) from the water frequency at frequency offsets around -0.5 to -6 ppm (Figure 2.8, cyan box). However, rNOE originating from aromatic protons can also be detected in the corresponding downfield region of the Z-spectra around +0.5 to +6 ppm.

- Water molecules in macromolecular structures are less mobile than in the water pool, which results in a very short T_2 and, hence, a broad absorption line shape of the ssMT (Figure 2.8, green box), which is the most significant effect in vivo after the DS. This influence can be seen on the Z-spectrum over a wide range of offsets in the area of ± 50 ppm with a maximum at $\Delta\omega \approx -2.5$ ppm.3

2.4.3 The CEST pulse sequence

The CEST experiment, as previously mentioned, consists of two blocks: the saturation block in which the CEST-pool s is saturated for a time t_{sat} (as shown in Figure 2.9), and the subsequent image readout in which the modified water signal is acquired. For a sufficient acquisition of the modified signal, the image readout has to be performed immediately after saturation, and fast imaging readouts are favorable for CEST-MRI. This process is repeated until all desired frequency offsets are acquired. Presaturation can be achieved by using a continuous-wave (cw) irradiation at a single frequency with a duration t_{sat} and an RF amplitude B_1 (Figure 2.9 top). For whole-body MRI, the cw irradiation can only be used in a limited manner due to specific absorption rate (SAR) limitations. However, a series of n RF pulses can be used to reduce the SAR [65] (Figure 2.9, bottom). In this work, Gaussian pulses with a pulse length of 20 ms were used, corresponding to a bandwidth of approximately $BW \approx \frac{1}{t_{\mathrm{p}}}$. With the inter-pulse delay t_{d} and the pulse length t_{p}, the duty cycle (DC) can be described as:

$$DC = \frac{t_{\mathrm{p}}}{t_{\mathrm{p}} + t_{\mathrm{d}}}. \tag{2.44}$$

The saturation time can be calculated as follows:

$$t_{\mathrm{sat}} = n \cdot t_{\mathrm{p}} + (n-1) \cdot t_{\mathrm{d}} = (n-1) \cdot \frac{t_{\mathrm{p}}}{DC} + t_{\mathrm{p}} \tag{2.45}$$

where n is the number of pulses.

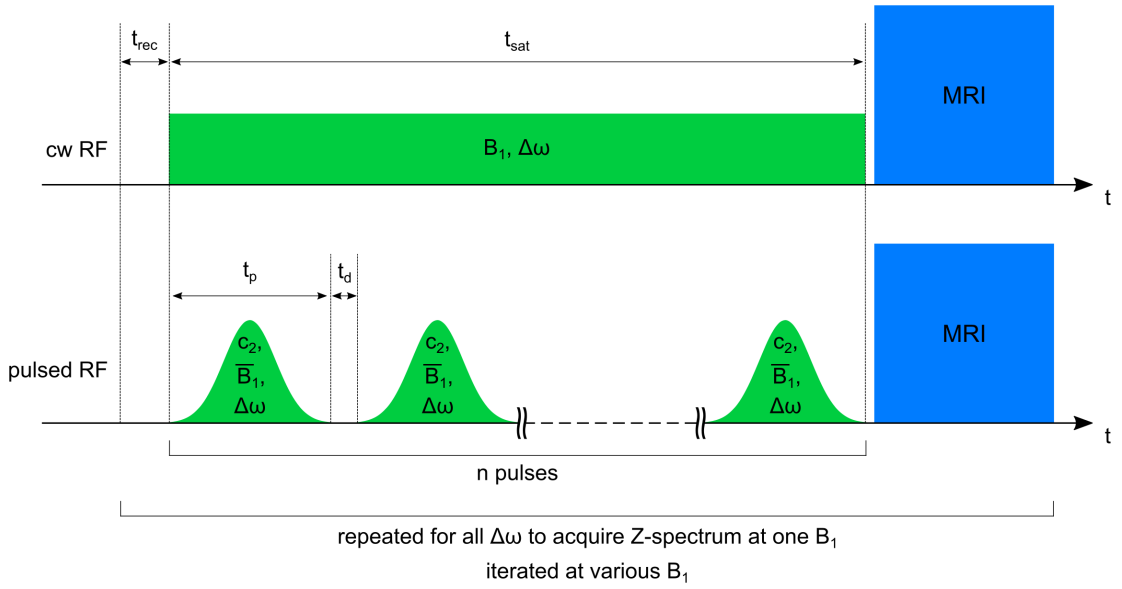

Figure 2.9: The CEST experiment consists of two blocks: (1) The saturation block, in which the CEST-pool s is saturated during time t_{sat} (green) and (2) the subsequent image readout, in which the modified water signal is acquired (blue). In this thesis, both a cw saturation (top) and the pulsed saturation (bottom) were used. c_1 and c_2 are form factors that represent the intra pulse DC (c_1) and the presaturation pulse shape (c_2). Reprinted from [47].

2.5 Theory of CEST and quantitative CEST contrast

In this section, the theoretical background of magnetization transfer experiments is detailed. Further information on all topics described in the following section is provided in the review articles [10, 11, 12, 25, 61].

2.5.1 Bloch-McConnell equations

The theoretical description of the CEST experiment is based on the pool model. A simple version is a two-pool model, including the protons from an abundant water pool w and the labile protons of a solute pool s. The protons included in each of the two pools are described by identical resonance frequencies, relaxation rates, and exchange rates with the other pool as shown in Figure 2.10.

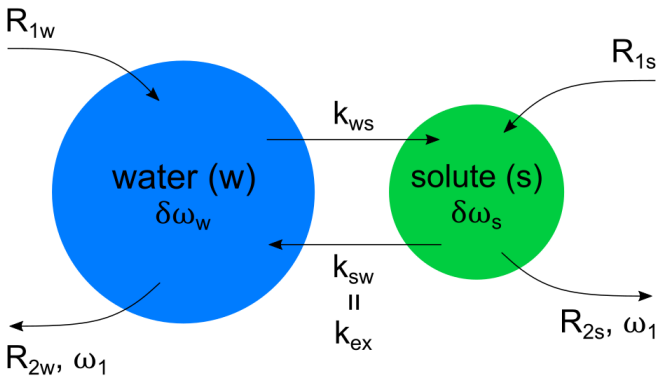

Figure 2.10: Depiction of the two-pool model, including the protons from an abundant water pool w and the labile protons of a solute pool s. The model describes the magnetization transfer between the two pools. The protons included in each of the two pools $i = w, s$ are described by identical resonance frequencies $\delta\omega_i$, relaxation rates R_{1i} and R_{2i}, and exchange rates with the other pool k_{sw} and k_{ws}. Reprinted from [47].

McConnell first formulated the mathematical equation for the time evolution of the magnetization vector $\vec{M}_w$ and $\vec{M}_s$ for the two-pool model, where a transfer of magnetization to one another takes place [66]. The so-called Bloch-McConnell equations extend the Bloch equations (eq. 2.20) by adding the exchange terms between the two pools.

$$\begin{aligned}
\tfrac{\mathrm{d}}{\mathrm{d}t}M_{xw} &= -\Delta\omega_w M_{\overline{yw}} R_{2w} M_{xw} && +k_{sw}M_{xs} - k_{ws}M_{xw} \\
\tfrac{\mathrm{d}}{\mathrm{d}t}M_{yw} &= +\Delta\omega_w M_{\overline{xw}} R_{2w} M_{yw} - \omega_1 M_{zw} && +k_{sw}M_{ys} - k_{ws}M_{yw} \\
\tfrac{\mathrm{d}}{\mathrm{d}t}M_{zw} &= +\omega_1 M_{yw} - R_{1w}(M_{zw} - M_{0,w}) && +k_{sw}M_{zs} - k_{ws}M_{zw} \\
\tfrac{\mathrm{d}}{\mathrm{d}t}M_{xs} &= -\Delta\omega_s M_{\overline{ys}} R_{2s} M_{xs} && -k_{sw}M_{xs} + k_{ws}M_{xw} \\
\tfrac{\mathrm{d}}{\mathrm{d}t}M_{ys} &= +\Delta\omega_s M_{\overline{xs}} R_{2s} M_{ys} - \omega_1 M_{zs} && -k_{sw}M_{ys} + k_{ws}M_{yw} \\
\tfrac{\mathrm{d}}{\mathrm{d}t}M_{zs} &= +\omega_1 M_{ys} - R_{1s}(M_{zs} - M_{0,s}) && -k_{sw}M_{zs} + k_{ws}M_{zw}
\end{aligned} \tag{2.46}$$

with the equilibrium condition:

$$k_{sw} \cdot M_{0,s} = k_{ws} \cdot M_{0,w} \tag{2.47}$$

and the exchange rates k_{sw} from pool s into pool w and vice versa k_{ws}. The R_{nm} are the longitudinal ($n = 1$) and transversal ($n = 2$) relaxation rates for the water pool ($m = w$) and the solute pool ($m = s$). The amplitude of the RF field at the resonance frequency $\Delta\omega$ is $B_1 = \frac{\omega_1}{\gamma}$ and the frequency offset of the RF field from pool s $\Delta\omega_s = \omega_{\mathrm{RF}} - \omega_s = \Delta\omega - \delta\omega_s$ is zero with on-resonant irradiation ($\omega_{\mathrm{RF}} = \omega_s \leftrightarrow \Delta\omega = \delta\omega_s$).

In this context, the proton fraction f_s can be defined as:

$$f_s = \frac{M_{0,s}}{M_{0,w}} = \frac{k_{ws}}{k_{sw}} \tag{2.48}$$

with the equilibrium magnetizations $M_{0,s}$ and $M_{0,w}$. The equation can be extended to a multi-pool model by including additional solute pools. Assuming that there is no interaction between the solute pools, which is valid for $N_s \ll N_w$, three additional equations have to be added for each additional pool (one equation for each spatial dimension).

2.5.2 Analytical solution of the Bloch-McConnell equations

An analytical solution to the first-order linear differential equations can be obtained by employing an eigenspace ansatz [26, 25, 67]:

$$\vec{M}(t) = \begin{pmatrix} M_{xw} \\ M_{yw} \\ M_{zw} \\ M_{xs} \\ M_{ys} \\ M_{zs} \end{pmatrix} = \sum_{n=1}^{6} e^{\lambda_n \cdot t} \cdot \vec{\nu_n} + \vec{M}^{\text{ss}} \tag{2.49}$$

where $\vec{M}(t)$ is the magnetization vector of the two pool system, $\vec{\nu_n}$ the eigenvectors with the corresponding eigenvalues λ_n, and the steady-state solution $\vec{M}^{\text{ss}}$. However, for sufficiently long saturation $t_{\text{sat}} \gg 1/R_{2,w}$, the only relevant contribution is represented by λ_1 with the eigenvector $\vec{\nu_1}$, that is co-linear to the effective magnetic field $\vec{B}_{\text{eff}}$. In the rotating frame, the eigenvalue can be approximated by:

$$\lambda_1 = -R_{1\rho} \tag{2.50}$$

where $R_{1\rho}$ [26, 68] is analogous to R_1 and defined as the spin-lattice relaxation rate in the rotating frame of reference. The magnetization transfer can be described as an exchange-dependent relaxation rate R_{ex} additional to the intrinsic relaxation rate of pool w R_{eff}. Therefore during the saturation pulse, the magnetization decays along $\vec{B}_{\text{eff}}$ with the rate $R_{1\rho}$, which is given for a two-pool system by:

$$R_{1\rho} = R_{\text{eff}}(\Delta\omega) + R_{\text{ex}}(\Delta\omega) \tag{2.51}$$

Defining the angle $\Theta(\Delta\omega) = \arctan\left(\frac{\omega_1}{\Delta\omega}\right)$ as the angle between $\vec{B}_0$ and $\vec{B}_{\text{eff}}$. The rate for the single water pool without exchange, $R_{1\rho,w}$ [68], is given by:

$$\begin{aligned} R_{1\rho,w}(\Delta\omega) = R_{\text{eff}}(\Delta\omega) &= R_{1w} \cdot \cos^2\Theta(\Delta\omega) + R_{2w} \cdot \sin^2\Theta(\Delta\omega) \\ &= R_{1w} + (R_{2w} - R_{1w}) \cdot \tfrac{\omega_1^2}{\omega_1^2 + \Delta\omega^2} \end{aligned} \tag{2.52}$$

Interestingly, the magnetization transfer can be understood as a spectral selective relaxation pathway. Therefore, the z-magnetization upon saturation for a time t_{sat} at a frequency offset $\Delta\omega$ is represented by the mono-exponential decay of the initial magnetization Z_i as follows:

$$Z(\Delta\omega, t_{\text{sat}}) = \left(Z_i \cdot \cos^2\Theta(\Delta\omega) - Z^{\text{ss}}(\Delta\omega)\right) \cdot e^{-R_{1\rho}(\Delta\omega)\cdot t_{\text{sat}}} + Z^{\text{ss}}(\Delta\omega) \tag{2.53}$$

where $Z^{\text{ss}}(\Delta\omega)$ is the steady state magnetization which is described by:

$$Z^{\text{ss}}(\Delta\omega) = \cos^2\Theta(\Delta\omega) \cdot \frac{R_{1,w}}{R_{1\rho}(\Delta\omega)} \tag{2.54}$$

Under the assumption that the water pool dominates the low-concentrated solute pool (meaning $f_w \gg f_s$, $k_{\text{ex}} \gg k_{ws}$, and $R_{1s} \ll k_{\text{ex}}$) the exchange dependent term only contains parameters of the exchanging pool and can be understood as a Lorentzian resonance around the resonance frequency $\delta\omega_s$ with a linewidth given by:

$$\Gamma_s = 2\sqrt{(R_{2s} + k_{\text{ex}})^2 + \omega_1^2 \cdot \frac{R_{2s} + k_{\text{ex}}}{k_{\text{ex}}}} \tag{2.55}$$

For in-vivo condition assuming $k_{\text{ex}} \gg R_{2w}$, R_{ex} can be approximated by [25]:

$$R_{\text{ex}}(\Delta\omega) = f_s \cdot k_{\text{ex}} \cdot \frac{\delta\omega_s^2}{\omega_1^2 + \Delta\omega^2} \cdot \frac{\omega_1^2}{\omega_1^2 + k_{\text{ex}}^2 + \Delta\omega_s^2} \tag{2.56}$$

Labeling efficiency

A further simplification of the R_{ex} can be assumed for the large-shift limit, meaning $\delta\omega_s \gg \omega_1$. The R_{ex} in the large-shift limit is given by [69]:

$$R_{\text{ex}}(\Delta\omega = \delta\omega_s) = f_s \cdot k_{\text{ex}} \cdot \alpha \tag{2.57}$$

where α is the so-called labeling efficiency [26, 70] given by:

$$\alpha = \frac{\omega_1^2}{\omega_1^2 + k_{\text{ex}} \cdot (k_{\text{ex}} + R_{2s})} = \frac{(\gamma B_1)^2}{(\gamma B_1)^2 + k_{\text{ex}} \cdot (k_{\text{ex}} + R_{2s})} \tag{2.58}$$

with $B_1 = \omega_1/\gamma$.

Multi pool system

When considering a multi-pool system where, as mentioned earlier, multiple solute pools exchange with the water pool but not with each other, and thus the exchange-dependent relaxation rates can be added to the water relaxation rate in the rotating frame as follows:

$$R_{1\rho}(\Delta\omega) = R_{1\rho,\text{wmt}}(\Delta\omega) + R_{\text{ex},s1}(\Delta\omega) + R_{\text{ex},s2}(\Delta\omega) + ... \tag{2.59}$$

where $R_{1\rho,\text{wmt}}(\Delta\omega)$ is the water relaxation rate, including the ssMT pool contribution. By including the ssMT and at least one exchanging solute pool, the steady-state magnetization equation changes to:

$$Z^{\text{ss}}(\Delta\omega) = \cos^2\Theta(\Delta\omega) \cdot \frac{R_{1,\text{obs}}}{R_{1\rho,\text{wmt}} + R_{\text{ex}}(\Delta\omega)} \tag{2.60}$$

where $R_{1,\text{obs}}$ is the observed longitudinal relaxation rate, which slightly differs from $R_{1,w}$ depending on the tissue composition.

2.5.3 CEST contrasts

To isolate an individual contribution of a CEST experiment, which often involves multiple exchanging solute pools, the concept of label and reference Z-spectra is utilized. The label Z-spectrum is the full CEST spectrum after irradiation at the solute resonance. On the other hand, the reference Z-spectrum should have minimal CEST labeling at the solute resonance but includes all other contributions of the label scan.

In reality, however, obtaining a reference scan with no solute labeling is impossible because one cannot keep the same amount of ssMT and DS effects and get rid of the solute-exchange effects. To approximate the reference scan, background estimations or asymmetry analysis using the opposite frequency are used in practice. In steady-state, the ideal label and reference values are determined by:

$$Z^{\text{ss}}_{\text{ref}} = \cos^2\Theta(\Delta\omega) \cdot \frac{R_{1,\text{obs}}}{R_{1\rho,\text{wmt}}}, \quad Z^{\text{ss}}_{\text{lab}} = \cos^2\Theta(\Delta\omega) \cdot \frac{R_{1,\text{obs}}}{R_{1\rho,\text{wmt}} + R_{\text{ex}}} \tag{2.61}$$

Magnetisation transfer ratio

With the established reference and label scan, the CEST effect of a single solute pool can be isolated with the simple approach of the $\mathrm{MTR_{LD}}$ (magnetization transfer ratio, linear difference (LD)) [71], which, in steady state, is given by:

$$MTR_{\mathrm{LD}} = Z^{\mathrm{ss}}_{\mathrm{ref}} - Z^{\mathrm{ss}}_{\mathrm{lab}} = \cos^2\Theta(\Delta\omega) \cdot \frac{R_{\mathrm{ex}} \cdot R_{1,\mathrm{obs}}}{R_{1\rho,\mathrm{wmt}} \cdot (R_{1\rho,\mathrm{wmt}} + R_{\mathrm{ex}})} \tag{2.62}$$

Spillover dilution

Although Equation 2.62 isolates the CEST effect of one solute pool, it still depends on $R_{1\rho,\mathrm{wmt}}$, which in turn means that an increase of the $R_{1\rho,\mathrm{wmt}}$, e.g. by increasing B_1, would lead to a decrease of the relative contributions of R_{ex}. Therefore, the observed CEST signals become diluted with the increasing size of the background effects. This effect is called spillover dilution and can be approximated as follows [61]:

$$\sigma' = Z^2_{\mathrm{ref}} = \left(\cos^2\Theta(\Delta\omega) \cdot \frac{R_{1\mathrm{obs}}}{R_{1\rho,\mathrm{wmt}}}\right)^2 \tag{2.63}$$

Using the spillover dilution and assuming $R_{\mathrm{ex}} \ll R_{1\rho,\mathrm{wmt}}$ equation 2.62 can be approximated as:

$$MTR_{\mathrm{LD}} \approx \cos^2\Theta(\Delta\omega) \cdot \frac{R_{\mathrm{ex}} \cdot R_{1,\mathrm{obs}}}{R^2_{1\rho,\mathrm{wmt}}} = \frac{f_s \cdot k_s}{R_{1,\mathrm{obs}}} \cdot \alpha \cdot \sigma' \tag{2.64}$$

When combining the labeling efficiency and spillover dilution, one can see that the spillover dilution has a strong influence on the optimal CEST effect, as an increase of the saturation power B_1 increases the labeling efficiency but also increases the spillover dilution, and vice versa.

Relaxation-compensated $\mathrm{MTR_{Rex}}$

The $\mathrm{MTR_{Rex}}$ [26, 25, 24, 72] is a metric primarily constructed to isolate the CEST effect of one solute pool and cancel the spillover dilution term, making it independent of DS and ssMT. Hence, the $\mathrm{MTR_{Rex}}$ allows for quantitative investigation of the CEST experiment and is given by:

$$MTR_{\mathrm{Rex}}(\Delta\omega) = \frac{1}{Z^{\mathrm{ss}}_{\mathrm{lab}}(\Delta\omega)} - \frac{1}{Z^{\mathrm{ss}}_{\mathrm{ref}}(\Delta\omega)} = \frac{R_{\mathrm{ex}}}{R_{1,\mathrm{obs}}} = \frac{f_s k_{\mathrm{ex}} \alpha}{R_{1,\mathrm{obs}}} \tag{2.65}$$

In the case of a pulsed presaturation, the equation changes to:

$$MTR^{\mathrm{pulsed}}_{\mathrm{Rex}}(\Delta\omega) = DC \cdot c_1 \cdot \frac{f_s k_{\mathrm{ex}}}{R_{1,\mathrm{obs}}} \cdot \frac{(\gamma B_1)^2}{(\gamma B_1)^2 + k_{\mathrm{ex}}(k_{\mathrm{ex}} + R_{2s}) \cdot c_2^2} \tag{2.66}$$

where c_1 and c_2 are form factors that represent the intra pulse DC (c_1) and the presaturation pulse shape (c_2). However, although the spillover dilution term was canceled, the $\mathrm{MTR_{Rex}}$ still depends on spillover dilution, as the accompanied contrast to noise ratio (CNR) loss cannot be reversed [61].

Amide proton transfer-weighted (APTw)

The most common metric used to analyze CEST experiments is the asymmetry analysis. This form of analysis is originally based on the assumption that there is only one exchanging solute pool and that the concomitant effects like DS and ssMT are symmetric with respect to the water signal. Therefore, the contributions of the DS and ssMT could be estimated by choosing the offset on the other side of the Z-spectrum. With a simple subtraction of Z-values, one could, therefore, isolate the exchanging solute pool. The $\mathrm{MTR_{asym}}$ can be calculated as follows [14, 70]:

$$MTR_{\mathrm{asym}}(\Delta\omega) = Z^{\mathrm{ss}}(-\Delta\omega) - Z^{\mathrm{ss}}(+\Delta\omega) = Z^{\mathrm{ss}}_{\mathrm{ref}} - Z^{\mathrm{ss}}_{\mathrm{lab}} \tag{2.67}$$

However, in vivo, the assumption is invalid, as there are multiple exchanging solute pools on both sides of the Z-spectrum, and the ssMT is known to be asymmetric. Although the calculation mixes all the contributors, it is still widely used as only a reduced number of offsets have to be acquired, limiting the acquisition time. In the remainder of this work, the $\mathrm{MTR_{asym}}(\Delta\omega)$ evaluated at $\Delta\omega = +3.5$ ppm will be referred to as APTw, as is common in the field.

2.6 Machine learning

This section covers the theoretical basis for the used machine learning (ML) models. For any further and more detailed descriptions, the interested reader may refer to the book 'The Elements of Statistical Learning' [45].

2.6.1 Linear regression

The basis of a linear regression (LR) model [73, 45] is the assumption that the regression function $E(y/\vec{x})$ is linear in the inputs x_j. The prediction generated by a LR model for an output centered around 0 has the form:

$$f(\vec{x}) = \sum_{j=1}^{p} x_j \beta_j \tag{2.68}$$

Where $\vec{x}$ is the input vector and β_j are the regression coefficients. The most popular method to estimate the coefficients β_j is the least squares method, where the residual sum of squares is minimized for a set of training data ($\vec{x}_1$,y_1)...($\vec{x}_N$,y_N), where each $\vec{x}_i$ is a vector of feature measurements with p features for N observations:

$$\hat{\vec{\beta}} = \underset{\vec{\beta}}{\operatorname{argmin}} \sum_{i=1}^{N} \left(y_i - \sum_{j=1}^{p} x_{ij}\beta_j \right)^2 = \underset{\vec{\beta}}{\operatorname{argmin}} \, ||\vec{y} - X\vec{\beta}||^2 \tag{2.69}$$

Where $\vec{y}$ is the N-vector of outputs in the training set, and X is the $N \times p$ matrix where each row represents one input vector. The unique analytical solution can now be determined with the Moore-Penrose pseudoinverse $X^+ = (X^T X)^{-1} X^T$ [74] as follows:

$$\hat{\vec{\beta}} = (X^T X)^{-1} X^T \vec{y} = X^+ \vec{y} \tag{2.70}$$

2.6.2 Gradient boosting tree regression

In this subsection, the theoretical background of gradient boosting (GB) tree regression is summarized, starting with an introduction to decision trees in general, followed by an explanation of GB trees in particular, with mean absolute error (MAE) as the employed loss function.

Decision tree regression

The regression tree [75] is the basis of GB tree regression. Starting with a dataset consisting of p input features for N observations $\vec{x}_i = (x_{i,1}, x_{i,2}, ..., x_{i,p})^T$ $(i \in N)$ and one output feature y_i, the algorithm aims to create a partition into M regions R_m and give each region a response value c_m. The combination of input feature values then decides what value c_m a data point $\vec{x}$ will get. This can be described with the following formula:

$$f(\vec{x}) = \sum_{m=1}^{M} c_m I(\vec{x} \in R_m) \tag{2.71}$$

where I is the partition function which is 1 for $\vec{x} \in R_m$ and 0 otherwise. The corresponding c_m, using the sum of squares as the minimization criterion, is simply the mean of the y_i in the region R_m:

$$\hat{c}_m = \text{ave}(y_i | \vec{x}_i \in R_m) \tag{2.72}$$

The regions themselves are created via recursive binary partitions of the dataset. First, the dataset is split into 2 regions. Then, one or both of these regions are split into two more regions. This process is repeated until a stopping criterion has been met. In regression trees, these splits are found by greedy algorithms, which means the splits are the locally optimal solution at each stage. When one looks at all data and considers the splitting variable j and splitting point s the two resulting regions can be defined as:

$$R_1(j,s) = \{\vec{x}_i | \vec{x}_{ij} \leq s\} \text{ and } R_2(j,s) = \{\vec{x}_i | \vec{x}_{ij} > s\} \tag{2.73}$$

The splitting variable j and splitting point s are therefore found by solving:

$$(j,s) = \underset{j,s}{\text{argmin}} \left[\sum_{\vec{x}_i \in R_1(j,s)} (y_i - c_1(j,s))^2 + \sum_{\vec{x}_i \in R_2(j,s)} (y_i - c_2(j,s))^2 \right] \tag{2.74}$$

with $\hat{c}_1 = \text{ave}(y_i | \vec{x}_i \in R_1(j,s))$ and $\hat{c}_2 = \text{ave}(y_i | \vec{x}_i \in R_2(j,s))$. This process is repeated until the desired number of terminal regions (regions that are not split any further) or an early stopping parameter is reached.

Gradient boosting tree regression

Based on the description of decision tree regression, the GB tree regression will now be explained. Boosting as a strategy combines the outputs of many base learners (decision tree, individual learner for an ensemble learning method) in a stage-wise fashion to produce a powerful model (ensemble learning method: combining multiple base learners to one powerful learner). The algorithm for creating a GB model [76, 77] can be described as follows (adapted from [45]):

1. The GB process is initialized with a first guess $f_0 = \underset{\gamma}{\operatorname{argmin}} \sum_{i=1}^{N} L(y_i, \gamma)$, where L is the loss function and γ the single response value for initialization.

2. Following for each $m = 1$ to M (maximum number of decision trees), these 4 steps are executed:

   (a) For $i = 1$ to N (number of observations), compute the negative gradient r_{im} based on all previous iterations ($f(\vec{x}_i)$ is the combination of all previously trained decision trees (f_1 - f_{m-1}) and the first guess f_0):

   $$r_{im} = -\left[\frac{\partial L(y_i, f(\vec{x}_i))}{\partial f(\vec{x}_i)}\right]_{f=f_{m-1}} \tag{2.75}$$

   (b) Fit a regression tree using the least squares method as described for the decision tree regression (previous paragraph) to the targets r_{im} to get regions R_{jm}, with j being the number of terminal regions.

   (c) The corresponding response values γ_{jm} are then calculated for each terminal region j as follows

   $$\gamma_{jm} = \underset{\gamma}{\operatorname{argmin}} \sum_{\vec{x}_i \in R_{jm}} L(y_i, f_{m-1}(\vec{x}_i) + \gamma) \tag{2.76}$$

   (d) Finally, the combined model is updated as follows:

   $$f_m(\vec{x}) = f_{m-1}(\vec{x}) + \sum_{j=1}^{J_m} \gamma_{jm} I(\vec{x} \in R_{jm}) \tag{2.77}$$

3. The final output of the model after M trees were created given an arbitrary input vector $\vec{x}$ can be calculated using:

   $$\hat{f}(\vec{x}) = f_M(\vec{x}) \tag{2.78}$$

Within this thesis, the absolute error was used as the loss function, and therefore, the negative gradient was the sign of the residuals:

$$L(y_i, f(\vec{x}_i)) = |y_i - f(\vec{x}_i)| \tag{2.79}$$

$$-\frac{\partial L(y_i, f(\vec{x}_i))}{\partial f(\vec{x}_i)} = \operatorname{sign}[y_i - f(\vec{x}_i)] \tag{2.80}$$

.

2.7 Interpretable machine learning methods

This section explains the theoretical background for the least absolute shrinkage and selection operator (LASSO) method, which introduces sparsity into the linear regression model, as well as the Shapley values, which are the theoretical basis for the Shapley additive explanations (SHAP) values. In this thesis, these concepts are crucial, as they allow for the interpretation of the ML models by creating insight into their decision-making process.

2.7.1 Least absolute shrinkage and selection operator

The least absolute shrinkage and selection operator (LASSO) method [78, 45] is a shrinkage method introducing sparsity into the model by penalizing large regression coefficients. The regression coefficient estimate (equation 2.69) is extended as follows:

$$\hat{\vec{\beta}} = \underset{\vec{\beta}}{\operatorname{argmin}} \left[\sum_{i=1}^{N} \left(y_i - \sum_{j=1}^{p} x_{ij}\beta_j \right)^2 + \lambda \sum_{j=1}^{p} |\beta_j| \right] = \underset{\vec{\beta}}{\operatorname{argmin}} \left(||\vec{y} - X\vec{\beta}||_2^2 + \lambda ||\vec{\beta}||_1 \right) \tag{2.81}$$

where $|| \cdot ||_1$ is the $\ell 1$ norm. The resulting optimization function no longer has an analytical solution, but still has a globally optimal solution [79] based on the $\ell 1$-regularization parameter λ. By increasing the value of λ, regression coefficients are constrained to be exactly zero, therefore creating a sparse solution. This process leads to a continuous parameter subset selection by increasing the value of λ. One problem is the introduction of a bias in the least squares objective function for the non-zero regression coefficients by the $\ell 1$-regularization term. This problem can be solved by dropping any regression coefficients from the set of variables after they are reduced to zero by the LASSO method, and then recomputing the current least squares optimization.

2.7.2 Shapley values

The Shapley value [80] (theoretical basis of the SHAP value Section 4.4.2) is a method from competitive game theory that enables the computation of feature contributions for a single prediction for any machine learning model. For linear models, such a calculation can be easily performed as there are no dependencies between the input features. The feature contribution ϕ_j of the j-th feature (total p-features) for one data instance $\hat{f}(\vec{x}) = \beta_1 x_1 + \beta_2 x_2 + ... + \beta_p x_p$, with $\hat{f}(\vec{x})$ being the predicted value, can be calculated as follows:

$$\phi_j(\hat{f}) = \beta_j x_j - E(\beta_j X_j) \tag{2.82}$$

where $E(\beta_j X_j)$ is the mean effect estimate for feature j. If summed over all features, one arrives at the following result:

$$\sum_{j=1}^{p} \phi_j(\hat{f}) = \hat{f}(\vec{x}) - E(\hat{f}(X)) \tag{2.83}$$

which is the prediction for data point x minus the average predicted value. The Shapley values enable the calculation of the feature contributions for single predictions as just performed by the linear model. The Shapley value can be calculated with the following function:

$$\phi_j(val_x) = \sum_{S \subseteq \{1,...,p\} \backslash \{j\}} \frac{|S|!(p - |S| - 1)!}{p!}(val_x(S \cup \{j\}) - val_x(S)) \tag{2.84}$$

where val_x is the value function for a subset of features S ($S \subseteq \{1, ..., p\} \backslash \{j\}$) used to build the model, defined as the prediction calculated by marginalizing over features P not included in S, as follows:

$$val_x(S) = \int \hat{f}(x_1, ..., x_p) \mathrm{d}(P)_{x \notin S} - E_X(\hat{f}(X)). \tag{2.85}$$

These formulas enable the calculation of Shapley values for each data point. The Shapley values are often used, as they are the only attribution method that satisfies the efficiency, symmetry, dummy, and additivity properties. Efficiency is given as the Shapley values add up to the difference of prediction x and the average similar to the linear model in equation 2.83. Symmetry results from the fact that two equally contributing features will get the same Shapley values. Additionally, a feature without contribution to the prediction always gets a Shapley value of 0, giving it the dummy property. Finally, additivity occurs because if one looks at two separate models and calculates the Shapley values, a combination of the separate models into one model would lead to an addition of the Shapley values.

Chapter 3

MR-based methods

In this chapter, the CEST-MRI related materials and methods are introduced. This includes a description of the used hardware, the software, the data acquisition protocol, the post-processing and data preparation, and finally, a description of the patient cohort.

3.1 MR imaging system

All measurements in this work were conducted using a whole-body MR scanner (MAGNETOM Prismafit, Siemens Healthineers, Erlangen, Germany; Figure 3.1 left) with a static magnetic field of $B_0 \approx 3$ T, leading to an ^{1}H resonance frequency of $\nu_0 \approx 127.74$ MHz. The signal acquisition was performed using a 64-channel receive head/neck coil (Figure 3.1 right), and the integrated transmit body coil was used for RF irradiation. The receive head/neck coil is made for high-resolution anatomical and functional head and neck examinations (Dimensions: 435 mm × 395 mm × 350 mm). To ensure that the B_0 magnetic field were as homogeneous as possible during the experiment, an automated 3D shim was performed beforehand utilizing additional shim coils.

Figure 3.1: The used 3 T whole-body MR scanner MAGNETOM Prismafit (Siemens Healthineers, Erlangen, Germany) at the national center for tumor diseases (NCT) in Heidelberg (left). The 64-channel receive head/neck coil from Siemens (right) is mounted at the end of the patient table facing the scanner bore.

3.2 Acquisition of MR data

In the following section, the CEST-related sequences used in this work are introduced, and the corresponding parameter settings are described. The used sequences are two low-power CEST scans, an APTw CEST scan, a water shift and B_1 (WASABI) scan, and a saturation recovery T_1 measurement. All of these scans are based on the Snapshot-CEST-Sequence by Zaiss et al. [81, 82] with a similar readout but variations in the recovery and saturation phase. The schematic description of the CEST pulse sequence can be found in Subsection 2.4.3.

3.2.1 Image readout

All images were acquired using a 3D spiral-centric-reordered gradient-echo acquisition. Because of the relaxation of the magnetization, a spiral path through the k-space starting in the center is chosen, which acquires the more critical lines in the k-space center first [81]. The readout parameters were selected as proposed by Goerke et al. [83] and are listed below.

Table 3.1: Image readout settings of the 3D spiral-centric-reordered gradient-echo acquisition as proposed by Goerke et al. [83]

FOV	220 x 179 x 48 mm^3
Matrix size	128 x 104 x 16
Resolution	1.7 x 1.7 x 3 mm^3
GRAPPA acceleration factor	2
Echo time (TE)	2.75 ms
Repetition time (TR)	5.5 ms
Bandwidth	340 Hz/pixel
Flip angle α_{flip}	7°
Elongation factor	0.5

The acquisition duration based on the chosen settings was $t_{\text{acq}} = 3.6$ s per 3D image.

3.2.2 Acquisition of CEST data

This subsection describes the saturation schemes for the low-power CEST scans and the APTw CEST scan. The image readout was performed equally in both cases, as described in the previous subsection.

Acquisition protocol for APTw CEST

The presaturation for the APTw protocol was performed as proposed by Zhou et al. [84], which is in line with the recently published consensus recommendations [40] . A total of 4 rectangular RF pulses with a B_1 amplitude of 2 µT, pulse length (t_{p}) of 0.2 s, and a 95% DC were used for saturation. This led to a total saturation time (t_{sat}) of 0.83 s. The Z-spectrum acquired with this saturation scheme entailed 16 offsets. The sampling was focused around the -3.5 ppm and +3.5 ppm offsets in the following manner: ±4 ppm (1 repetition), ±3.75 ppm (2 reps.), ±3.5 ppm (2 reps.),

±3.25 ppm (2 reps.), and ±3 ppm (1 rep.) (Figure 3.2, left). The recovery time before saturation was set to 2 s for all offsets. Additionally to these offsets, one fully relaxed M_0 measurement was acquired for normalization purposes at the beginning of the scan after off-resonant saturation at -300 ppm and with a recovery time of 12 s. The total acquisition time of the APTw scan was exactly 2 minutes.

Low-power fully-sampled Z-spectra

The presaturation for the two low-power fully-sampled Z-spectra was performed using 148 Gaussian-shaped RF pulses as proposed by Goerke et al. [83]. These RF pulses used had a mean B_1 amplitude (flip angle equivalent) of $B_1 = \alpha_{\text{flip}}/(\gamma \cdot t_{\text{p}}) =$ 0.6 µT and 0.9 µT, a length of $t_{\text{p}} = 20$ ms, and a DC of 80%. The resulting overall saturation time (t_{sat}) was 3.7 seconds. The Z-spectra acquired with this saturation scheme entailed 57 unequally distributed offsets ranging between ± 250 ppm (Figure 3.2, middle and right). Consecutive offsets were acquired without any recovery time. For normalization purposes, two fully relaxed M_0 measurements were acquired (i.e., one at the beginning and one the end of each CEST scan) to enable the calculation of an individual M_0 for each offset (recovery time = 12 s). The total acquisition time for one complete CEST image series was 7:36 min per B_1.

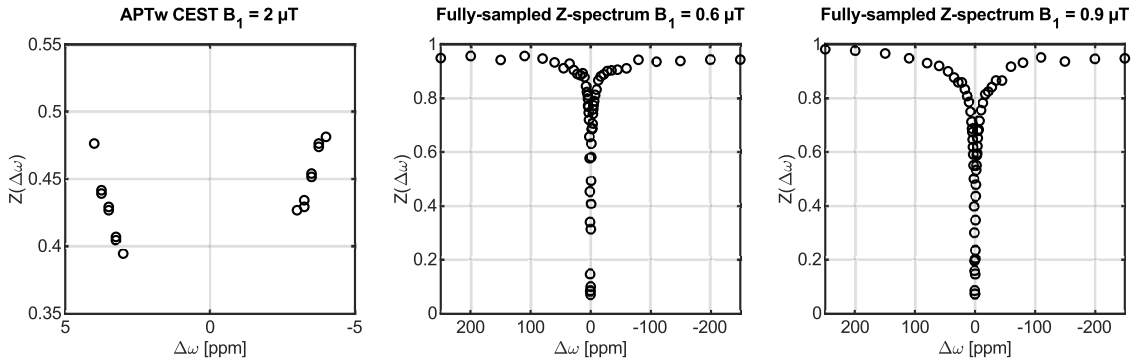

Figure 3.2: Unpost-processed Z-spectra acquired with the protocol for APTw imaging (left, B_1 = 2 µT) and with the protocol for low-power fully sampled Z-spectra (middle, B_1 = 0.6 µT; right, B_1 = 0.9 µT). The offsets at ±3.75 ppm, ±3.5 ppm, and ±3.25 ppm for the APTw imaging protocol were acquired twice to increase the signal-to-noise ratio (SNR).

3.2.3 WASABI scan

A water shift and B_1 (WASABI) scan was performed to map B_0 and B_1 field inhomogeneities. The measurement was conducted using a short rectangular preparation pulse with a pulse length of 5 ms and B_1 of 3.7 µT as described by Schuenke et al. [85]. This short off-resonant pulse induces a Rabi oscillation, resulting in a sinc-like Z-spectrum in the $\Delta\omega$ offset dimension, dependent on B_1 and the water frequency ω_0. The spectrum acquisition was performed using 31 equally distributed offsets between ±2 ppm with a recovery time of 3 seconds. Additionally, a fully relaxed M_0 measurement was acquired at the beginning of the measurement for normalization purposes (recovery time 12 seconds). The acquired WASABI-spectrum was fitted

with the following function to extract B_1 and ΔB_0 via $\Delta B_0 = \gamma \cdot \delta\omega$:

$$Z(\Delta\omega) = \left| c - d \cdot \sin^2\left(\tan^{-1}\left(\frac{\gamma \cdot B_1}{\Delta\omega - \delta\omega}\right)\right) \cdot \sin^2\left(\sqrt{(\gamma \cdot B_1)^2 + (\Delta\omega - \delta\omega)^2} \cdot \frac{t_p}{2}\right)\right| \tag{3.1}$$

With c and d as parameters that describe the amplitude and modulation of the oscillation.

3.2.4 T_1 determination

For determination of the relaxation time T_1, a saturation recovery sequence [44] was used. The signal preparation before the established image readout is a combination of saturation by three consecutive adiabatic half-passage pulses with $\mu = 6$, $t_p = 8$ ms, and BW=1200 Hz and a delay called recovery time ($t_{recover}$) in which the longitudinal relaxation of the protons back to the equilibrium magnetization is possible. In total, 11 images with 11 different recovery times were acquired to fit the recovery of the longitudinal magnetization M_z with the following function to extract the T_1:

$$M_z(t_{recover}) = M_0 + (M_z(0) - M_0) \cdot e^{-t_{recover}/T_1} \tag{3.2}$$

3.3 Study design

In this section, the study design is described, including an extensive description of the patient cohort and the examination protocol used for all measurements. This study was part of a German Research Foundation (DFG) project (project number: 445704496) with the primary goal of assessing the value of CEST-MRI as a potential biomarker for early prediction of therapy response for patients with glioma at a clinical field strength of 3 T.

3.3.1 Patient cohort

The local institutional review board committee approved this study. Written informed consent was obtained from each participant before study inclusion. Inclusion criteria were a minimum age of 18 years, a Karnofsky-Performance-Score of 50 or higher, and the legal capacity to consent to the study inclusion. From July 2018 until December 2022, 156 study participants who were being treated for diffuse glioma at the Department of Radiation-oncology of the University Hospital Heidelberg were prospectively enrolled in the study and underwent CEST imaging at least once (Figure 3.3). Of the total 156 patients, 89 study participants underwent 3 T CEST-MRI at baseline before radiotherapy (RT) (time point A), 72 patients at the first follow-up 4-6 weeks after completion of RT (time point B), and 19 patients spread between the second and fifth follow up after completion of RT (time point C). As a part of this thesis, only a subcohort was used for evaluation, where, only patients from time points A and B were included to get a balanced dataset, as point C would be underrepresented if included. Additionally, datasets were excluded if the quality assessment was unsuccessful or the dataset was incomplete due to problems during the acquisition process. These restrictions led to a total evaluated patient

cohort with 125 participants, of which 73 underwent CEST-MRI at baseline and 63 at the first follow-up after RT.

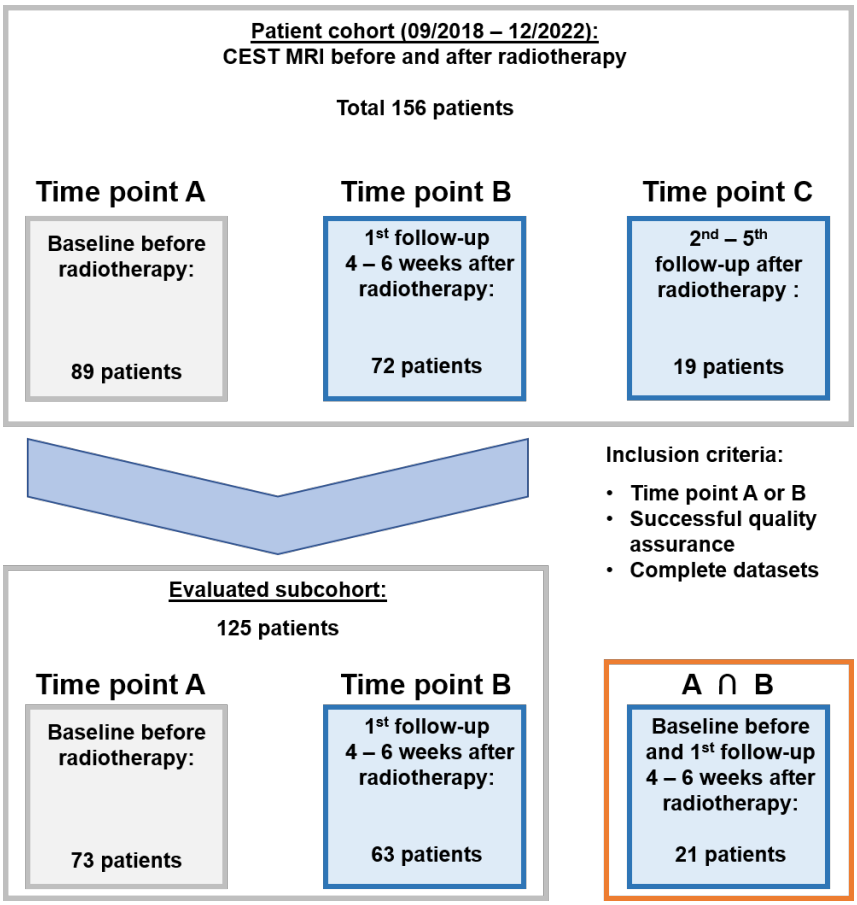

Figure 3.3: Description of the patient cohort and the evaluated subcohort. The entire patient cohort, including all 3 measurement time points before and after radiotherapy (RT) and the corrupted datasets, consisted of 156 patients and 180 datasets. After the exclusion of the corrupted datasets and the datasets acquired after the 1st follow-up, a total of 125 patients were included in this work.

3.3.2 Examination protocol

The CEST experiments were part of the clinical standard acquisition protocol. The entire acquisition protocol is 54:46 min long and can be split into 3 parts, beginning with a first block of clinical sequences (13:59 min), continuing with the CEST-MRI measurements as described in Section 3.2.2 (22:04 min), and ending with a second block of clinical sequences starting after injection of a gadolinium contrast agent (18:43 min):

- **1st block of clinical scans (13:59 min):** The 1st block of clinical sequences starts with an automated head scout sequence for positioning of the field of view. Subsequently, a T_1-weighted sequence, a T_2-weighted sequence, a diffusion-weighted imaging sequence, and a susceptibility-weighted imaging sequence are acquired as high-resolution 3D anatomical images.
- **WASABI scan (3:41 min):** Execution of the WASABI scan for B_0 and B_1 mapping as detailed in Subsection 3.2.3.

- **T_1 saturation recovery scan (1:15 min):** Execution of the T_1 saturation recovery sequence for quantitative T_1-mapping of water as detailed in Subsection 3.2.4.
- **Low-power fully-sampled CEST scan B_1=0.6 µT (7:34 min):** Acquisition of low-power fully-sampled Z-spectra with a nominal B_1 of 0.6 µT as described in the paragraph 'Low-power fully-sampled Z-spectra' in Subsection 3.2.2.
- **Low-power fully-sampled CEST scan B_1=0.9 µT (7:34 min):** Acquisition of low-power fully-sampled Z-spectra with a nominal B_1 of 0.9 µT as described in the paragraph 'Low-power fully-sampled Z-spectra' in Subsection 3.2.2.
- **APTw CEST (2:00 min):** Execution of the sparsely sampled APTw CEST sequence with a nominal B_1 of 2 µT as described in the paragraph 'Acquisition protocol for APTw CEST' in Subsection 3.2.2.
- **2nd block of clinical scans after injection of a contrast agent (18:43 min):** The second block of clinical sequences starts after injection of a Gadolinium contrast agent, comprising three T_2w sequences, a perfusion weighted sequence, and a T_1-weighted sequence.

3.4 Post-processing and data preparation

This section details the entire post-processing workflow of the CEST data and the data preparation for the ML methods. All evaluations are based on the reconstructed data from the scanner, which was exported using the digital imaging and communications in medicine (standard data format) (DICOM) file format. All post-processing was performed using in-house and self-written code in MATLAB© (The MathWorks Inc., Natick, USA, Version R2019b) if not stated otherwise.

3.4.1 Low-power CEST post-processing workflow

In this subsection, the post-processing steps necessary to calculate the B_1-corrected-relaxation compensated MTR_{Rex} contrasts based on the fully-sampled low-power Z-spectra (B_1 = 0.6 µT and 0.9 µT; from now on called low-power CEST) are described.

Image registration

As the acquisition of one fully-sampled low-power Z-spectrum takes around 7:34 minutes and the entire acquisition protocol, including WASABI and T_1 measurement, lasts around 20 minutes, intra-scan and inter-scan mismatches due to motion are very likely to occur. Therefore, a combined motion correction and image registration was the first step in the post-processing procedure. The image registration for the low-power CEST scans is based on the medical imaging interaction toolkit (MITK) [86] "slabbed Head" algorithm and was performed as proposed by Breitling et al. [87]. The motion correction procedure can be summarized in three steps. First, the

images were registered pairwise with Mattes' mutual information [88] as a similarity metric and a step gradient descent optimization [86, 89]. As the target image, the M_0 of the WASABI measurement was chosen to correct for inter-measurement motion. This image was chosen as a reference image for all maps included in the evaluation because all maps must align precisely to enable a voxelwise translation of the low-power data to the APTw contrast. Secondly, the proposed method by Breitling et al. [87] for the identification and mitigation of sporadic artifacts close to the direct water saturation was applied. Finally, the motion correction was performed with an adapted transformation for the identified artifact-afflicted offsets.

Normalization

After motion correction, the acquired low-power CEST data was normalized according to $Z(\Delta\omega) = \frac{M_{\text{sat}}(\Delta\omega)}{M_0(\Delta\omega)}$ to obtain the Z-spectra as described in Section 2.4.2. As a part of the low-power CEST scan, an M_0 image was acquired at the beginning and the end. This enables the calculation of an individual $M_0(\Delta\omega)$ for each offset $\Delta\omega$ by performing a linear interpolation.

B_0-correction

The correction for B_0 inhomogeneities was performed based on the ΔB_0-map extracted from the fit of the WASABI measurement (Section 3.2.3). The correction is necessary, as the B_0-inhomogeneities lead to a spectral shift of the entire Z-spectrum, which would impair the performance of the following denoising when unattended. The correction is performed voxelwise by shifting each Z-spectrum along the frequency dimension according to the corresponding ΔB_0 from the WASABI measurement. The shifting is performed as follows: First, the uncorrected Z-spectrum is fitted using a smoothing spline fit with a smoothing parameter of 0.999. Afterward, the $Z(\Delta\omega_{\text{corrected}})$ is extracted by evaluating the fitted spline function at $\Delta\omega_{\text{uncorrected}} + \Delta B_0$, which yields the B_0-corrected Z-spectrum after performed for every offset.

Denoising

It is challenging to isolate the individual components of the Z-spectra by using multi-pool Lorentzian fitting due to the inherently small magnitude of CEST effects at 3 T combined with the many free fit parameters. An increase of the SNR by averaging was not feasible, as this setup was meant for clinical use, and the necessary averages would lead to a significant scan time increase. However, due to the many spectra available through the 3D imaging protocol, a statistical denoising approach based on a principle component analysis (PCA) as described by Breitling et al. [90] was feasible. The PCA was performed per patient and low-power CEST spectrum, including only the brain voxels selected by an automated gradient-based brain segmentation. After this, the selected voxels were projected onto the first 13 components (mean PCA components of a patient subset selected with the Malinowskis factor (empirical) indicator function [91, 92]) from the PCA to generate the denoised Z-spectra only, including the components relating to the signal. The 13 first components were chosen as a the evaluation based on a subset of the

Fitting

A multi-pool Lorentzian fit [15, 93] was used to isolate the contributions to the Z-spectrum from concomitant effects. The basic assumption for the fit model is that a Lorentzian-shaped function can describe all pools. Due to the spectral resolution at 3 T, only the DS, the amide, rNOE, and ssMT pool can be reliably fitted. The Lorentzian function for the amide, rNOE, and ssMT pool is given by:

$$\mathcal{L}_s = A_s \cdot \frac{\frac{\Gamma_s^2}{4}}{\frac{\Gamma_s^2}{4} + (\Delta\omega - \delta_s)^2} \tag{3.3}$$

where δ_s is the resonance frequency of pool s, $\Delta\omega$ is the measured offset, A_s the amplitude, and Γ_s the FWHM of the Lorentzian. To account for the apparent bandwidth artifacts due to using a pulsed presaturation at 3 T, the Lorentzian of the DS, in addition to equation 3.3, includes a plateau as suggested by Deshmane et al. [82]:

$$\mathcal{L}_w = A_w \cdot \frac{\frac{\Gamma_w^2}{4}}{\frac{\Gamma_w^2}{4} + (x \cdot H(x) + y \cdot H(-y))^2} \tag{3.4}$$

where H is the Heaviside function, which was approximated with $H(z) = 0.5 + 0.5 \cdot \tanh(1000 \cdot z)$, $x = \Delta\omega - \delta_w - \frac{BW}{2}$, $y = \Delta\omega - \delta_w + \frac{BW}{2}$, and the bandwidth (BW) is the width of the plateau. With these functions the entire Z-spectrum can be fitted by a superposition as follows:

$$Z_{\text{lab}} = Z_{\max} - (\mathcal{L}_{\text{DS}} + \mathcal{L}_{\text{ssMT}} + \mathcal{L}_{\text{AMIDE}} + \mathcal{L}_{\text{rNOE}}) \tag{3.5}$$

$Z_{\max}$ is a constant offset to the Z-spectrum to account for possibly, incomplete relaxation of the water signal. The fitting was performed using the Levenberg–Marquardt algorithm [94] within MATLAB© (Version R2019b) and the fit parameters were optimized in previous work by Goerke et al. [83] and are provided in Table 3.2. An exemplary fit of the Z-spectra acquired at a $B_1 = 0.6$ µT and $B_1 = 0.9$ µT, respectively, is shown in Figure 3.4.

Table 3.2: Fit parameters used to fit the low-power Z-spectra (pools only). The parameters are presented in the following order: lower boundary | starting value | upper boundary.

Pool s	δ_s [ppm]	B_1 [µT]	Amplitude [-]	FWHM [ppm]
DS	-0.3 | 0 | 0.3	0.6	0.4 | 0.9 | 1.0	1.0 | 2.3 | 6.0
		0.9	0.4 | 0.9 | 1.0	1.0 | 2.3 | 6.0
APT	3.5	0.6	0.0 | 0.0 | 0.2	1 | 2 | 10
		0.9	0.00 | 0.06 | 0.20	1 | 2 | 15
rNOE	-3.5	0.6	0.0 | 0.1 | 0.2	2.0 | 4.0 | 12.5
		0.9	0.0 | 0.1 | 0.2	2.0 | 4.0 | 17.5
ssMT	-2.5	0.6	0.0025 | 0.1 | 0.3	30 | 60 | 100
		0.9	0.0025 | 0.1 | 0.3	30 | 70 | 170

Table 3.3: Fit parameters for $Z_{\max}$ and BW used to fit the low-power Z-spectra. The parameters are presented in the following order: lower boundary | starting value | upper boundary.

Parameter	B_1 [µT]	Value [-]
Z_{max}	0.6	0.5 | 1.0 | 1.0
	0.9	0.5 | 1.0 | 1.0
BW	0.6	0.0 | 0.3 | 0.7
	0.9	0.0 | 0.0 | 0.7

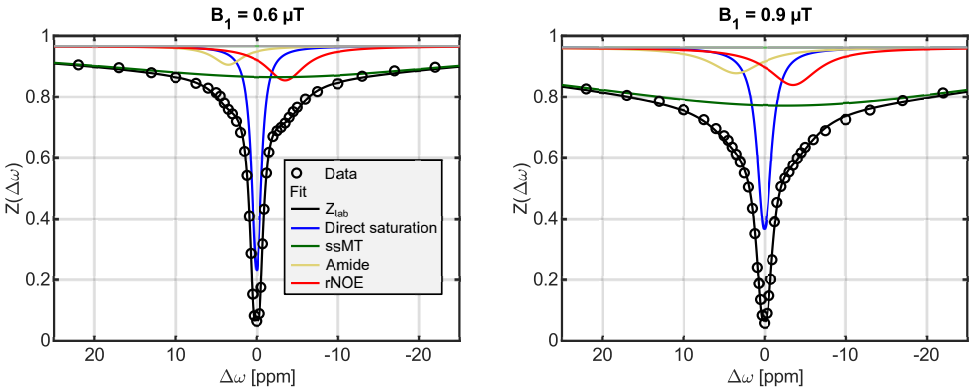

Figure 3.4: Exemplary multi-pool Lorentzian-fit of an exemplary acquired in vivo Z-spectra located in the normal-appearing white matter (NAWM). The spectra were acquired at $B_1 = 0.6$ µT (left) and $B_1 = 0.9$ µT (right). The boundaries and starting values of the fit parameters are listed in Table 3.2 and 3.3.

MTR_{Rex} contrast calculation

With the fit results from the muti-pool Lorentzian-fit, the label-spectrum (Z_{lab}) and reference spectrum (Z_{ref}) can be extracted for calculation of the MTR_{Rex} contrasts [25]. The label Z-spectrum represents all pools as described in equation 3.5 ($Z_{\text{lab}} = Z_{\text{fitted}}$). In contrast, the reference Z-spectrum Z_{ref} corresponds to the Z-spectrum Z_{lab} without the one specified pool s, described by:

$$Z_{\text{ref},s} = Z_{\text{fitted}} + \mathcal{L}_s \tag{3.6}$$

With this information, the isolated, spillover-corrected and relaxation-compensated MTR_{Rex} contrast can be calculated for the amide, rNOE, and ssMT pool according to equation 2.65. MTR_{Rex} values were calculated separately for each B_1.

B_1-correction

The B_1-correction of the MTR_{Rex} contrasts was performed using the relative B_1 maps acquired from the WASABI measurement. A correction for B_1 field inhomogeneities is crucial, as the CEST effect strongly depends on the saturation power B_1 through the labeling efficiency α, and therefore, local field differences would lead to different CEST effects for identical tissues. The correction was performed separately for the MTR_{Rex} AMIDE, MTR_{Rex} rNOE, and MTR_{Rex} ssMT using the 2-point correction method by Windschuh et al. [95]. For this method, 2 low-power CEST

measurements with different nominal B_1 amplitudes are required. The acquired contrasts at their local B_1 amplitude ($B_{1,\text{local}} = B_{1,\text{nominal}} \cdot B_{1,\text{rel}}$) and the additional data point at $MTR_{\text{Rex}}(B_1 = 0\ \mu\text{T}) = 0$ can then be used for reconstruction of the MTR_{Rex} contrast at any specific B_1 amplitude via interpolation. Within this work, the MTR_{Rex} contrasts were reconstructed to a B_1 field strength of 0.7 µT.

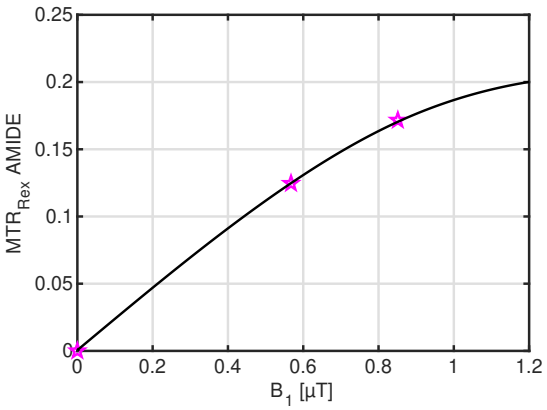

Figure 3.5: Interpolated MTR_{Rex} rNOE as performed for B_1 contrast correction with data acquired at two different nominal B_1. The stars indicate the two measurements and the point MTR_{Rex} rNOE ($B_1 = 0\ \mu\text{T}$) = 0.

3.4.2 APTw CEST post-processing workflow

This subsection details the post-processing steps necessary to calculate the APTw contrast. For the extraction and correction of the APTw contrast, only the APTw CEST scan and the WASABI measurement, for B_0 correction, are needed.

Image registration

Although the measurement time of the APTw CEST scan is only two minutes, thus reducing the risk of intra-measurement motion compared to the fully-sampled CEST scans, a motion correction is still mandatory for two reasons. First, as the purpose of this thesis is to create a voxelwise translation of the low-power CEST data into the APTw contrast, it is of high importance that all images align perfectly. Secondly, difference images are prone to motion-induced artifacts, as shown by Zaiss et al. [96] for dynamic CEST measurements. Therefore, it is also mandatory that all intra-measurement motion is reduced to a minimum, especially for a contrast that exhibits motion-induced artifacts in a similar order of magnitude compared to the expected effects. To ensure the best possible alignment, an image registration was validated for APTw imaging as a part of this work. The validation is thoroughly presented in Appendix A. The used image registration for the APTw CEST scan was the MITK "slabbed Head" algorithm [86]. The motion correction procedure is similar to the one for fully-sampled spectra, only leaving out the outlier detection, as it is unnecessary due to the absence of direct water saturation offsets. Therefore, only the pairwise image registration with Mattes' mutual information [88] as a similarity metric and a step gradient descent optimization [86, 89] was needed. As the target image, the M_0 of the WASABI measurement was chosen to align the WASABI, the two different low-power CEST scans, the T_1 measurement, and the APTw CEST scan as good as possible.

Normalization

After motion correction, the APTw CEST data was normalized according to $Z(\Delta\omega) = \frac{M_{\mathrm{sat}}(\Delta\omega)}{M_0}$ to obtain the Z-spectra as described in Section 2.4.2. The M_0 used was acquired at the beginning of the APTw CEST scan.

Averaging

Although fitting is not needed in the case of the APTw contrast, an increase of the SNR is still desirable due to the small size of the CEST effect. Because only 10 offsets are needed to calculate a B_0-corrected APTw contrast, the scan time is significantly reduced compared to the fully sampled spectra, making a repeated scan of the offsets ±3.25 ppm, ±3.5 ppm, and ±3.75 ppm possible while keeping a short acquisition time. In this post-processing step, the SNR was increased by averaging the repeated offsets.

B_0-correction

The B_0-correction was performed for the same reason and analogous to the one described for the low-power Z spectra on the averaged APTw Z-spectrum. Again, the correction was performed based on the ΔB_0-map extracted from the fit of the WASABI measurement(Section 3.2.3).

APTw contrast calculation

After B_0 correction, the contrast calculation using the asymmetry approach as described in Section 2.5.3 was performed. For this step, only the offsets at +3.5 ppm and -3.5 ppm are needed. The unit of the final contrast is %, and the contrast is calculated using $APTw = 100 \cdot (Z(-3.5\text{ ppm}) - Z(-3.5\text{ ppm}))$.

3.4.3 Evaluation pipeline

To handle the large amount of datasets described in Subsection 3.3.1 an evaluation pipeline was introduced as part of this work. The aim was to create a modular structure with high flexibility that is easy to execute by inexperienced users and enables a carefree and reliable evaluation of the CEST-MRI data.

To this end, a pipeline was created in MATLAB© (Version R2019b) that can be controlled with so-called evaluation tables. These tables, as presented in Figure 3.6, set the evaluation scheme for our datasets. Each row in these tables corresponds to one measurement, and the columns correspond to evaluation modules, which are the previously in-house written post-processing functions that will be executed for each measurement based on the parameters provided within the corresponding cell. The functions indicated by the module names are called consecutively by a control function, starting with module 1, row 1, and evaluating the function for each measurement with a non-empty cell in the same module column. When one module is successfully finished, the next module begins, building up on the previously executed modules. With the help of this pipeline, the entire patient cohort can be

reproducibly evaluated with only a few lines of code. The evaluation tables are always stored with the evaluated data structures to enable retracing of the executed evaluation steps.

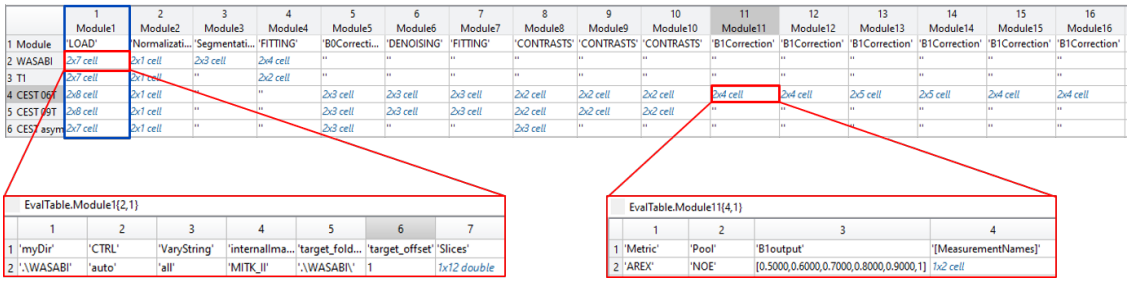

Figure 3.6: In this figure, the evaluation table used during this work is depicted. The rows are the different CEST-MRI measurements needed for evaluation, and in the columns, the different modules that need to be evaluated consecutively are listed. On the bottom the cell contents (settings for the evaluated functions) of two exemplary cells are shown. In the first row, the parameter name is listed, and in the second row, the parameter value is stored.

3.4.4 Quality assurance

A second problem caused by the large dataset is the inability to ensure the quality of every single dataset by hand. Therefore, an automated quality assurance check was implemented to, on the one hand, highlight highly problematic datasets that should be checked individually and, on the other, make automated adjustments for the bulk of patients by marking all voxels that do not follow specific quality criteria. When the marked voxels reached a limit specific to each criterion, an individual check was conducted. The criteria that should be met to not require an individual quality check were:

- **$7 <$ number of PCA denoising components < 15:** To get a quick assessment of the spectral quality of the fully sampled low-power Z-spectra, the denoising step was performed a second time without a fixed number of denoising components. Instead, the components were determined using the Malinowskis factor (empirical) [91] indicator function as described by Breitling et al. [90]. Then, all datasets with a number of determined denoising components lower than 15 and higher than 7 for both low-power CEST scans were deemed unproblematic. On the other hand, most patients with higher or lower components did show prominent artifacts or significantly noisier spectra. The threshold was found by analyzing the distribution of denoising components of a representative subset of the patient cohort.

- **Co-registration maximum $\mathbf{d_{RMS,meas}} < 5$ mm:** This measure was used to identify significant misalignments between the WASABI M_0 measurement and the offsets from the low-power Z-spectra before motion correction. The metric used for evaluation is the image misalignment d_{RMS} [97]. This metric calculated the misalignment of a voxel 7 cm away from the image center based on the transformation matrix T (determined by the registration algorithm). The metric can be calculated for each offset as follows:

$$d_{\mathrm{RMS}}(\mathbf{R}, \mathbf{t}) = \sqrt{\frac{1}{5} r^2 \cdot \mathrm{tr}(\mathbf{R}^T \mathbf{R}) + \mathbf{t}^T \mathbf{t}} \tag{3.7}$$

where $\mathbf{R}$ is the 3×3 rotation matrix, $\mathbf{t}$ is the 3×1 translation vector, and r is the radius specifying the volume of interest, which was set to 7 cm due to the acquired head geometry. If the $d_{RMS,meas}$ of any measurement per dataset exceeded 5 mm, the dataset exhibited possibly heavy motion or an erroneous image registration; therefore, an individual check was made in these cases.

The automated adjustments for the bulk of patients, meaning the exclusion of some voxels from evaluation, were performed using the following criteria:

- **Goodness of fit $<$ 0.95:** The goodness of fit is a measure of fit quality ranging from 0 to 1. All voxels with a fit quality of less than 0.95 were excluded from further evaluation as the fit results were considered untrustworthy in these cases. This criterion only affected the low-power spectra.

- **$|\Delta B_0|$ inhomogeneities $>$ 0.5 ppm:** Although both the low power Z-spectra and the APTw Z-spectrum were B_0-corrected, all voxels with a $|\Delta B_0|$ bigger then 0.5ppm were excluded. This criterion was introduced due to the sampling of the APTw Z-spectrum, which is restricted to a range of ±0.5ppm around the offsets +3.5ppm and -3.5ppm, which are necessary for evaluation. Therefore, every time ΔB_0 exceeds this range, the corresponding +3.5ppm and -3.5ppm APTw spectrum offsets must be extrapolated, making them untrustworthy. When only low-power data is evaluated, this range can be extended to ±1 ppm as the sampling of these spectra exceeds this range.

- **|relative $|B_1|$ inhomogeneities - 100%| $>$ 30%:** This rule was introduced for similar reasons as the previous $|\Delta B_0|$ criterion. However, in this case, it is because of the 2 B_1 power levels that were chosen and the reconstruction of the B_1-corrected contrasts at 0.7 µT (B_1). With a relative $|B_1|$ of 130% and 70%, the resulting MTR_{Rex} contrast maps can still be confidently reconstructed as shown by Windschuh et al. [95] but exceeding this limit, deviations are to be expected, and therefore the voxels to which the criterion applies were excluded from evaluations.

- **$MTR_{Rex,0.6\ \mu T} > (MTR_{Rex,0.9\ \mu T} \cdot 0.9)$:** The final criterion was chosen based on the fact, that theoretically, the MTR_{Rex} contrast of pool s, independent of the evaluated pool, should never be lower for a higher saturation power, as long as the other saturation parameters stay the same. Thus, a violation of this relationship would hint toward an erroneous voxel that should be excluded from evaluation. The error can arise from multiple ambiguous reasons. The factor 0.9 was introduced because voxels with small contrast values should not be excluded due to noise.

If these criteria combined led to the exclusion of more than 1000 voxels in the evaluated brain regions, the patient was also individually checked for exclusion from the cohort.

3.4.5 Brain annotation

In this subsection, the brain annotation process is described. This post-processing step was essential to differentiate between tissues and, therefore, enable brain region-specific evaluations. Additionally, brain regions known to express advanced artifacts can be excluded from the dataset or easily identified. The annotation process was performed in two steps, which are described in the following two paragraphs.

Tumor segmentation

A radiologist with experience in neuroimaging performed the 3D segmentation of the tumor region using an in-house developed segmentation tool in MATLAB© (Version R2019b).

The basis of the segmentation were the T_1-weighted contrast-enhanced (Matrix: 640 $\times$ 640 $\times$ 176; Voxel size: 0.4 $\times$ 0.4 $\times$ 1.0 mm^3) and the T_2-weighted (Matrix: 896 $\times$ 672 $\times$ 45; Voxel size: 0.3 $\times$ 0.3 $\times$ 3.0 mm^3) images. The segmented region was split into the whole tumor (WT) volume, comprised of the contrast-enhancing tumor volume plus peritumoral T_2w hyperintense signal alterations, the necrotic tissue, and the resection cavity. All relevant surgical-induced changes were excluded from the volumes of interest. A representative patient with tumor region of interest (ROI) is displayed in Figure 3.7 A.

Automated segmentation of normal appearing brain tissue

Following the tumor segmentation, the automated segmentation of the normal-appearing brain tissue was performed with a MATLAB© (Version R2019b) script, which was written within the scope of this work, based on statistical parametric mapping (SPM)12 [98] and the extension automatic anatomical labeling atlas 3 [99].

The basis of the automated 3D segmentation was the T_1w and a T_2w imaging data prior to injection of the contrast agent, same as for tumor segmentation. To enable reliable gray and white matter segmentation using the unified segmentation framework incorporated into SPM, the previously segmented tumor regions were substituted by NaNs for the input images. Following the framework, which enables image registration, tissue classification, and bias correction, and combines a tissue classification approach and a registration via template approach, could be executed successfully. The segmentation provides normal-appearing grey matter (NAGM), normal-appearing white matter (NAWM), cerebral spinal fluid (CSF), soft tissue, bone, and air/background masks. To enable regional analysis, the created masks for NAGM and NAWM were consequently combined with the SPM extension automatic anatomical labeling atlas 3, which provides a fully labeled brain atlas to generate gray and white matter ROIs in the frontal lobe, parietal-temporal region, and occipital lobe. Representative gray and white matter masks, as well as combined atlas-based ROIs, are illustrated in Figure 3.7 B and C.

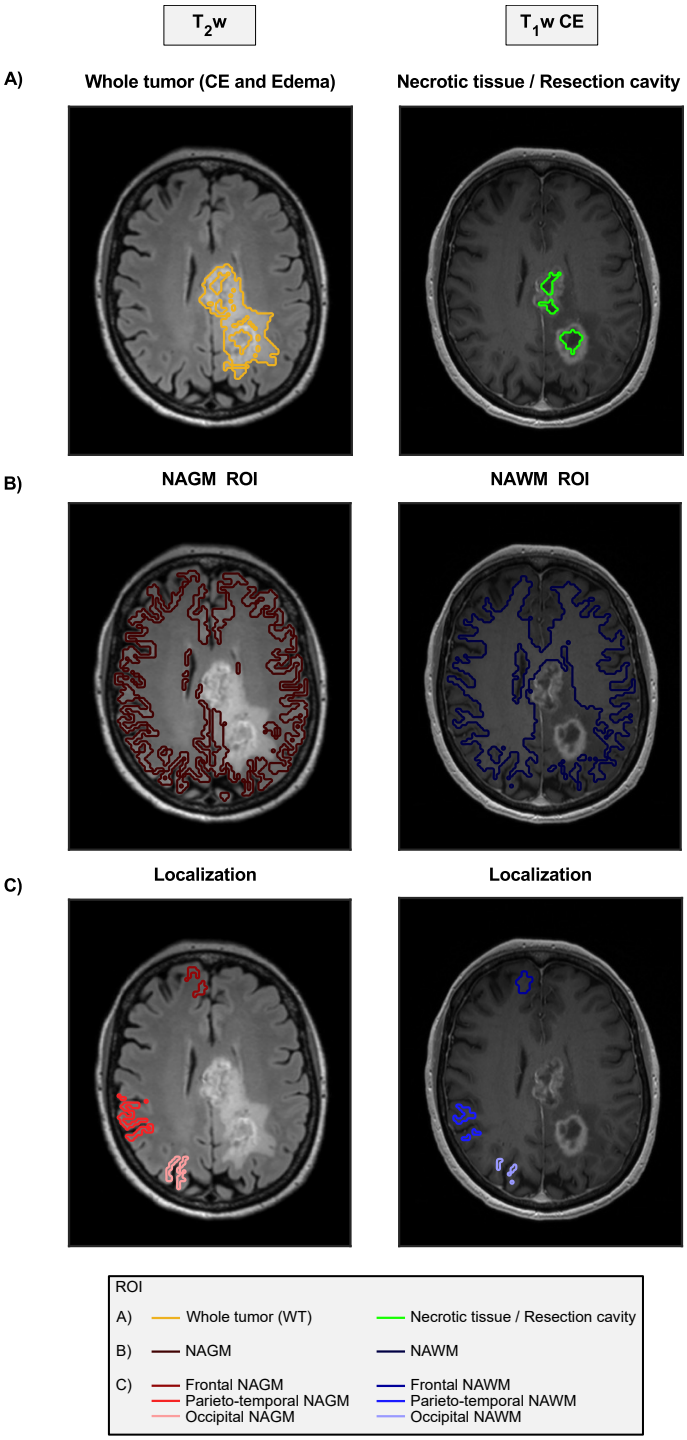

Figure 3.7: The basis of the segmentation were the T_1-weighted contrast-enhanced (right row) and the T_2-weighted images (left row). (A) A radiologist with experience in neuroimaging performed the 3D segmentation of the tumor region. The segmented region was split into the WT volume (top left), the necrotic tissue, and the resection cavity (shown combined in the top right). (B) The representative gray (left middle) and white matter (right middle) masks shown were created using the unified segmentation framework incorporated into SPM. (C) Finally, gray (left middle) and white matter (right middle) masks were combined with the automatic anatomical labeling atlas 3, to generate gray and white matter ROIs in the frontal lobe, parietal-temporal region, and occipital lobe. The regions were only displayed for the contralateral side for visualization purposes.

Chapter 4

ML-based methods

The goals of this thesis were to (i) use machine learning (ML) to create a working black-box model able to predict the high-power APTw contrast from low-power CEST data, proving that a transformation between the different saturation schemes is possible, followed by (ii) an in-depth analysis of the model using explainable artificial intelligence (AI) methods, and finally (iii) to combine the information to create a physically interpretable model (PIM), which enables an enhanced biophysical understanding of the APTw contrast in vivo and deciphers its underlying mechanisms.

This chapter begins by introducing the available dataset in its entirety and explaining the known influences on the APTw contrast (Section 4.1). In the following Section 4.2, the setup of the used machine learning models is described in detail. Section 4.3 explains the importance and dimensionality reduction methods employed in the context of the used models and the study's aim. Subsequently, the dependence plots used to interpret the model's differences are described (Section 4.4), and finally, the setup of the PIM based on the combination of a grid, partitioning the relevant B_1 and T_1 range into uniform-sized bins, and multiple linear regression models is explained in detail (Section 4.5).

4.1 Description of the dataset and the APTw contrast

In this section, the dataset used for all the trained models is introduced in its entirety. Additionally, the influences on the APTw contrast known from the literature will be described.

4.1.1 General description of the available data

The description of the dataset will be done on two levels. First, the voxel-wise available information will be described, followed by a report of the visual characteristics of the interpretable contrasts used for the PIM.

Available information per voxel

In the following list, all the information used to train the different ML models during this thesis is presented. As the post-processing is already described in Section 3.4, the focus of this section is on the reason why and the form in which the data was used for training. If not stated otherwise, the dimensionality of the listed features is 1.

- **APTw:** The final APTw contrast was always used as the singular endpoint for the different models after full post-processing as described in Section 3.4.
- **Low-power Z-spectra (B_1 = 0.6 µT and 0.9 µT):** The fully sampled low-power Z-spectra included 57 unevenly distributed offsets for each of the two B_1 saturation powers, ranging from -250 ppm to 250 ppm. The data was always used after correction of B_0-inhomogeneities but without any denoising or correction of B_1-inhomogeneities. This decision was made since denoising or the additional B_1-correction would dilute the information content of the spectra, and as the fully sampled spectra were used as a means of proving the feasibility of the prediction and not for interpretation, the data was needed as unaltered as possible. The B_0-correction had to be performed nevertheless, as the final contrast is also B_0- corrected, and an increase in complexity of the training task was unwanted.
- **ΔB_0:** The ΔB_0 was extracted from the WASABI-scan and mostly needed for quality assurance purposes. For APTw imaging, no QA restrictions regarding max B_0 inhomogeneities were in place for general evaluation of the contrast, but, due to the placement of the acquired offsets, B_0 inhomogeneities larger than |0.5 ppm| will have larger deviations and were therefore always excluded from the training and test data.
- **rel. ΔB_1:** The rel. ΔB_1 was also extracted from the WASABI-scan. This information was added to all training as input feature, since the APTw contrast was saturated with a much higher B_1 (2 µT) compared to the low power Z-spectra (0.6 µT and 0.9 µT). Additionally, the APTw contrast was not corrected for B_1-inhomogeneities, and therefore, theory dictates that the APTw contrast should be necessary to successfully predict the contrast, especially when using the B_1 corrected MTR_{Rex} contrasts as input features.
- **T_1:** T_1 was calculated from the saturation recovery scan. The T_1 value was included in all measurements, as saturation schemes and times were different between the two measurements, and both measurements were not performed in a steady state, making the relaxation time, in theory, vital for a successful prediction.
- **MTR_{Rex} AMIDE, rNOE, and ssMT:** The relaxation compensated contrasts were extracted from the fully post-processed low-power Z-spectra, including B_0-correction, denoising, and fitting of the spectra. The contrasts were then calculated and B_1-corrected (reconstructed at B_1 = 0.7 µT). After these post-processing steps, the contrasts are independent of one another, of B_1, and of B_0, and were therefore chosen as the basis of the PIM.

- **Tumor annotations:** The tumor annotations were provided by physicians. The annotations are binary calssification annotations provided for the tumor tissue tissue including edema and the combination of necrotic tissue and resection cavity. These annotations are critical as they are used to discriminate between tissues for evaluation and data selection purposes and enable performance analysis based on only tumor voxels. For more information about the annotation process and the available annotations, see Section 3.4.5.
- **Normal appearing tissue segmentation:** The normal appearing tissue segmentation was automatically performed as described in Subsection 3.4.5. The annotations are again in the form of binary classification annotations for each available ROI. The purpose of the segmentation was similar to the tumor annotation. On the one hand, the analysis of only NAGM and NAWM was enabled, and more crucially, the exclusion of CSF voxels from the evaluation was enabled, which is essential, as these voxels are more likely to exhibit artifacts.

The input features used for each model will be described at the beginning of each results section for clarity reasons.

Visual characteristics of the $\mathbf{MTR_{Rex}}$ AMIDE, $\mathbf{MTR_{Rex}}$ rNOE, $\mathbf{MTR_{Rex}}$ ssMT, and $\mathbf{T_1}$

In this paragraph, the visual characteristics of the relaxation compensated MTR_{Rex} AMIDE, rNOE, and ssMT as well as T_1 are described to enable a better understanding of the possible connection to the APTw contrast. Figure 4.1 shows the mentioned maps for one representative patient. T_1 is, as expected, increased in grey matter compared to white matter and even higher in CSF regions. Additionally, a slight increase can be observed in the tumor and edema region. When looking at the relaxation compensated contrasts, rNOE and ssMT have similar characteristics to one another. Both show decreased gray matter contrast and a hypointense WT region. The MTR_{Rex} AMIDE contrast, on the other hand, shows a reversed contrast behavior with a slightly increased contrast-enhanced region and a hyperintense NAGM contrast.

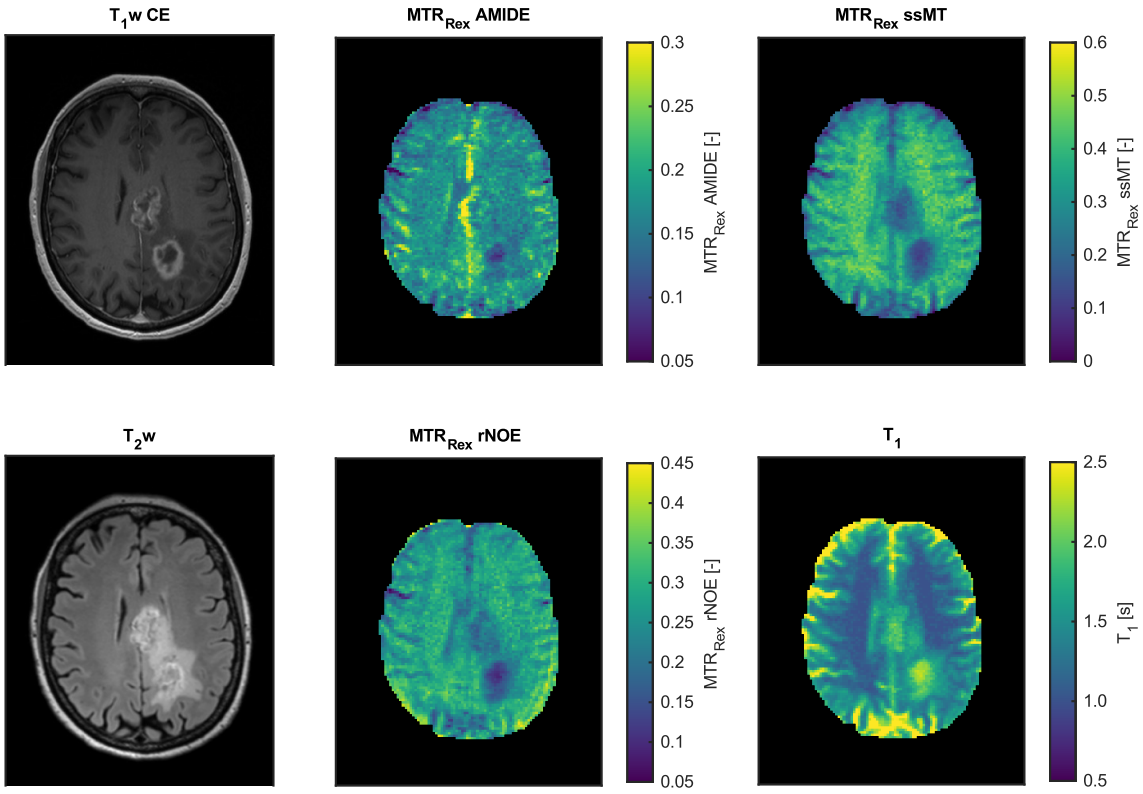

Figure 4.1: The relaxation compensated MTR_{Rex} AMIDE (top middle), rNOE (bottom middle), and ssMT (top right) as well as T_1 (bottom right) are displayed to discuss the visual characteristics of the contrasts. In addition, a T_1-weighted contrast-enhanced (CE) and a T_2-weighted map was added for orientation purposes.

4.1.2 Known influences on the APTw contrast in vivo

In this section, the known influences on the APTw contrast in the case of brain tumors as known from the literature are summarized [40]. In total, there are 6 dominant causes mentioned throughout the literature that seek to explain the increased APTw contrast in tumor tissue compared to normal-appearing brain tissue:

- **Increase of the amide proton signal:** The first mentioned confounder for an increased APTw contrast signal is the increase of the amide proton signal at 3.5 ppm. This increase can have multiple causes, such as the increase of mobile protein concentration (shown by proteomics [100] and in vivo MR spectroscopy [101]) or an increased exchange rate governed by an increase in intracellular pH-value (shown by phosphorus MR spectroscopy [102]).
- **Asymmetry of the ssMT:** A possible reduced asymmetry of the ssMT [103] in tumor voxels would also result in an increased APTw contrast, as the asymmetry promotes a lower Z-value on the upfield region compared to the downfield region of the spectrum due to its center frequency of approximately -3.5 ppm.

- **Change in the rNOE contributions:** Both upfield and downfield rNOE signals have possible implications on the APTw contrast. A decreased contrast in the tumor of the aliphatic rNOEs of mobile macromolecules around -3.5 ppm would lead to an increased APTw contrast [10, 15, 104, 105]. However, the downfield rNOEs from aromatic residues are located around +3.5 ppm and will, therefore, counteract the upfield rNOE [106, 28].

- **CEST signals from amine, hydroxyl, and guanidino protons:** The CEST signals from exchangeable amine, hydroxyl, and guanidino protons can also interact with the APTw contrast signal, enhancing it if there is a rise in any of the pool signals. Although the amines and hydroxyls are in the fast exchange regime at 3 T, the reduced extracellular pH may reduce their exchange rates and make them detectable at 3 T [107]. The guanidino protons from the intermediate exchange regime located at 2 ppm have an effective linewidth of around 2.0-2.5 ppm at 3 T and are, therefore, partially irradiated at 3.5 ppm [108].

- **Spillover and ssMT dilution:** Another influence on the signal is spillover and ssMT dilution [25]. The rNOE and APTw signals are always diluted by ssMT, and spillover of the direct water saturation is present in the case of the APTw contrast. Therefore, ssMT and T_2 water changes will also change the APTw contrast depending on the rNOE and amide signal.

- **Contamination through T_1 changes:** Finally, the T_1 of water also influences the APTw contrast in two opposing ways. On the one hand, the T_{1w} recovery effect increases the APTw signal contribution with higher T_{1w}, but on the other hand, a rising T_{1w} leads to lower Z-spectra, increasing dilution and therefore decreasing the APTw contrast [25, 109], therefore creating two opposing effects with a nonlinear relationship.

These mechanisms can also be used to describe other biological effects and their influence on the APTw contrast, such as liquefactive necrosis, which shows a hyperintense APTw contrast due to a high amount of proteins with high mobility and reduced dilution effects [34, 84].

4.2 Setup of the ML models

In this section, the data preparation and the setup of the LR and GB model are described in detail. Additionally, the reasoning for the choice of these selected models is presented. All training was performed on a workstation using an AMD Ryzen 9 5900X 3.7 GHz with 12 cores and 64 GB RAM.

4.2.1 Training data

The patient cohort used in this thesis comprises a total of 125 patients and 146 different datasets (21 patients had data acquired pre- and 4-6 weeks post-RT). The patient cohort is described in detail in Section 3.3.1, and the available features are described in the previous Section 4.1.1. This subsection gives an overview of the train-eval-test split and the total number of voxels available for training.

The training of the models, initial evaluations for model tuning, and hyperparameter tuning were always performed using the train and evaluation datasets. Only the final evaluations were done using the held-out test dataset. All splits in training, evaluation, and test datasets were performed on each acquired timepoint individually to ensure that time points were evenly distributed in all three splits. The test dataset was chosen as 20% of the total patient datasets available for each timepoint (pre- and post-RT). All splits were performed on a patient and not voxel level to ensure that there are no voxels in my test dataset that are from a patient that is also represented in my training dataset. The evaluation dataset was again chosen to be 20% of the residual datasets. All the information regarding the splits is summarized in Table 4.1.

Table 4.1: Overview of the train, evaluation and test splits of the datasets and corresponding voxel numbers per split and timepoint. All splits were performed on a patient and not voxel level

Timepoint	Datasets			Voxels		
	train	eval	test	train	eval	test
pre RT	53	13	17	2,587,459	678,516	837,051
post RT	40	10	13	1,926,456	513,726	583,772
overall	93	23	30	4,513,915	1,192,242	1,420,823

4.2.2 Setup of the linear regression models

A theoretical description of the linear regression (LR) model is found in Section 2.6.1. The LR model was used because the APTw contrast metric calculation is additive by nature, as seen in formula 2.67. Furthermore, LR models often provide adequate performance for tasks containing low CNR data, as is the case for the APTw contrast.

The solution of the model displayed as a weighted sum also makes it easily interpretable and transparent. Moreover, it is mathematically and computationally easy to estimate the regression coefficients, and finding the optimal coefficients is guaranteed. This makes approaches like LASSO (Section 4.3.1) feasible for a LR model, as the calculations only take about 1 s each. Finally, the inputs can be transformed or restricted to expand the application possibilities of the method to nonlinear problems.

The most significant downside is that LR models can only display linear relationships by nature, and all nonlinearities must be added by hand. Therefore, unknown nonlinear interactions will be oversimplified.

Setup

The LR was performed using MATLAB (Version R2019b). First, the input data matrix X and the output vector $\vec{y}$ were standardized to a column-wise mean zero and variance one to avoid the need for a constant intersect term and, more crucially, enable the comparison of the regression coefficients [45]. Afterward, the linear least

squares problem described in Section 2.6.1 was solved using the "pinv" function from MATLAB (Version R2019b) by calculating the pseudoinverse of the standardized input data matrix $Std.X_{\text{train}}$. This enables the calculation of the regression coefficients by multiplication with the standardized output vector $Std.y_{\text{train}}$. The prediction for the test dataset is then calculated as follows:

$$\vec{y}_{\text{test}} = Std.X_{\text{test}} \cdot \vec{\beta} \cdot SD(y_{\text{train}}) + \bar{y}_{\text{train}} \tag{4.1}$$

where $Std.X_{\text{test}}$ is the standardized test dataset, $\vec{\beta}$ is the vector of regression coefficients and $SD(y_{\text{train}})$ and $\bar{y}_{\text{train}}$ are the standard deviation (SD) and the mean of the output vector $\vec{y}$ calculated on the training data.

4.2.3 Setup of the gradient boosting tree regression models

When using tabular datasets, gradient boosting (GB) tree regression is one of the most popular and powerful ML techniques. This is due to their ability to find nonlinear relationships between the model features and target and their capability to deal with outliers and missing values. This makes the GB model essential for this work, as one aim is to extract or find the non-linearities in the prediction tasks. Additionally, the high amount of tuning possibilities enables further quality improvements of our model based on the underlying dataset, which is impossible with the LR model. Finally, the predictive power of GB trees also enables a good estimation for a best-case model.

The most significant downside of GB trees is, however, the missing interpretability of the models without any model agnostic interpretable AI methods, as well as the very long training times compared to LR.

A theoretical description of the GB tree regression can be found in Section 2.6.2.

Setup

All GB tree experiments were performed using Python (3.10) and the LightGBM library (version 3.3.5) [110] in its Python scikit-learn application programming interface [111]. Additionally, the scikit-learn (Version 1.2.1) [112] library was installed to enable grid search, cross-validation, and calculation of permutation importance.

The LightGBM library was chosen, as it has a higher training speed and lower memory usage than the comparable XGBoost algorithm [113] due to the usage of discrete bins instead of continuous features, therefore being well suited for large datasets, as in this case. The algorithm also performs with higher accuracy due to its ability to produce more complex trees, since the splits are made leafwise and not levelwise, as typical for regression trees.

In the following, the setup of the modeling process will be discussed. All models were trained using 5-fold cross-validation and were hyperparameter optimized using the combined grid search and cross-validation function 'RandomizedSearchCV' from scikit-learn. This function aims to reliably find the best suitable combination of hyperparameters for the corresponding task.

The process of cross-validation can be quickly described as follows: To perform n-fold cross-validation of a model [114], the training dataset is first split into n equally sized subsets. A model is then trained on $n-1$ of the n subsets and the last subset is used for performance evaluation. This process is performed for all n combinations of training and evaluation datasets possible with the n subsets to ensure a reliable evaluation of the model settings.

The 'RandomizedSearchCV' function uses this method and combines it with a randomized grid-search of the hyperparameters as follows: (i) First, a random combination of hyperparameters from a grid defined previous to training is selected by the algorithm. (ii) The combination is used for training and testing using the described cross-validation process. (iii) Steps (i) and (ii) are repeated for as many different combinations of hyperparameters as one defines. (iv) The mean performance per combination is calculated, and the best-performing combination is used to train the model again on all training data.

The non-default hyperparameters used for model tuning are shortly described in the following list:

- **boosting_type / drop_rate:** All training has been performed using the dropouts meet multiple additive regression trees (DART) [115] boosting type, enabling the use of the 'drop_rate' hyperparameter (0.2 for all models). The dropout hyperparameter means that x percent of the previously trained trees are ignored when calculating the pseudo-residuals for the current tree. The ignored trees are randomly chosen. This setting helps to reduce overfitting and the influence of the first-trained trees on the model predictions by increasing the predictive power of the later-trained ones.

- **metric:** As the metric for optimization, the MAE was chosen. This decision was made as the MAE puts less emphasis on observations with large residuals than e.g. the mean squared error, and is therefore more stable in datasets with many outliers, making it suitable for this work, as the datasets involved are realistic datasets including artifacts. The theoretical approach to creating such a model was described in Section 2.6.2.

- **n_estimators:** Is the number of trees trained. This parameter was determined with the grid-search algorithm, setting the maximum number of trees to 2500 to reduce the likelihood of overfitting.

- **num_leaves:** Maximum amount of tree leaves for a single regression tree. This parameter was determined via grid-search, and the maximum number was set to 32 leaves to reduce the maximum complexity of the individual trees. The tree leaves correspond to the terminal regions during the theoretical part.

- **lambda_l1:** Represents the ℓ_1-regularization term on weights. This parameter was determined via grid-search. The lambda_l1 hyperparameter adds an ℓ_1-regularization term of the form $\lambda_{\ell_1} \cdot \sum_{j=1}^{N} |w_j|$ (w_j: weights per leaf, N: number of leaves) when defining the weights on the leaves of each tree.

- **lambda_l2:** Represents the ℓ_2-regularization term on weights. This parameter was determined via grid-search. The lambda_l2 hyperparameter adds an ℓ_2-regularization term of the form $\lambda_{\ell_2} \cdot \sum_{j=1}^{N} w_j^2$ (w_j: weights per leaf, N: number of leaves) when defining the weights on the leaves of each tree.

- **feature_fraction / feature_freq:** The feature_fraction parameter reduced the total amount of input features that should be used to fit each tree. The feature frequency, on the other hand, dictates for what fraction of trees this should be performed. The selection of features is random every time. These parameters are beneficial, as a decreased feature space promotes diversity in the splitting features, which can mitigate overfitting. The parameters were determined via grid-search.

- **bagging_fraction / bagging_freq:** The bagging fraction specifies the fraction of training data that should be used for each tree, meaning that not the entire training dataset is used for training of each consecutive tree. The selection is random. The frequency dictates how often a subset should be taken. Reducing the input data has a positive influence on training speed and reduces overfitting. These parameters were determined via grid-search.

- **learning_rate :** The learning rate l influences the update of the model function in step 2.d. in the GB algorithm (Subsection 2.6.2) in a way that it affects how fast the model learns. The updated formula 2.77 looks as follows:

$$f_m(\vec{x}) = f_{m-1}(\vec{x}) + l \cdot \sum_{j=1}^{J_m} \gamma_{jm} I(\vec{x} \in R_{jm}) \tag{4.2}$$

  This parameter was determined via grid-search.

The hyperparameters for each model are listed in the results at the beginning of the corresponding subsection where the model was employed.

4.3 Feature importance and dimensionality reduction

The best-case models (Section 5.2.1) are created using as much information as possible (117 different input features). This high dimensionality reduces the interpretability of the models. To reduce the feature number and isolate the critical features for training, to ultimately create a PIM, 3 different techniques were used. The approaches used differ for the GB and LR models. For LR, the LASSO approach was used to reduce the dimensionality of the input features. However, this approach is not sensible for GB models. Therefore the intrinsic gain importance from LightGBM and permutation feature importance were calculated to isolate the most critical features for the trained model's performance.

4.3.1 Application of the least absolute shrinkage and selection operator

In this subsection, the least absolute shrinkage and selection operator (LASSO) approach, as employed in Section 5.2.2, is described. The theoretical background to the method can be found in Section 2.7.1.

The ℓ_1-regularization introduced with the LASSO approach leads to a sparse solution of the fit. This means that a certain number of regression coefficients are 0, and therefore, the corresponding input features can be removed from the model, enabling better interpretability. There is no analytical solution to the problem, but there is a globally optimal solution for every number of remaining coefficients. As the LR model fit only takes about 1 second each, it is possible to calculate many different solutions for different ℓ_1-regularization parameters and, with this, calculate solutions for any number of retained input features. The calculations were performed using MATLAB (Version R2019b) based on the fast iterative shrinkage-thresholding algorithm (FISTA) algorithm [116, 79].

After evaluating the different remaining coefficients, one can extract the combined inputs that are crucial for a successful prediction depending on the number of retained features.

For GB models, a similar approach is impossible, as a simple ℓ_1-regularization in the calculation of weights would have a different result as for LR. The output of the leaves would simply be 0, which does not affect the dimensionality of the input features. Additionally, the training time for a single model is too long to adapt the approach as described to GB models.

4.3.2 Feature importance for gradient boosting tree regression models

To inquire information about the most essential features of the GB models, two different approaches were chosen. Both approaches are applied after a model is successfully created based on all input features, and solely the contribution to this model can be analyzed with these methods. First, the LightGBM intrinsic gain feature importance, and second, the model agnostic permutation feature importance from scikit-learn were calculated. Both approaches have the advantage that they provide a global insight into the model, and the model does not have to be retrained to calculate them.

Gain feature importance

The gain feature importance from LightGBM can be automatically calculated during the fitting procedure by setting the 'importance_type' hyperparameter to 'gain'. This provides importance for each input feature depending on the improvement in the model's accuracy by choosing a specific feature to split the data. With this importance, the quantity and quality of splits are included. The gain is calculated as the differences in variance of the output feature before and after splitting of the

data points and is reserved for tree-based ML methods.

Permutation feature importance

The permutation feature importance [117] is a model-agnostic global method to evaluate the increase of the prediction error when feature values are randomly permuted. This permutation breaks the connection between a feature and its true outcome. This can be performed multiple times to ensure that there are no 'fortunate' permutations (especially important on small datasets). In theory, the permutation importance can be easily calculated using the following equation:

$$i_j = s - \frac{1}{K}\sum_{k=1}^{K} s_{kj} \tag{4.3}$$

where s is the reference unpermuted score of the model, j the feature, K the number of repetitions, and s_{kj} the score of the permuted dataset. In this work, the permutation feature importance was calculated using the scikit-learn function 'permutation_importance' with 5 repetitions per feature. The permutation importance was always calculated on the test dataset, as influences from possible overfitting should be excluded.

4.4 Dependence plots

To analyze the influence of the input features on the predicted APTw contrast, dependence plots were used [76]. These dependence plots enable the depiction of the input feature influences for GB trees as well as for LR models, thus building the basis for deciphering similarities and differences between the prediction processes. When the predicted APTw contrast is seen as a sum of p (number of total features) contributions, the dependence plot can be seen as a visualization tool that shows the contribution of one of the features j towards the predicted contrast value depending on the value of feature j. For a linear regression model, this dependency is a linear function, as there are no interactions between the input features (the contribution increases with increasing feature value for positive regression coefficients and decreases with increasing contrast value for negative regression coefficients). However, since GB tree regression is a nonlinear model enabling interactions between the input features, the contribution of feature j not only depends on its own value but possibly also on the value of other input features; therefore, this contribution has to be calculated separately depending on the combination of input feature values.

Figure 4.2 displays an exemplary plot and its components. The figure was created using in-house written code in MATLAB (Version R2023a). The figure can be split into two parts. First, the linear relationship between the input feature (MTR_{Rex} rNOE) and the following contribution to the APTw contrast from the LR model is depicted as a straight orange line. This relationship indicates that an increasing MTR_{Rex} rNOE leads to a decreased or negative predicted APTw contrast since the contribution changes from positive to negative with increasing MTR_{Rex} rNOE value. Secondly, the scatter plot shows the SHAP values of each evaluated voxel plotted against the feature value. However, as mentioned before, the GB tree is a nonlinear

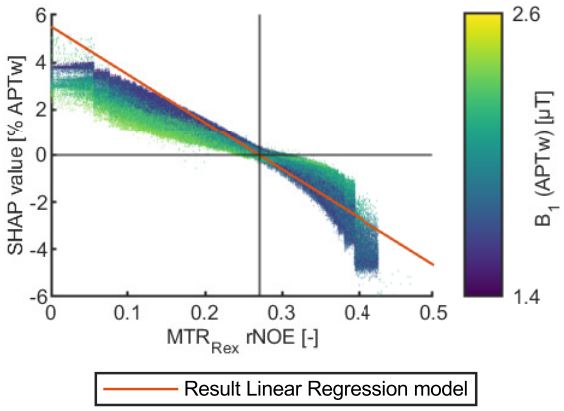

Figure 4.2: Exemplary dependence plot for the interpretable MTR_{Rex} rNOE contrasts. The scatter plot shows the SHAP values (calculated for the GB model) for each predicted voxel depending on its input feature value. Additionally, the contributions from the input features on the APTw contrast calculated by the LR model are displayed as an orange line. The coloring of the data points is based on its B_1 value.

model enabling interactions. Therefore, the contribution of the MTR_{Rex} rNOE also depends on possible other input features, meaning that for one MTR_{Rex} rNOE value, different influences on the predicted APTw contrast are possible depending on the value of the other input features. To visualize these possible interactions between features, the feature value of a third variable, such as T_1 or B_1, can be added via color-coding of the individual contributions. In this case, the color-coding highlights the interactions between the displayed MTR_{Rex} rNOE and B_1, indicating that the contribution for a fixed MTR_{Rex} rNOE contrast value will be closer to 0 for high B_1 values. How to calculate the information displayed in the plots is described in the following subsections.

4.4.1 Additive contributions of linear regression models

The results of the LR model can be easily divided into additive contributions. When looking at only one data point, formula 4.1 already provides all the necessary information. The formula for the linear dependency of feature j is as follows:

$$\Delta APTw_j(x_j) = \frac{x_j - \bar{x}_{j,\text{train}}}{SD(x_{j,\text{train}})} \cdot \beta_j \cdot SD(APTw_{\text{train}}) \tag{4.4}$$

With $\Delta APTw_j(x_j)$ as the partial contribution of feature j to the final contrast, x_j as the j-th feature's value, $\bar{x}_{j,\text{train}}$ as the mean of all x_j from the training dataset, $SD(x_{j,\text{train}})$ as the SD of the same x_j from the training dataset, β_j as the corresponding regression coefficient, and $SD(APTw_{\text{train}})$ as the SD of the APTw contrast calculated from the training dataset.

4.4.2 treeSHAP

Shapley additive explanations (SHAP) values [118], which are based on the Shapley values described in Section 2.7.2, can be calculated to gather similar information from the GB trees.

The SHAP value is the partial contribution of feature j (of total p features) to the final predicted contrast, similar to the coefficients from the linear regression model. The predicted APTw contrast $APTw_{\text{pred}}(\vec{x})$ for a data point $\vec{x}$ can be calculated using SHAP values and equation 2.83 as follows:

$$APTw_{\text{pred}}(\vec{x}) = E(APTw_{\text{pred}}(X)) + \sum_{j=1}^{p} SHAP_j(APTw_{\text{pred}}, \vec{x}) \tag{4.5}$$

Where $E(APTw_{\text{pred}}(X))$ is the average predicted value, $SHAP_j(APTw_{\text{pred}})$ is the SHAP value depending on the model, on $APTw_{\text{pred}}$, and on the data point $\vec{x}$ (not only the feature x_j as interactions are allowed which leads to an influence of the other input features). $SHAP_j(APTw_{\text{pred}}, \vec{x})$ is also what is displayed in the dependence plots and can be interpreted similarly to $\Delta APTw_j(x_j)$ for the LR model (Equation 4.4). Therefore, the additive contributions from the LR model and the SHAP values can be displayed in the same plot as they contain similar information. However, because $SHAP_j(APTw_{\text{pred}}, \vec{x})$ is dependent on all input features ($\vec{x}$) and not just the independent x_j ,as for the LR model, the information is not depicted as a straight line but rather as a point cloud.

As the calculation of the SHAP values is very inefficient and complex and, therefore, very time-consuming, the authors of the SHAP paper published a second paper focusing on a fast estimation method to calculate SHAP values for tree and ensemble tree models [119]. The method, called treeSHAP, was used to calculate the SHAP values for the GB trees. The tree SHAP function used in this work is a part of the Python library SHAP and reduces the complexity of the calculation to $O(TLD^2)$ (T: number of trees; L: number of leaves per tree; D: max depth per tree) and therefore SHAP values were calculated within approximately 3 minutes (using the workstation described in Section 4.2). An extensive explanation of the method can be found in the paper [119].

4.5 Construction of the physically interpretable model (PIM)

The aim of this thesis was to create a physically interpretable model (PIM), which enables an enhanced (bio)physical understanding of the APTw contrast in vivo and deciphers its underlying mechanisms. This was provided by the possibility to decompose the APTw contrast into its contributors and create non-black-box dependencies of the contributors on the saturation power B_1 and the longitudinal relaxation time T_1. To create the PIM, the information about the existence of B_1 and T_1 dependencies gathered from the dependence plots was used to combine the interpretability of the LR model with the non-linear features of the GB model. This was performed by partitioning the dataset based on a grid creating uniform-sized bins in the relevant

B_1 and T_1 range (only B_1 and T_1 due to the dependence plot analysis), followed by the creation of a LR model as described in Section 5.2 for each individual bin.

The standardization was performed separately for all bins to enable comparability of the calculated regression coefficients. Because of the introduced grid, the function for predicting the APTw contrast 4.1 needs to be adapted, as the SDs, mean values, and regression coefficients now depend on T_1 and B_1. The standardized input features are therefore described by:

$$Std.x_{n,j}(B_1, T_1) = \frac{x_{n,j} - \bar{x}_{j,\text{train}}(B_1, T_1)}{SD(x_{j,\text{train}}(B_1, T_1))} \tag{4.6}$$

for each data point n and feature j. The APTw contrast for each data point can now be calculated dependent on T_1 and B_1 via:

$$y_n = Std.\vec{x}_n^T(B_1, T_1) \cdot \vec{\beta}(B_1, T_1) \cdot SD(y_{\text{train}}(B_1, T_1)) + \bar{y}_{\text{train}}(B_1, T_1) \tag{4.7}$$

The final PIM was created with three input features (MTR_{Rex} AMIDE, rNOE, and ssMT) and only the APTw contrast as output feature. Since each of these four features has both a mean and a SD, there is a total of eight maps available for standardization. These eight maps give an overview of possible dependencies of the input and output features from T_1 and B_1. However, because the standardization is performed bin-wise, possible scaling factors of the input and output features, which depend on B_1 or T_1, will be removed during the standardization process. This makes differentiating between the standardized input and output features and the unstandardized ones essential.

Additionally, a map can be generated for the T_1 and B_1 dependencies of each of the regression coefficients corresponding to the three input features. Due to the standardization of inputs and output, the regression coefficients can be directly compared and can be interpreted as how many SDs change is introduced to my output if the corresponding input is changed by one SD. In other words, because of the standardization, the interpretation of the regression coefficients can be seen as the sensitivity of the Std. APTw contrast on changes in the Std. input features. However, the standardized APTw contrast is not comparable to the APTw contrast as possible dependencies on B_1 and T_1 would be corrected for during the standardization process. By multiplying the respective regression coefficient maps with the APTw SD map, these possible dependencies of the APTw contrast will be reintroduced, and the resulting maps can be seen as the sensitivity of the APTw contrasts on changes in the Std. input features. These maps enable physical interpretations directly connecting the input features and the APTw contrast and will be called sensitivity maps. The sensitivity maps are calculated as follows:

$$Sensitivity\ Std.x_j(B_1, T_1) = \beta_j(B_1, T_1) \cdot SD(APTw_{\text{train}}(B_1, T_1)) \tag{4.8}$$

Chapter 5

Results

This thesis aims to expand the current knowledge about the APTw contrast, which has proven clinically relevant for neuro-oncological questions, but continues to exhibit an inconclusive molecular origin. To this end, other more interpretable CEST metrics (i.e., MTR_{Rex} of AMIDE, rNOE, and ssMT) were employed to create a physically interpretable model (PIM), which aims to enable an enhanced (bio)physical understanding of the APTw contrast in vivo to decipher its underlying mechanisms.

The foundation of this work is an extensive clinical cohort including 146 CEST-MRI datasets. Crucially, this vast dataset allowed the application of ML methods to extract previously unexplored features in the CEST dataset. An approach such as this one was previously impossible due to the lack of data and the high complexity of a (hypothetical) analytically derived function to describe the calculation of the APTw contrast based on interpretable CEST metrics.

As a prerequisite to evaluating the quality of the predictions, the level of the intrinsic contrast fluctuations across the APTw datasets will be identified (Section 5.1). To this end, the contrast fluctuations in NAWM and NAGM will be analyzed to estimate the APTw contrast deviations in healthy brain tissue. Furthermore, the influence of motion on the APTw contrast will be analyzed to quantify the impact of motion-induced artifacts and enable the detection of these artifacts, which cannot be predicted by a ML model trained on tabular data.

Subsequently, to validate the hypothesis that a calculation of the high-power APTw contrast from low-power spectral CEST data is possible regardless of the different saturation schemes, proof-of-concept ML models will be created using low-power spectral CEST data as input features (Section 5.2). By analyzing the essential features for successful predictions, it will be shown that the models used physically relevant information.

Consequently, these insights will be used to create a LR and GB model based on interpretable contrasts (i.e., relaxation-compensated MTR_{Rex} contrasts, B_1 and T_1) (Section 5.3). Subsequently, the GB model will be thoroughly analyzed using interpretable ML methods to extract its nonlinear components. With this information at hand, a novel PIM will be developed, that combines the interpretability of the LR model with the non-linearities extracted from the GB model.

Finally, the PIM will be analyzed thoroughly to evaluate its physical information content to enable a comparison to the theoretical expectations from the underlying physics (Section 5.4).

5.1 Intrinsic fluctuations of the APTw contrast

In order to robustly and reliably assess the performance of the models created in this thesis, the intrinsic contrast fluctuations of the measured APTw contrast needed to be investigated. More specifically, to assess the prediction quality of the employed ML models, the contrast fluctuations in brain regions with comparable tissue composition and B_1 field strength were investigated, and the magnitude of ringing and motion artifacts, which are expected to decrease the predictive performance of the ML models, were evaluated in representative datasets. This information was used to create matching levels, which are estimations of the best possible predictive performance, for the different model settings.

The assessment of the contrast fluctuations in distinct ROIs, excluding changes based on different tissues and field inhomogeneities, resulted in a mean absolute deviation (MAD) of 0.75% for the frontal lobe NAWM ROI. For the model evaluation, this NAWM ROI was chosen as the matching level due to the absence of artifacts in this region. On the other hand, the MAD was found to be up to 1.37% (occipital NAGM ROI) in regions exhibiting evident ringing artifacts (Subsection 5.1.1). Subsequently, the influence of motion on the APTw contrast was thoroughly investigated, as motion-induced artifacts are impossible to predict for a ML model based on tabular data. The analysis of a representative subject showed that a voxel-shift by one voxel led to a MAE of 1.33%, and even after motion correction, the error still amounted to around 0.5% MAE due to partial volume and interpolation effects (Subsection 5.1.2).

5.1.1 Regional fluctuations of the APTw contrast

To obtain a thorough overview of the contrast fluctuations of the measured APTw contrast within the human brain, an in-depth analysis of a single representative subject was performed. This analysis is crucial, as the observed regional contrast fluctuations determine the matching level for the model predictions in the following sections. The matching level can, thereby, be chosen by calculating the MAD (all models were evaluated using the MAE) in a brain region with minimal ringing artifacts and minimal partial volume effects to exclude possible variations due to tissue type and location. As a further advantage, the analysis of regional contrast fluctuations also provides information about the influence of ringing artifacts on the APTw contrast, therefore showing whether and to what extent the matching level has to be adapted for models created with the interpretable MTR_{Rex} contrasts, as the information about the artifacts gets diluted during post-processing.

The representative subject was chosen based on three strict criteria to ensure that unwanted artifacts do not influence the analysis: (i) Most critical was the absence

of motion during the measurement to minimize the influence of motion-induced artifacts. Furthermore, (ii) B_1 field inhomogeneities should be minimal to enable the comparison of APTw contrast values in different brain regions, as the APTw contrast is B_1 dependent. Lastly, (iii) the subject should exhibit areas with and without ringing artifacts to better estimate not only the matching level in artifact-free regions, but also the influence of artifacts on the APTw contrast.

To exclude possible variations due to tissue type and location, small ROIs were automatically generated using the in-house build tool for brain segmentation described in Section 3.4.5 for the selected subject. The generated ROIs were placed in the frontal, parieto-temporal, and occipital regions of the NAWM and NAGM (Figure 5.1, red, blue, and green ROIs, respectively). These locations enabled the analysis of the ringing artifacts as they vary in strength depending on the brain region. Finally, the voxels failing the quality assurance criteria described in Section 3.4.4 were excluded from the evaluation. However, an additional criterion limiting the B_1 inhomogeneity to $\pm 5\%$ was implemented to minimize possible B_1 influences.

A representative subject fulfilling all inclusion criteria is shown in Figure 5.1. In addition to the APTw contrast map, ΔB_0 and rel. ΔB_1 maps are provided for an estimate of the field inhomogeneity.

The evaluation of the generated regions of interest, displayed in the first column of Figure 5.1, provides a realistic example of the regional APTw contrast fluctuations. An analysis of the mean values shows a clear hyperintense frontal lobe (Figure 5.1, red) compared to the parieto-temporal and occipital regions (Figure 5.1 blue and green) for both NAWM and NAGM. Additionally, the data shows only a slight difference in mean value between NAWM and NAGM in the respective regions.

Furthermore, it is noticeable that the MAD in NAGM is increased by about 0.2% (APTw) compared to NAWM, which is most likely influenced by the voxel positions, as NAGM voxels are more likely to include partial CSF influences than NAWM ROIs. The NAWM ROI deviations range from 0.75% to 1.16%, with the lowest value found in the ringing artifact-free frontal lobe region. This region was chosen as the prediction matching level in the following sections due to the absence of ringing artifacts and minimal partial volume effects. When ringing artifact-affected areas affected by ringing artifacts are evaluated, the MAD increases to 0.94% in the parieto-temporal NAWM and to 1.16% in the occipital NAWM. The summarized regional evaluation can be found in Table 5.1.

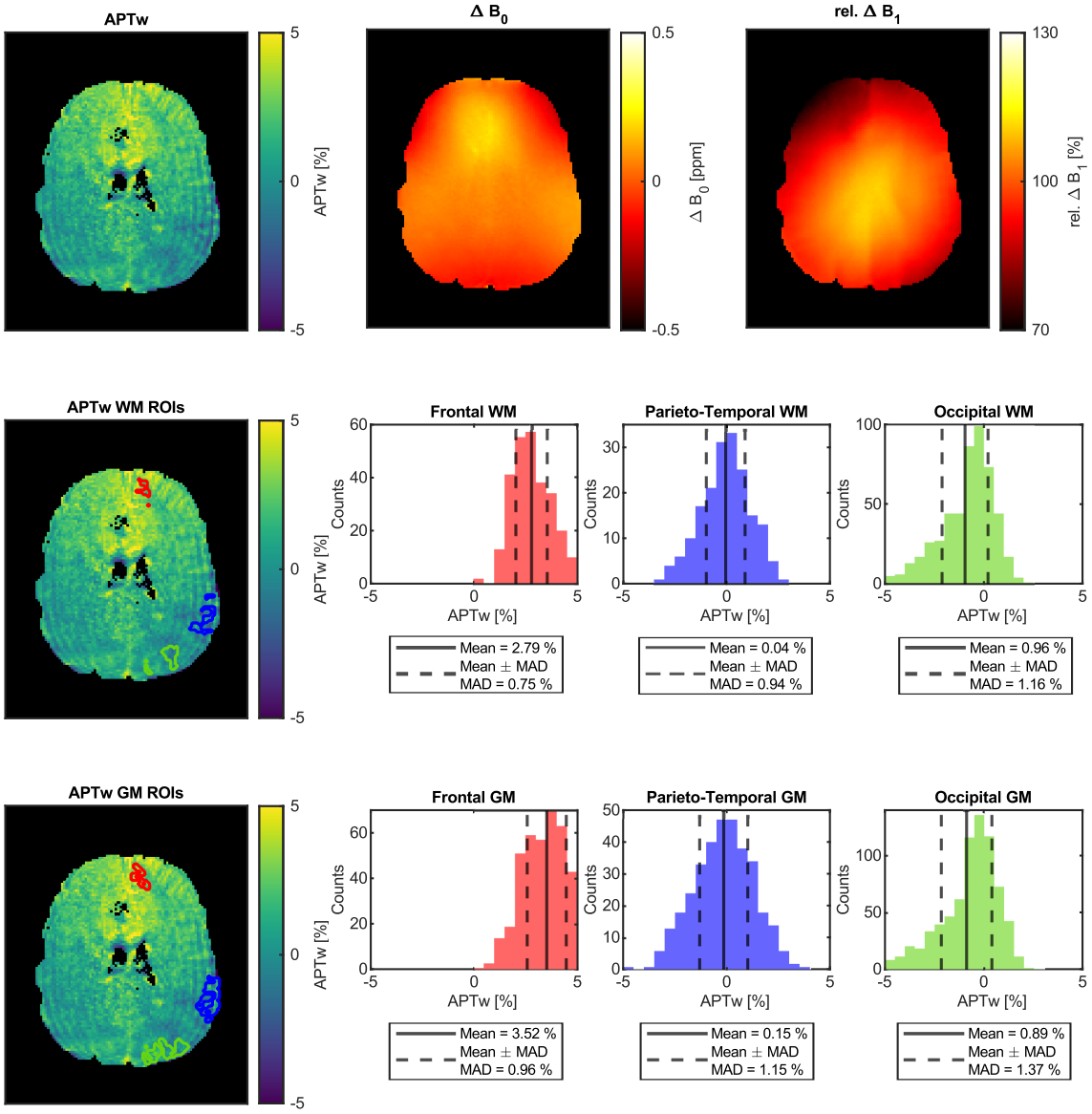

Figure 5.1: In-depth analysis of the regional fluctuations of the APTw contrast within the human brain for a single representative subject. The APTw contrast map and the corresponding ΔB_0 and rel. ΔB_1 map of the same slice are displayed in the top row. The middle and bottom rows show the automatically selected and evaluated ROIs in the frontal lobe (red), parieto-temporal region (blue), and occipital region (green) for NAWM (middle row) and NAGM (bottom row), respectively. Most noticeable is the hyperintense frontal lobe, compared to the parieto-temporal and occipital regions. The ROIs are restricted to rel. ΔB_1 values between 0.85 and 0.95 to limit B_1-inhomogeneities. Additionally, the histograms for the corresponding 3D-ROIs, with mean and MAD, are displayed.

Table 5.1: Summary of the analysis of the APTw contrast fluctuations in the NAWM and NAGM tissue for the frontal, parieto-temporal, and occipital regions of the brain as shown in Figure 5.1. The mean and MAD for the evaluated ROIs, restricted to rel. ΔB_1 values between 0.85 and 0.95 to limit B_1-inhomogeneities, are provided. Most noticeable is the clear difference in mean value with the hyperintense frontal lobe area and the decreased MAD in the NAWM tissue.

Region	Tissue	Mean (%)	MAD (%)
Frontal	NAGM	3.52	0.96
	NAWM	2.79	0.75
Parieto-temporal	NAGM	-0.15	1.15
	NAWM	-0.04	0.94
Occipital	NAGM	-0.89	1.37
	NAWM	-0.96	1.16

5.1.2 Analysis of motion-induced artifacts in APTw imaging

To enable a more realistic assessment of the performance of the models created in this thesis, which are based on measured subject datasets, a thorough investigation of the influence of subject motion on the APTw contrast is crucial, as motion-induced artifacts are impossible to predict for any ML model based on tabular data with no connection between the voxels. This limitation prevents a successful prediction of the motion-induced artifacts even if the motion pattern is known. As this is one of the main limitations of the predictive power of the models, a motion correction for APTw imaging that minimizes the influence of motion on the APTw contrast was proposed and validated as part of this work. The established correction method is described in detail in the methods (Section 3.4.2).

To highlight the importance of the introduced motion correction, the dataset of a subject with prominent edema and advanced movement during the measurement was identified. Three consecutive slices of the T_1-weighted CE images and the corresponding APTw contrast maps are shown in Figure 5.2, displaying prominent motion artifacts (red arrows). The artifacts are especially evident in regions with transitions between tissues (i.e. near CSF and edema), limiting the potential predictive power of the models.

To quantify the motion-induced artifacts, the established correction was used to identifiy the dataset of a subject with minimal motion during the measurement (Figure 5.3). Following, the quantification of the motion-induced aritfacts was performed using the +3.5 ppm and -3.5 ppm offsets from the acquired APTw spectrum after B_0 correction, leaving only the subtraction of the offsets' Z-values ($(Z(3.5\text{ ppm}) - Z(-3.5\text{ ppm})) \cdot 100$) to calculate the APTw contrast. The artificial motion patterns were introduced to the -3.5 ppm offset, and afterward, the APTw contrast was calculated as described in Section 2.67.

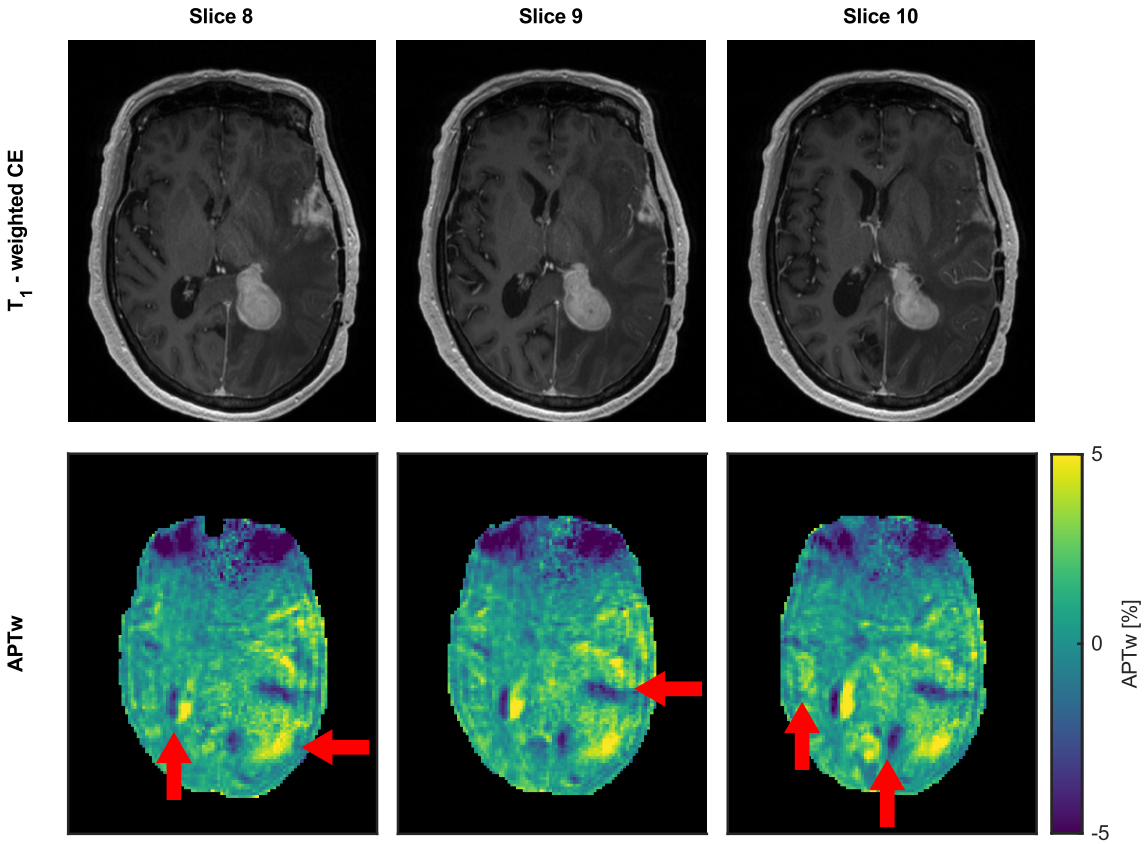

Figure 5.2: The dataset of a subject with prominent edema and advanced movement during the measurement is displayed. In total, three consecutive slices of the T_1-weighted CE images (for orientation purposes) and the corresponding APTw contrast maps for the subject with advanced edema (hypointense region on the T_1-weighted image; right hemisphere) are shown. The subject was selected due to increased motion during the APTw contrast acquisition. The combination of motion and edema makes this subject a suitable example of motion-induced artifacts, highlighted with red arrows. The siginificant artifacts, recognizable by the change from hyper- to hypointensity, can be observed at the edges of the CSF and the edema.

Three different types of motion and interpolation artifacts were investigated during this work, the resulting MAE are summarized in Table 5.2:

- **Voxel-shift along the y-axis** (Figure 5.3, second column): To isolate the motion-induced artifact from possible interpolation artifacts, a simple displacement by one voxel in the y-direction was artificially imposed on the data. This change led to a MAD of 1.33% compared to the ground truth. Visually, there are also apparent differences between the moved and ground truth images. Most noticeable are the artifacts originating in regions with changing tissues, especially at the borders of the CSF. These artifacts are characteristic of motion, as they exhibit changes between hyper- and hypointensities at the edges of the tissues.

- **Realistic motion + interpolation** (Figure 5.3, third column): A realistic motion pattern was introduced to the -3.5 ppm offset ($\Delta_x = -0.1$ mm,

$\Delta_y = -0.5$ mm, $\Delta_z = 0.4$ mm, $\theta_x = -0.1°$, $\theta_y = 0.5°$, $\theta_z = 0°$). Since the rotation and shifts are not an integer multiple of the voxel size, an interpolation was performed after the translation. The resulting MAD resulting from this realistic motion pattern is 0.47%. Visually, the deviations are not noticeable on the APTw contrast maps (top row), but looking at the difference maps, the alternating hyper- and hypointensities at the transitions between tissues can be observed again (middle row).

- **2 × interpolation** (Figure 5.3, fourth column): In a third analysis, the -3.5 ppm offset from pattern (ii) was placed in its original position. This operation removes any displacement between the two images but adds a second interpolation step that interestingly, leads to a MAD of 0.53%. Visually, the deviations appear similar to the pattern after transformation (ii).

Additionally to the individual changes, it is noticeable that the motion and/or interpolation interacts with the ringing artifacts in all cases. In conclusion, these results highlight the necessity of a motion correction for APTw CEST data, as motion-induced artifacts significantly decrease the potential of a successful contrast prediction. However, intra-measurement motion cannot be corrected perfectly as the interpolation process introduces a minor error in all cases.

Table 5.2: Summary of the MAE introduced to the APTw contrast of a representative dataset by different combinations of artificial motion and interpolation as shown in Figure 5.3. The artificial motion patterns are as described in captions of Figure 5.3.

	MAE (%)
Single voxel-shift along y-axis	1.33
Realistic motion + Interpolation	0.47
2x Interpolation	0.53

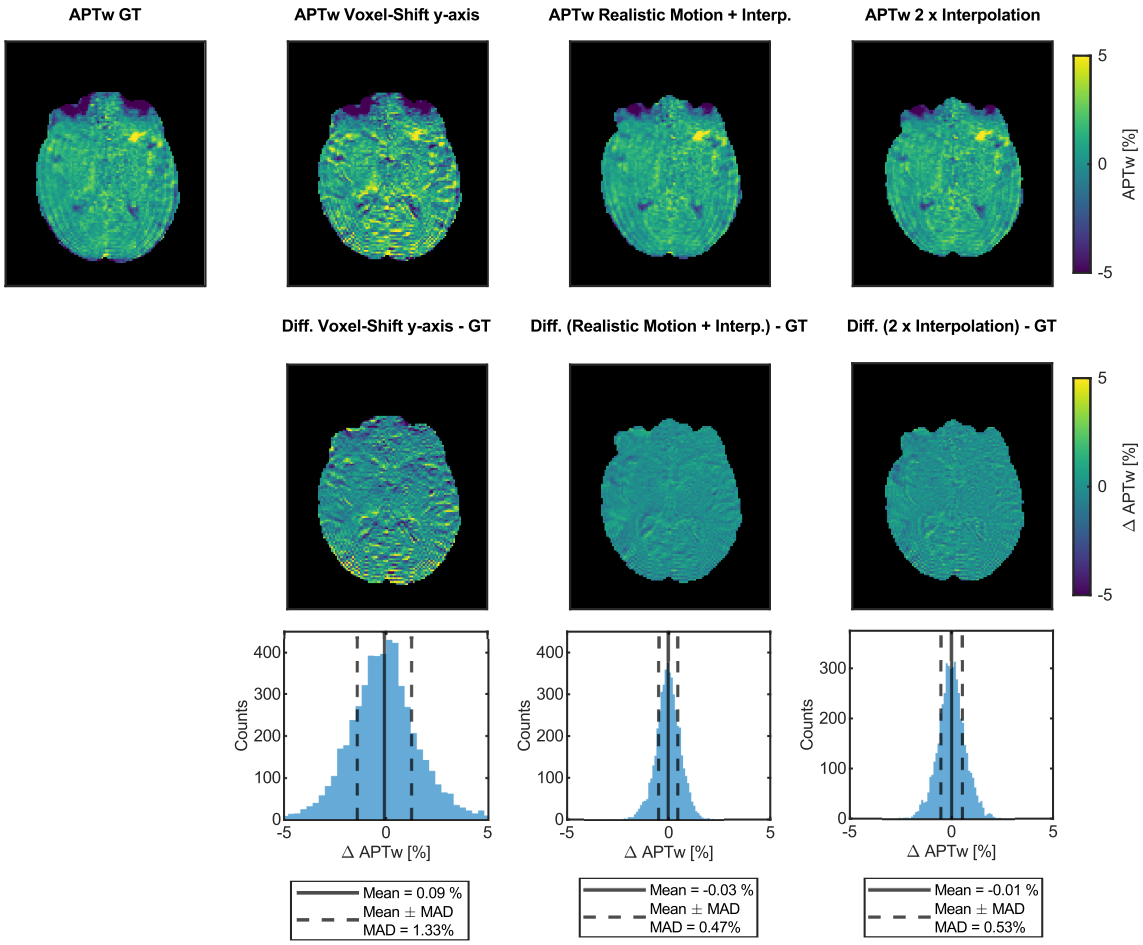

Figure 5.3: To investigate the influence of subject motion on the APTw contrast, different artificial motion patterns were imposed on a dataset. On the top left, the ground truth APTw contrast map after motion correction (described in Section 3.4.2) is displayed for a representative subject with minimal motion. The following columns show different artificial motion patterns imposed on the same dataset. Additionally, the difference images compared to the ground truth and histograms of the difference maps are displayed (second row), combined with the mean and MAD values. The artificial motion was introduced to the -3.5 ppm offset as follows: Column 2: ($\Delta_x = 0$ mm, $\Delta_y = 1.71875$ mm (one voxel), $\Delta_z = 0$ mm, $\theta_x = 0°$, $\theta_y = 0°$, $\theta_z = 0°$). Column 3: ($\Delta_x = -0.1$ mm, $\Delta_y = -0.5$ mm, $\Delta_z = 0.4$ mm, $\theta_x = -0.1°$, $\theta_y = 0.5°$, $\theta_z = 0°$). Column 4: Perfect back transformation of the second transformation. Most strikingly is that, although the transformation in column 3 removes any displacement between the two images, the two interpolation steps combined lead to a MAD of 0.53%.

5.2 Initial predictions of the APTw contrast using ML models

As the aim of this thesis is to create a sophisticated model that enables the study of the APTw contrast mechanisms in vivo based on the relaxation-compensated MTR_{Rex} contrasts, it is imperative first to prove the feasibility of predicting the high-power APTw (B_1=2 µT) contrast from low-power CEST data, T_1, ΔB_0, and

rel. ΔB_1. Consequently, this would show that a data-driven translation of the different saturation schemes into one another is, in principle, possible. Furthermore, to ensure that creating a PIM that enables the prediction of APTw contrast based on the relaxation-compensated contrasts is feasible, it is crucial to validate that the model predictions are performed based on physically relevant information, i.e. effects related to chemical exchange.

Thus, in the first step, (i) the translation of the different saturation schemes into one another was accomplished by training ML models using as much unbiased input information as possible, regardless of dependencies between the input features (Section 5.2.1). Because such input features have the highest possible information content, the created models can be considered as the best-case model and will be referred to as such. Subsequently, (ii) an assessment of which input information is crucial for successful model predictions was realized, by calculating the input parameter feature contributions. Lastly, (iii) to validate that the model predictions are performed based on physically relevant information, the training features were systematically restricted to distinct Z-spectra regions (Section 5.2.2).

Interestingly, both utilized models, i.e. the LR and GB model, could predict the contrast with a MAE in the range of the previously established matching level. Nevertheless, an individual evaluation of the MAE for each dataset revealed fluctuations, highlighting that the predictive performance for datasets with advanced motion-induced artifacts was significantly worse. Additionally, it was shown that the chemical exchange and rNOE region of the Z-spectra were essential for a successful prediction.

5.2.1 Prediction of the APTw contrast using fully sampled low-power Z-spectra

In this section, the feasibility of predicting the APTw contrast from low-power CEST data was shown, proving that a translation of the different saturation schemes is possible. This is a crucial first step to create a PIM that enables the study of the APTw contrast based on the relaxation-compensated MTR_{Rex} contrasts.

To create the best possible prediction, all available information was used to train an LR and GB model. The input features were selected regardless of dependencies between them as follows: T_1, ΔB_0, rel. ΔB_1, and the fully sampled Z-spectra (B_1 = 0.6 µT and B_1 = 0.9 µT), which were only corrected for motion and B_0-inhomogeneities. Subsequently, to identify the shortcomings of each model, the results were compared to the ground truth visually and quantitatively (first for all available datasets together and then for each dataset individually).

Dataset

The input features were chosen to be maximally unrestricted to increase the possibility of a successful prediction of the APTw contrast. Specifically, the fully sampled low-power Z-spectra (B_1=0.6 µT and B_1=0.9 µT, 57 saturation frequency offsets each), T_1, ΔB_0, and rel. ΔB_1 were used as input features. The only post-processing

steps performed were a motion correction and a correction for B_0-inhomogeneity of the Z-spectra; the latter was necessary due to the APTw contrast being B_0-corrected. To lose as little information as possible, denoising was not performed. All voxels that were assigned to NAGM, NAWM, CSF, WT, necrotic tissue, and resection cavity during the annotation process were included for training and testing. The exclusion criteria for data points were described in detail in the methods (Section 3.4.4). These criteria led to a total of 117 features for 4,513,915 training voxels and 1,420,823 test voxels.

ML models

The models trained to predict the APTw contrast were a LR model (described in Section 4.2.2) and a GB model (described in Section 4.2.3). The LR model was chosen as a simple out-of-the-box model that suits the task well, as the APTw contrast metric calculation is additive by nature. The GB model was chosen for the task due to its ability to model nonlinear relationships and its high customizability. The optimal hyperparameters found for the GB model via the grid-search algorithm are displayed in Table 5.3.

Table 5.3: Employed hyperparameters for the GB model when using fully sampled Z-spectra, ΔB_1, rel. ΔB_1 , and T_1 as input features (best-case) as determined via grid-search algorithm.

# estimators	# leaves	learning rate	bagging fraction	drop rate	feature fraction
2000	31	0.1	0.8	0.2	0.8

Results

The performance of both ML models on the evaluation dataset is summarized in Table 5.4. Looking at the overall performance, both models closely align with the matching level determined in the previous Section 5.1. Furthermore, it is worth noting that the GB model performs better than the LR model in all evaluated regions (0.04% (APTw) for overall and NAWM and NAGM, 0.03% (APTw) for WT). Most striking, however, is the difference in predictive performance between the evaluation of the combined NAWM and NAGM voxels and the WT voxels. The MAE of both models is decreased for the NAWM and NAGM voxels compared to the overall evaluation by around 0.06% (APTw). However, a significantly increased MAE by 0.14% for the LR and by 0.15% in the WT voxels for the GB model can be observed. These differences can be explained by the biological diversity of the WT voxels, which is expected to be higher compared to the NAWM and NAGM voxels and, therefore, more difficult to predict. Furthermore, the WT regions are smaller in size and, therefore, more heavily impacted by motion-induced artifacts than NAWM and NAGM regions.

Table 5.4: Summary of the predictive performance of the LR and GB model, based on the fully sampled Z-spectra, ΔB_1, rel. ΔB_1, and T_1 as input features, evaluated for all voxels, combined NAGM and NAWM voxels, and WT voxels. Both performances align with the matching level determined in Section 5.1.

Model		Overall MAE (%)	NAWM & NAGM MAE (%)	WT MAE (%)
Best-case	LR	0.77	0.71	0.91
	GB	0.73	0.67	0.88

In Figure 5.4, the prediction (total 1,420,823 voxels, comprising all datasets) is displayed as a scatter plot showing the predicted contrast value on the y-axis and ground truth value on the x-axis. Plots were created for (i) all voxels, (ii) voxels from NAGM and NAWM only, and (iii) WT voxels only. For visual guidance, an angle bisector is also displayed in each plot to indicate an ideal prediction (Figure 5.4, orange lines) and kernel density marginal histograms are displayed to provide a better understanding of the data point distribution (mean and SD of the distributions are listed in Appendix B Table 8.1). As expected from the MAE, a strong agreement between the ground truth and predicted values can be observed for the LR and GB models in all evaluated subgroups. Although the data point distributions for both models are centered around the ideal prediction, the distribution for the GB model is narrower, yielding the slightly decreased MAE. Furthermore, when looking at the data point distributions of the ground truth values in the corresponding regions, one can see a decreased mean value for NAWM and NAGM voxels (0.18%) and an increased mean value for WT voxels (1.06%) when compared to the overall analysis (0.23%). These same variations were predicted by both the LR (Overall: 0.26%; NAWM & NAGM: 0.22%; WT: 1.06%) and GB (Overall: 0.25%; NAWM & NAGM: 0.20%; WT: 1.04%) models and are especially visible for the WT voxels in the scatter plot.

Deviations from the ideal prediction can nevertheless be observed for both models. Most strikingly, the decreased slope of the data points compared to the ideal prediction shows that the predictions are more likely to be closer to 0%, therefore underestimating the absolute ground truth value. This effect is observable for the positive as well as the negative value range and can be quantified when comparing the SD from the ground truth APTw contrast with the predicted contrast values. The SD for all voxels is reduced from 1.81% to 1.48% for the LR model and to 1.47% for the GB model, indicating the reduced value range of the predicted voxels. Interestingly, the GB model is slightly more impacted by this effect, especially for the WT voxels. The ground truth SD for the WT voxels is 1.52%, and the APTw contrast predicted by the LR model exhibits a SD of 1.08% compared to 0.92% for the GB model prediction.

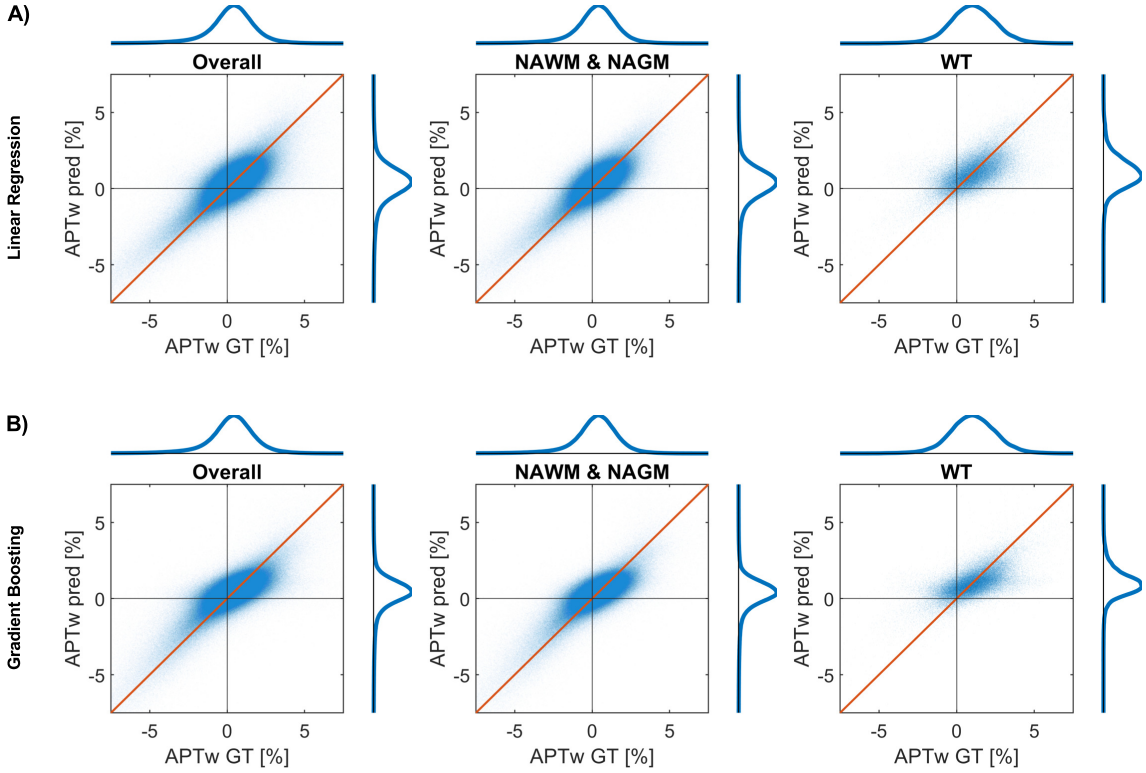

Figure 5.4: Analysis of the predictive performance of the best-case models. The voxelwise predicted APTw contrast, based on the fully sampled Z-spectra, ΔB_1, rel. ΔB_1, and T_1 as input features, is displayed for the LR model in subfigure A and for the GB model in subfigure B. For visual guidance an angle bisector (orange lines) was added for each subplot to indicate an ideal prediction. To better understand the voxel distributions, kernel density marginal histograms are displayed on each axis (mean and SD of the distributions are listed in Appendix B Table 8.1). A scatter plot was created for all voxels (left column) and two subgroups containing the combined NAGM and NAWM voxels (middle column) and only whole tumor (Edema + CE) voxels (right column).

Figure 5.5 shows the voxelwise predicted APTw contrast by LR and GB for a representative subject. Looking at the images, a high level of agreement can be observed between the predicted and the ground truth image. Notably, both algorithms successfully reproduced all main features, such as the hyperintense tumor area, the NAGM and NAWM contrast, and the hypointensities towards the posterior part of the brain. When taking a closer look at the hyperintensity in the CE region of the tumor, a split into three hotspots can be observed in the ground truth image and the predicted images from both models. The only apparent difference between the predictions and the ground truth is a decreased noise level in the predicted contrast maps, especially for the GB model. The excellent match was confirmed when examining the difference maps created by subtracting the ground truth from the predicted contrast values. These difference maps exhibit mostly noise except in regions close to CSF. A second representative patient is displayed in Appendix C.

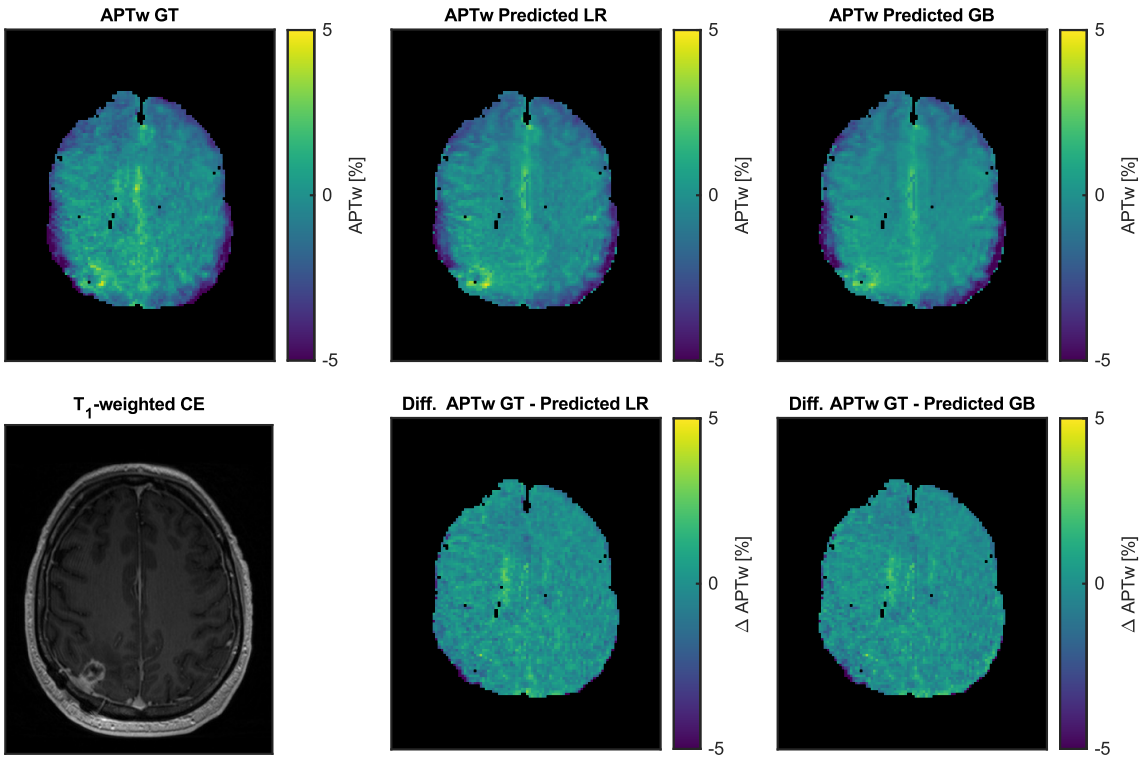

Figure 5.5: The voxelwise predicted APTw contrast by LR (Column 2) and GB (Column 3) based on the maximally unrestricted input features (described at the beginning of this Section 5.2) are displayed for a representative subject and slice. In addition, a T_1-weighted CE map is included for orientation purposes, and the APTw ground truth image and the difference maps between ground truth and predictions are shown. Notably, the algorithms successfully reproduced all main features, such as the hyperintense tumor area, the NAGM and NAWM contrast, and the hypointensities towards the posterior part of the brain.

Evaluation of individual subjects

To enable a better comparison of the models and identify their respective possible shortcomings, the MAE for each individual test dataset is illustrated in Figure 5.6. Most noticeably, both models performed equally well for each individual dataset, but there is a significant performance difference between individual datasets. The SD of the GB and LR model performance is 0.12% in both cases, with a maximum MAE of 1% for GB and LR and a minimum MAE of 0.56% for the GB model and 0.57% for the LR model. Investigating one of the datasets with a high MAE

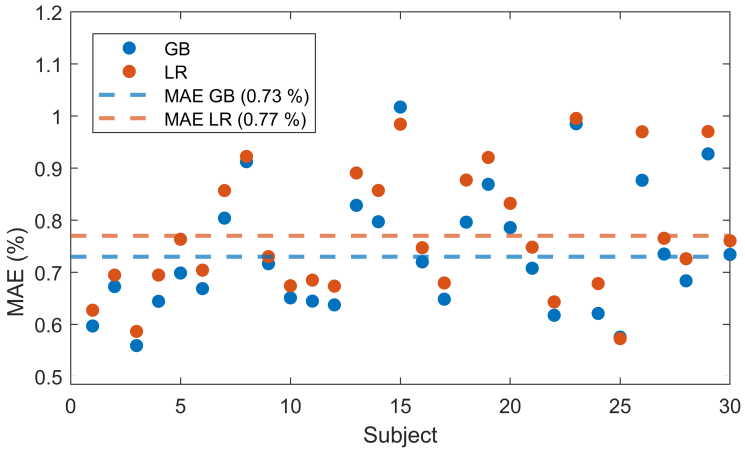

Figure 5.6: The MAE of the LR (orange) and GB (blue) model are displayed for each dataset individually to compare the models and identify possible shortcomings. Furthermore, the average MAE of the LR and GB models are shown as dashed lines. The good performance match between the two models is most striking, although the GB model performs slightly better for 27 of the 29 datasets (LR performs better for Subject 15 and 25), mirroring the overall evaluation.

(0.99% for GB, 1.00% for LR) displayed in Figure 5.7, a clear difference between ground truth and predicted images is observable. The ground truth image depicts advanced motion-induced artifacts in most parts of the edema. As the models do not predict these artifacts, they lead to an increased MAE. When looking at the side contralateral to the tumor, the difference maps show only minor deviations that are comparable to the deviation from the subject presented in Figure 5.5. The ringing artifacts, visible in the ground truth image, were successfully predicted by both models, albeit with a lower intensity. Lastly, both predictions match each other very well, even predicting a slight hyperintensity in the tumor area. However, this hyperintensity is less prominent in the ground truth APTw contrast map.

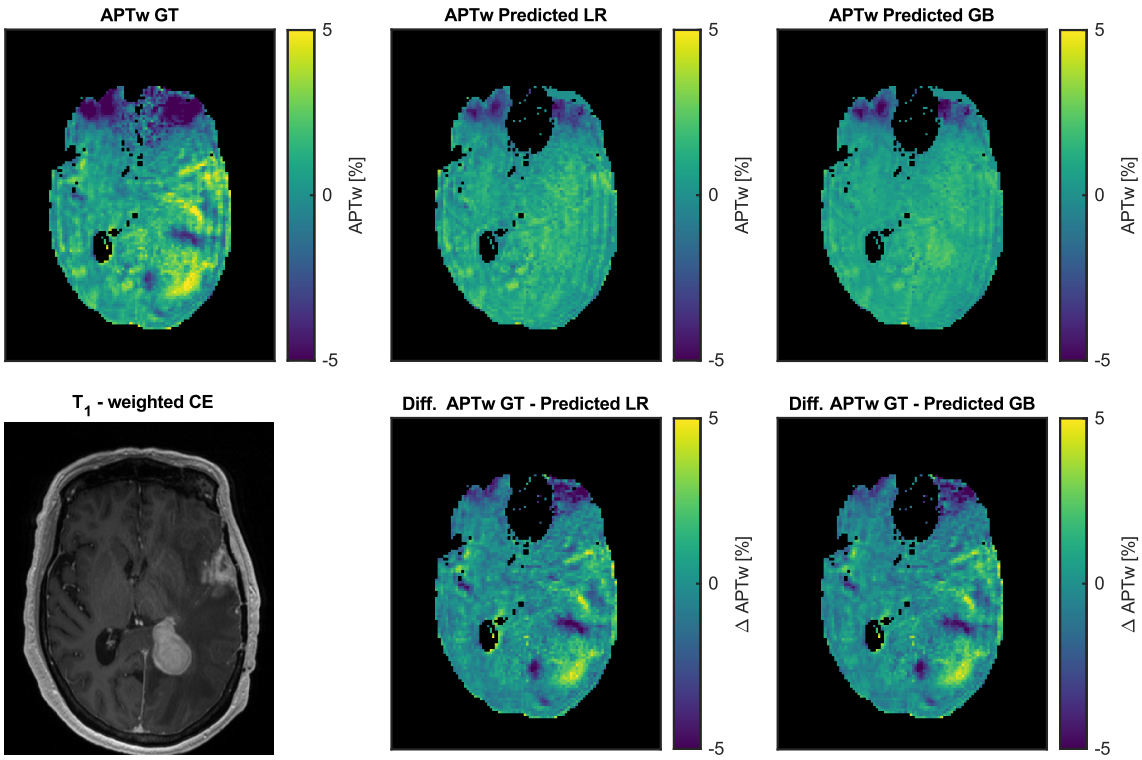

Figure 5.7: Investigation of a subject with high MAE. The voxelwise predicted APTw contrast by LR (Column 2) and GB (Column 3) based on the maximally unrestricted input features are displayed. The subject displayed is the same as shown in Figure 5.2 and was selected due to its high MAE of 1.00% for LR and 0.99% for GB. In addition, a T_1-weighted CE map is added for orientation purposes, and the APTw ground truth image and the difference maps between ground truth and predictions are shown. The ground truth image depicts advanced motion-induced artifacts in most parts of the edema. However, the models do not predict these artifacts, leading to the increased MAE.

5.2.2 Identification of the main contributors

In the previous subsection, it was demonstrated that a prediction of the APTw contrast based on low-power Z-spectra, T_1, ΔB_0, and rel. ΔB_1 is, in fact, feasible. However, it is equally essential to ensure that the prediction was performed based on physically relevant information, i.e. effects related to chemical exchange, to justify the use of the interpretable relaxation-compensated MTR_{Rex} contrasts as input features (Section 5.3). To do so, the main contributors for a successful prediction have to be identified. Furthermore, the information exclusivity has to be proven to ensure that the identified inputs actually contain the necessary information needed for the prediction process and are not chosen arbitrarily.

To achieve this, the following two steps were executed. First, a LASSO approach (described in Section 4.3.1) and permutation and gain feature importance (described in Section 4.3.2) were calculated to identify the most critical features for a successful prediction of the APTw contrast. Secondly, the feature space was reduced to 6 subsets including only certain Z-spectra regions, for which GB models were trained.

These models were consequently analyzed to evaluate if the most essential features that were previously extracted have exclusive information or were chosen arbitrarily.

LASSO and feature importance

In Figure 5.8, the MAE is plotted against the number of remaining features for the LASSO optimization (see Section 4.3.1). The figure shows that all inputs, except for around 20, can be left out for prediction without losing much predictive power. A significant increase of the MAE can be observed only by further reduction of the number of input features. At 20 remaining features, the MAE increases only by 0.02% for the LR method to 0.79%. Interestingly, a matching observation can be made when analyzing the permutation and gain importance of the GB model (see Section 4.3.2). The graphs show that, in both cases, only around 20 features have a significant importance value. These elbow points observed for the LASSO and permutation and gain importance of the GB model are why, in the following, only the 20 most important features are analyzed.

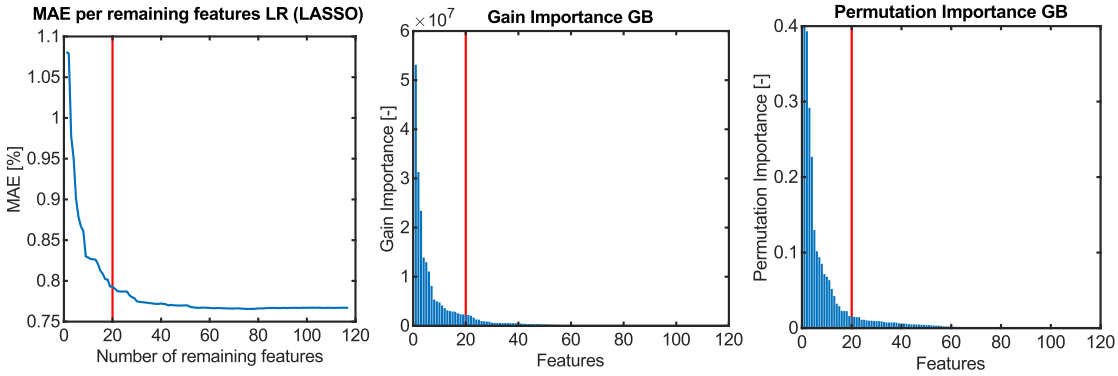

Figure 5.8: To identify the crucial contributors of the best-case models' importance, three different metrics were calculated. The LASSO approach, for the LR model, described in Section 4.3.1 was used to reduce the number of included features for training and following the MAE, depending on the remaining number of inputs, was calculated (left). A calculation like LASSO can not be performed for the GB model, so gain importance (middle), and permutation importance (right) were calculated for each feature (Section 4.3.2) to provide a similar insight. This insight can be created by sorting the importance of the input features in a descending manner. Interestingly, all graphs show that only around 20 features have significant importance values (marked with red lines).

Figure 5.9 and Table 5.5 show the 20 most essential features extracted by each method. Interestingly, all three evaluation approaches provided very similar results. For both models, rel. ΔB_1 was considered important, and twice as many frequency offsets were selected from the 0.9 µT spectra as from 0.6 µT. However, T_1 was not found significant for any model, and generally, the downfield (positive ppm range) side was more densely probed than the upfield (negative ppm range) side. Most strikingly, the sampling is restricted to frequency offsets close to 0 ppm, and the furthest selected frequency offset is at -7.5 ppm for all methods.

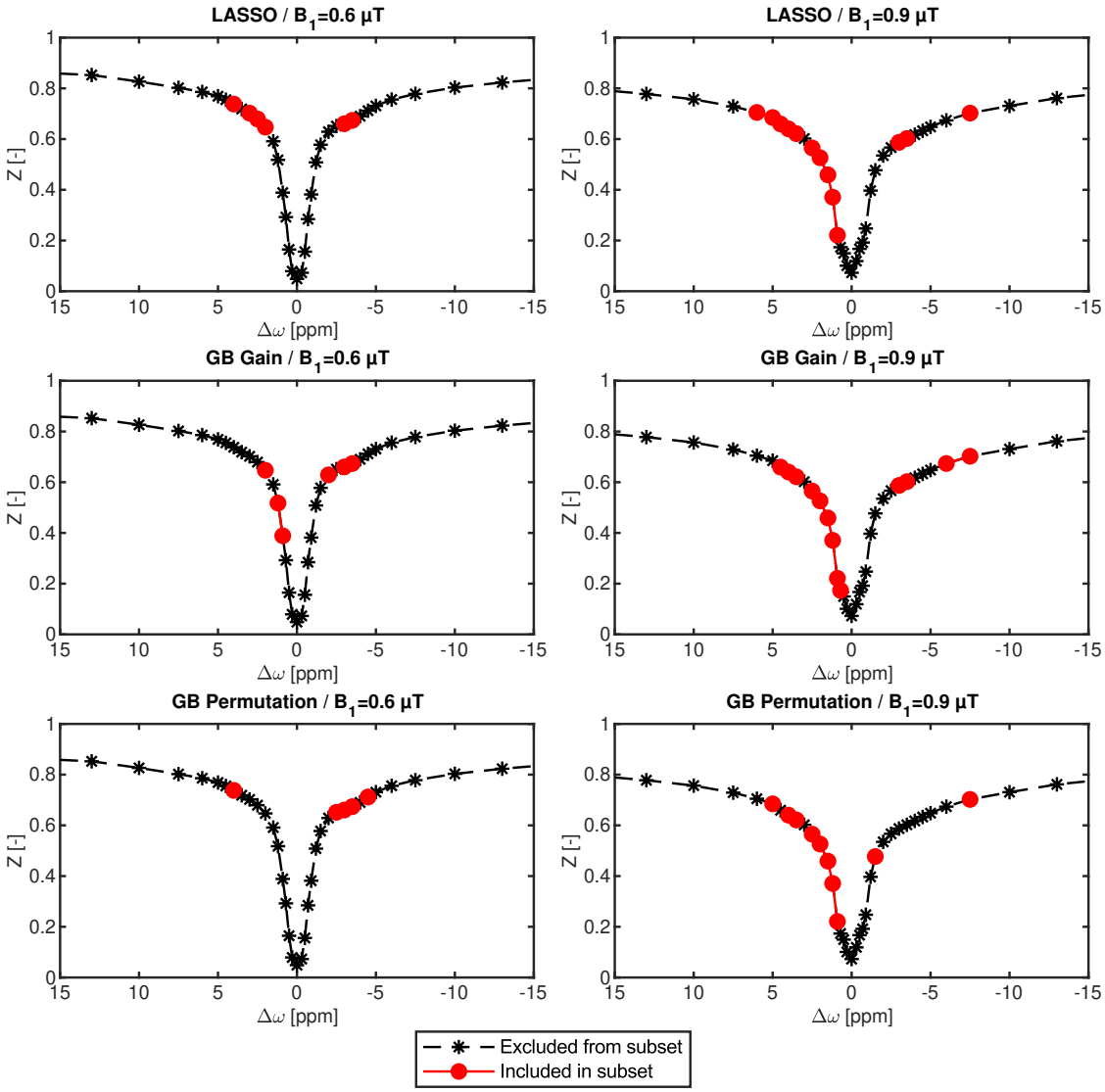

Figure 5.9: For visualization purposes, the top 20 features selected by the LASSO method (LR only, top), the gain importance (GB only, middle), and the permutation importance (GB only, bottom) listed in Table 5.5 are displayed. The left column shows an exemplary spectrum with the important regions from the Z-spectrum acquired with $B_1 = 0.6$ µT, and on the right, the same information for the Z-spectrum acquired with $B_1 = 0.9$ µT is provided. In addition to the marked regions, rel. ΔB_1 was among the 20 features with the highest importance for all evaluations.

Table 5.5: Display of the 20 most important features determined by LASSO (LR), permutation (GB), and gain importance (GB). Note that in this table, the input features are not sorted by importance. Interestingly, all three evaluation approaches provided very similar results. For both models, rel. ΔB_1 was considered important, and twice as many frequency offsets were selected from the 0.9 µT Z-spectra as from the 0.6 µT Z-spectra.

LR LASSO		GB Gain		GB Perm	
-3.5	Z-spectrum offsets with 0.6 µT [ppm]	-3.5	Z-spectrum offsets with 0.6 µT [ppm]	-4.5	Z-spectrum offsets with 0.6 µT [ppm]
-3		-3		-3.5	
2		-2		-3	
2.5		0.9		-2.5	
3		1.2		4	
4		2		-7.5	Z-spectrum offsets with 0.9 µT [ppm]
-7.5	Z-spectrum offsets with 0.9 µT [ppm]	-7.5	Z-spectrum offsets with 0.9 µT [ppm]	-4	
-3.5		-6		-3.5	
-3		-3.5		-3	
0.9		-3		-2.5	
1.2		0.7		-1.5	
1.5		0.9		0.9	
2		1.2		1.2	
2.5		1.5		1.5	
3.5		2		2	
4		2.5		2.5	
4.5		3.5		3.5	
5		4		4	
6		4.5		5	
rel. ΔB_1		rel. ΔB_1		rel. ΔB_1	

Evaluation of feature subsets

To analyze whether the information necessary for predicting the APTw contrast is exclusively found in the previously determined frequency offsets, six subsets of the Z-spectra were created, and GB models were trained on these subsets.

The dataset used for this task was similar to the one described in Subsection 5.2.1. Only the number of input features was reduced, i.e. subsampled low-power Z-spectra, T_1, rel. ΔB_1, and ΔB_0. The Z-spectra subsets were defined as follows (see Figure 5.10):

- (i) downfield only (29 frequency offsets per Z-spectrum, 0 to 250 ppm)
- (ii) upfield only (29 frequency offsets per Z-spectrum, -250 to 0 ppm)
- (iii) only the chemical exchange region (13 frequency offsets per Z-spectrum, 0.7 to 7.5 ppm)
- (iv) only the rNOE region (13 frequency offsets per Z-spectrum, -7.5 to -0.7 ppm)

- (v) everything except the chemical exchange and rNOE regions (31 frequency offsets per Z-spectrum, ±0.7 to±7.5 ppm excluded)
- (vi) everything except the chemical exchange, rNOE and direct water saturation regions (26 frequency offsets per Z-spectrum, -7.5 to 7.5 ppm excluded)

For all subsets T_1, rel. ΔB_1, and ΔB_0 were added, and the described frequency offsets were taken from both low-power spectra.

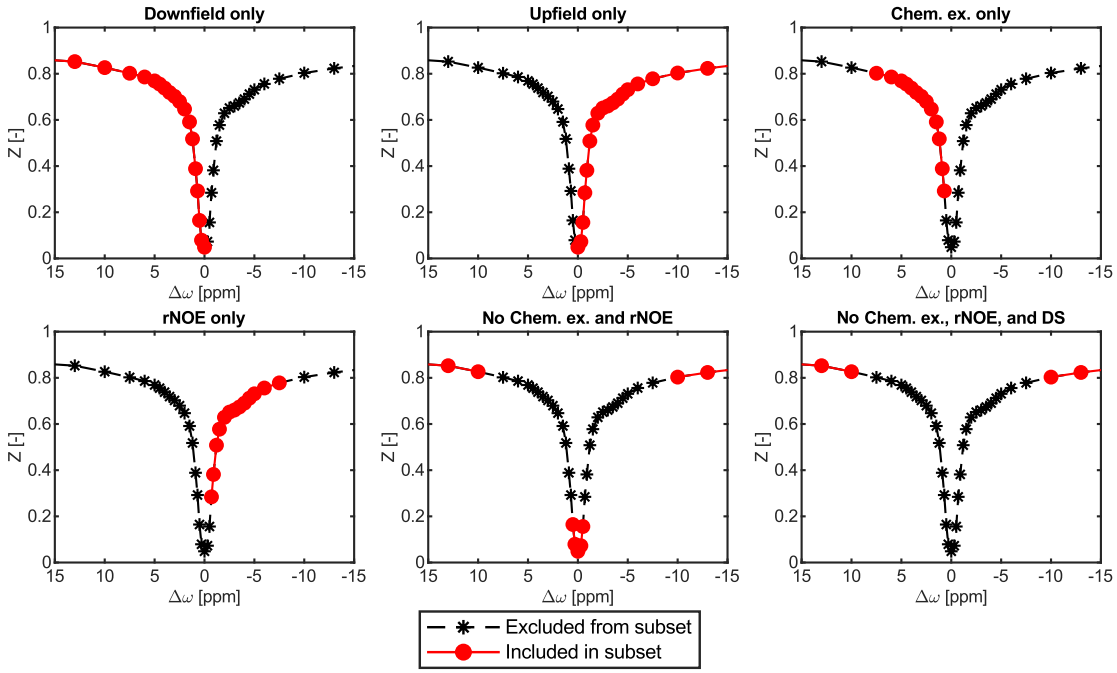

Figure 5.10: The subsets used to identify the most important features are visualized for a better understanding. The data points at 10 and 13 ppm are indicative for the entire downfield region: if the data points at 10 and 13 ppm were excluded, all not-displayed data points until 250 ppm were also excluded (Similarly for -10 and -13 ppm and the upfield region, and if they were included, the rest of the upfield region was also included). In each subset, the marked Z-spectrum regions were selected from both low-power Z-spectra (i.e., B_1=0.6 and 0.9 µT); additionally, rel. ΔB_1, ΔB_1, and T_1 were also included as inputs in each subset.

After the creation of the subsets, the GB models were also trained as described in the previous Section 5.2.1, and the resulting hyperparameters are shown in Table 5.6.

Table 5.6: Employed hyperparameters for the GB models trained on different subsets of the Z-spectra as determined by the grid-search algorithm. The hyperparameter optimization was conducted for each subset individually. However, the optimization yielded the same parameters for subsets (i)-(v).

Subset	# estimators	# leaves	learning rate	bagging fraction	drop rate	feature fraction
Subsets (i)-(v)	2000	31	0.1	0.8	0.2	0.8
No Chem. Ex. / rNOE / DS	1250	15	0.1	0.8	0.2	0.8

Table 5.7 shows the resulting predictive performances after the GB model was trained on the different subsets. If the subset contains no chemical exchange, rNOE, or direct saturation, the performance was the lowest, with an MAE of 1.12 % (all voxels). The chemical exchange region only, downfield only, and no chemical exchange and rNOE region subsets with an MAE of around 1% performed second worst. Most interesting is that the upfield side performed best with an MAE of 0.83%. However, this error is still 0.10% higher compared to using the entire spectrum. Furthermore similar tendencies when comparing the predictive power for all voxels, NAWM and NAGM voxels, and WT voxels can be observed as described for the model using the entire spectrum.

Table 5.7: Summary of the predictive performance of the GB models trained on the different Z-spectrum subsets. The MAE is given for all voxels, combined NAGM and NAWM voxels, and WT voxels.

	Overall MAE (%)	NAWM & NAGM MAE (%)	WT MAE (%)
Downfield only	1.00	0.92	1.06
Upfield only	0.83	0.75	0.99
Chem. Ex. only	1.01	0.93	1.10
rNOE only	0.85	0.78	1.01
No Chem. Ex. / rNOE	1.00	0.91	1.03
No Chem. Ex. / rNOE / DS	1.12	1.02	1.31

5.3 Development of a physically interpretable model (PIM) of the APTw contrast

Within this section, the physically interpretable model (PIM) for the APTw contrast is constructed. To create an interpretable model, by definition, the input features of the model must be interpretable as well as independent. The different frequency offsets in the Z-spectrum are conversely neither clearly interpretable nor independent. However, it is possible to choose appropriate input features that represent the critical sections of the Z-spectrum based on the previously identified most essential features (previous Section 5.2.2). With this, a LR and a GB model can be created to verify that a prediction is feasible using these interpretable input features. Furthermore, because a LR model can only model linear relations, the interpretable machine learning method SHAP can be used to break down the predictions of the GB model into components comparable to the LR model, enabling the identification of non-linearities in the GB models.

The following analysis provides the necessary information to create a more sophisticated and physically interpretable model (PIM) based on multiple LR models, each designed for a uniform-sized bin that is created by a grid extending over the relevant B_1 and T_1 range. Ultimately, this grid enables the physical interpretation of the model to develop an enhanced (bio)physical understanding of the APTw contrast in vivo and its underlying mechanisms.

5.3.1 Prediction of the APTw contrast using relaxation compensated MTR_{Rex} contrasts, T_1, and B_1

To reach the goal of creating a PIM, the feasibility of predicting the APTw contrast using physically interpretable contrasts (i.e., low-power, relaxation-compensated MTR_{Rex} contrasts for the AMIDE, rNOE and ssMT, as well as, B_1 and T_1) is investigated in this section.

The three quantitative relaxation-compensated MTR_{Rex} contrast for the AMIDE, rNOE, and ssMT CEST signal were chosen as they have similar information content as the identified crucial regions of the Z-spectra, while simultaneously being independent. The voxels' actual B_1 from the APTw CEST measurement (rel. $\Delta B_1 \times$ 2 µT) and T_1 was selected as additional input features because the APTw contrast has known B_1 dependencies (described in detail in Section 4.1.2). Furthermore, as the saturation scheme differed for the relaxation-compensated contrasts and the high-power APTw CEST acquisition, T_1 was added to the input features.

Dataset

The input features were chosen to be interpretable and independent to enable the interpretation of the model using the SHAP values. Combining the restrictions for interpretability and the information gathered in the previous section, the MTR_{Rex} AMIDE, MTR_{Rex} rNOE, MTR_{Rex} ssMT (each corrected for B_1 inhomogeneities and reconstructed at $B_1 = 0.7$ µT), T_1, and the voxels' actual B_1 from the APTw CEST measurement (rel. $\Delta B_1 \times$ 2 µT) were selected as input features. The chosen MTR_{Rex} contrasts underwent extensive post-processing as described in Section 3.4.1, making them B_1 independent. The output APTw contrast, on the other hand, is not corrected for B_1, and therefore, the B_1 corresponding to the voxel from the APTw CEST measurement was added as an input feature. As the saturation scheme differed for the relaxation-compensated contrasts and the high-power APTw CEST acquisition, T_1 was added to the input features. All voxels that were assigned to NAGM, NAWM, CSF, WT, necrotic tissue, and resection cavity during the annotation process were included for training and testing. Exclusion criteria for data points are described in the methods Section 3.4.4. These criteria led to a total of 5 features (i.e., MTR_{Rex} AMIDE, MTR_{Rex} rNOE, MTR_{Rex} ssMT, B_1, and T_1) for 4,513,915 training voxels and 1,420,823 test voxels.

ML models

Two models were trained to predict the APTw contrast: a LR model (described in Section 4.2.2) and a GB model (described in Section 4.2.3). The optimal hyperparameters for the GB model are listed in Table 5.8.

Table 5.8: Employed hyperparameters for the GB model as determined via grid-search algorithm when using the interpretable MTR_{Rex} AMIDE, MTR_{Rex} rNOE, MTR_{Rex} ssMT, B_1, and T_1 as input features.

# estimators	# leaves	learning rate	bagging fraction	drop rate	feature fraction
2000	15	0.1	0.8	0.2	0.8

Results

Table 5.9 summarizes the LR and GB model performances on the evaluation dataset. Compared to the best-case models, both models showed an increased MAE. This decrease is expected due to the post-processed contrasts used as input features, which dilute the information content and therefore increase the matching level, and the generally reduced input features, which might lead to an underrepresentation of necessary features for a successful prediction. The MAE of the GB model increased by 0.19%, and the LR model showed an even higher increase of 0.23% when evaluated for all voxels. Furthermore, the performance was again dependent on the selected subgroup of voxels, as the NAWM and NAGM voxels were again predicted with a lower MAE compared to the overall analysis and the WT voxel show again an increased MAE for both the LR and GB model.

Table 5.9: Summary of the predictive performance of the LR and GB model, based on the interpretable MTR_{Rex} AMIDE, MTR_{Rex} rNOE, MTR_{Rex} ssMT, B_1 , and T_1 as input features. The evaluation was performed for all voxels, combined NAGM and NAWM voxels, and WT voxels. Additionally, the results from the best-case model (created in the previous Section 5.2) are displayed for comparison in the bottom two rows.

Model		Overall MAE (%)	NAWM & NAGM MAE (%)	WT MAE (%)
Interpretable	LR	1.00	0.94	1.12
	GB	0.92	0.87	1.06
Best-case	LR	0.77	0.71	0.91
	GB	0.73	0.67	0.88

In Figure 5.11, the prediction (total 1,420,823, all patients) is displayed as a scatter plot (analogously to the previous Section 5.2). The points are displayed with the predicted contrast value on the y-axis and the ground truth value on the x-axis. Again, plots were created for (i) all voxels, (ii) voxels from NAGM and NAWM only, and (iii) WT voxels only. For visual guidance, an angle bisector is also displayed in each plot to indicate an ideal prediction (Figure 5.11, orange lines) and kernel density marginal histograms are displayed to provide a better understanding of the data point distributions (mean and SD of the distributions are listed in Appendix B Table 8.1). As expected from the increased MAE compared to the best-case models, the association between the ground truth and predicted values decreased. However, the data point distributions for both models are still centered around the ideal prediction (Figure 5.11, orange lines), and looking at the density

distributions of the predicted APTw contrast values in the corresponding regions, a decreased mean value for NAWM and NAGM voxels (LR: 0.12%; GB: 0.13%) and an increased mean value for WT voxels (LR: 0.51%; GB: 0.63%) can be observed when compared to the overall analysis (LR: 0.16%; GB: 0.17%). Regardless of the similar tendencies, it is striking that the mean predicted WT contrast is decreased by more than 0.4% for both models when compared to the best-case prediction.

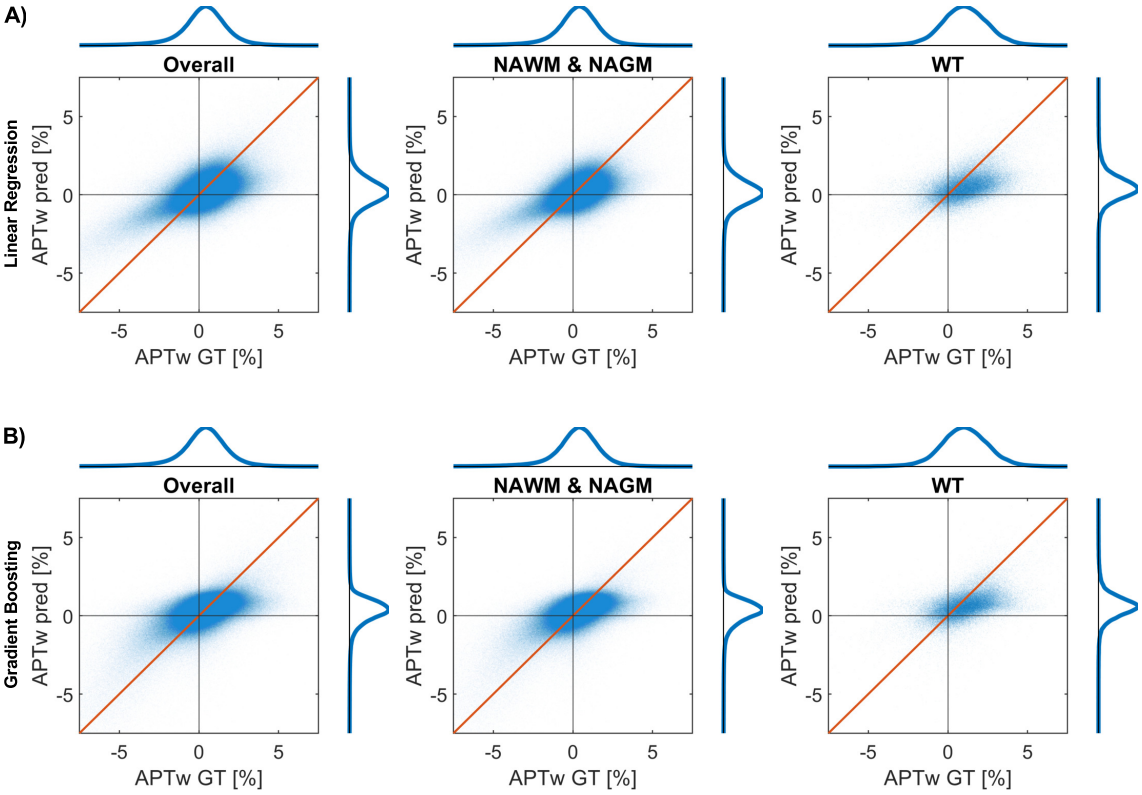

Figure 5.11: Analysis of the predictive performance of the LR and GB model created using physically interpretable MTR_{Rex} contrasts, B_1, and T_1 as input features. The voxelwise predicted APTw contrast is displayed for the LR model in subfigure A and the GB model in subfigure B. For visual guidance an angle bisector (orange lines) is displayed in each plot to indicate an ideal prediction. To understand the voxel distributions, kernel density marginal histograms are displayed on each axis (mean and SD of the distributions are listed in Appendix B Table 8.1). A scatter plot was created for all voxels (left column) and two subgroups containing the combined NAGM and NAWM voxels (middle column) and only whole tumor (WT = edema + CE) voxels (right column).

Furthermore, the deviations from the ideal prediction previously observed can be observed again for both models. The slope of the data points compared to the ideal prediction decreased further, showing that the predictions are even more likely to be closer to 0%, therefore underestimating the absolute ground truth value. This is the case for both the positive as well as the negative value range and can again be quantified by comparing the SD from the ground truth APTw contrast with the predicted contrast values. However, in this case, the SD for all voxels is reduced further (ground truth: 1.81%; best-case LR: 1.48%; best-case GB: 1.47%) to 1.08% for the GB model and 1.24% for the LR model, indicating the reduced value range

of the predicted voxels. Nevertheless, the LR model is more heavily impacted by this effect, especially for ground truth APTw contrast values below -2.5%.

Figure 5.12 shows the same evaluated patient as for the best-case models (cf. Figure 5.5). When comparing the model outputs to the ground truth, a reasonable match can be found for the GB model, with matching regions of hyper and hypo intensities, a similar NAWM and NAGM matter contrast, and a slightly increased contrast in the tumor region. The predicted values are generally closer to the mean as observed in the scatter plots, decreasing the predicted APTw contrast value range compared to the ground truth. Except for a mismatch in the tumor region, indicative for the decreased value range, only noise can be seen on the difference map (Figure 5.12, second row). The LR model performs similarly to the GB model when comparing regions with hyper and hypo intensities, but the value range is decreased even further, and regions with low APTw contrast value are poorly represented. A second representative patient is displayed in Appendix C.

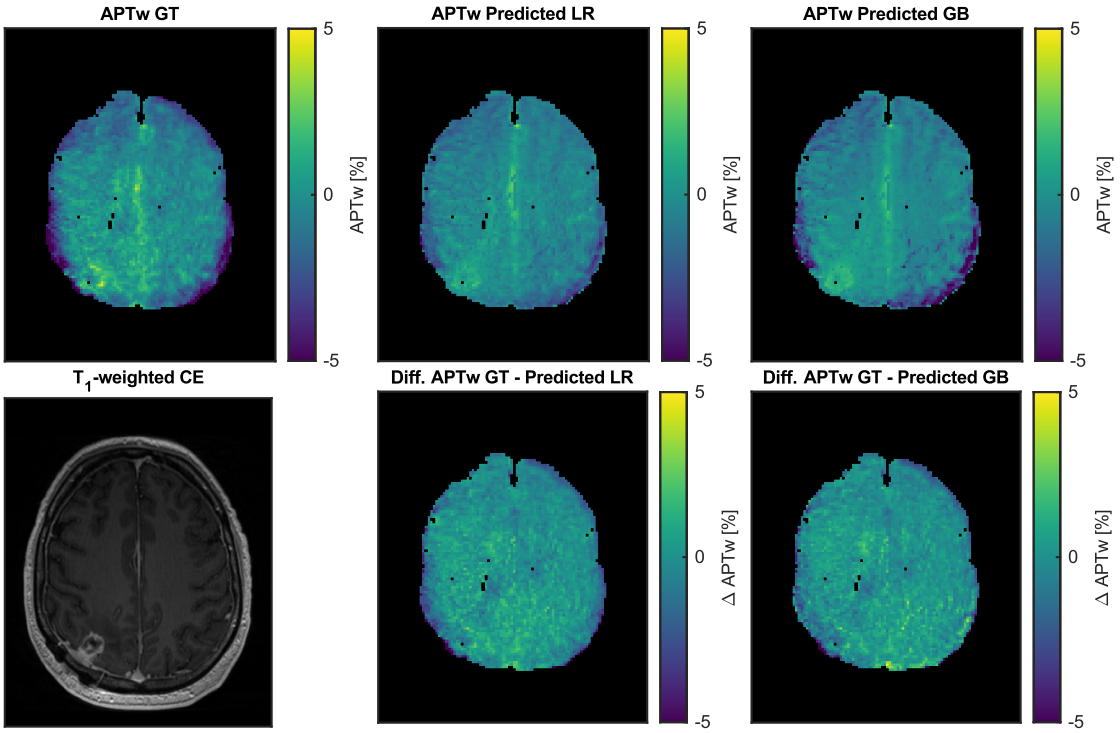

Figure 5.12: In this Figure, the voxelwise predicted APTw contrast by LR (Column 2) and GB (Column 3) based on the interpretable MTR_{Rex} contrasts, B_1, and T_1 as input features are displayed for a representative subject and slice. In addition, a T_1-weighted CE map is added for orientation purposes, and the APTw ground truth image and the difference maps between ground truth and predictions are shown. Notably, both algorithms predict with a decreased contrast range compared to the ground truth APTw image.

Furthermore, the importance plots and regression coefficients shown in Figure 5.13 demonstrate a close agreement with the identification of the crucial input features based on the fully sampled Z-spectra, translating the applied MTR_{Rex} contrast to corresponding offsets of the Z-spectra (Section 5.2.2). For both models, the dominant influence is the MTR_{Rex} rNOE, followed by MTR_{Rex} AMIDE and rel. B_1.

Interestingly, MTR_{Rex} ssMT and T_1 do not have as much influence on the prediction.

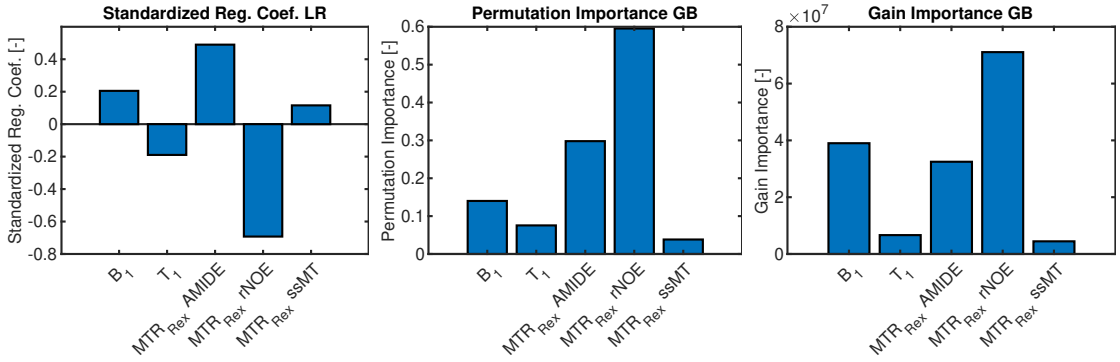

Figure 5.13: As a measure of importance for the input features, the standardized regression coefficients are displayed for the LR model (left). Importantly, these coefficients show the model's sensitivity towards changes of the corresponding contrast, and whether an increase in interpretable contrast value leads to an increase or decrease of the predicted contrast. When using the interpretable contrasts, the MTR_{Rex} AMIDE and rNOE are the dominant influences for the LR model. As a comparable measure, the permutation importances and gain importances (Section 4.3.2) were calculated for the GB model (middle and right, respectively). Similar to the LR model, both importances show a higher importance of the MTR_{Rex} AMIDE and rNOE. Noticeably, B_1 can be identified as a crucial contributor when looking at the Gain importance.

5.3.2 ML model analysis using dependence plots

In the previous Subsection 5.3.1, the performance of the LR and GB models to predict the APTw contrast based on the MTR_{Rex} AMIDE, MTR_{Rex} rNOE, MTR_{Rex} ssMT (each reconstructed at $B_1 = 0.7$ µT), T_1, and B_1 was evaluated. Most striking was the decreased performance of the LR model compared to the GB model. To understand the origin of the prediction discrepancy, the models are compared using dependence plots (described in Section 4.4). The differences in the predictions and with this the non-linearities of the GB model can be extracted by calculating the SHAP values for the GB model and comparing them to the regression coefficients from the LR model.

Dependence plots

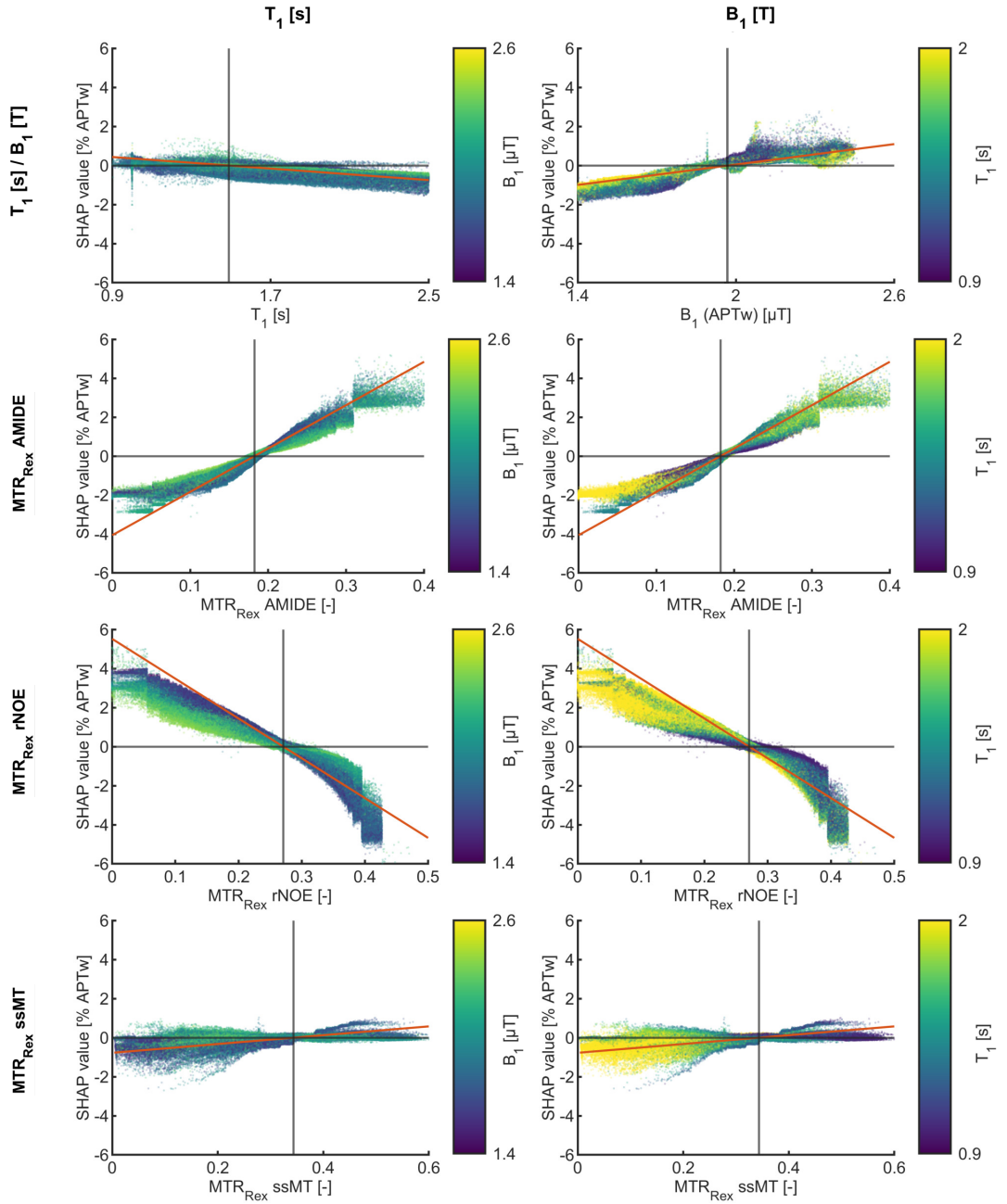

Figure 5.14: Dependence plots for the interpretable MTR_{Rex} contrasts, B_1, and T_1 are displayed as described in Section 4.4. The dependence plots show the SHAP values (Calculated for the GB model) for each predicted voxel depending on its input feature value. Additionally, the contributions from the input features on the APTw contrast calculated by the LR model are displayed as orange lines. The different coloring of the data points refers to the corresponding values of B_1 (left) or T_1 (right). Importantly, a good match between dependence plots and the dependencies calculated from the LR model can be observed (cf. data points and orange lines). Additionally, the influences of the MTR_{Rex} AMIDE and MTR_{Rex} rNOE outweigh the other three input features.

Figure 5.14 displays the partial dependence plots showing the SHAP values (influence of the corresponding input contrast value on the predicted contrast) for all voxels based on the feature value. The individual data points are colored based on their B_1 (left) or T_1 (right) value, along with the results from the LR model added to the plot as a straight line, as described in Section 4.4. By comparing the regression coefficients with the SHAP values, a good match for the MTR_{Rex} ssMT, B_1, and T_1 can be observed. However, for the MTR_{Rex} rNOE and AMIDE, a clear dispersion between the SHAP values and regression coefficients can be seen, although the regression coefficients are a good approximation of the mean influence at each feature value. Furthermore, the influences of MTR_{Rex} AMIDE and MTR_{Rex} rNOE are twice as strong as for the remaining three input features. They range from approximately -2 to 3 for the MTR_{Rex} AMIDE and from approximately -4 to 4 for the MTR_{Rex} rNOE.

Additional information can be extracted by looking at the dependence plots for B_1 and T_1 (Figure 5.14). Firstly, there is no clear dependency of the B_1 and T_1 SHAP values from each other. Secondly, the MTR_{Rex} ssMT shows low dependencies as the SHAP values at a fixed MTR_{Rex} ssMT contrast value only fan out marginally depending on the B_1. On the other hand, T_1 seems to correlate with the MTR_{Rex} ssMT value, but not with the SHAP value. Conversely, the SHAP values of the MTR_{Rex} AMIDE and rNOE both show dependencies on T_1 and B_1 and indicate a bigger value range for both low B_1 and high T_1 values.

Dependence plots for restricted T_1 and B_1 ranges

This paragraph aimed to further investigate the revealed dependencies of the MTR_{Rex} AMIDE's and rNOE's SHAP values on B_1 and T_1. To do so, four different combinations of T_1 and B_1 restrictions were employed, and the SHAP and MTR_{Rex} AMIDE contrast of the data points within these ranges were plotted as dependence plots (Figure 5.15). A linear fit was added to the dependence plots to visualize a linear approximation of the contribution of the MTR_{Rex} to the APTw contrast and whether the slope of this approximation changes depending on B_1 and T_1.

When looking at the different subplots in Figure 5.15, it is clearly visible that the linear approximation of the relationship between MTR_{Rex} AMIDE and rNOE and the contribution to the APTw contrast is reasonable, but only within discrete B_1 and T_1 ranges. When B_1 and T_1 change, the influence the MTR_{Rex} AMIDE and rNOE have on the final contrast also changes (the slope and, therefore, the contribution increases with increasing T_1 and decreases with increasing B_1). Based on this information, a grid of sufficiently small bin sizes to keep the B_1 and T_1 comparable within each bin was introduced. More importantly, these incremental value ranges justify the validity of a linear model describing inherently nonlinear dependencies, as the dependencies behave approximately linearly for small ranges. The minimum number of voxels per bin was set to 1000, and with that, the resulting grid was chosen as follows: B_1 : from 1.6 to 2.3 µT with a bin size of 0.05 µT (total 14 bins), T_1 : from 0.9 to 2 s with a bin size of 100 ms (total 11 bins).

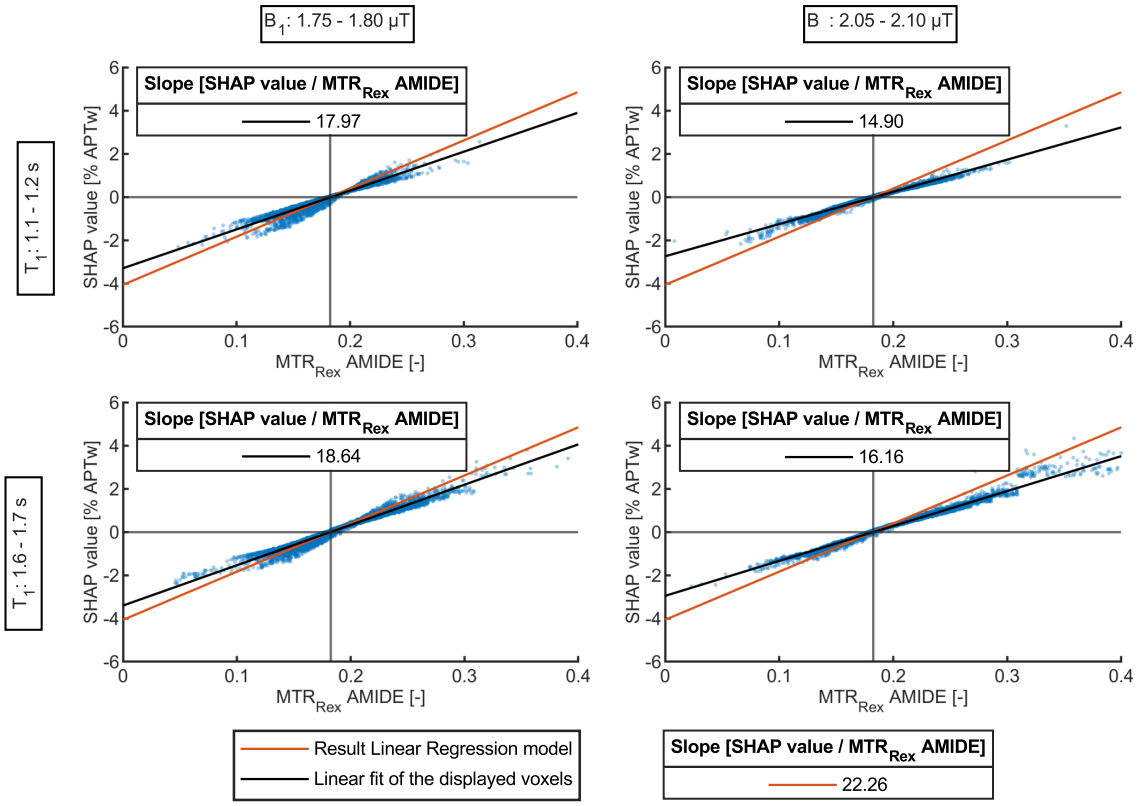

Figure 5.15: Dependence plots for MTR_{Rex} AMIDE, B_1, and T_1 are displayed for 4 combinations of restricted B_1 and T_1 values. The dependence plots show the SHAP values (calculated for the GB model) for each predicted voxel within the given B_1 and T_1 range depending on its input feature value. Additionally, the contributions from the input features on the APTw contrast calculated by the LR model are displayed as orange lines, and a linear fit of the displayed voxels (SHAP values GB model) was performed and is displayed with a black line. The plot shows the approximation of the contribution of the MTR_{Rex} AMIDE to the APTw contrast with a linear fit is reasonable provided that the B_1 and T_1 range is restricted.

5.3.3 Formation of the physically interpretable model (PIM) using the B_1-T_1 grid

The previous Section 5.3.1 showed that a linear approximation of the contrast contributions to the APTw contrast is justified as long as the B_1 and T_1 range is restricted. Using this insight, a PIM, based on a grid extending over the relevant B_1 and T_1 range and exploiting one trained LR model per bin, was constructed as described in Section 4.5 and is assessed in the following.

Dataset

For each of the B_1-T_1 subsets, the input features were the three MTR_{Rex} contrasts of the AMIDE, the rNOE, and the ssMT pool. Note that B_1 and T_1 were explicitly not included as input features, as the purpose of the individual B_1-T_1 subsets was to eliminate any T_1 or B_1 dependencies. However, the B_1 and T_1 dependencies are implicitly included within the standardization parameters of the input and output

values, as the standardization is performed bin-wise. The data points per bin are provided in Figure 5.16 for all voxels, as well as NAGM, NAWM, and WT voxels. Most notably, due to the narrow range of T_1 values observed in NAWM (Figure 5.16, bottom left subpanel), the distributions show a high number of NAWM voxels in the bins with a T_1 of 1 s - 1.1 s. In contrast, the NAGM and WT voxels are more evenly distributed between a T_1 of 1.2 s - 1.8 s (Figure 5.16, top and bottom right subpanels). In the B_1 dimension, a higher density around 2 µT can be observed (i.e. the nominal B_1 amplitude of the APTw contrast), corresponding to a relative B_1 of 100%. The bin size was set to a minimum voxel number of 1000 voxels per bin. As for the previous models, all voxels that were assigned to NAGM, NAWM, CSF, WT, necrotic tissue, and resection cavity during the annotation process were included for training and testing. Exclusion criteria for data points were described in the Methods (Section 3.4.4), but due to the minimum number of voxels per bin, an additional maximal and minimal B_1 as well as T_1 restriction were introduced. With this, 3,597,783 training voxels and 1,181,649 test voxels were included.

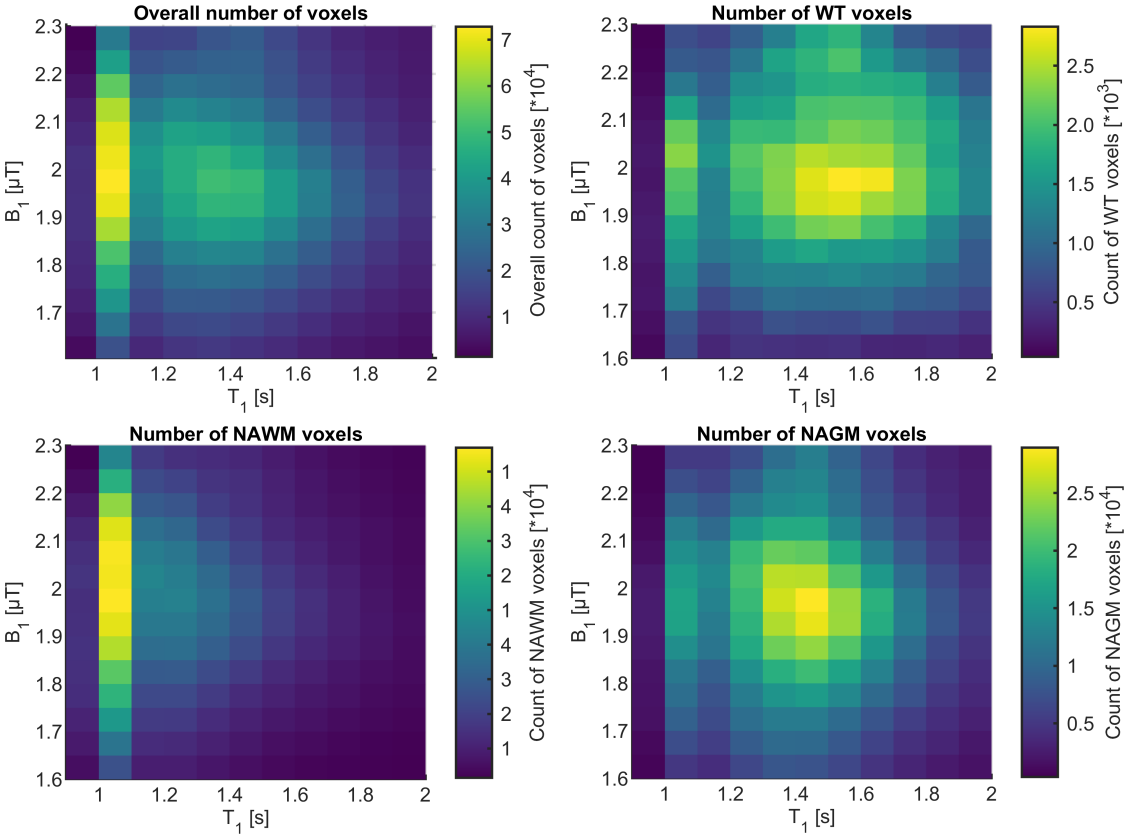

Figure 5.16: The overall number of voxels and the distribution of the WT, NAWM, and NAGM voxels in each B_1-T_1 bin are illustrated. Most notably, due to the narrow range of T_1 values observed in NAWM (bottom left subpanel), the distributions show a high number of NAWM voxels in the bins with a T_1 of 1 s - 1.1 s. In contrast, the NAGM and WT voxels are more evenly distributed between a T_1 of 1.2 s - 1.8 s (top and bottom right subpanels). In the B_1 direction, a higher density around 2 µT (i.e., the nominal B_1 amplitude of the APTw contrast) can be observed, corresponding to a relative B_1 of 100%.

ML models

The model used for training the PIM is described in Section 4.5. This model requires a dataset split into subsets with similar B_1 and T_1 values (i.e., bins in Figure 5.16). Crucially, for each subset (i.e., B_1-T_1 bin), a separate LR model was created.

Results

Table 5.10 summarizes the performance of all previously trained models (Best-case, GB and LR based on the MTR_{Rex}, B_1, and T_1 contrasts) evaluated on the reduced dataset (reduction by approximately 80%) described within this section (max. and min. B_1 and T_1 value restriction due to the grid). Remarkably, the restriction of B_1 and T_1 leads to a decrease in MAE for all previously evaluated models. Strikingly, the newly established PIM performs better than the LR model using the interpretable contrast without the grid, i.e., exhibiting an MAE decrease of 0.04% in the overall evaluation. However, the MAE of the GB model using the interpretable contrast is still 0.03% lower than for the PIM.

Table 5.10: Summary of the predictive performance of the PIM, and the LR and GB models for both best-case and with interpretable input features. The evaluation was performed for all voxels, NAGM and NAWM voxels, and WT voxels. Additionally, all models were only evaluated for voxels residing within the restricted range through the min. and max. B_1 and T_1 grid values, explaining the differing performance.

Model		Overall MAE (%)	NAWM & NAGM MAE (%)	WT MAE (%)
PIM		0.92	0.88	1.07
Interpretable	LR	0.96	0.93	1.12
	GB	0.89	0.86	1.06
Best-case	LR	0.73	0.69	0.90
	GB	0.69	0.66	0.88

In Figure 5.17, similar trends can be observed for the PIM as for the previously created GB and LR models using the interpretable inputs (cf. Figure 5.11). However, the mean values of the predicted APTw contrast values using the PIM are closer to the ground truth than the predictions of the previously created GB and LR models using the interpretable inputs for all voxels, for the NAWM and NAGM voxels, and for the WT voxels (mean and SD of the distributions are listed in Appendix B Table 8.2). Furthermore, the value range decreases less severely when compared to the LR model based on the interpretable inputs. Comparing the SDs for all voxels, a clear increase of the value range (PIM: 1.12%) can be seen compared to the LR prediction based on the interpretable inputs (ground truth: 1.73%; interpretable LR: 1.00%; interpretable GB: 1.19%).

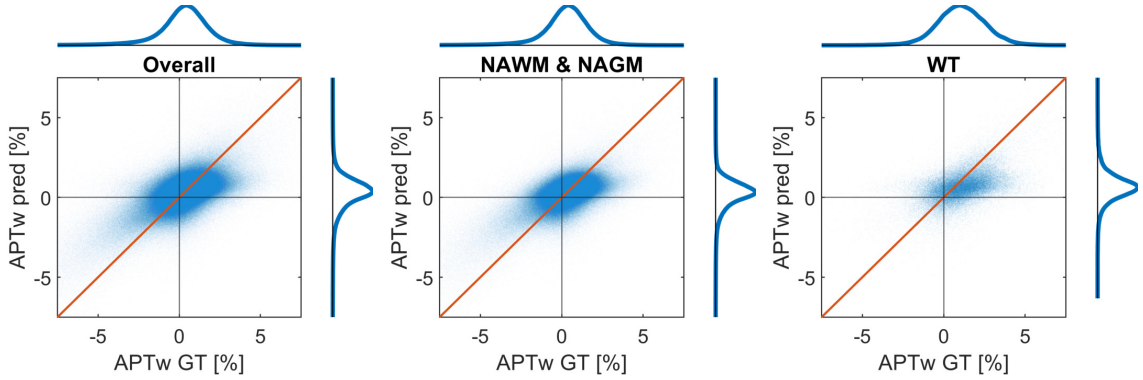

Figure 5.17: Analysis of the predictive performance of the PIM based on the physically interpretable MTR_{Rex} contrasts. For visual guidance an angle bisector (orange lines) is also displayed in each plot to indicate an ideal prediction. To understand the voxel distributions, kernel density marginal histograms are displayed on each axis (mean and SD of the distributions are listed in Appendix B Table 8.2). A scatter plot was created for all voxels (left column) and two subgroups containing the combined NAGM and NAWM voxels (middle column) and only whole tumor (edema + CE) voxels (right column).

Examining the predicted APTw contrast maps for the same representative patient as in the previous sections (Figure 5.18, regions exceeding the grid limits are blacked out), an clear increase in the value range is visible. The hypointense tumor region is depicted more clearly, and the whole tumor region shows an increased contrast closer to the ground truth than the prediction from the GB and LR model based on the interpretable input features (cf. Figure 5.12). Furthermore, the difference map shows no clear shortcomings of the prediction, as it is primarily noise-like. A second representative patient is displayed in Appendix C.

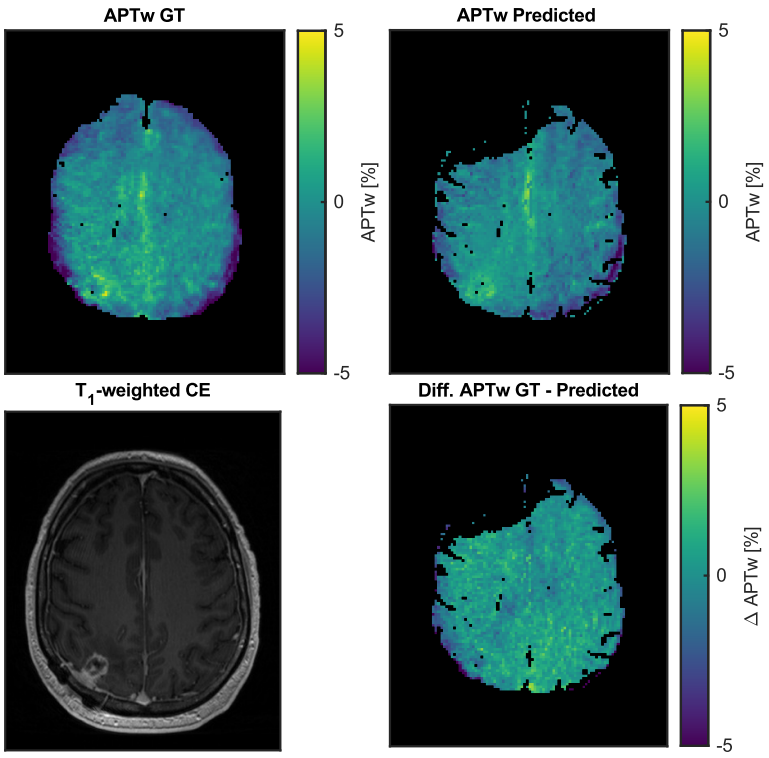

Figure 5.18: In this Figure, the voxelwise predicted APTw contrast using the PIM for a representative subject and slice is displayed. In addition, a T_1-weighted CE map is added for orientation purposes, and the APTw ground truth image and the difference map between ground truth and prediction are shown. Notably, regions with high and low APTw ground truth values are predicted closer to the ground truth when compared to the LR model trained on the interpretable input features (Figure 5.12).

5.4 In-depth analysis of the physically interpretable model (PIM)

In order to assess whether the model is in line with the underlying physics, the PIM is analyzed in detail in this section. Initially, the standardization parameters were analyzed to get an overview of possible correlations between the input parameters and B_1 or T_1, as they could decrease the interpretability of the PIM and are essential for the interpretation of the standardized MTR_{Rex} contrasts (Section 5.4.1).

After this, the regression coefficients calculated for the PIM (Appendix D) multiplied with the $SD(APTw(B_1, T_1))$ (Figure 5.19, bottom row right column; Equation 4.8, Section 4.5) were analyzed, as they are representative of the sensitivity of the predicted APTw contrast on changes of the respective Std. MTR_{Rex} input parameters (Section 5.4.2). The product of regression coefficients and $SD(APTw(B_1, T_1))$ is called sensitivity during the rest of this thesis. This analysis showed that the sensitivity and influence of the Std. MTR_{Rex} AMIDE and Std. MTR_{Rex} rNOE dominate the APTw contrast compared to the ssMT's, which seems almost negligible. Therefore, in the last step, the ratio of the absolute Std. MTR_{Rex} AMIDE and Std. MTR_{Rex} rNOE sensitivity maps was analyzed to investigate which of the two

main contributors is the predominant one and whether this changes depending on the B_1 and T_1 bin (Section 5.4.3). Most strikingly, it was found that an increasing B_1 leads to a change of the predominant contributor from Std. MTR_{Rex} rNOE to Std. MTR_{Rex} AMIDE at approximately 2 µT.

5.4.1 Analysis of the standardization parameters

In order to compare the sensitivities of the PIM in a meaningful manner, it was necessary first to standardize the input and output data. For standardization, the mean and SD in each bin was calculated. However, in addition to enabling a comparison of the sensitivities, the standardization parameters also provide information about possible correlations between the relaxation-compensated contrasts and B_1 and T_1. This information is crucial, because the standardization is performed bin-wise, which leads to a correction of possible scaling factors depending on B1 or T1 in the input and output contrasts. Therefore, a thorough analysis is vital for the interpretation of the calculated sensitivities. All standardization parameters for MTR_{Rex} and APTw contrast can be found in Figure 5.19.

Standardization of the relaxation-compensated MTR_{Rex} contrasts

Looking at the mean values (Figure 5.19, left column), it is apparent that the behavior of the MTR_{Rex} AMIDE contrast differs from MTR_{Rex} ssMT and MTR_{Rex} rNOE. Both the MTR_{Rex} ssMT and MTR_{Rex} rNOE show minimal B_1 dependencies but strongly correlate with T_1. Both of these contrasts exhibit increased mean contrast values with decreasing T_1 relaxation time. Conversely, the MTR_{Rex} AMIDE does not exhibit the same dependency. On the other hand, the MTR_{Rex} AMIDE contrast shows a slightly increased mean contrast value in the bins between 1.3-1.8 s T_1 and 1.9-2.2 µT B_1 (hotspot in Figure 5.19, top left). However, looking at the SD (Figure 5.19, right column), the MTR_{Rex} contrasts show similar tendencies, exhibiting little B_1 dependencies but an increased SD with increasing T_1 values.

Standardization of the APTw contrast

Contrary to the relaxation-compensated contrasts, the mean of the APTw contrast displays changes with changing T_1 as well as B_1 values (Figure 5.19, bottom left). The mean value is highest for high T_1 and high B_1 values, and seems to decrease steadily with decreasing B_1 and T_1 values. Looking at the SDs, an increase can be observed in the regions with B_1 values below 1.8 µT (Figure 5.19, bottom right). Additionally, an increase with increasing T_1 can be seen.

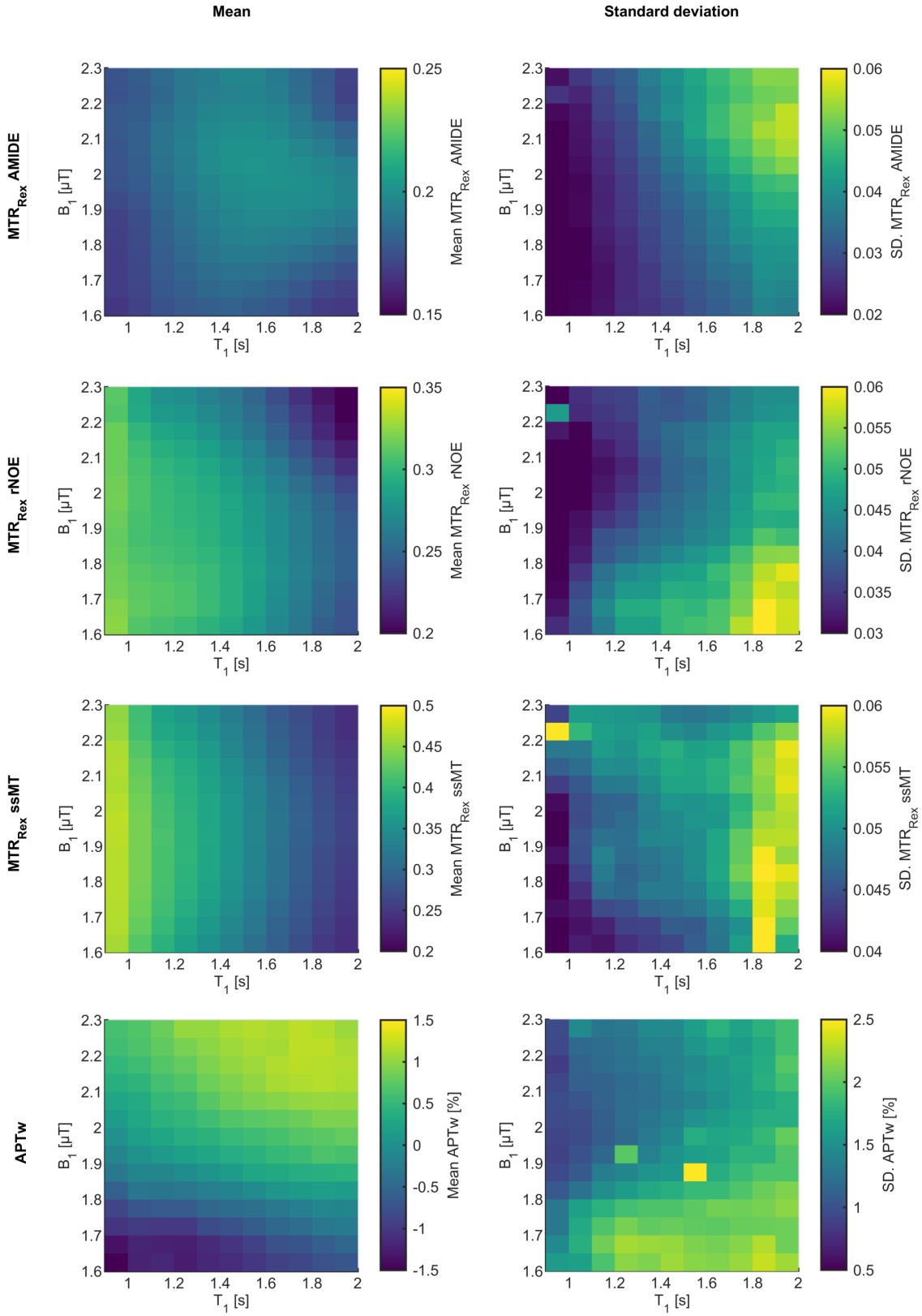

Figure 5.19: The mean (left column) and SD (right column) of the three employed MTR_{Rex} contrasts and the APTw contrast for each of the 154 bins in the grid are displayed. Note that this information is necessary for a bin-wise standardization of the input and output features. Additionally, insights into possible changes in the mean and SD of the contrasts depending on B_1 and T_1 values are provided.

5.4.2 Analysis of the APTw contrast sensitivities

The regression coefficients generated by the PIM are a crucial tool for the assessment of the physical information content, since the product of regression coefficients (Appendix D) and $SD(APTw(B_1, T_1))$ (Figure 5.19, bottom row right column) are representative of the sensitivity of the predicted APTw contrast on changes of the respective standardized input parameters (Std. MTR_{Rex}). Therefore, in this subsection, the sensitivities were analyzed.

The sensitivities are displayed for each B_1-T_1 bin in Figure 5.20. Additionally, the sensitivity maps are shown as sets of curves, once plotted with fixed B_1 to highlight the changes of the sensitivities based on increasing T_1, and vice versa (Figure 5.20, middle and right). For visibility reasons, the set of curves was reduced to 5 curves per plot.

Starting with the sensitivities of the Std. MTR_{Rex} AMIDE (Figure 5.20, left column), which suggest a higher sensitivity change based on T_1 than B_1 (cf. Figure 5.20, top middle and top right). However, a decreasing sensitivity for small T_1 and high B_1 values can be observed. Furthermore, the sensitivities of the Std. MTR_{Rex} AMIDE are positive for every bin. The Std. MTR_{Rex} rNOE, on the other hand, has only negative sensitivities. Comparable to the Std. MTR_{Rex} AMIDE is the convergence of the sensitivity towards 0 with increasing B_1 and decreasing T_1 values. Finally, the Std. MTR_{Rex} ssMT has the smallest sensitivities compared to the Std. MTR_{Rex} AMIDE and Std. MTR_{Rex} rNOE (cf. the different scaling in Figure 5.20). Additionally, the Std. MTR_{Rex} ssMT is the only contrast with positive and negative sensitivities. The sensitivity predominantly changes with B_1 and is primarily stable with T_1. With an increasing B_1 value, the sensitivities change from around +0.2 to -0.1.

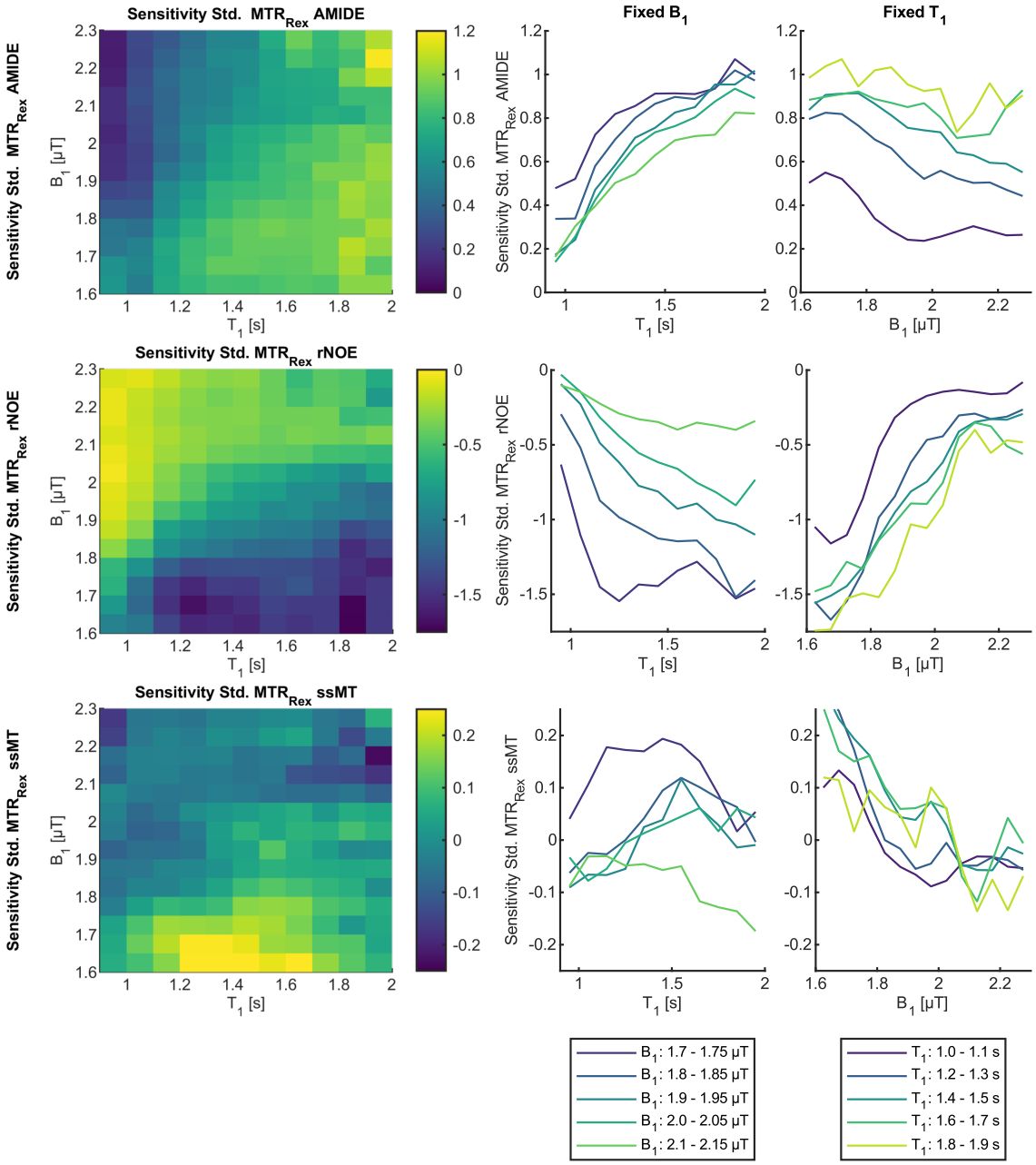

Figure 5.20: The sensitivities for the Std. MTR_{Rex} AMIDE (top), rNOE (middle), and ssMT (bottom) were determined for each bin by an individual LR model. It is important to note that the MTR_{Rex} AMIDE contrast has exclusively positive sensitivities, the rNOE exclusively negative sensitivities, and the sensitivities of the ssMT range from around -0.2 at high B_1 and low T_1 to 0.1 at low B_1. For visualization purposes, the maps are also displayed as sets of curves, once plotted with fixed B_1 to highlight the changes of the sensitivities based on increasing T_1, and vice versa. The sets were reduced to 5 curves per plot with equidistant B_1 or T_1 values.

5.4.3 Ratio analysis of the absolute Std. MTR_{Rex} AMIDE and Std. MTR_{Rex} rNOE sensitivities

To conclude the analysis, the ratio of the dominant absolute Std. MTR_{Rex} AMIDE and absolute Std. MTR_{Rex} rNOE sensitivities was calculated (|sensitivity Std.

MTR_{Rex} AMIDE| / |sensitivity Std. MTR_{Rex} rNOE|; absolute as sensitivity Std. MTR_{Rex} rNOE has a negative value range). Therefore, a ratio > 1 indicates a higher sensitivity towards changes in Std. MTR_{Rex} AMIDE than towards changes in Std. MTR_{Rex} rNOE. As the aim of this analysis was to isolate changes that are different between the two contrasts, the ratio is a favorable metric. For example, variations due to ssMT spillover should be diminished, as both contrasts should be affected similarly. Figure 5.21 shows the ratio of the sensitivities as a map and a set of curves as in the previous subsection 5.4.2. When looking at the ratio, it is apparent that there is no influence from T_1, meaning that the sensitivities for Std. MTR_{Rex} AMIDE and rNOE scale similarly with changing T_1 values (Figure 5.21, middle). However, there are evident changes in the B_1 direction (Figure 5.21, right). The ratio steadily increases from 0.5 at the minimum B_1 of 1.7 µT to 1.75 at the maximum B_1 value of 2.3 µT. However, the ratio already starts to stagnate at around 2.1 µT. Remarkably, this B_1 dependency changes the dominant contrast sensitivity from Std. MTR_{Rex} rNOE to Std. MTR_{Rex} AMIDE at around $B_1 = 2$ µT, which is identical for all T_1 values. These insights enable the determination of two separate regimes, i.e. (i) an AMIDE-dominated regime for values > 1 and (ii) a rNOE-dominated regime for values < 1.

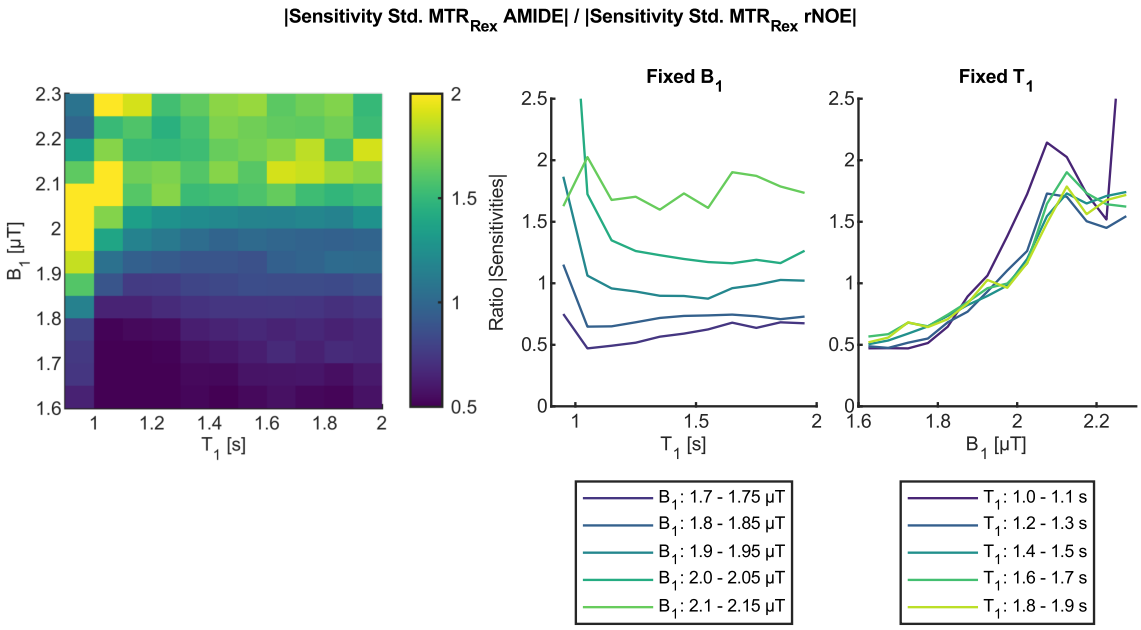

Figure 5.21: The ratio of the sensitivities was calculated by dividing the absolute sensitivities of the Std. MTR_{Rex} AMIDE by the absolute sensitivities of the Std. MTR_{Rex} rNOE. Therefore, a ratio > 1 indicates a higher sensitivity towards Std. MTR_{Rex} AMIDE than Std. MTR_{Rex} rNOE changes, and vice versa for values < 1. For visualization purposes, the maps are also displayed as sets of curves, once plotted with fixed B_1 to highlight the changes of the sensitivities based on increasing T_1, and vice versa. The sets were reduced to 5 curves per plot with equidistant B_1 or T_1 values. Striking is the independence of the ratio with regard to changes in T_1 (middle, approximately constant values) and the clear change from a dominant Std. MTR_{Rex} rNOE sensitivity to a dominant Std. MTR_{Rex} AMIDE sensitivity with increasing B_1 (right, change occurs around 2 µT).

Chapter 6

Discussion

The imaging of the amide proton transfer-weighted (APTw) contrast is an emerging molecular technique that has found rising interest in recent years because of its proven clinical relevance for neuro-oncological questions. Initially, the ability of the APTw contrast to support clinical decision-making in tumor and stroke imaging was accounted for by its sensitivity to protein content and pH changes. However, over time, the understanding of the APTw contrast evolved from an initially very simplistic to a complex model with many contributors interacting with one another. To provide an insight into the interactions, a PIM was developed by utilizing various ML methods combined with an extensive clinical dataset comprising 125 patients to extract previously unexplored features in the APTw CEST data. This PIM enables for the first time the examination of the underlying mechanisms and interactions between the contributors to the APTw contrast in vivo. The main steps of the modeling process are summarized shortly:

1. Creation of a matching level for evaluation of the models by investigation of the APTw contrast features and variations in vivo.

2. Implementation of best-case models to prove that (i) a prediction of the high-power APTw contrast from low-power data is actually possible, and therefore, (ii) a transfer between the different saturation schemes is feasible.

3. Identification of the crucial features exploited by the best-case models (step 2) to prove that the models exploit physically relevant information and to identify suitable interpretable input features for the PIM.

4. Evaluation of the possibility of predicting the APTw contrast using the identified interpretable contrast (MTR_{Rex} AMIDE, MTR_{Rex} rNOE, MTR_{Rex} ssMT, B_1, T_1) as input features for a GB or LR model.

5. In-depth analysis of the models (step 4) using interpretable ML methods (Dependence plots, SHAP) to understand the prediction process of the models and to extract the differences that distinguish the models (non-linearities of the GB model).

6. Combination of (i) the non-linearities of the GB model approach and (ii) the interpretability of the LR model approach by the development of a PIM which is based on a grid (covering the relevant B_1 and T_1 range) and the subsequent

creation of an individual LR model for each unifrom-sized bin partitioned by the grid.

6.1 Current applications and challenges of the APTw contrast

Since the first mentioning of the APTw contrast in 2003 [14] and its first application to brain tumor patients three years later [33], several different applications for neuro-imaging, as well as for imaging of other regions of the human body, have been investigated using the APTw contrast with varying success [35, 36, 37, 38, 39].

The varying success is partly due to the many challenges of APTw imaging when applied in vivo, such as the unclear interpretation of the APTw contrast due to its simplistic calculation (i.e., merely the substraction of two acquired CEST images), which includes multiple contributors to the Z-spectrum to calculate the APTw contrast as well as the influences of saturation schemes and artifacts on the APTw contrast [40].

Therefore, an effort has been made by many groups to identify the possible shortcomings and develop alternatives to enable the clinical applicability of the APTw contrast. However, many of the approaches focus on the effect of parameters like the B_1 power on the final APTw contrast, neglecting the dependencies between the contributors, or are based on theoretical models that are only applicable to some extent to a realistic patient cohort. This highlights the necessity of a physically interpretable model (PIM), which enables the isolation of the contributors to the APTw contrast in a clinical cohort.

6.1.1 Applications of the APTw contrast in neuro-imaging

Applications of the APTw contrast can be found for a multitude of different medical questions regarding the human brain, ranging from brain tumors over stroke to neurodegenerative diseases (e.g. Alzheimer's disease [120], Parkinson's disease [121, 122], and multiple sclerosis [123]). An overview of the two main applications will be provided in the following.

Brain tumors

The APTw contrast is most commonly used in brain tumor imaging as it has the potential to provide a non-invasive molecular diagnosis that complements the standard of care. Initially, the focus of the application was on detecting brain tumors, as the hyperintense APTw contrast of tumor tissue differs from edema and contralateral brain tissue [33, 124]. However, the scope of the application has since expanded to include tumor grading [35, 36] and the identification of genetic markers like the Isocitratdehydrogenase (IDH) mutation status [125] and O(6)-Methylguanine-DNA-methyltransferase (MGMT) methylation status [126]. Furthermore, the APTw contrast was found helpful in assessing therapy response, enabling the differentiation between progressive disease and stable disease [37, 38, 39].

However, while there is much clinical evidence for the use of the APTw contrast in brain tumor imaging, the origins of its effectiveness are often only assumptions and cannot be clearly associated with one specific mechanism, which in turn hampers the clinical interpretability.

Stroke

Because of the success of APTw imaging in the scope of brain tumors, considerable interest in the APTw contrast was generated, leading to its translation to other pathologies. The second most studied pathology is stroke, where the APTw contrast has shown promising sensitivity to pH changes during early ischemia [127, 128] and blood leakage into tissue during hemorrhage and successfully differentiates between the two [129]. However, until now, it has been considered as an addition to the current workflow of perfusion and diffusion-weighted imaging because, while amide and rNOE signals have potential enhancing interplay for brain tumors, they counteract each other for stroke imaging, highlighting the fact that a more specific contrast or an insight into the mechanisms would be beneficial.

Both applications demonstrate the enormous potential of APTw contrast for clinical use, but the lack of knowledge about the APTw contrast's origin is a clear drawback since it limits the interpretation of the clinical findings.

6.1.2 Challenges of APTw imaging in vivo

The APTw contrast encompasses multiple Z-spectrum contributors (as discussed in Section 4.1.2). However, these contributors are interconnected (e.g. spillover) and also depend on the experimental conditions, such as the saturation scheme (B_1 amplitude, saturation duration, pulse length, pulse shape, and inter-pulse spacing) and B_0 field strength [40]. Consequently, this reduces the interpretability of the APTw contrast, making it less transferable to pathologies that have not been thoroughly studied using this contrast. Nevertheless, numerous efforts have been made to address these issues.

Challenges

The challenges faced in APTw imaging of the human brain, specifically in brain tumor imaging, can be categorized into technical challenges and interpretability issues related to biological changes.

The technical issues faced are as follows:

- Typically, the APTw contrast measures changes in the water signal in the range of 5 - 10%, leading to a value range of the APTw contrast from -5% to 5%. This small value range poses a significant challenge for the APTw contrast as the low SNR heavily impacts the repeatability of measurements of the APTw contrast. Therefore, the APTw contrast is likely to produce false positive and negative findings, thus limiting the clinical applicability.

- The sensitivity towards B_0 inhomogeneities further reduces the repeatability, especially in infratentorial regions. B_0 inhomogeneities lead to a shift of the entire Z-spectrum and, therefore, heavily impact the APTw contrast due to the asymmetry analysis.

- Furthermore, APTw imaging is prone to motion-induced artifacts because the analysis is based on a difference analysis of two frequency offsets. This is problematic, as movements between the two offsets lead to a mismatch of voxels, impacting the APTw contrast value and leading to a MAE in the range of 1.33 % (APTw) (13% of the APTw value range) even for a mismatch by just one voxel (Section 5.1.2).

- Finally, the APTw contrast heavily depends on the saturation scheme, such as B_1 amplitude, saturation duration, pulse length, pulse shape, and inter-pulse spacing. These parameters all influence the labeling efficiency and the spillover dilution of the pools involved in the Z-spectra, therefore changing the APTw contrast. This is particularly problematic, as it decreases the comparability of studies between different imaging sites. The dependency on the B_1 amplitude can already be observed for B_1 fluctuations caused by field inhomogeneities, as shown in the map displaying the mean APTw contrast value dependent on B_1 and T_1 (Figure 5.19, bottom row left column). This map shows that the mean APTw contrast for a T_1 = 1 s to 1.1 s changes from -1.2% at B_1=1.6 µT to 0.69% at B_1=2.3 µT which is a change of approximately 19% of the entire value range of the APTw contrast (-5% to 5%).

These technical challenges transfer to the interpretability issues related to biological changes. As stated earlier, the APTw contrast is calculated using two frequency offsets with different signal contributions. The +3.5 ppm offset has contributions from the DS, ssMT, amides, amines, guanidino, and downfield rNOEs and is subtracted from the -3.5 ppm offset, which has contributions from DS, ssMT, and aliphatic rNOE signals, introducing many possible contrast contributors. Furthermore, as mentioned earlier, all of the contributors are additionally dependent on the T_1 and T_2 of water, as well as, B_0, and saturation scheme, which makes the interpretation very challenging. Therefore, areas of liquefactive necrosis, hemorrhage, large vessels, or post-surgical cavities filled with proteinaceous fluid often exhibit hyper-intense contrast values and can be mistaken as tumors because of the reduced ssMT and, with that, reduced spillover dilution.

Recent developments

Although there are many challenges for APTw imaging, the increased interest due to its clinical potential led to many developments, aiming to provide a more stable contrast in vivo.

To make the APTw contrast more reproducible, a B_0 correction was introduced, which can be easily implemented by shifting the Z-spectrum based on an additionally acquired B_0-map (either from an extra measurement or using a sequence extension). Furthermore, a motion correction, as suggested as a part of this work (Appendix A), should be performed to suppress the artifacts described in Figure 5.3.

Combining these methods with the repeated acquisition of the offsets used for the APTw contrast calculation to increase SNR is essential for improving the repeatability of APTw imaging. However, the different saturation schemes used at different imaging sites still impede the comparability between one another. To this end, in 2023, an effort was made as part of a consensus recommendation paper [40] to generalize a specific saturation scheme and highlight the differences between schemes, with the aim of improving the comparability of studies conducted at different imaging sites.

These advances, although helpful for comparability and reproducibility, did not increase the interpretability of the APTw contrast. To this end, different efforts have been made in the past two decades, aiming to exclude single contributions to the APTw contrast or aiming to analyze the effect of B_1 and T_1 on the APTw contrast value.

A first effort to isolate the rNOE and amide components was made by estimating the ssMT contributions from the acquired data and subsequent subtraction from the evaluated offsets. However, to achieve this, a more considerable offset range (64 offsets) had to be acquired, increasing the measurement time and, therefore, decreasing the clinical applicability [130, 131].

In contrast, a more clinically applicable method aiming to tackle the hyperintensities stemming from liquid compartments was made with the introduction of fluid-suppressed APTw imaging [132, 133, 134]. This approach helps to improve the readability of the APTw contrast, since it removes the artifacts from liquid compartments by suppressing the spillover effects from the ssMT and DS.

Furthermore, studies on the T_1 of water, water proton fraction, and B_1 dependency of the APTw contrast were performed. The survey of the T_1 and the water proton fraction showed that, in non-steady-state acquisitions with very short presaturation time, both have no apparent influence on the final APTw contrast [135, 109]. For the B_1 changes, however, it was observed that an increased B_1 leads to an increased APTw contrast value, which can be reasonably explained by the influence of B_1 on spillover and labeling efficiency [105, 84]. Although it is crucial to optimize the APTw contrast in vivo, both of the analyses were performed using different setups, making the results not representative for every saturation scheme. Furthermore, the studies were conducted to generate optimal tumor contrast without any insights into the changes for the individual contributors, limiting the interpretation possibilities.

A single effort was made to identify contributors and their interactions and, in particular, to isolate possible amine and guanidino influences on the APTw contrast [136]. The study showed that the guanidino and amine signal, in fact, influences the downfield (+ 3.5 ppm) signal contribution of the APTw contrast significantly. However, the analysis was performed based on simulations and rat measurements at $B_0 = 4.7$ T and has, therefore, only limited transferability to patient measurements at 3 T.

Shortcomings

Interestingly, most of the efforts to improve the APTw contrast were mainly conducted to improve the tumor contrast, not to understand the mechanisms in vivo. Therefore, most studies have only been performed using the final APTw contrast as an endpoint, not the components leading to the APTw contrast, which decreases the value as dependencies could potentially be destructive in one case but constructive in another. Additionally, most of the analyses trying to advance the interpretability have been performed either at field strengths higher than 3 T or based on contrasts which themselves are not interpretable, as they are neither independent of B_1, nor compensated for spillover. These shortcomings can be explained because extensive studies of these dependencies are inherently difficult for multiple reasons:

- To extract interpretable contrasts, a multi-pool Lorentzian fit or other fitting approaches need to be performed on the Z-spectra. However, the extraction of the pools at higher B_1 is challenging, mostly due to the high spillover dilution and dominating ssMT, which decrease the amplitude of the pool of interest significantly as can be seen in the simulated Z-spectra at a nominal B_1 of 2 µT (Figure 6.1, A). Furthermore, APTw CEST measurements are not performed in a steady-state, which, by definition, renders the calculation of spillover-corrected and relaxation-compensated contrasts like the MTR_{Rex} infeasible, even if the pool of interest were to be successfully extracted.

- Another approach would be a simulation study. However, although there is knowledge about how many contributing pools are needed for a good estimation, the exchange rates and proton fraction necessary for a successful simulation are not well-known for every tissue required to get a good overview of the mechanisms in vivo. Therefore, a simulation is, to this point, not an adequate representation of the entire range of possible spectra in vivo.

- Lastly, an approach could be made to extract the pools at a lower B_1 amplitudes, as isolation of the pools at $B_0 = 3$ T can be performed for $B_1 < 1$ µT (Figure 6.1, B). This approach, however, would need a translation function of the APTw contrasts to a high B_1, as the labeling efficiency is dependent on the B_1 power (Equation 2.58). The theoretical construction, however, is very challenging as APTw imaging is not performed in steady-state, and many parameters (proton fraction f_s, exchange rates k_s, and relaxation times $T_{1,s}$ and $T_{2,s}$) needed for a translation are unknown.

However, a data-driven approach might be able to estimate these necessary parameters to translate low-power contrasts into a high-power contribution to the APTw contrast, possibly providing a first insight into the APTw contrast contributions.

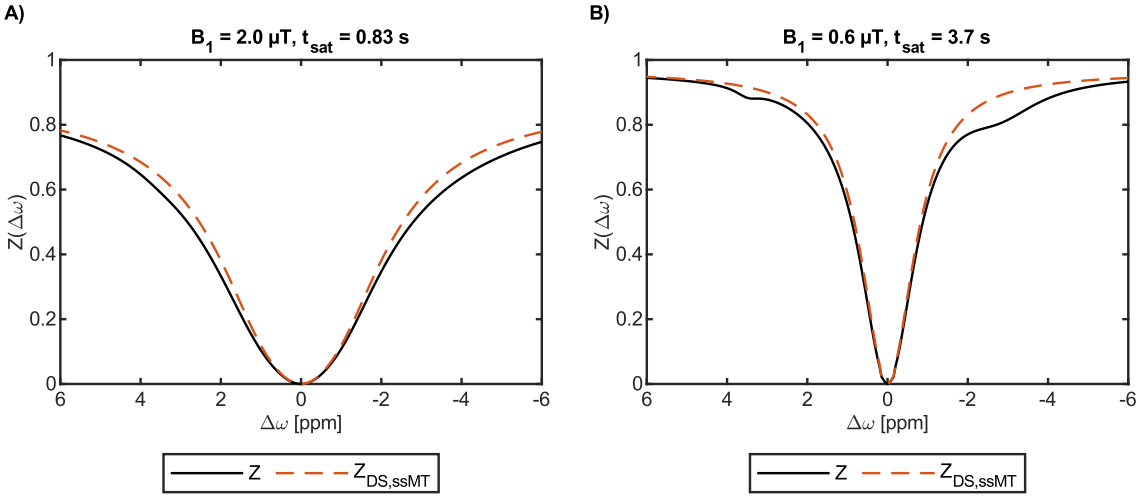

Figure 6.1: Simulated Z-spectra with a B_1 of 2 µT (left, $t_{sat} = 0.83$ s) and 0.6 µT (right, $t_{sat} = 3.7$ s) using the Bloch McConnell simulation parameters described in Appendix E. The Z-spectra were simulated based on the saturation schemes used for the patient measurements used within this thesis. However, note that in this figure, the DC is 100%, and the pulse shape is a continuous wave for both Z-spectra. The pools included for modeling were the DS, ssMT, rNOE, amide, amine, guanidino, and hydroxyl pools.

6.1.3 ML in CEST

The use of ML methods in CEST imaging has rapidly expanded over the past few years. However, its primary application has been the acceleration of the acquisition (undersampling of k-space or of frequency offsets) [137, 138] and post-processing (extraction of pool parameters) processes [139, 140], which are still a significant limitation for in vivo CEST applications. Furthermore, classical ML applications, such as tissue classification tasks [141], have been performed, but the generation of knowledge about the underlying mechanisms of CEST MRI has not been a major focus.

Only two applications can be found, which are exceptions to the trend. Zaiss et al. [142] demonstrated in a proof-of-principle study the feasibility of predicting 9.4 T Z-spectra from 3 T Z-spectra using deep-learning (DL), suggesting that combined applications of CEST and ML might be able to generate more insight into the CEST phenomenon. Furthermore, a recently published article [143] showed that a reconstruction of steady-state CEST Z-spectra from transient-state Z-spectra is feasible using ML, which for the first time hints towards the plausibility of translating between saturation schemes.

In summary, until now, there has been only a small effort to generate new knowledge with the combined application of CEST and ML, but the successful translation between saturation schemes and translation between different B_0 field strengths already suggests that the set aim of calculating a high-power APTw contrast from low-power MTR_{Rex} contrasts might be feasible.

6.2 Physical validation of the ML models

In order to develop the PIM of the APTw contrast and validate the modeling process, (i) it is necessary to generate a matching level for the different model iterations to enable a fair validation (Section 5.1), and (ii) it is essential to ensure that the model actually exploits physically relevant information (i.e., effects related to e.g. chemical exchange or rNOE) to warrant interpretation (Section 5.2.2).

6.2.1 Successful implementation of ML models

To create a matching level for a fair validation of the different APTw contrast models, naturally occurring APTw contrast deviations in normal-appearing tissue were assessed (Section 5.1). Furthermore, the influences of artifacts on the APTw contrast were estimated, since the basis of this work is actual patient data from a clinical study, including imaging and motion-induced artifacts. The MAE was the selected evaluation metric for the APTw contrast prediction, as it is less dependent on outliers that are to be expected in a clinical dataset. To enable a comparison to the MAE, the MAD was chosen to evaluate the APTw contrast fluctuations.

As a matching level for a near-perfect prediction (approximately 0.75%), the frontal lobe NAWM ROI was chosen because, for the analyzed patient, this brain region was free of any artifacts and provided the best possible MAD of the APTw contrast within the examined regions (Figure 5.1). In comparison, for the NAGM ROI in the same frontal lobe region, one can observe a considerable increase of the MAD (MAD = 0.96 %), which can be attributed to partial volume effects, as NAGM voxels are more likely to have contributions of CSF (CSF displays an evident change in contrast compared to NAGM) than the NAWM voxels. However, this does not mean that the NAWM ROIs are free of such effects, which is why the actual noise level can be expected to be slightly smaller than the calculated MAD.

Partial volume effects are also relevant when investigating the influence of motion-induced artifacts on the APTw contrast. Although all used contrasts or Z-spectra offsets were motion-corrected to reduce mismatches between voxels from different acquisitions, motion-induced artifacts cannot be perfectly corrected. This is due to the size of the voxels and the therefore originating partial volume effects which cannot be reversed. Furthermore, an interpolation is performed when applying a motion correction, which introduces artifacts (2x interpolation lead to MAE = 0.53%; Section 5.1.2). However, a motion correction is crucial, as significant mismatches between the offsets used for calculating the APTw contrast or the B_0 map and the APTw contrast would have a more significant impact on the final APTw contrast (single voxelshift along y-axis lead to MAE = 1.33%; Section 5.1.2). Therefore, the matching level needs to be adapted for subjects with advanced motion-induced artifacts, which should additionally depend on the size of the edema or CSF regions because these regions are most prone to exhibit strong artifacts due to the significantly different ssMT contributions.

Another necessity for a fair assessment of the models was the investigation of the ringing artifacts (Section 5.1.1). The observed ringing artifacts are most likely Gibbs

ringing or truncation artifacts and originate from the partial Fourier readout of the image acquisition [144] and are visible for the APTw contrast as the APTw contrast values are in a range of a few percent (approximately -5% to 5%). However, it is essential to note that this artifact only impacts the predictive performance of the models based on the interpretable contrasts (3 different MTR_{Rex}, B_1 and T_1). This is the case because the information about the artifact is available for the best-case models, as the Z-spectra used as input features were acquired with the same readout and are barely post-processed, and therefore contain the same artifact. However, the interpretable contrasts are generated through many post-processing steps, which dilute the information about the artifacts and, in turn, reduce the quality of the potential best-performing model. This makes another adaption of the expected matching level necessary for the models based on the interpretable contrasts, which should be inspired by the MAD in the regions affected by ringing artifacts, such as the parieto-temporal NAWM region where a MAD of 0.94% was observed. However, one should remember that these artifacts are not apparent in all patients and not throughout the entire brain.

Based on the created matching levels and taking into account the information about the motion-induced artifacts (Section 5.1.2) and ringing artifacts (Section 5.1.1), one can now fairly assess the created models. This assessment shows that all models were successfully implemented and showed deviations within the expected ranges, considering the expected shortcomings. The evaluation of the best-case models (LR: MAE= 0.77% and GB: MAE= 0.73% for the overall evaluation) showed a good agreement with the matching level created based on frontal lobe NAWM ROI (0.75%), and all subjects with increased MAE were later assessed to exhibit evident motion-induced artifacts, reducing the prediction quality as previously established. Furthermore, the increased MAD (LR: MAE= 1.00% and GB: MAE= 0.92% for the overall evaluation) for the models based on the interpretable contrasts (3 different MTR_{Rex}, B_1,T_1) can be assigned to the dilution of contrast information through the extensive post-processing, which in turn lead to missing information about the ringing artifacts and therefore to a decreased APTw contrast value range. However, the visual correlations between the GB model and the ground truth were still as expected, and through the implementation of the PIM, the LR model's initial lack of contrast was restored.

6.2.2 Use of physically relevant information by the best-case model

To create a physically interpretable model, it is mandatory to validate that the models exploit physically relevant information and to show that, conversely, a model based on physically irrelevant information cannot perform a successful prediction. To this end, the results from the importance analysis of the best-case LR and GB model (Section 5.2.2) are discussed in this subsection, whereas the PIM and the interpretation of its underlying mechanism are discussed in detail in the next Section 6.3. The calculated importance metrics provide information about which features are crucial for a successful prediction. However, because the individual offsets of the Z-spectra are not independent of one another, an additional analysis using different regions of the Z-spectrum as input features for a model was conducted to prove that

the previously identified crucial offsets contain necessary information that cannot be found in other regions of the Z-spectra. These analyses also provided the basis to identify interpretable representations of the crucial Z-spectra regions that were used as input features for the PIM.

When analyzing the 20 most important features (Table 5.5, the limit of 20 features was selected via the elbow method) from the best-case models, it is essential to note that the LASSO approach and the gain and permutation importance are not created for the same model and are calculated differently. However, they have a similar interpretation for our use case.

The analysis showed that the 20 most important features evaluated by the different methods align very well with one another, and all selections can be explained with the known influences on the APTw contrast in vivo (Section 4.1.2). In particular, all feature importance methods selected the rel. ΔB_1, which is easily explained because the labeling efficiency and spillover dilution of the different pools contributing to the Z-spectra are heavily dependent on the saturation power (Equations 2.58 and 2.63). Therefore, the information is crucial to predict the APTw contrast in regions with B_1 inhomogeneities. Furthermore, as expected, only offsets in the region of -7.5 ppm to 6 ppm were selected (Table 5.5), which is where all the chemically exchanging, as well as rNOE pools, are located. Another interesting agreement is that more than double the offsets were chosen from 0.9 µT than from 0.6 µT Z-spectra. This is physically plausible because the nominal B_1 of the APTw sequence is 2 µT, and therefore, the labeling scheme of the 0.9 µT spectrum is closer to the scheme used for APTw imaging. A fourth striking agreement between the methods was that more frequency offsets on the downfield side of the Z-spectrum than on the upfield side were chosen. This is most likely the case because the upfield side of the Z-spectrum is only influenced by the rNOE and ssMT pool. The downfield side, however, has influences from amide, downfield rNOE, amine, ssMT, hydroxyl, and guanidino pools. Therefore, a denser sampling of the downfield side seems reasonable to generate an adequate representation of all pools. This hypothesis is supported by the fact that the chosen offsets on the downfield side start at 0.7 ppm, which is a region where the influence of the hydroxyl and guanidino resonance can already be measured due to their broad resonances caused by their high exchange rates (Section 2.4.2) and the B_0 of 3 T. Lastly, the offset at -7.5 ppm of the 0.9 µT Z-spectrum was selected by all methods. This offset could be crucial to estimate possible spillover dilution and, with that, the ssMT effect. In conclusion, one can say that, based on the analysis of the 20 most important features, the models did exploit physically relevant information to enable the prediction of the APTw contrast based on low power Z-spectra, B_1, B_0, and T_1.

To prove that the selected offsets have exclusive information that cannot be found in other frequency offsets and to prove that a model based on physically irrelevant information cannot perform a successful prediction, GB models were trained on feature subsets representing only certain regions of the Z-spectrum (e.g., downfield only or rNOE only). This analysis showed that a successful prediction based on just one side of the Z-spectrum is not possible, and, in fact, both sides of the Z-spectrum are critical for a successful prediction. Importantly, it was shown that both the chemical

exchanging and rNOE regions are crucial for a successful prediction, and using only the ssMT and DS is insufficient information for the task of predicting the APTw contrast. Therefore, the best-case models seem to exploit the physical information content to predict the APTw contrast successfully. Furthermore, the amide and rNOE signals are essential for a successful prediction, and the 20 most important features hint towards an influence of amine, hydroxyl, and guanidino resonances, in coherence with literature [136].

6.3 Interpretation of the PIM

The PIM's most significant advantage is that all of its components are interpretable. This is crucial in understanding the physical dependencies of the model and comparing it to the theoretical basis. Ultimately, this helps to decipher the underlying mechanism of the APTw contrast.

The valuable information the PIM provides about the APTw contrast and input features is given by the standardization coefficients and the calculated sensitivity maps (Figure 5.20, left column i.e., regression coefficients $(\beta_i(B_1, T_1)) \cdot SD(APTw(B_1, T_1)))$. These standardization coefficients and sensitivity maps can be used to calculate the contributions $\Delta APTw_{n,i}$ to the predicted APTw contrasts in voxel n for each feature $i \in \{MTR_{\text{Rex}}\ AMIDE,\ MTR_{\text{Rex}}\ rNOE,\ MTR_{\text{Rex}}\ ssMT\}$ via:

$$\Delta APTw_{n,i}(B_1, T_1) = \frac{x_{n,i} - \bar{x}_{i,\text{train}}(B_1, T_1)}{SD(x_{i,\text{train}}(B_1, T_1))} \cdot \beta_i(B_1, T_1) \cdot SD(APTw_{\text{train}}(B_1, T_1)) \tag{6.1}$$

where $\bar{x}_{i,\text{train}}(B_1, T_1)$ and $SD(x_{i,\text{train}}(B_1, T_1))$ are the mean value and SD of feature i (Figure 5.19, first three rows of left and right column, respectively) and $SD(APTw_{\text{train}}(B_1, T_1))$ the SD of the APTw contrast (Figure 5.19, bottom right) calculated with the training dataset for the corresponding B_1-T_1 bin. Using equation 6.1, the APTw contrast can then be calculated using:

$$APTw_n(B_1, T_1) = \overline{APTw_{\text{train}}}(B_1, T_1) + \sum_{i=1}^{3} \Delta APTw_{n,i}(B_1, T_1) \tag{6.2}$$

where $\overline{APTw_{\text{train}}}(B_1, T_1)$ is the mean value of the APTw contrast (Figure 5.19, bottom left) calculated with the training dataset for the corresponding B_1-T_1 bin. These equations (6.1 and 6.2) are crucial for the interpretation of the PIM and will be referred to throughout this section.

6.3.1 Physical interpretation of the standardization of the PIM's input and output features

The standardization is an essential step to make the regression coefficients comparable with each other and also provides a basic understanding of the B_1 and T_1 dependency of all input and output features (Section 5.4.1). However, because the standardization is performed bin-wise, possible scaling factors depending on B_1 or T_1 will be inherently corrected for during the standardization process. The implication

of this correction will be described separately for the input and output parameters. Furthermore, one cannot exclude the possibility of changes in mean and SDs, which are not caused by physical effects but rather due to the biological ensemble included in each bin, meaning that it is likely that not every B_1-T_1 bin includes voxels from every tissue type.

MTR_{Rex} standardization parameters

The interpretation of the standardization coefficients (Figure 5.19) and the implications for the standardized MTR_{Rex} contrasts will be discussed first. The mean values of all MTR_{Rex} contrasts are almost entirely independent from B_1 changes, which is as expected, as a B_1-correction was performed for all MTR_{Rex} contrasts. Similarly, the MTR_{Rex} AMIDE is also independent of T_1 changes (mean MTR_{Rex} AMIDE max = 0.20 and min = 0.17). However, the ssMT and rNOE both show noticeable T_1 dependencies with decreasing mean values towards high T_1 values. The mean MTR_{Rex} ssMT (within the B_1 bin ranging from 2 - 2.05 µT) decreases from 0.47 (T_1: 1.9 - 2 s) to 0.26 (T_1: 0.9 - 1 s) and the mean MTR_{Rex} rNOE decreases from 0.32 (T_1: 0.9 - 1 s) to 0.23 (T_1: 1.9 - 2 s). A combination of three effects can explain this dependency. (i) The most likely origin for the increase of the mean values with lower T_1 values is the voxel distribution of the NAWM voxels (Figure 5.16, bottom left), which indicates that most of the NAWM voxels are located in the low T_1 range, which is as expected from earlier T_1 measurements in NAWM tissue. Therefore, the increased mean value can be expected because both ssMT and rNOEs contrast are hyperintense in the NAWM tissue. Furthermore, (ii) the ssMT and T_1 may correlate as the measured T_1 is not the isolated T_{1w} of water. Instead, it is influenced by the ssMT as described by Zaiss et al. [71], which leads to a reduction of the T_1 with increasing ssMT pool proton fraction. However, this would not explain the increased mean of the rNOE for low T_1 values. (iii) Possible shortcomings of the fit model can explain this effect because the rNOE and ssMT pools are fitted with a center frequency of -3.5 and -2.5 ppm, respectively, leading to an overlap of the pools, which could lead to an incorrect assignment of signal intensities.

To understand the SD, one needs to consider that the SD is not dominated by noise but by the range of possible contrast values. All three relaxation compensated MTR_{Rex} contrast show an increase in the SD towards higher T_1 values (Figure 5.19. The SD increases for the MTR_{Rex} contrast (within the B_1 bin ranging from 2 - 2.05 µT) from 0.017 (T_1: 0.9 - 1 s) to 0.052 (T_1: 1.9 - 2 s) for the MTR_{Rex} AMIDE, 0.027 (T_1: 0.9 - 1 s) to 0.049 (T_1: 1.9 - 2 s) for the MTR_{Rex} rNOE, and 0.041 (T_1: 0.9 - 1 s) to 0.060 (T_1: 1.9 - 2 s) for the MTR_{Rex} ssMT. These increases can be explained since the MTR_{Rex} contrasts are scaled by T_1 (Equation 2.65), which leads to a larger contrast value range with longer T_1. Therefore, when assuming that (i) within each B_1-T_1 bin, the proton fractions f_s, exchange rate k_s, and labeling efficiency α_s are independent of B_1 and T_1 changes and that (ii) all B_1-T_1 bins express the same variations in the three parameters, the standardized (Std.) MTR_{Rex} contrasts (i.e., after the process of performing the bin-wise standardization) can be interpreted as a T_1-corrected MTR_{Rex} contrast and can be described as follows:

$$Std.\ MTR_{Rex} \approx f_s \cdot k_s \cdot \alpha_s \tag{6.3}$$

APTw contrast standardization parameters

Prior research conducted by various authors [135, 109, 105, 84] investigated the effect of different B_1 and T_1 values on the mean value of the APTw contrast. All of the published articles on this topic confirm that the mean value of the APTw contrast increases with increasing values of B_1 and T_1, as observed in this thesis (Figure 5.19, bottom left). The mean APTw contrast value increases with increasing T_1 (within the B_1 bin ranging from 2 - 2.05 µT) from 0.15% (T_1: 1.9 - 2 s) to 0.90% (T_1: 0.9 - 1 s) and with increasing B_1 (within the T_1 bin ranging from 1.4 - 1.5 s) from -1.11% (B_1: 1.6 - 1.65 µT) to 1.12% (B_1: 2.25 - 2.3 µT). However, the reason for the increase in the mean value was not previously investigated. Therefore, it is unclear whether there are potential effects from T_1 and B_1 on the contributors that might cancel each other out. Additionally, the decreasing SD with increasing B_1 (Figure 5.19, bottom right) can be explained by considering the effect of spillover dilution on the Z-spectrum (within the T_1 bin ranging from 1.4 - 1.5 s the SD APTw decreases from 2.20% (B_1: 1.6 - 1.65 µT) to 1.44% (B_1: 2.25 - 2.3 µT)). Since spillover dilution increases with increasing B_1 (Equation 2.63), the chemically exchanging and rNOE pool contributions to the Z-spectrum decrease, resulting in a decreased APTw contrast value range.

6.3.2 Physical interpretation of the sensitivity maps

Although the standardization parameters already give an exciting insight into the APTw contrast dependencies on B_1 and T_1, the origin of the APTw contrast deviations can not be explained entirely based on their analysis. However, a more advanced insight into the APTw contrast can be extracted from the sensitivity maps (Section 5.4.2). The sensitivity maps are calculated by multiplying the regression coefficients (Figure 8.4) for each of the input features with the $SD(APTw(B_1, T_1))$. They can be interpreted as the sensitivity of the APTw contrast to changes in the corresponding standardized MTR_{Rex} contrast since they are the scaling factor of the standardized MTR_{Rex} contrasts when calculating the APTw contrast contribution (Equation 6.1). The multiplication with the SD of the APTw contrast is crucial as otherwise the sensitivity of the standardized APTw contrast would be investigated, which would lead to misinterpretations when regions with different value ranges due to B_1 or T_1 (as assessed in Section 6.3.1) are compared.

APTw sensitivity on Std. MTR_{Rex} AMIDE and Std. MTR_{Rex} rNOE changes

To validate and interpret the respective sensitivities, one needs to understand the calculation which the model has to perform in order to predict the APTw contrast contribution for the three Std. MTR_{Rex} contrasts. If a four-pool model (amide, rNOE, ssMT, and DS) can be assumed and the ssMT pool is assumed symmetric around 0 ppm due to the high B_1 field strength used for APTw imaging and low B_0 field strength (Figure 6.1), the calculations that need to be performed to make this transformation from low-power Std. MTR_{Rex} contrast to the contribution of the APTw contrast must include:

1. Transformation between saturation schemes
   - B_1 = 0.7 µT (low-power) → B_1 = 2 µT (high-power)
   - pulsed saturation (Gaussian) → continuous wave saturation (rectangular)
   - t_{sat} = 3.7 s (steady-state) → t_{sat} = 0.83 s (transient-state)
2. Influence of spillover dilution through ssMT and DS which is dependent on B_1 and T_1 ($\sigma'(\Delta\omega, B_1, T_1)$)
3. Influence of B_1 dependencies of the labeling efficiencies due to field inhomogeneities $\left(\frac{\alpha(\Delta\omega,B_1)}{\alpha(\Delta\omega,2\,\mu\mathrm{T})}\right)$
4. Reintroduction of the T_1 scaling, which was compensated for by the standardization process of the MTR_{Rex} contrasts (equation 6.3)

The transformation between saturation schemes (1) is very challenging and can only be analytically solved with many estimations. However, if one assumes that this transformation is already performed, the missing three operations (2-4) combined can be assumed to be proportional to the B_1 and T_1 sensitivity of the MTR_{LD} at 2 µT. This assumption can be made as the $MTR_{LD}(\Delta\omega, B_1) = f_s \cdot k_s \cdot \sigma'(\Delta\omega, B_1, T_1) \cdot \alpha(\Delta\omega, B_1) \cdot T_1$ [61] is the linear difference between the reference Z-spectrum including DS and ssMT and the label Z-spectrum including all pools and is therefore representative of the pools' influence on the Z-spectrum. The MTR_{LD} can be estimated from a B_1-corrected Std. MTR_{Rex} (at B_1=2 µT) with the following equation:

$$MTR_{LD}(\Delta\omega, B_1) \approx Std.\, MTR_{Rex}(\Delta\omega, 2\,\mu\mathrm{T}) \cdot \sigma'(\Delta\omega, B_1, T_1) \cdot \frac{\alpha(\Delta\omega, B_1)}{\alpha(\Delta\omega, 2\,\mu\mathrm{T})} \cdot T_1 \quad (6.4)$$

When comparing equation 6.4 with the MTR_{LD} equation 2.64, it is apparent that the B_1 and T_1 dependent translation parameters are the same as the B_1 and T_1 dependencies of the MTR_{LD}, implying that proportionality between the MTR_{LD} and the sensitivity maps is to be expected. The dependencies of the MTR_{LD} on B_1 and T_1, regardless of the transformation between the saturation schemes, can be easily simulated using Bloch-McConnell simulations (all simulation parameters are described in Appendix E). However, the calculations performed within the simulation depend on one specific set of parameters $\Delta\omega$, f_s, k_s, $T_{1,s}$, and $T_{2,s}$ for each pool (i.e, one set of tissue-specific parameters). Therefore, the simulation can be performed for a specific combination but is not generalized to any combination of parameters detected in vivo. Furthermore, the parameters are just approximations, as they are inherently difficult to measure at 3 T in vivo. The parameters used to simulate the B_1 and T_1 dependencies of the MTR_{LD} are an estimation for NAWM tissue and are displayed in Table 8.3 in Appendix E (adapted from Zaiss et al. [61]). Using these parameters as our basis, the MTR_{LD} was calculated for the B_1-T_1 range of the PIM's grid.

Figure 6.2 provides the simulated MTR_{LD} dependencies evaluated at $\Delta\omega$ = 3.5 and -3.5 ppm, respectively, including (i) only the DS, ssMT, amide and rNOE pools (i.e., 4-pool model, Figure 6.2, top and bottom) and (ii) the DS, ssMT, amide, rNOE, amine, guanidino, and hydroxyl pools (i.e., 7-pool model, Figure 6.2, middle). The

MTR_{LD} rNOE is multiplied by -1 to enable the comparison to Figure 5.20 because an increasing rNOE pool leads to a decrease in the APTw contrast.

When comparing Figure 6.2 and Figure 5.20, one can clearly see an excellent match between the sensitivities of the standardized MTR_{Rex} rNOE and the MTR_{LD} rNOE, with a decrease of MTR_{LD} with increasing B_1 value. The added spillover dilution can plausibly explain this behavior. Furthermore, in the simulation, there is only a minimal T_1 dependency present leading to a slight increase with increasing T_1, matching the results from the observed sensitivity analysis.

The MTR_{LD} AMIDE from the 4-pool model (Figure 6.2, top row) and the corresponding sensitivity (Figure 5.20, top row) only agree to a certain extent. When looking at the B_1 dependency, the simulation and the sensitivity maps show a similar behavior to the rNOE pool for the T_1 range smaller than 1.6 s, displaying a decrease with increasing B_1. However, T_1 changes have a more considerable influence on the amide signal for both simulation and sensitivity maps, showing an increase of MTR_{LD} AMIDE and sensitivity with increasing T_1. Most striking, however, is the discrepancy between the sensitivity map and the MTR_{LD} AMIDE for T_1 values larger than 1.6 s. In this range, the sensitivity maps do not depend much on B_1 or T_1; however, the MTR_{LD} AMIDE still shows B_1 and T_1 dependencies. These discrepancies between simulation and sensitivity maps can be explained when one includes pool contributions from amine, guanidino, and hydroxyl protons, which was hinted at in the previous analysis of the 20 most important features of the best-case models in Section 6.2.2 (Table 5.5).

With this information, a second simulation, which additionally included the amine, guanidino, and hydroxyl pools, was conducted with the following evaluation of the MTR_{LD} at $\Delta\omega = 3.5$ ppm (Figure 6.2, middle row). The resulting MTR_{LD} dependencies display an inverted B_1 dependency when compared to the simulation using the 4-pool model. This effect can be explained by the faster exchange rates of the added pools (compared to the amide pool), which lead to a labeling efficiency (Equation 2.58) of the combined pools that is still increasing with B_1 even around 2 µT, thus counteracting the reduction of the contributions due to the increased spillover dilution with increasing B_1 (Equation 2.58). Although the simulated MTR_{LD} AMIDE dependencies do not agree perfectly with the sensitivity maps, they suggest that the right combination of pool sizes and exchange rates, which to this point are only estimations for NAWM matter, would lead to similar B_1 and T_1 dependencies. Furthermore, this analysis supports the previously stated significant influences of the amine, guanidino, and hydroxyl pools on the APTw contrast as suggested by Sun et al. [136].

Despite the great match, one should remember that the simulation is based on one combination of f_s, k_s, $T_{1,s}$, and $T_{2,s}$ of the included pools, which was approximated for NAWM, and changes in these would impact the MTR_{LD} dependencies. Furthermore, the simulation does not include the transformation of the saturation schemes, which definitely influences the sensitivities. However, as the B_1 and T_1 tendencies of the simulated MTR_{LD} and the sensitivity maps of the PIM are in coherence, this simulation further support the validity of the developed PIM and extend the current

knowledge about the underlying mechanisms of the APTw contrast in vivo.

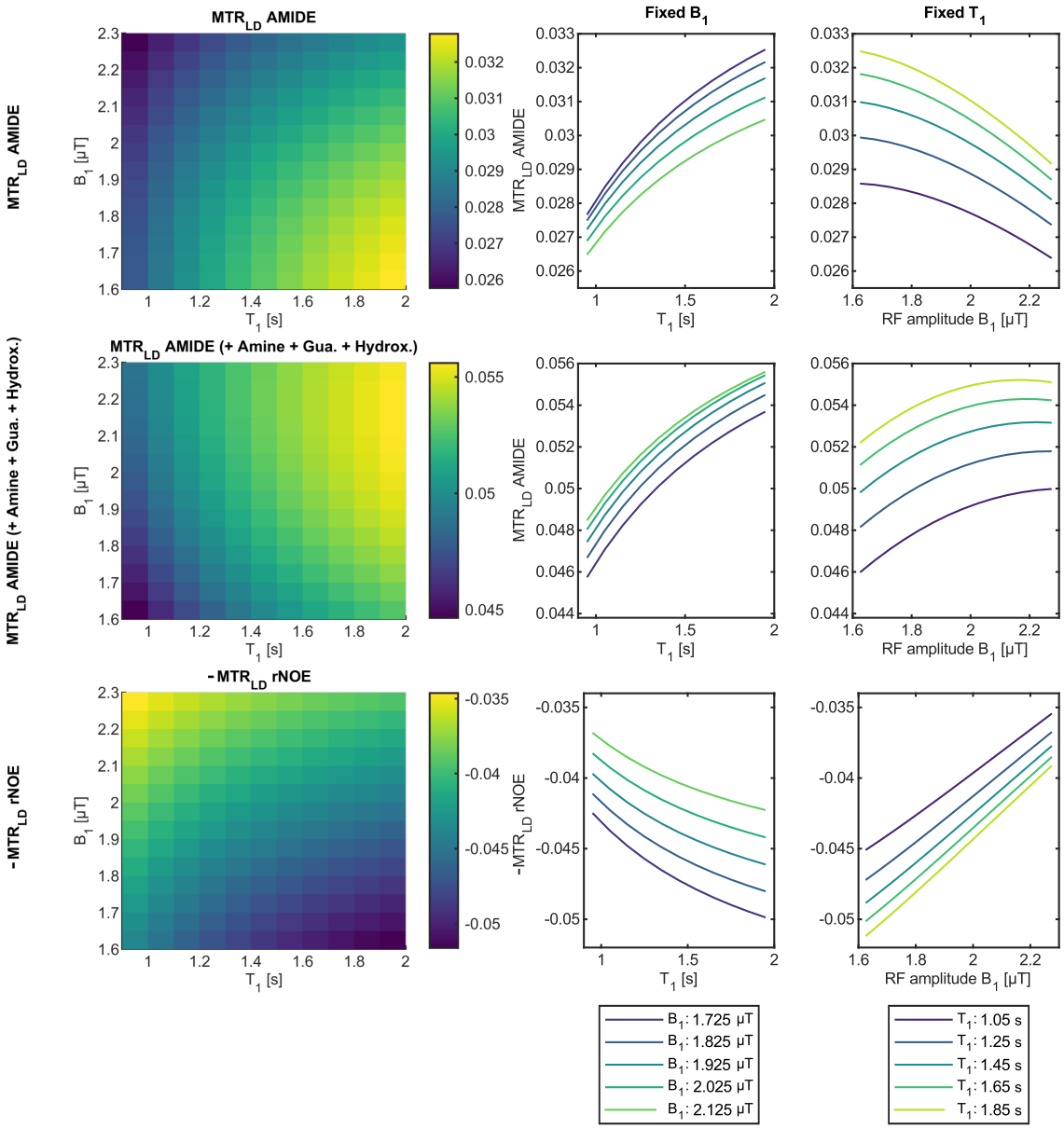

Figure 6.2: Simulated B_1-T_1 dependencies of MTR_{LD} for (i) a 4-pool model (top row: MTR_{LD} AMIDE; bottom row: MTR_{LD} rNOE; simulated pools: DS, ssMT, amide, and rNOE, respectively) and (ii) a 7-pool model (middle row: MTR_{LD} AMIDE; simulated pools: DS, ssMT, amide, rNOE, amine, guanidino, and hydroxyl). In order to enable the comparison to Figure 5.20, the MTR_{LD} rNOE is multiplied by -1 because an increasing rNOE pool leads to a decrease in the APTw contrast. For visualization purposes, the maps are also displayed as sets of curves, once plotted with fixed B_1 to highlight the changes of the MTR_{LD} based on increasing T_1, and vice versa. The sets were reduced to 5 curves per plot with equidistant B_1 or T_1 values. The used simulation and simulation parameters are described in Appendix E.

Std. MTR_{Rex} ssMT sensitivity map

To understand the origin of the Std. MTR_{Rex} ssMT sensitivity map (Figure 5.20, bottom row), one first needs to take a look at the ratio of the Std. MTR_{Rex} AMIDE and Std. MTR_{Rex} rNOEs sensitivity maps (Figure 5.21). Looking at the ratio (Figure 5.21), one can see a change of dominant contributor from the Std. MTR_{Rex} rNOE at low B_1 to the Std. MTR_{Rex} AMIDE at high B_1. This change is most likely the reason why the Std. MTR_{Rex} ssMT sensitivities change from a positive value at low B_1 to a negative value at high B_1, as the ssMT is the leading cause for the spillover dilution, leading to more substantial suppression of the contrast (Std. MTR_{Rex} AMIDE or Std. MTR_{Rex} rNOE) with a higher potential contribution for high Std. MTR_{Rex} ssMT values and an enhancement for low Std. MTR_{Rex} ssMT values, explaining the origin of the Std. MTR_{Rex} ssMT sensitivity map.

Ratio of the absolute Std. MTR_{Rex} AMIDE and Std. MTR_{Rex} rNOE sensitivity maps

The ratio of the absolute Std. MTR_{Rex} AMIDE and the absolute Std. MTR_{Rex} rNOE sensitivity maps was exploited (Figure 5.21), in particular, as the ratio permits the elimination of dependencies that are similar for both sensitivity maps, therefore allowing for an enhanced interpretation. Interestingly, the ratio showed no dependencies on T_1. This is reasonable when looking at the description of the transformation through the MTR_{LD} (Equation 6.4). The only T_1 dependencies of the MTR_{LD} are in the spillover dilution term and the scaling T_1 term. Again, when assuming that the ssMT is symmetric, one would expect the T_1 term in the MTR_{LD} equation and the T_1 dependency in the spillover dilution term (Equation 2.63) to be similar for the MTR_{LD} AMIDE and MTR_{LD} rNOE (i.e., $\sigma'(\Delta\omega = 3.5 \text{ ppm}) \approx \sigma'(\Delta\omega = -3.5 \text{ ppm})$), therefore canceling each other out by calculation of the ratio. However, the labeling efficiency differs between the two contrasts (i.e., $\alpha(\Delta\omega = 3.5 \text{ ppm}) \neq \alpha(\Delta\omega = -3.5 \text{ ppm})$), leading to a split into two sensitivity regimes, i.e. (i) one dominated by the amide contribution for values > 1 (Figure 5.21, left, at around $B_1 > 2$ µT) and (ii) one dominated by the rNOE contribution for values < 1 (Figure 5.21, left, at around $B_1 < 2$ µT). Nevertheless, one needs to remember that these are only sensitivity regimes, which means that the relative contributions of the amide and rNOE to the actual APTw contrast are mostly dependent on the MTR_{Rex} values of each pool.

In conclusion, the developed PIM is in accordance with the available literature and even extends beyond the current knowledge about the APTw contrast.

6.3.3 Limitations and future opportunities

Although the results look very promising, there are a few noticeable limitations of the model. However, these limitations also provide many opportunities for future projects.

Z-spectra fit model

The first limitation caused by the Z-spectra fit model is apparent when looking at the discussion of the sensitivity maps of the PIM (Section 6.3.2). The fit model (Section 3.4.1) used is a 4-pool Lorentzian model including DS, ssMT, rNOE, and amide pools; however, the analysis of the sensitivities showed that there is most likely a contribution from amine, guanidino, and hydroxyl groups. This problem cannot be solved because of the limited spectral resolution at $B_0 = 3$ T combined with the very low labeling efficiency of these pools at a B_1 of 0.6 or 0.9 µT, respectively ($\alpha_s < 0.05$ for all pools and both B_1 when calculated using parameters from Table 8.3). Furthermore, the downfield rNOE was also not included in the model. However, the downfield rNOE can also not be extracted based on the acquired Z-spectra.

The first exciting idea to counteract the shortcomings of the current fit model would be an extension of the fit model by using an ssMT pool with a variable resonance frequency offset instead of a fixed one and, using this information, to gain some insights about the asymmetry of the ssMT pool and its implications on the APTw contrast, which was assumed symmetric throughout this discussion. In addition, one could also try to estimate the T_2 time via the water pool width and add it as information about the spillover dilution originating from the direct water saturation. Furthermore, a more sophisticated Bloch McConnell fit model could help extract the f_s and k_s and, with that, enable a more detailed insight into the APTw contrast.

Saturation scheme

The different saturation schemes and the discrepancies in saturation level have a significant impact on the PIM, as both high and low-power (for $T_1 >$ approximately 1.5 s) measurements are acquired in the transient state, and therefore, the saturation level changes with changing T_1, which impacts the APTw contrast as well as the MTR_{Rex} contrast.

To get more detailed information about the dependencies on the saturation level, the dataset could be extended in the future by acquiring CEST Z-spectra with different t_{sat} and therefore gathering more information about the dependencies of the CEST contrast in vivo on the saturation time.

A second limitation of the current saturation scheme is that the APTw data was not acquired at different B_1 values; instead, the B_1 range originates from the field inhomogeneities. Therefore, biological effects could influence the observed results as some brain areas are more likely to present field inhomogeneities than others. This could be tackled by acquiring APTw scans at multiple different B_1 powers; this extension would also increase the range in which the APTw contrast and its dependencies can be analyzed.

Further machine learning projects

To further use the power of the acquired dataset, one could try to use more advanced deep learning models to use the spatial information and possibly invert the model to predict the more isolated MTR_{Rex} contrasts from the high-power Z-spectra, improving the clinical applicability of the MTR_{Rex} contrast through a shorter ac-

quisition time.

Lastly, the pattern recognition abilities of the models could be used to directly predict clinical endpoints based on all acquired Z-spectra (low-power and APTw), followed by extraction of the crucial offsets, which could be used to create more advanced clinically feasible CEST protocols.

6.4 Clinical implications

In addition to being the basis for future studies with a physical focus, this dataset is the first that enables the decomposition of the APTw contrast into its contributors, providing a first basis for the interpretation of the APTw contrast changes in vivo and for extensions to the APTw contrast in its current form.

6.4.1 Interpretation basis for the APTw contrast in a clinical context

The main downside of the APTw contrast in its current form is the lack of interpretation possibilities in vivo. This is highlighted by the fact that contrast changes between different pathologies cannot be solely attributed to one contribution; instead, a series of experiments have to be performed, changing only one contributor at a time to gather more information about the origin of the APTw contrast change, which is often impossible when applied to clinical questions.

Using the PIM, it is possible to isolate the contributions from the MTR_{Rex} contrasts to the final APTw contrast (Equation 6.1). These contributions can now be calculated for the patient datasets acquired prior to radiotherapy (RT) and those acquired 4-6 weeks after completion of RT to analyze whether the hyperintense whole tumor (WT) contrast (apparent at both time points) has different origins. Looking at the origin for all predicted APTw contrast values above 2% for both time points individually (Figure 6.3, A), no difference between the origins can be observed. In both cases, the high APTw contrast values originate from a high amide or low rNOE contrast. However, when looking at the same evaluation but only for WT voxels over 2% (Figure 6.3, B), one clearly sees that the APTw contrast origin differs between the time points. Utilizing the PIM, the increased APTw contrast value before RT is now predominantly based on a high amide contribution, but the data acquired after RT suggests that only the decreased rNOE contrast value causes the hyperintense APTw contrast. This discrepancy is not surprising because RT should induce changes in the tissue biology. However, the discrepancy could lead to significant changes in the predictive power of the APTw contrast between the two examination time points. The same analysis approach could now be used to assess different influences, like the changes in proteinaceous fluid departments in edema.

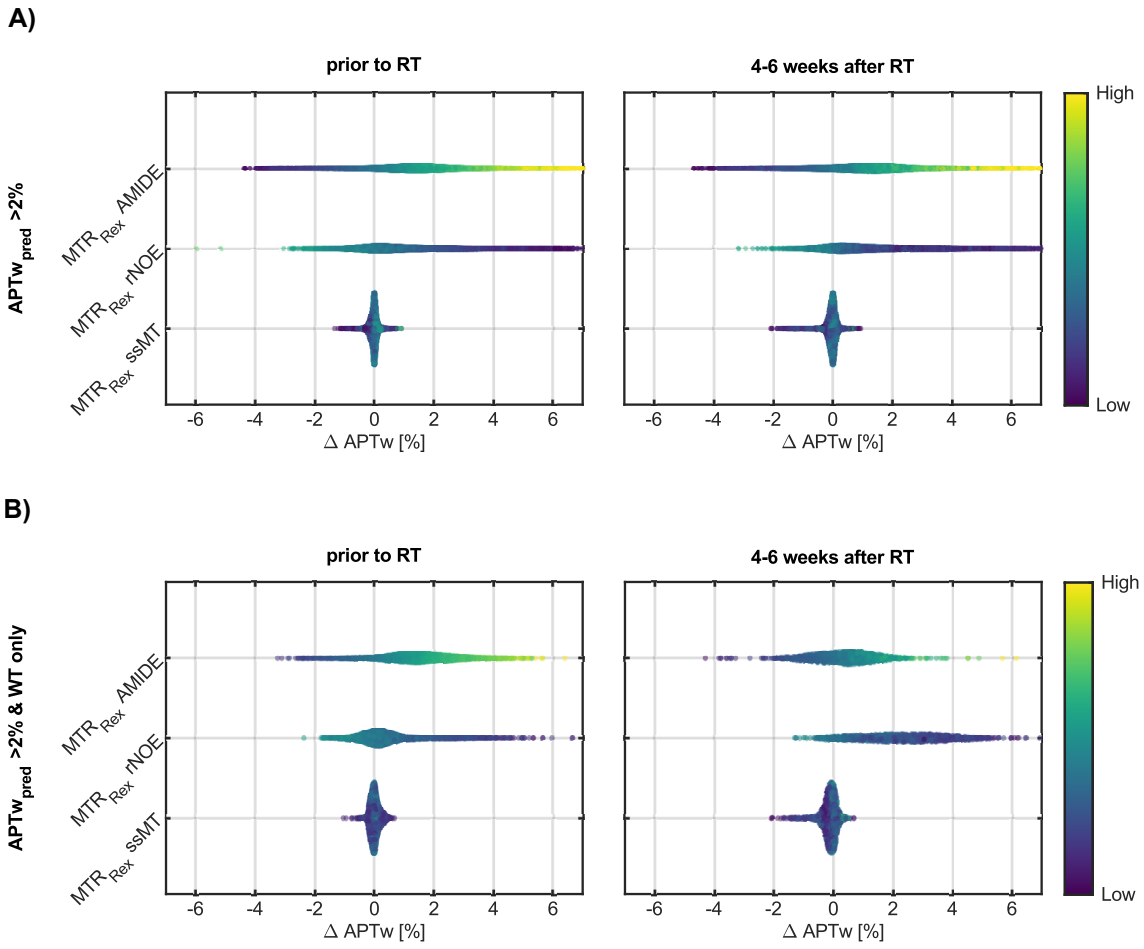

Figure 6.3: Decomposition of the APTw contrast for hyperintense WT voxels prior to RT (left) and 4-6 weeks after RT (right). The top row shows the contributions from MTR_{Rex} AMDIE, MTR_{Rex} rNOE and MTR_{Rex} ssMT for all voxels with a predicted APTw contrast above 2%, and the bottom row shows the contributions only for the WT voxels with a predicted APTw contrast above 2%. Interestingly, the evaluation for the WT voxels indicates clear differences for the hyperintense APTw contrast origin between the two time points (compare MTR_{Rex} AMDIE and MTR_{Rex} rNOE in bottom left to bottom right).

6.4.2 Contrast corrections or adaptions

The model cannot only explain the current APTw contrast, but it can also provide the possibility to create a B_1 correction to calculate the APTw contrast for a fixed B_1 saturation power without any field inhomogeneities to estimate its true clinical potential or to vary the B_1 (within the grid) to estimate the APTw contrast for different B_1 field strengths.

Correction for B_1 inhomogeneities

A B_1 correction could be performed on two different levels. First, one could use the standardization parameter maps for the APTw contrast (mean and SD) to standardize the APTw contrast within the grid ranges. This would increase the stability of the APTw contrast towards changes caused by B_1 and T_1 alterations. However,

the impact of the B_1 and T_1 changes on the contributors would not be corrected using this method.

Secondly, it would also be possible to calculate the APTw contrast based on the MTR_{Rex} contrast for a fixed B_1 field strength, therefore calculating a contrast without any B_1 inhomogeneities. This could help estimate the true clinical potential of the APTw contrast without any field inhomogeneities. However, this approach is only viable for this particular dataset because the APTw contrast depends on the saturation scheme, which means that other setups would need a separate model implemented explicitly for the corresponding setup.

APTw 2.0

In addition to creating a B_1 inhomogeneity-free contrast, one could also vary the B_1 value and calculate the APTw contrast at different nominal B_1 to assess whether a different saturation power might increase the tumor contrast or even help with the problems described in Subsection 6.4.1. Furthermore, one could investigate whether multiple APTw scans at different saturation powers would be helpful for the evaluation or prediction of therapy endpoints. Lastly, one could also vary the regression coefficients to generate a contrast that may be more beneficial for a previously determined clinical endpoint.

Chapter 7

Summary

CEST-MRI is an emerging molecular imaging technique that has already proven to be clinically relevant for neuro-oncological questions. In recent years, APTw imaging has garnered immense clinical interest because of its potential predictive power, but the molecular origin of the contrast is still under debate. This thesis aimed to expand the current knowledge about the APTw contrast mechanism by generating a PIM which enables an enhanced (bio)physical understanding of the APTw contrast in vivo and its underlying mechanisms.

As a novel approach to improve the interpretability of the APTw contrast, suitable data-driven techniques were implemented within the frame of this thesis. The basis for these techniques was an extensive clinical study where low-power fully sampled Z-spectra and APTw imaging data was collected from 125 different patients. The vast amount of available data allowed the application of ML methods that were able to extract previously unexplored features in CEST data. Specifically, the goal was to predict the APTw contrast from more specific low-power contrasts using ML and subsequently to interpret the features exploited by the implemented techniques. The initial predictions were performed using (i) a simple LR approach as a 'linear' model, as well as (ii) a GB tree algorithm as a 'non-linear' method (state-of-the-art for tabular regression problems). To extract the dependencies underlying the models that are required to develop the physically interpretable model (PIM), the interpretable AI method SHAP was used to evaluate the contribution of the input features to the final predicted APTw contrast value. The PIM was subsequently constructed as multiple LR models, each one trained for a single bin contained in a grid extending over B_1 and T_1.

As a prerequisite to evaluating the quality of the predictions, the level of the intrinsic contrast fluctuations across the APTw datasets had to be identified. A mean contrast deviation of around 0.75% was found even in regions with restrictions regarding tissue composition and B_1 field strength. Additionally, a mean absolute error of 0.5% was extracted in a subsequent analysis examining the influence of motion and interpolation in the process of motion correction, thus quantifying the impact of motion-induced artifacts on the final contrast. With this information, the matching level was constructed to facilitate a fair assessment of the created models.

A significant milestone in the creation of the PIM was the initial successful predic-

tion of the APTw contrast using low-power fully sampled Z-spectra. Both models proved to be equally capable of predicting the APTw contrast within the earlier defined matching level and showed that a translation of the different saturation schemes is feasible by utilizing the statistical models. As proof that these models used physically relevant information to relate the datasets, an additional analysis revealed that the predictions heavily relied on the chemically exchanging and rNOE region of the Z-spectra, and models excluding these regions were incapable of succesful predictions.

Consequently, these insights were used to train GB and LR models based on the interpretable relaxation-compensated MTR_{Rex} contrasts. The results showed that only the GB model could predict the APTw contrast successfully, as the LR model heavily lacked contrast intensity. The essential non-linearities of the GB model were then successfully extracted using the interpretable machine learning methods. With this information at hand, the PIM was successfully developed, combining the interpretability of the LR model with the non-linear features of the GB model.

As a final step, the PIM was thoroughly analyzed to evaluate its physical information content. The PIM sensitivity maps enable the translation of the input contrasts into a contribution to the APTw contrast by reversing the relaxation compensation and adding spillover and labeling efficiency differences. A careful examination of the sensitivities showed that the contributions from amide and rNOE outweigh the contributions from the ssMT. Additionally, the amide and rNOE contrasts both exhibited a decrease of the sensitivity with higher B_1, which can be explained by the increased spillover dilution; however, the amides decrease is not as drastic as for the rNOE, which is expected, as the amides still increase in labeling efficiency, therefore counteracting the decrease through spillover dilution. The changes due to T_1 most likely originate from the translation between the two saturation schemes and the change in saturation level, as both measurements were performed in a transient state and are, therefore, dependent on T_1. However, the higher spillover dilution with increasing T_1 due to the correlation between the ssMT and the observed T_1 value is likely a concomitant effect. Overall, the generated PIM was shown to contain physically relevant information.

Summarized, the central findings of this thesis were:

- ML models were successfully implemented based on a large dataset containing realistic patient data, including several artifacts, thus enabling the prediction of the APTw contrast from low-power CEST data.

- The implemented ML models exploit physically relevant and interpretable information (non-black-box models). This is also valid for the more challenging extractable features, e.g., varying saturation efficiencies.

- Amides and rNOE were identified as the dominant contributors to the APTw contrast, in close agreement with current consensus.

- Nevertheless, there is a strong contribution of B_1 and T_1 on the APTw contrast that still needs to be accounted for.

- Leading to the identification of amide- and rNOE-driven sensitivity regimes of the APTw contrast.

In conclusion, this thesis successfully established a model that provides valuable insights about the essential molecular contributions to the APTw contrast through its ability to decompose the APTw contrast for the used dataset. Ultimately, this enables a better biophysical understanding of the CEST phenomenon in vivo and, thus potentially improving the clinical assessment of brain cancers.

Chapter 8

Appendix

A Validation of the motion correction for APTw imaging

The used image registration for the APTw CEST scan was the MITK "slabbed Head" algorithm [86]. The motion correction procedure is similar to the one described by Breitling et al. [87] for fully-sampled Z-spectra, only leaving out the outlier detection, as it is unnecessary due to the absence of direct water saturation offsets. Therefore, only the pairwise image registration with Mattes' mutual information [88] as a similarity metric and a step gradient descent optimization [86, 89] was performed. To validate the correction method, a patient with minimal motion was selected. Subsequently, a random rigid motion pattern was introduced to the measurement. To ensure realistic motion, the following prerequisites to the motion pattern were introduced:

- General continuity and smoothness of the motion pattern
- Individual motion amplitude for each measurement (i.e. simulation repetition)
- Possibility of sudden motion

For more details, see [87]. Importantly, because the patient with minimal motion is not motion-free, one first needs to perform a motion correction of the minimal motion dataset and remove it from the estimated motion by the correction method after the artificially introduced motion to compare the estimated motion by the correction method with the artificially introduced motion. This can be performed as follows: Image series with minimal motion (I_1); I_1 corrupted with extra motion(I_{C1}); I_1 motion corrected (I_{noMo1})

$$\begin{aligned} &I_1 \times M_c = I_{C1} \\ &I_1 \times M_{noMo} = I_{noMo1} \\ &I_{C1} \times M_{noMo2} = I_{noMo1} \\ &\Rightarrow M_{noMo} \times M_{noMo2}^{-1} = M_c \end{aligned} \tag{8.1}$$

Where M_c, M_{noMo}, and M_{noMo2} are transformation matrices: $M = \begin{pmatrix} & \mathbf{R} & & \mathbf{t} \\ 0 & 0 & 0 & 0 \end{pmatrix}$ with 3×3 rotation matrix R and the 3×1 translation vector t. Using the last equation, one can now verify whether the motion correction works as expected. Figure

8.1 shows the performance of the motion correction for a representative dataset and artificially induced motion pattern, showing that the motion correction performs well in extracting the motion. The same can be seen when looking at 20 different artificial motion patterns introduced to the same dataset. When evaluating the mean image misalignment calculated by equation 3.7, one can see a clear improvement compared to the motion introduced to the datasets, proving that the motion correction works sufficiently well.

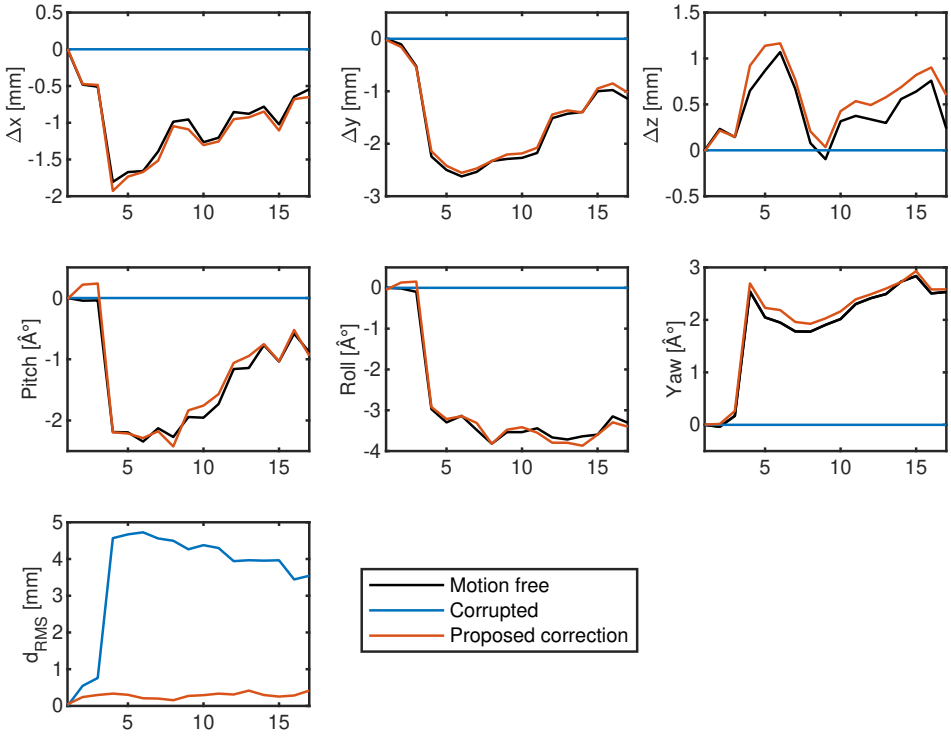

Figure 8.1: Evaluation of a representative artificially induced motion pattern (top and middle row). Representative artificial motion pattern (blue), motion pattern necessary to remove the artificial motion (black; ground truth), and the estimate of the proposed motion correction after removal of the correction calculated for the motionless images (orange) (bottom row). Image misalignment for each image after motion correction (orange) and for the corrupted images (blue) show a near-perfect correction of the introduced misalignment.

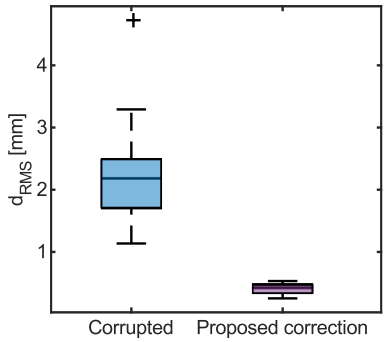

Figure 8.2: Performance of the proposed motion correction for 20 artificially introduced motion patterns. One can see a clear improvement compared to the motion introduced to the datasets, proving that the motion correction works sufficiently well.

B Mean and standard deviation of the predicted APTw contrast values

To better understand the voxel distributions of the scatter plots showing the predicted APTw contrast values (y-axis) and their ground truth APTw contrast values (x-axis), kernel density marginal histograms were displayed for each of the figures (Best-case: Figure 5.4; interpretable: Figure 5.11; PIM: Figure 5.17). The mean and SDs of these kernel density marginal histograms are listed in this section. Table 8.1 provides the mean and SD of the predicted APTw contrast values for the best-case models and the models based on the interpretable contrasts for all voxels included in the full dataset (Section 5.2) without the exclusion of data points based on the limits of the grid. Table 8.2, however, provides the mean and SD of the predicted APTw contrast values for the best-case models, the models based on the interpretable contrasts, and the PIM for the reduced dataset (reduction by approximately 80%) after exclusion of data points based on the limits of the grid described in Section 5.3.3.

Table 8.1: Mean and SD of the predicted APTw contrast values for the best-case models and the models based on the interpretable contrasts. The evaluation was performed using the full dataset (Section 5.2) without the exclusion of data points based on the limits of the grid.

Model		Overall Mean ± SD (%)	NAWM & NAGM Mean ± SD (%)	WT Mean ± SD (%)
Interpretable	LR	0.16 ± 1.08	0.12 ± 0.97	0.51 ± 0.86
	GB	0.17 ± 1.24	0.13 ± 1.15	0.63 ± 0.85
Best-case	LR	0.26 ± 1.48	0.22 ± 1.38	1.06 ± 1.08
	GB	0.25 ± 1.47	0.20 ± 1.37	1.04 ± 0.92
Ground truth		0.23 ± 1.81	0.18 ± 1.66	1.06 ± 1.52

Table 8.2: Mean and SD of the predicted APTw contrast values for the best-case models, the models based on the interpretable contrasts, and the PIM. The evaluation was performed using the reduced dataset through the implementation of the B_1-T_1 grid described in Section 5.3.3.

Model		Overall Mean ± SD (%)	NAWM & NAGM Mean ± SD (%)	WT Mean ± SD (%)
PIM		0.23 ± 1.12	0.18 ± 1.04	0.67 ± 0.91
Interpretable	LR	0.17 ± 1.00	0.13 ± 0.93	0.51 ± 0.86
	GB	0.20 ± 1.19	0.16 ± 1.12	0.63 ± 0.84
Best-case	LR	0.29 ± 1.43	0.24 ± 1.35	1.06 ± 1.07
	GB	0.28 ± 1.43	0.23 ± 1.35	1.06 ± 0.92
Ground truth		0.26 ± 1.73	0.21 ± 1.62	1.10 ± 1.51

C Voxelwise predicted APTw contrast using all models for a second representative subject

In this section, the voxelwise predicted APTw contrast for a second representative subject is displayed. The contrast maps were created for the best-case models (Section 5.2.1), the LR and GB models based on the interpretable contrasts (Section 5.3.1) and the PIM (Section 5.3.3). Similar to the other patient, a high level of agreement can be observed between the predicted images from the best case models (Figure 8.3, top row right column) and the ground truth image. Notably, both algorithms again successfully reproduced all main features, such as the hyperintense tumor area, the NAGM and NAWM contrast, and the hypointensities towards the posterior part of the brain. Furthermore, when looking at the models based on the interpretable contrasts (Figure 8.3, bottom row right column), one can again observe predicted values that are generally closer to the mean value, decreasing the predicted APTw contrast value range compared to the ground truth. However, the PIM (Figure 8.3, bottom row left column) this time only provides a marginally clearer tumor region, depicted closer to the ground truth than the models based on the interpretable contrasts.

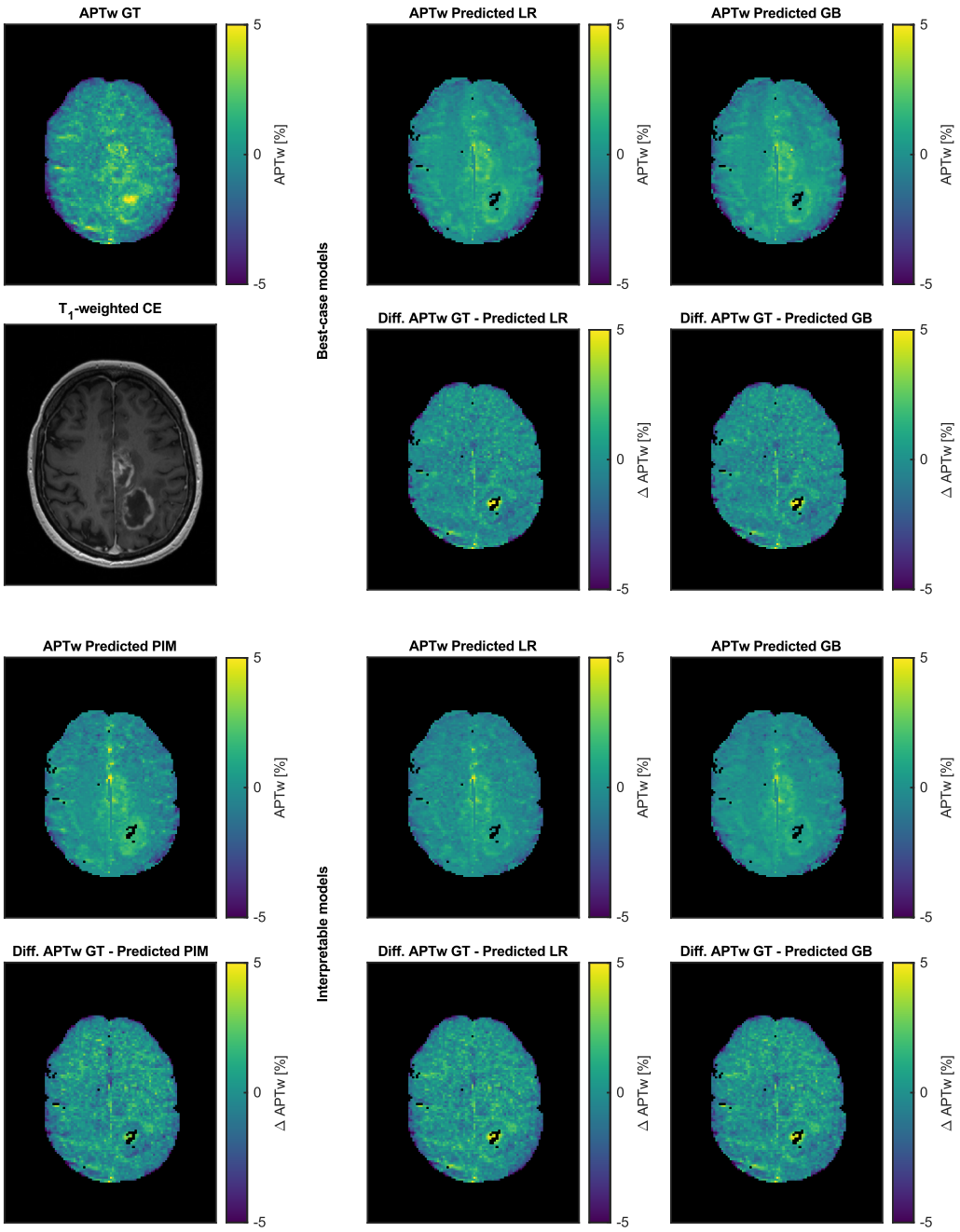

Figure 8.3: In this Figure, the voxelwise predicted APTw contrast using all created models (best-case top right, PIM bottom left, Interpretable bottom right) for a second representative subject and slice is displayed. In addition, a T_1-weighted CE map is added for orientation purposes, and the APTw ground truth image and the difference map between ground truth and prediction are shown.

D Standardized regression coefficients

The regression coefficients generated by the PIM are displayed for completeness (Figure 8.4). However, as they represent the sensitivity of the predicted standardized APTw contrast on changes of the respective standardized MTR_{Rex} input parameters, they have no clear interpretation as the standardized APTw contrast cannot be

interpreted and is not the desired output. However, the dependencies on B_1 and T_1 are very similar to those of the sensitivities described in Section 5.4.2. Solely the T_1 dependencies of the MTR_{Rex} AMIDE are less pronounced for the regression coefficients (Figure 8.4, top row).

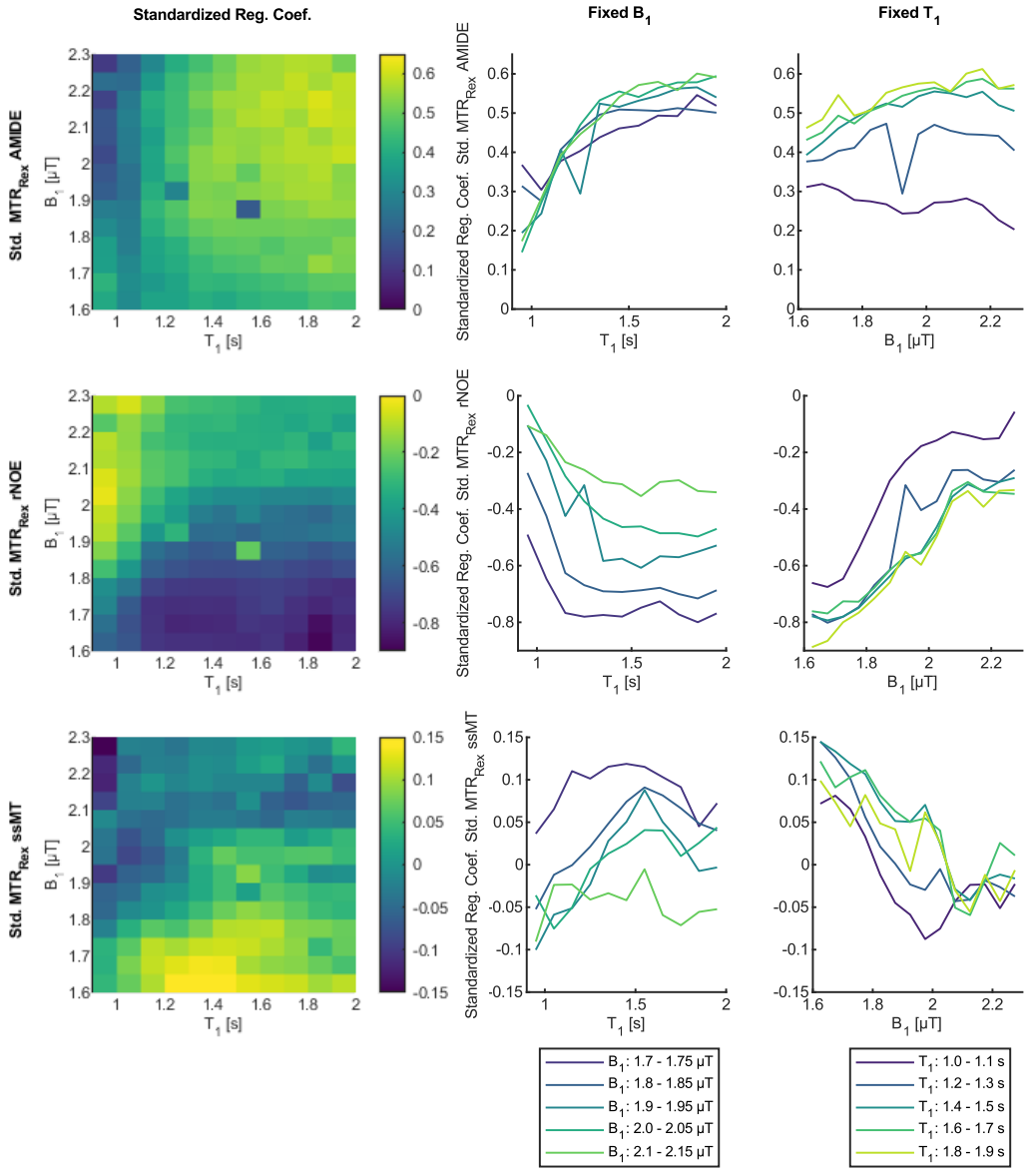

Figure 8.4: The standardized regression coefficients for the MTR_{Rex} AMIDE (top), rNOE (middle), and ssMT (bottom) were determined for each bin by an individual LR model. It is important to note that the AMIDE contrast has exclusively positive regression coefficients, the rNOE exclusively negative regression coefficients, and the regression coefficients of the ssMT range from around -0.10 at high B_1 and low T_1 to 0.05 at low B_1. For visualization purposes, the maps are also displayed as sets of curves, once plotted with fixed B_1 to highlight the changes of the regression coefficients based on increasing T_1, and vice versa. The sets were reduced to 5 curves per plot with equidistant B_1 or T_1 values.

E Simulation parameters of the Bloch-McConnell simulation

The Bloch-McConnell simulations used within the discussion Sections 6.1.2 and 6.3.2 were performed using the Pulseq-CEST library (https://github.com/kherz/pulseq-cest-library). Furthermore, the CEST simulation parameters were adapted from Zaiss et al. [61]. Only the ssMT proton fraction f was reduced from 28.9% to 15%. This adaption was necessary as in Section 6.3.2 MTR_{LD} contrasts were simulated for different $T_{1,obs}$; however, to enable the simulation of $T_{1,obs}$ values around 2 s (observed within the acquired dataset) by changing the T_{1w} time the ssMT pool proton fraction had to be reduced.

Table 8.3: Bloch-McConnell simulation parameters for 3T white matter tissue. The ssMT lineshape was set to Lorentzian, and the saturation scheme was cw B_1 = 2µT and t_{sat} = 0.87 s. Values were adapted from Zaiss et al. [61]

Pool	$\Delta\omega$ (ppm)	k (s^{-1})	f (%)	T_1 (s)	T_2 (s)
Water (DS)	0	-	100	2.5	0.062
ssMT	-3.5	4.7751	15	0.2459	0.00043
Amide	3.5	150	0.05	1	0.015
Guanidino	2	1100	0.090	1	0.015
Amine	3	5500	0.12	1	0.015
Hydroxyl	1.3	3500	0.018	1	0.015
rNOE	-2.75	16	1	1	0.0025

List of Figures

List of Tables

List of Scientific Publications

The scientific publications I contributed to are listed below. Contributions used in this thesis are marked as follows: **(Used in this thesis)**

Journal articles

von Knebel Doeberitz, Nikolaus; **Kroh, Florian**; Breitling, Johannes; König, Laila; Maksimovic, Srdjan; Graß, Svenja; Adeberg, Sebastian; Scherer, Moritz; Unterberg, Andreas; Bendszus, Martin; Wick, Wolfgang; Bachert, Peter; Debus, Jürgen; Ladd, Mark E.; Schlemmer, Heinz-Peter; Korzowski, Andreas; Goerke, Steffen; Paech, Daniel: *CEST imaging of the APT and ssMT predict the overall survival of patients with glioma at the first follow-up after completion of radiotherapy at 3T.* Radiotherapy & Oncology. 2023; 184:109694. doi:10.1016/j.radonc.2023.109694

Kroh, Florian; von Knebel Doeberitz, Nikolaus; Breitling, Johannes; Maksimovic, Srdjan; König, Laila; Adeberg, Sebastian; Scherer, Moritz; Unterberg, Andreas; Bendszus, Martin; Wick, Wolfgang; Bachert, Peter; Debus, Jürgen; Ladd, Mark E.; Schlemmer, Heinz-Peter; Korzowski, Andreas; Goerke, Steffen; Paech, Daniel: *Semi-solid MT and APTw CEST-MRI predict clinical outcome of patients with glioma early after radiotherapy.* Magnetic Resonance in Medicine. 2023; 90(4): 1569-1581. doi:10.1002/mrm.29746
(Used in this thesis)

von Knebel Doeberitz, Nikolaus; **Kroh, Florian**; König, Laila; Boyd, Philip S.; Graß, Svenja; Bauspieß, Cora; Scherer, Moritz; Unterberg, Andreas; Bendszus, Martin; Wick, Wolfgang; Bachert, Peter; Debus, Jürgen; Ladd, Mark E.; Schlemmer, Heinz-Peter; Goerke, Steffen; Korzowski, Andreas; Paech, Daniel: *Post-Surgical Depositions of Blood Products Are No Major Confounder for the Diagnostic and Prognostic Performance of CEST MRI in Patients with Glioma.* Biomedicines. 2023; 11(9):2348. doi:10.3390/biomedicines11092348

Conference and workshop contributions

Boyd, Philip S.; **Kroh, Florian**; Breitling, Johannes; Franke, Vanessa L.; Ladd, Mark E.; Bachert, Peter; Goerke, Steffen; Korzowski, Andreas: *Quantitative volumetric mapping of intracellular pH in the human brain at 7 T using endogenous CEST-MRI: A proof of principle study.* Proceedings of the 31th Annual Meeting of the ISMRM, Toronto, CA, 2023 (Digital Poster | Video Presentation)

Platek, Justyna; **Kroh, Florian**; Franke, Vanessa L.; Boyd, Philip S.; Weckesser, Nina; Schlemmer, Heinz-Peter; Paech, Daniel; Ladd, Mark E.; Bachert, Peter; Korzowski, Andreas: *Analysis of regional differences in pH values obtained via ^{31}P MRSI at 7T*. Proceedings of the 31th Annual Meeting of the ISMRM, Toronto, CA, 2023 (Digital Poster | Video Presentation)

Kroh, Florian; Boyd, Philip S.; von Knebel Doeberitz, Nikolaus; Schlemmer, Heinz-Peter; Ladd, Mark E.; Bachert, Peter; Paech, Daniel; Korzowski, Andreas: *Relaxation-compensated CEST-MRI at 3 T exhibits regional differences in gray matter and white matter contrasts of glioma patients*. Proceedings of the 31th Annual Meeting of the ISMRM, Toronto, CA, 2023 (Talk | Video Presentation)
(Used in this thesis)

Karimian-Jazi, Kianush; Sturm, Volker; Schregel, Katharina; Hunger, Jessica; Turco, Verena; Enbergs, Noah; Boztep, Berin; Fischer, Manuel; Streibel, Yannik; von Knebel Doeberitz, Nikolaus; Korzowski, Andreas; Goerke, Steffen; **Kroh, Florian**; Ladd, Mark E.; Schlemmer, Heinz-Peter; Paech, Daniel; Rodell, Christopher B.; Platten, Michael; Wick, Wolfgang; Heiland, Sabine; Bendszus, Martin; Breckwoldt, Michael O.: *Metabolic Imaging of malignant gliomas during immunotherapeutic intervention using chemical exchange saturation transfer (CEST) MRI at 9.4T*. Proceedings of the 31th Annual Meeting of the ISMRM, Toronto, CA, 2023 (Digital Poster | Video Presentation)

von Knebel Doeberitz, Nikolaus; **Kroh, Florian**; König, Laila; Maksimovic, Srdjan; Graß, Svenja; Debus, Jürgen; Bachert, Peter; Schlemmer, Heinz-Peter; Ladd, Mark E.; Korzowski, Andreas; Goerke, Steffen; Paech, Daniel: *CEST Imaging of the APT and ssMT predict the overall survival of patients with glioma at the first follow-up after completion of radiotherapy at 3T*. Proceedings of the 31th Annual Meeting of the ISMRM, Toronto, CA, 2023 (Talk | Video Presentation)

von Knebel Doeberitz, Nikolaus; **Kroh, Florian**; König, Laila; Maksimovic, Srdjan; Graß, Svenja; Debus, Jürgen; Bachert, Peter; Schlemmer, Heinz-Peter; Ladd, Mark E.; Korzowski, Andreas; Goerke, Steffen; Paech, Daniel: *CEST Imaging of the APT and ssMT Predict the Overall Survival of Patients with Glioma at the First Follow-Up after Completion of Radiotherapy at 3T*. Proceedings of the Annual Meeting of the ASNR, Chicago, USA, 2023

von Knebel Doeberitz, Nikolaus; **Kroh, Florian**; Breitling, Johannes; Maksimovic, Srdjan; König, Laila; Debus, Jürgen; Bachert, Peter; Schlemmer, Heinz-Peter; Ladd, Mark E.; Korzowski, Andreas; Goerke, Steffen; Paech, Daniel: *Glioma response assessment by asymmetry-based, Lorentzian-fit-based and relaxation-compensated CEST MRI of the APT and ssMT is influenced by glioma location at 3T*. Proceedings of the International Workshop CEST Imaging 9, Atlanta, USA, 2022 (Talk | Video Presentation)

Kroh, Florian; von Knebel Doeberitz, Nikolaus; Breitling, Johannes; Maksimovic, Srdjan; König, Laila; Debus, Jürgen; Bachert, Peter; Schlemmer, Heinz-Peter; Ladd, Mark E.; Korzowski, Andreas; Goerke, Steffen; Paech, Daniel: *ssMT*

and APT-weighted CEST imaging predict clinical outcome in the first follow up after completion of radiotherapy in glioma patients at 3T. Proceedings of the International Workshop CEST Imaging 9, Atlanta, USA, 2022 (Talk | Video Presentation)

Karimian-Jazi, Kianush; Sturm, Volker; Schregel, Katharina; Hunger, Jessica; Turco, Verena; Fischer, Manuel; Streibel, Yannik; von Knebel Doeberitz, Nikolaus; Korzowski, Andreas; Goerke, Steffen; **Kroh, Florian**; Ladd, Mark E.; Schlemmer, Heinz-Peter; Paech, Daniel; Rodell, Christopher B.; Platten, Michael; Wick, Wolfgang; Heiland, Sabine; Bendszus, Martin; Breckwoldt, Michael O.: *Metabolic Imaging of malignant gliomas during immunotherapeutic intervention using chemical exchange saturation transfer (CEST) MRI at 9.4 Tesla*. Proceedings of the 57th Annual Meeting of the DGNR, Kassel, GER, 2022

von Knebel Doeberitz, Nikolaus; **Kroh, Florian**; Breitling, Johannes; Maksimovic, Srdjan; König, Laila; Debus, Jürgen; Bachert, Peter; Schlemmer, Heinz-Peter; Ladd, Mark E.; Goerke, Steffen; Paech, Daniel: *APTw imaging outperforms relaxation-compensated CEST-MRI at 3T in assessing glioma progression after radiotherapy - a preliminary analysis*. Proceedings of the 30th Annual Meeting of the ISMRM, London, UK, 2022 (Talk | Video Presentation)

Kroh, Florian; Breitling, Johannes; von Knebel Doeberitz, Nikolaus; Schlemmer, Heinz-Peter; Ladd, Mark E.; Bachert, Peter; Paech, Daniel; Goerke, Steffen: *Comparison study between APT-weighted and relaxation-compensated CEST-MRI in human glioma at 3T*. Proceedings of the 30th Annual Meeting of the ISMRM, London, UK, 2022 (Digital Poster | Video Presentation)

Bibliography

[1] I. I. Rabi, J. R. Zacharias, S. Millman, and P. Kusch. A New Method of Measuring Nuclear Magnetic Moment. *Physical Review*, 53:318–318, 1938.

[2] F. Bloch, W. W. Hansen, and Martin Packard. Nuclear Induction. *Physical Review*, 69:127–127, 1946.

[3] E. M. Purcell, H. C. Torrey, and R. V. Pound. Resonance Absorption by Nuclear Magnetic Moments in a Solid. *Physical Review*, 69:37–38, 1946.

[4] W. G. Proctor and F. C. Yu. The Dependence of a Nuclear Magnetic Resonance Frequency upon Chemical Compound. *Physical Review*, 77:717–717, 1950.

[5] WC Dickinson. Dependence of the f 19 nuclear resonance position on chemical compound. *Physical Review*, 77(5):736, 1950.

[6] P. C. Lauterbur. Image Formation by Induced Local Interactions: Examples Employing Nuclear Magnetic Resonance. *Nature*, 242:190–191, 1973.

[7] Peter Mansfield and Peter K Grannell. Nmr'diffraction'in solids? *Journal of Physics C: solid state physics*, 6(22):L422, 1973.

[8] Steven D Wolff and Robert S Balaban. NMR imaging of labile proton exchange. *Journal of Magnetic Resonance (1969)*, 86:164–169, 1990.

[9] K.M Ward, A.H Aletras, and R.S Balaban. A New Class of Contrast Agents for MRI Based on Proton Chemical Exchange Dependent Saturation Transfer (CEST). *Journal of Magnetic Resonance*, 143:79–87, 2000.

[10] Peter C. M. van Zijl and Nirbhay N. Yadav. Chemical exchange saturation transfer (CEST): What is in a name and what isn't? *Magnetic Resonance in Medicine*, 65:927–948, 2011.

[11] Guanshu Liu, Xiaolei Song, Kannie W. Y. Chan, and Michael T. McMahon. Nuts and bolts of chemical exchange saturation transfer MRI. *NMR in Biomedicine*, pages n/a–n/a, 2013.

[12] M. T. McMahon, A. A. Gilad, J. W. M. Bulte, and P. C. M. van Zijl. *Chemical Exchange Saturation Transfer Imaging*. Pan Stanford Publishing Pte. Ltd., 2016.

[13] Michael T McMahon, Assaf A Gilad, Jeff WM Bulte, and Peter CM Van Zijl. *Chemical exchange saturation transfer imaging: advances and applications*. CRC Press, 2017.

[14] Jinyuan Zhou, Jean-Francois Payen, David A. Wilson, Richard J. Traystman, and Peter C. M. van Zijl. Using the amide proton signals of intracellular proteins and peptides to detect pH effects in MRI. *Nature Medicine*, 9:1085–1090, 2003.

[15] Craig K. Jones, Alan Huang, Jiadi Xu, Richard A.E. Edden, Michael Schaer, Jun Hua, Nikita Oskolkov, Domenico Zaca, D., Jinyuan Zhou, Michael T. McMahon, Jay J. Pillai, and Peter C. M. van Zijl. Nuclear Overhauser enhancement (NOE) imaging in the human brain at 7t. *NeuroImage*, 77:114–124, 2013.

[16] Peter C. M. van Zijl, Jinyuan Zhou, Noriko Mori, Jean-Francois Payen, David Wilson, and Susumu Mori. Mechanism of Magnetization Transfer During On-Resonance Water Saturation. A New Approach to Detect Mobile Proteins, Peptides, and Lipids. *Magnetic Resonance in Medicine*, 49:440–449, 2003.

[17] Kun Yan, Zongming Fu, Chen Yang, Kai Zhang, Shanshan Jiang, Dong-Hoon Lee, Hye-Young Heo, Yi Zhang, Robert N. Cole, Jennifer E. Van Eyk, and Jinyuan Zhou. Assessing Amide Proton Transfer (APT) MRI Contrast Origins in 9 L Gliosarcoma in the Rat Brain Using Proteomic Analysis. *Molecular Imaging and Biology*, pages 1–9, January 2015.

[18] Tao Jin, Ping Wang, T Kevin Hitchens, and Seong-Gi Kim. Enhancing sensitivity of ph-weighted mri with combination of amide and guanidyl cest. *Neuroimage*, 157:341–350, 2017.

[19] Philip S. Boyd, Johannes Breitling, Andreas Korzowski, Moritz Zaiss, Vanessa L. Franke, Karin Mueller-Decker, Andrey Glinka, Mark E. Ladd, Peter Bachert, and Steffen Goerke. Mapping intracellular ph in tumors using amide and guanidyl cest-mri at 9.4 t. *Magnetic Resonance in Medicine*, 87(5):2436–2452, 2022.

[20] Phillip Zhe Sun. Demonstration of magnetization transfer and relaxation normalized ph-specific pulse-amide proton transfer imaging in an animal model of acute stroke. *Magnetic Resonance in Medicine*, 84(3):1526–1533, 2020.

[21] Steffen Goerke, Johannes Breitling, Karel D Klika, Mark E Ladd, and Peter Bachert. Dependence of rnoe-cest signals on molecular weight. *Proc. Jt. Annu. Meet. ISMRM-ESMRMB*, (2228), 2018.

[22] Steffen Goerke, Johannes Breitling, Moritz Zaiss, Johannes Windschuh, Patrick Kunz, Patrick Schuenke, Daniel Paech, Dario L Longo, Karel D Klika, Mark E Ladd, et al. Dual-frequency irradiation cest-mri of endogenous bulk mobile proteins. *NMR in Biomedicine*, 31(6):e3920, 2018.

[23] Moritz Zaiß, Benjamin Schmitt, and Peter Bachert. Quantitative separation of CEST effect from magnetization transfer and spillover effects by Lorentzian-line-fit analysis of z-spectra. *Journal of Magnetic Resonance*, 211(2):149–155, August 2011.

[24] Moritz Zaiss, Junzhong Xu, Steffen Goerke, Imad S. Khan, Robert J. Singer, John C. Gore, Daniel F. Gochberg, and Peter Bachert. Inverse Z-spectrum analysis for spillover-, MT-, and T1-corrected steady-state pulsed CEST-MRI – application to pH-weighted MRI of acute stroke. *NMR in Biomedicine*, 27:240–252, 2014.

[25] Moritz Zaiss and Peter Bachert. Chemical exchange saturation transfer (CEST) and MR Z-spectroscopy in vivo: a review of theoretical approaches and methods. *Physics in Medicine and Biology*, 58:R221–R269, 2013.

[26] Moritz Zaiss and Peter Bachert. Exchange-dependent relaxation in the rotating frame for slow and intermediate exchange – modeling off-resonant spin-lock and chemical exchange saturation transfer. *NMR in Biomedicine*, 26:507–518, 2013.

[27] Moritz Zaiss, Johannes Windschuh, Daniel Paech, Jan-Eric Meissner, Sina Burth, Benjamin Schmitt, Philip Kickingereder, Benedikt Wiestler, Wolfgang Wick, Martin Bendszus, Heinz-Peter Schlemmer, Mark E. Ladd, Peter Bachert, and Alexander Radbruch. Relaxation-compensated CEST-MRI of the human brain at 7T: Unbiased insight into NOE and amide signal changes in human glioblastoma. *NeuroImage*, 112:180–188, 2015.

[28] Moritz Zaiss, Johannes Windschuh, Steffen Goerke, Daniel Paech, Jan-Eric Meissner, Sina Burth, Philipp Kickingereder, Wolfgang Wick, Martin Bendszus, Heinz-Peter Schlemmer, et al. Downfield-noe-suppressed amide-cest-mri at 7 tesla provides a unique contrast in human glioblastoma. *Magnetic resonance in medicine*, 77(1):196–208, 2017.

[29] Daniel Paech, Johannes Windschuh, Johanna Oberhollenzer, Constantin Dreher, Felix Sahm, Jan-Eric Meissner, Steffen Goerke, Patrick Schuenke, Moritz Zaiss, Sebastian Regnery, et al. Assessing the predictability of idh mutation and mgmt methylation status in glioma patients using relaxation-compensated multipool cest mri at 7.0 t. *Neuro-oncology*, 20(12):1661–1671, 2018.

[30] Jan-Eric Meissner, Andreas Korzowski, Sebastian Regnery, Steffen Goerke, Johannes Breitling, Ralf Omar Floca, Jürgen Debus, Heinz-Peter Schlemmer, Mark Edward Ladd, Peter Bachert, et al. Early response assessment of glioma patients to definitive chemoradiotherapy using chemical exchange saturation transfer imaging at 7 t. *Journal of Magnetic Resonance Imaging*, 50(4):1268–1277, 2019.

[31] Sebastian Regnery, Sebastian Adeberg, Constantin Dreher, Johanna Oberhollenzer, Jan-Eric Meissner, Steffen Goerke, Johannes Windschuh, Katerina Deike-Hofmann, Sebastian Bickelhaupt, Moritz Zaiss, et al. Chemical exchange saturation transfer mri serves as predictor of early progression in glioblastoma patients. *Oncotarget*, 9(47):28772, 2018.

[32] Kimberly L Desmond, Hatef Mehrabian, Sofia Chavez, Arjun Sahgal, Hany Soliman, Radoslaw Rola, and Greg J Stanisz. Chemical exchange saturation transfer for predicting response to stereotactic radiosurgery in human brain metastasis. *Magnetic resonance in medicine*, 78(3):1110–1120, 2017.

[33] Craig K. Jones, Michael J. Schlosser, Peter C.M. van Zijl, Martin G. Pomper, Xavier Golay, and Jinyuan Zhou. Amide proton transfer imaging of human brain tumors at 3t. *Magnetic Resonance in Medicine*, 56(3):585–592, 2006.

[34] Zhibo Wen, Shuguang Hu, Fanheng Huang, Xianlong Wang, Linglang Guo, Xianyue Quan, Silun Wang, and Jinyuan Zhou. Mr imaging of high-grade brain tumors using endogenous protein and peptide-based contrast. *Neuroimage*, 51(2):616–622, 2010.

[35] Osamu Togao, Takashi Yoshiura, Jochen Keupp, Akio Hiwatashi, Koji Yamashita, Kazufumi Kikuchi, Yuriko Suzuki, Satoshi O Suzuki, Toru Iwaki, Nobuhiro Hata, et al. Amide proton transfer imaging of adult diffuse gliomas: correlation with histopathological grades. *Neuro-oncology*, 16(3):441–448, 2014.

[36] Yukihisa Takayama, Akihiro Nishie, Osamu Togao, Yoshiki Asayama, Kousei Ishigami, Yasuhiro Ushijima, Daisuke Okamoto, Nobuhiro Fujita, Kenzo Sonoda, Tomoyuki Hida, et al. Amide proton transfer mr imaging of endometrioid endometrial adenocarcinoma: association with histologic grade. *Radiology*, 286(3):909–917, 2018.

[37] Jinyuan Zhou, Erik Tryggestad, Zhibo Wen, Bachchu Lal, Tingting Zhou, Rachel Grossman, Silun Wang, Kun Yan, De-Xue Fu, Eric Ford, et al. Differentiation between glioma and radiation necrosis using molecular magnetic resonance imaging of endogenous proteins and peptides. *Nature medicine*, 17(1):130–134, 2011.

[38] Hatef Mehrabian, Kimberly L Desmond, Hany Soliman, Arjun Sahgal, and Greg J Stanisz. Differentiation between radiation necrosis and tumor progression using chemical exchange saturation transfer. *Clinical Cancer Research*, 23(14):3667–3675, 2017.

[39] Florian Kroh, Nikolaus von Knebel Doeberitz, Johannes Breitling, Srdjan Maksimovic, Laila König, Sebastian Adeberg, Moritz Scherer, Andreas Unterberg, Martin Bendszus, Wolfgang Wick, et al. Semi-solid mt and aptw cest-mri predict clinical outcome of patients with glioma early after radiotherapy. *Magnetic Resonance in Medicine*, 2023.

[40] Jinyuan Zhou, Moritz Zaiss, Linda Knutsson, Phillip Zhe Sun, Sung Soo Ahn, Silvio Aime, Peter Bachert, Jaishri O. Blakeley, Kejia Cai, Michael A. Chappell, Min Chen, Daniel F. Gochberg, Steffen Goerke, Hye-Young Heo, Shanshan Jiang, Tao Jin, Seong-Gi Kim, John Laterra, Daniel Paech, Mark D. Pagel, Ji Eun Park, Ravinder Reddy, Akihiko Sakata, Sabine Sartoretti-Schefer, A. Dean Sherry, Seth A. Smith, Greg J. Stanisz, Pia C. Sundgren, Osamu Togao, Moriel Vandsburger, Zhibo Wen, Yin Wu, Yi Zhang, Wenzhen Zhu, Zhongliang Zu, and Peter C. M. van Zijl. Review and consensus recommendations on clinical apt-weighted imaging approaches at 3t: Application to brain tumors. *Magnetic Resonance in Medicine*, 88(2):546–574, 2022.

[41] E. Mark Haacke, Robert W. Brown, Michael R. Thompson, and Ramesh Venkatesan. *Magnetic Resonance Imaging: Physical Principles and Sequence Design*. John Wiley & Sons, New York, NY, USA, 1st edition edition, 1999.

[42] Robin A. de Graaf. *In Vivo NMR Spectroscopy: Principles and Techniques*. John Wiley & Sons, Chichester, England, 2nd edition edition, 2008.

[43] Charles P. Slichter. *Principles of Magnetic Resonance*. Springer-Verlag Berlin Heidelberg, 3. edition edition, 1990.

[44] Matt A. Bernstein, Kevin F. King, and Xiaohong Joe Zhou. *Handbook of MRI Pulse Sequences*. Elsevier, September 2004.

[45] Trevor Hastie, Robert Tibshirani, and Jerome Friedman. *The Elements of Statistical Learning*. Springer, New York, NY, USA, 2nd edition edition, 2017.

[46] F. Bloch. Nuclear Induction. *Physical Review*, 70(7-8):460, 1946.

[47] Philip Sebastian Boyd. *Mapping intracellular pH of tumors in vivo using CEST-MRI: methodological development and preclinical investigation*. Fakultät für Physik und Astronomie, Ruprecht-Karls-Universität Heidelberg, Dissertation, 2022.

[48] Jinyuan Zhou and Peter C. M. van Zijl. Chemical exchange saturation transfer imaging and spectroscopy. *Progress in Nuclear Magnetic Resonance Spectroscopy*, 48:109–136, 2006.

[49] Edvards Liepinsh and Gottfried Otting. Proton exchange rates from amino acid side chains— implications for image contrast. *Magnetic Resonance in Medicine*, 35:30–42, 1996.

[50] P. W. Atkins and Julio de Paula. *Physikalische Chemie*. WILEY-VCH, Weinheim, Deutschland, 4. auflage edition, 2006.

[51] Kurt Wuethrich. *NMR of Proteins and Nucleic Acids*. John Wiley & Sons, New York, NY, USA, 1st edition edition, 1986.

[52] I. Solomon. Relaxation Processes in a System of Two Spins. *Physical Review*, 99:559–565, 1955.

[53] Jiadi Xu, Nirbhay N. Yadav, Amnon Bar-Shir, Craig K. Jones, Kannie W. Y. Chan, Jiangyang Zhang, P. Walczak, Michael T. McMahon, and Peter C. M. van Zijl. Variable Delay Multi-Pulse Train for Fast Chemical Exchange Saturation Transfer and Relayed-Nuclear Overhauser Enhancement MRI. *Magnetic Resonance in Medicine*, 71:1798–1812, 2014.

[54] Joshua I. Friedman, Ding Xia, Ravinder R. Regatte, and Alexej Jerschow. Transfer Rate Edited experiment for the selective detection of Chemical Exchange via Saturation Transfer (TRE-CEST). *Journal of Magnetic Resonance*, 256:43–51, 2015.

[55] Tao Jin, Ping Wang, Xiaopeng Zong, and Seong-Gi Kim. Mr imaging of the amide-proton transfer effect and the ph-insensitive nuclear overhauser effect at 9.4t. *Magnetic Resonance in Medicine*, 69:760–770, 2013.

[56] Greg J. Stanisz, Ewa E. Odrobina, Joseph Pun, Michael Escaravage, Simon J. Graham, Michael J. Bronskill, and R. Mark Henkelman. T1, T2 relaxation and magnetization transfer in tissue at 3t. *Magnetic Resonance in Medicine*, 54:507–512, 2005.

[57] Steffen Goerke, Moritz Zaiss, and Peter Bachert. Characterization of creatine guanidinium proton exchange by water-exchange (WEX) spectroscopy for absolute-pH CEST imaging in vitro. *NMR in Biomedicine*, 27:507–518, 2014.

[58] Michael T. McMahon, Assaf A. Gilad, Jinyuan Zhou, Phillip Z. Sun, Jeff W. M. Bulte, and Peter C. M. van Zijl. Quantifying exchange rates in chemical exchange saturation transfer agents using the saturation time and saturation power dependencies of the magnetization transfer effect on the magnetic resonance imaging signal (QUEST and QUESP): pH calibration for poly-L-lysine and a starburst dendrimer. *Magn Reson Med*, 55(4):836–847, 2006.

[59] Dapeng Liu, Jinyuan Zhou, Rong Xue, Zhentao Zuo, Jing An, and Danny J. J. Wang. Quantitative characterization of nuclear overhauser enhancement and amide proton transfer effects in the human brain at 7 tesla. *Magnetic Resonance in Medicine*, 70:1070–1081, 2013.

[60] Xiang Xu, Jae-Seung Lee, and Alexej Jerschow. Ultrafast Scanning of Exchangeable Sites by NMR Spectroscopy. *Angewandte Chemie International Edition in English*, 52:8281–8284, 2013.

[61] Moritz Zaiss, Tao Jin, Seong-Gi Kim, and Daniel F. Gochberg. Theory of chemical exchange saturation transfer mri in the context of different magnetic fields. *NMR in Biomedicine*, 35(11):e4789, 2022.

[62] Peter C.M. van Zijl, Wilfred W. Lam, Jiadi Xu, Linda Knutsson, and Greg J. Stanisz. Magnetization transfer contrast and chemical exchange saturation transfer mri. features and analysis of the field-dependent saturation spectrum. *NeuroImage*, 168:222–241, 2018. Neuroimaging with Ultra-high Field MRI: Present and Future.

[63] Mohammad Haris, Ravi Prakash Reddy Nanga, Anup Singh, Kejia Cai, Feliks Kogan, Hari Hariharan, and Ravinder Reddy. Exchange rates of creatine kinase metabolites: feasibility of imaging creatine by chemical exchange saturation transfer MRI. *NMR in Biomedicine*, 25:1305–1309, 2012.

[64] Kejia Cai, Mohammad Haris, Anup Singh, Feliks Kogan, Joel H. Greenberg, Hari Hariharan, John A. Detre, and Ravinder Reddy. Magnetic resonance imaging of glutamate. *Nature Medicine*, 18:302–307, 2012.

[65] Volkert Roeloffs, Christian Meyer, Peter Bachert, and Moritz Zaiss. Towards quantification of pulsed spinlock and CEST at clinical MR scanners: an analytical interleaved saturation–relaxation (ISAR) approach. *NMR in Biomedicine*, 28:40–53, 2015.

[66] Harden M. McConnell. Reaction Rates by Nuclear Magnetic Resonance. *The Journal of Chemical Physics*, 28:430–431, 1958.

[67] Daniel Abergel and Arthur G. Palmer. Approximate Solutions of the Bloch–McConnell Equations for Two-Site Chemical Exchange. *ChemPhysChem*, 5:787–793, 2004.

[68] Oleg Trott and Arthur G. Palmer III. R1 Relaxation outside of the Fast-Exchange Limit. *Journal of Magnetic Resonance*, 154:157–160, 2002.

[69] Phillip Zhe Sun, Jinyuan Zhou, Judy Huang, and Peter van Zijl. Simplified quantitative description of amide proton transfer (APT) imaging during acute ischemia. *Magnetic Resonance in Medicine*, 57:405–410, 2007.

[70] Jinyuan Zhou, David A. Wilson, Phillip Zhe Sun, Judith A. Klaus, and Peter C. M. van Zijl. Quantitative Description of Proton Exchange Processes Between Water and Endogenous and Exogenous Agents for WEX, CEST, and APT Experiments. *Magnetic Resonance in Medicine*, 51:945–952, 2004.

[71] Moritz Zaiss, Zhongliang Zu, Junzhong Xu, Patrick Schuenke, Daniel F. Gochberg, John C. Gore, Mark E. Ladd, and Peter Bachert. A combined analytical solution for chemical exchange saturation transfer and semi-solid magnetization transfer. *NMR in Biomedicine*, 28:217–230, 2015.

[72] Moritz Zaiss and Peter Bachert. Exchange-dependent relaxation in the rotating frame for slow and intermediate exchange–modeling off-resonant spin-lock and chemical exchange saturation transfer. *NMR in Biomedicine*, 26(5):507–518, 2012.

[73] Sanford Weisberg. *Applied linear regression*, volume 528. John Wiley & Sons, 2005.

[74] Alvin C Rencher and G Bruce Schaalje. *Linear models in statistics*. John Wiley & Sons, 2008.

[75] Leo Breiman. *Classification and regression trees*. Routledge, 1984.

[76] Jerome H Friedman. Greedy function approximation: a gradient boosting machine. *Annals of statistics*, pages 1189–1232, 2001.

[77] Jerome H Friedman. Stochastic gradient boosting. *Computational statistics & data analysis*, 38(4):367–378, 2002.

[78] Robert Tibshirani. Regression shrinkage and selection via the lasso. *Journal of the Royal Statistical Society Series B: Statistical Methodology*, 58(1):267–288, 1996.

[79] Amir Beck and Marc Teboulle. A fast iterative shrinkage-thresholding algorithm for linear inverse problems. *SIAM journal on imaging sciences*, 2(1):183–202, 2009.

[80] Lloyd S Shapley et al. A value for n-person games. *Princeton University Press Princeton*, 1953.

[81] Moritz Zaiss, Philipp Ehses, and Klaus Scheffler. Snapshot-CEST: Optimizing spiral-centric-reordered gradient echo acquisition for fast and robust 3D CEST MRI at 9.4 T. *NMR in Biomedicine*, 31(4):e3879, 2018.

[82] Anagha Deshmane, Moritz Zaiss, Tobias Lindig, Kai Herz, Mark Schuppert, Chirayu Gandhi, Benjamin Bender, Ulrike Ernemann, and Klaus Scheffler. 3d gradient echo snapshot cest mri with low power saturation for human studies at 3t. *Magnetic resonance in medicine*, 81(4):2412–2423, 2019.

[83] Steffen Goerke, Yannick Soehngen, Anagha Deshmane, Moritz Zaiss, Johannes Breitling, Philip S. Boyd, Kai Herz, Ferdinand Zimmermann, Karel D. Klika, Heinz-Peter Schlemmer, et al. Relaxation-compensated apt and rnoe cest-mri of human brain tumors at 3 t. *Magnetic resonance in medicine*, 82(2):622–632, 2019.

[84] Jinyuan Zhou, Hye-Young Heo, Linda Knutsson, Peter C.M. van Zijl, and Shanshan Jiang. Apt-weighted mri: Techniques, current neuro applications, and challenging issues. *Journal of Magnetic Resonance Imaging*, 50(2):347–364, 2019.

[85] Patrick Schuenke, Johannes Windschuh, Volkert Roeloffs, Mark E Ladd, Peter Bachert, and Moritz Zaiss. Simultaneous mapping of water shift and B1 (WASABI)—Application to field-Inhomogeneity correction of CEST MRI data. *Magnetic resonance in Medicine*, 77(2):571–580, 2017.

[86] Marco Nolden, Sascha Zelzer, Alexander Seitel, Diana Wald, Michael Müller, Alfred M Franz, Daniel Maleike, Markus Fangerau, Matthias Baumhauer, Lena Maier-Hein, et al. The medical imaging interaction toolkit: challenges and advances. *International journal of computer assisted radiology and surgery*, 8(4):607–620, 2013.

[87] Johannes Breitling, Andreas Korzowski, Neele Kempa, Philip S. Boyd, Daniel Paech, Heinz-Peter Schlemmer, Mark E. Ladd, Peter Bachert, and Steffen Goerke. Motion correction for 3d cest imaging without direct water saturation artifacts. *NMR in Biomedicine*, page e4720, 2022.

[88] David Mattes, David R Haynor, Hubert Vesselle, Thomas K Lewellyn, and William Eubank. Nonrigid multimodality image registration. In *Medical imaging 2001: image processing*, volume 4322, pages 1609–1620. Spie, 2001.

[89] Ralf Floca. Matchpoint: on bridging the innovation gap between algorithmic research and clinical use in image registration. In *World Congress on Medical Physics and Biomedical Engineering, September 7-12, 2009, Munich, Germany: Vol. 25/4 Image Processing, Biosignal Processing, Modelling and Simulation, Biomechanics*, pages 1105–1108. Springer, 2009.

[90] Johannes Breitling, Anagha Deshmane, Steffen Goerke, Andreas Korzowski, Kai Herz, Mark E Ladd, Klaus Scheffler, Peter Bachert, and Moritz Zaiss. Adaptive denoising for chemical exchange saturation transfer mr imaging. *NMR in Biomedicine*, 32(11):e4133, 2019.

[91] Edmund R Malinowski. Determination of the number of factors and the experimental error in a data matrix. *Analytical Chemistry*, 49(4):612–617, 1977.

[92] Edmund R Malinowski. Theory of error in factor analysis. *Analytical Chemistry*, 49(4):606–612, 1977.

[93] Kimberly L. Desmond, Firas Moosvi, and Greg J. Stanisz. Mapping of Amide, Amine, and Aliphatic Peaks in the CEST Spectra of Murine Xenografts at 7 T. *Magnetic Resonance in Medicine*, 71:1841–1853, 2013.

[94] Manolis IA Lourakis et al. A brief description of the levenberg-marquardt algorithm implemented by levmar. *Foundation of Research and Technology*, 4(1):1–6, 2005.

[95] Johannes Windschuh, Moritz Zaiss, Jan-Eric Meissner, Daniel Paech, Alexander Radbruch, Mark E. Ladd, and Peter Bachert. Correction of B1-inhomogeneities for relaxation-compensated CEST imaging at 7T. *NMR in Biomedicine*, 28:529–537, 2015.

[96] Moritz Zaiss, Kai Herz, Anagha Deshmane, Mina Kim, Xavier Golay, Tobias Lindig, Benjamin Bender, Ulrike Ernemann, and Klaus Scheffler. Possible artifacts in dynamic CEST MRI due to motion and field alterations. *Journal of Magnetic Resonance*, 298:16–22, 2019.

[97] Mark Jenkinson, Peter Bannister, Michael Brady, and Stephen Smith. Improved optimization for the robust and accurate linear registration and motion correction of brain images. *Neuroimage*, 17(2):825–841, 2002.

[98] John Ashburner and Karl J. Friston. Unified segmentation. *NeuroImage*, 26(3):839–851, 2005.

[99] Edmund T. Rolls, Chu-Chung Huang, Ching-Po Lin, Jianfeng Feng, and Marc Joliot. Automated anatomical labelling atlas 3. *NeuroImage*, 206:116189, 2020.

[100] Susan K Hobbs, Gongyi Shi, Ron Homer, Griff Harsh, Scott W Atlas, and Mark D Bednarski. Magnetic resonance image–guided proteomics of human glioblastoma multiforme. *Journal of Magnetic Resonance Imaging: An Official Journal of the International Society for Magnetic Resonance in Medicine*, 18(5):530–536, 2003.

[101] FA Howe, SJ Barton, SA Cudlip, M Stubbs, DE Saunders, M Murphy, P Wilkins, KS Opstad, VL Doyle, MA McLean, et al. Metabolic profiles of human brain tumors using quantitative in vivo 1h magnetic resonance spectroscopy. *Magnetic Resonance in Medicine: An Official Journal of the International Society for Magnetic Resonance in Medicine*, 49(2):223–232, 2003.

[102] Daniel Paech, Nina Weckesser, Vanessa L Franke, Johannes Breitling, Steffen Görke, Katerina Deike-Hofmann, Antje Wick, Moritz Scherer, Andreas Unterberg, Wolfgang Wick, et al. Whole-brain intracellular ph mapping of gliomas using high-resolution 31p mr spectroscopic imaging at 7.0 t. *Radiology: Imaging Cancer*, 6(1):e220127, 2023.

[103] Jun Hua, Craig K Jones, Jaishri Blakeley, Seth A Smith, Peter CM Van Zijl, and Jinyuan Zhou. Quantitative description of the asymmetry in magnetization transfer effects around the water resonance in the human brain. *Magnetic Resonance in Medicine: An Official Journal of the International Society for Magnetic Resonance in Medicine*, 58(4):786–793, 2007.

[104] Tao Jin, Ping Wang, Xiaopeng Zong, and Seong-Gi Kim. MR Imaging of the Amide-Proton Transfer Effect and the pH-Insensitive Nuclear Overhauser Effect at 9.4 T. *Magnetic Resonance in Medicine*, 69:760–770, 2013.

[105] Jinyuan Zhou, Xiaohua Hong, Xuna Zhao, Jia-Hong Gao, and Jing Yuan. APT-Weighted and NOE-Weighted Image Contrasts in Glioma with Different RF Saturation Powers Based on Magnetization Transfer Ratio Asymmetry Analyses. *Magnetic Resonance in Medicine*, 70:320–327, 2013.

[106] Tao Jin and Seong-Gi Kim. In vivo saturation transfer imaging of nuclear Overhauser effect from aromatic and aliphatic protons: implication to APT quantification. *Proceedings of the 21th Annual Meeting ISMRM, Salt Lake City, UT, USA*, 2013.

[107] Robert J Harris, Timothy F Cloughesy, Linda M Liau, Robert M Prins, Joseph P Antonios, Debiao Li, William H Yong, Whitney B Pope, Albert Lai, Phioanh L Nghiemphu, et al. ph-weighted molecular imaging of gliomas using amine chemical exchange saturation transfer mri. *Neuro-oncology*, 17(11):1514–1524, 2015.

[108] Kejia Cai, Anup Singh, Harish Poptani, Weiguo Li, Shaolin Yang, Yang Lu, Hari Hariharan, Xiaohong J Zhou, and Ravinder Reddy. Cest signal at 2 ppm (cest@ 2ppm) from z-spectral fitting correlates with creatine distribution in brain tumor. *NMR in biomedicine*, 28(1):1–8, 2015.

[109] Dong-Hoon Lee, Hye-Young Heo, Kai Zhang, Yi Zhang, Shanshan Jiang, Xuna Zhao, and Jinyuan Zhou. Quantitative assessment of the effects of water proton concentration and water t1 changes on amide proton transfer (apt) and nuclear overhauser enhancement (noe) mri: The origin of the apt imaging signal in brain tumor. *Magnetic resonance in medicine*, 77(2):855–863, 2017.

[110] Guolin Ke, Qi Meng, Thomas Finley, Taifeng Wang, Wei Chen, Weidong Ma, Qiwei Ye, and Tie-Yan Liu. Lightgbm: A highly efficient gradient boosting decision tree. *Advances in neural information processing systems*, 30, 2017.

[111] Lars Buitinck, Gilles Louppe, Mathieu Blondel, Fabian Pedregosa, Andreas Mueller, Olivier Grisel, Vlad Niculae, Peter Prettenhofer, Alexandre Gramfort, Jaques Grobler, Robert Layton, Jake VanderPlas, Arnaud Joly, Brian Holt, and Gaël Varoquaux. API design for machine learning software: experiences from the scikit-learn project. In *ECML PKDD Workshop: Languages for Data Mining and Machine Learning*, pages 108–122, 2013.

[112] F. Pedregosa, G. Varoquaux, A. Gramfort, V. Michel, B. Thirion, O. Grisel, M. Blondel, P. Prettenhofer, R. Weiss, V. Dubourg, J. Vanderplas, A. Passos, D. Cournapeau, M. Brucher, M. Perrot, and E. Duchesnay. Scikit-learn: Machine learning in Python. *Journal of Machine Learning Research*, 12:2825–2830, 2011.

[113] Tianqi Chen and Carlos Guestrin. Xgboost: A scalable tree boosting system. In *Proceedings of the 22nd acm sigkdd international conference on knowledge discovery and data mining*, pages 785–794, 2016.

[114] M. Stone. Cross-validatory choice and assessment of statistical predictions. *Journal of the Royal Statistical Society: Series B (Methodological)*, 36(2):111–133, 1974.

[115] Rashmi Korlakai Vinayak and Ran Gilad-Bachrach. Dart: Dropouts meet multiple additive regression trees. In *Artificial Intelligence and Statistics*, pages 489–497. PMLR, 2015.

[116] Felix Glang, Moritz S. Fabian, Alexander German, Katrin M. Khakzar, Angelika Mennecke, Andrzej Liebert, Kai Herz, Patrick Liebig, Burkhard S. Kasper, Manuel Schmidt, Enrique Zuazua, Armin M. Nagel, Frederik B. Laun, Arnd Dörfler, Klaus Scheffler, and Moritz Zaiss. Linear projection-based chemical exchange saturation transfer parameter estimation. *NMR in Biomedicine*, 36(6):e4697, 2023.

[117] L Breiman. Random forests. *Machine Learning*, 45:5–32, 10 2001.

[118] Scott M Lundberg and Su-In Lee. A unified approach to interpreting model predictions. *Advances in neural information processing systems*, 30, 2017.

[119] Scott M Lundberg, Gabriel G Erion, and Su-In Lee. Consistent individualized feature attribution for tree ensembles. *arXiv preprint arXiv:1802.03888*, 2018.

[120] Rui Wang, Sa-Ying Li, Min Chen, Jin-Yuan Zhou, Dan-Tao Peng, Chen Zhang, and Yong-Ming Dai. Amide proton transfer magnetic resonance imaging of alzheimer's disease at 3.0 tesla: a preliminary study. *Chinese medical journal*, 128(05):615–619, 2015.

[121] Chunmei Li, Shuai Peng, Rui Wang, Haibo Chen, Wen Su, Xuna Zhao, Jinyuan Zhou, and Min Chen. Chemical exchange saturation transfer mr imaging of parkinson's disease at 3 tesla. *European radiology*, 24:2631–2639, 2014.

[122] Chunmei Li, Min Chen, Xuna Zhao, Rui Wang, Haibo Chen, Wen Su, Shuhua Li, Baohui Lou, Guodong Song, Shuai Zhang, et al. Chemical exchange saturation transfer mri signal loss of the substantia nigra as an imaging biomarker to evaluate the diagnosis and severity of parkinson's disease. *Frontiers in neuroscience*, 11:489, 2017.

[123] Adrienne N Dula, Elizabeth M Asche, Bennett A Landman, E Brian Welch, Siddharama Pawate, Subramaniam Sriram, John C Gore, and Seth A Smith. Development of chemical exchange saturation transfer at 7t. *Magnetic Resonance in Medicine*, 66(3):831–838, 2011.

[124] Jinyuan Zhou, Jaishri O Blakeley, Jun Hua, Mina Kim, John Laterra, Martin G Pomper, and Peter CM Van Zijl. Practical data acquisition method for human brain tumor amide proton transfer (apt) imaging. *Magnetic Resonance in Medicine: An Official Journal of the International Society for Magnetic Resonance in Medicine*, 60(4):842–849, 2008.

[125] Shanshan Jiang, Tianyu Zou, Charles G Eberhart, Maria AV Villalobos, Hye-Young Heo, Yi Zhang, Yu Wang, Xianlong Wang, Hao Yu, Yongxing Du, et al. Predicting idh mutation status in grade ii gliomas using amide proton transfer-weighted (aptw) mri. *Magnetic resonance in medicine*, 78(3):1100–1109, 2017.

[126] Shanshan Jiang, Qihong Rui, Yu Wang, Hye-Young Heo, Tianyu Zou, Hao Yu, Yi Zhang, Xianlong Wang, Yongxing Du, Xinrui Wen, et al. Discriminating mgmt promoter methylation status in patients with glioblastoma employing amide proton transfer-weighted mri metrics. *European radiology*, 28:2115–2123, 2018.

[127] Phillip Zhe Sun, Jinyuan Zhou, Weiyun Sun, Judy Huang, and Peter CM Van Zijl. Detection of the ischemic penumbra using ph-weighted mri. *Journal of Cerebral Blood Flow & Metabolism*, 27(6):1129–1136, 2007.

[128] George WJ Harston, Yee Kai Tee, Nicholas Blockley, Thomas W Okell, Sivarajan Thandeswaran, Gabriel Shaya, Fintan Sheerin, Martino Cellerini, Stephen Payne, Peter Jezzard, et al. Identifying the ischaemic penumbra using ph-weighted magnetic resonance imaging. *Brain*, 138(1):36–42, 2015.

[129] Meiyun Wang, Xiaohua Hong, Che-Feng Chang, Qiang Li, Bo Ma, Hong Zhang, Sinan Xiang, Hye-Young Heo, Yi Zhang, Dong-Hoon Lee, et al. Simultaneous detection and separation of hyperacute intracerebral hemorrhage and cerebral ischemia using amide proton transfer mri. *Magnetic resonance in medicine*, 74(1):42–50, 2015.

[130] Hye-Young Heo, Yi Zhang, Dong-Hoon Lee, Xiaohua Hong, and Jinyuan Zhou. Quantitative assessment of amide proton transfer (apt) and nuclear overhauser enhancement (noe) imaging with extrapolated semi-solid magnetization transfer reference (emr) signals: application to a rat glioma model at 4.7 tesla. *Magnetic resonance in medicine*, 75(1):137–149, 2016.

[131] Hye-Young Heo, Yi Zhang, Shanshan Jiang, Dong-Hoon Lee, and Jinyuan Zhou. Quantitative assessment of amide proton transfer (apt) and nuclear overhauser enhancement (noe) imaging with extrapolated semisolid magnetization transfer reference (emr) signals: Ii. comparison of three emr models and application to human brain glioma at 3 tesla. *Magnetic resonance in medicine*, 75(4):1630–1639, 2016.

[132] Jochen Keupp and Osamu Togao. Magnetization transfer ratio based metric for aptw or cestw mri suppressing signal from fluid compartments-initial application to glioblastoma assessment. In *Proceedings of the International Society of Magnetic Resonance in Medicine*, volume 3156, 2018.

[133] Laura Mancini, Stefano Casagranda, Guillaume Gautier, Philippe Peter, Bruno Lopez, Lewis Thorne, Andrew McEvoy, Anna Miserocchi, George Samandouras, Neil Kitchen, et al. Cest mri provides amide/amine surrogate biomarkers for treatment-naïve glioma sub-typing. *European Journal of Nuclear Medicine and Molecular Imaging*, 49(7):2377–2391, 2022.

[134] Jan-Rüdiger Schüre, Stefano Casagranda, Maria Sedykh, Patrick Liebig, Christos Papageorgakis, Laura Mancini, Sotirios Bisdas, Lucia Nichelli, Nandor Pinter, Laszlo Mechtler, et al. Fluid suppression in amide proton transfer-weighted (aptw) cest imaging: New theoretical insights and clinical benefits. *Magnetic Resonance in Medicine*, 91(4):1354–1367, 2024.

[135] Zhongliang Zu. Towards the complex dependence of mtrasym on t1w in amide proton transfer (apt) imaging. *NMR in Biomedicine*, 31(7):e3934, 2018.

[136] Casey Sun, Yu Zhao, and Zhongliang Zu. Evaluation of the molecular origin of amide proton transfer–weighted imaging. *Magnetic Resonance in Medicine*, 91(2):716–734, 2024.

[137] Jianping Xu, Tao Zu, Yi-Cheng Hsu, Xiaoli Wang, Kannie WY Chan, and Yi Zhang. Accelerating cest imaging using a model-based deep neural network with synthetic training data. *Magnetic Resonance in Medicine*, 91(2):583–599, 2024.

[138] Gang Xiao, Xiaolei Zhang, Hanjing Tang, Weipeng Huang, Yaowen Chen, Caiyu Zhuang, Beibei Chen, Lin Yang, Yue Chen, Gen Yan, et al. Deep learning for dense z-spectra reconstruction from cest images at sparse frequency offsets. *Frontiers in Neuroscience*, 17, 2023.

[139] Sajad Mohammed Ali, Nirbhay N Yadav, Ronnie Wirestam, Munendra Singh, Hye-Young Heo, Peter C van Zijl, and Linda Knutsson. Deep learning–based lorentzian fitting of water saturation shift referencing spectra in mri. *Magnetic resonance in medicine*, 2023.

[140] Leonie Hunger, Junaid R Rajput, Kiril Klein, Angelika Mennecke, Moritz S Fabian, Manuel Schmidt, Felix Glang, Kai Herz, Patrick Liebig, Armin M Nagel, et al. Deepcest 7 t: Fast and homogeneous mapping of 7 t cest mri parameters and their uncertainty quantification. *Magnetic Resonance in Medicine*, 89(4):1543–1556, 2023.

[141] Chongxue Bie, Yuguo Li, Yang Zhou, Zaver M Bhujwalla, Xiaolei Song, Guanshu Liu, Peter CM van Zijl, and Nirbhay N Yadav. Deep learning-based classification of preclinical breast cancer tumor models using chemical exchange saturation transfer magnetic resonance imaging. *NMR in Biomedicine*, 35(2):e4626, 2022.

[142] Moritz Zaiss, Anagha Deshmane, Mark Schuppert, Kai Herz, Felix Glang, Philipp Ehses, Tobias Lindig, Benjamin Bender, Ulrike Ernemann, and Klaus Scheffler. Deepcest: 9.4 t chemical exchange saturation transfer mri contrast predicted from 3 t data–a proof of concept study. *Magnetic resonance in medicine*, 81(6):3901–3914, 2019.

[143] Gang Xiao, Xiaolei Zhang, Guisheng Yang, Yanlong Jia, Gen Yan, and Renhua Wu. Deep learning to reconstruct quasi-steady-state chemical exchange saturation transfer from a non-steady-state experiment. *NMR in Biomedicine*, page e4940, 2023.

[144] Leo F Czervionke, Jeanne M Czervionke, David L Daniels, and Victor M Haughton. Characteristic features of mr truncation artifacts. *American journal of neuroradiology*, 9(5):815–824, 1988.

Acknowledgment

An dieser Stelle möchte ich mich herzlich bei allen Menschen bedanken, die mich seit dem Beginn meiner Promotion auf diesem Weg begleitet und unterstützt haben.

Prof. Dr. Peter Bachert möchte ich dafür danken, dass er mich in seiner Gruppe "NMR-Spektroskopie und CEST-Bildgebung" aufgenommen hat. Vielen Dank für Ihr Vertrauen und Ihre kontinuierliche Unterstützung.

Ich danke auch Prof. Dr. Mark E. Ladd dafür, dass er mir die Möglichkeit eröffnet hat bei ihm in der Abteilung zu promovieren, für die Erstbetreuung meiner Arbeit sowie für das Vertrauen, welches er mir während der letzten drei Jahre entgegengebracht hat.

Außerdem möchte ich mich bei, Prof. Leif Schröder, dafür bedanken, dass er sich die Zeit nimmt, dass Zweitgutachter für meine Dissertation zu erstellen.

Andi, Philip und Steffen danke ich für die hervorragende Betreuung meiner Arbeit während der letzten 3 Jahre und das ich bei Fragen immer auf sie zählen konnte! Ich danke Steffen für alles, was ich während meiner Bachelorarbeit, Masterarbeit und dem Beginn meiner Promotion von ihm lernen durfte und dafür, dass er seine Begeisterung für CEST mit mir geteilt hat. Außerdem möchte ich ihm dafür danken, dass er die Weichen für meine Promotion gestellt hat. Andi und Philip, danke ich für die vielen richtungsweisenden Gespräche die mir vor allem in den letzten zwei Jahren sehr geholfen haben. Außerdem bin ich dankbar für ihre tatkräftige Unterstützung während meiner gesamten Promotion aber vor allem auch während der letzten Wochen.

Vielen Dank auch an Daniel Paech und Nikolaus von Knebel Doeberitz für die gute Zusammenarbeit in den letzten Jahren.

Außerdem möchte ich Kris, Till, Fabian und Lukas für ihre Hilfestellungen bei Fragen bezüglich Machine learning bedanken, die sie immer wieder gerne zur Verfügung gestellt haben.

Auch möchte ich mich bei allen aktuellen und ehemaligen Mitgliedern der Arbeitsgruppe und insbesondere Büro F.02.065 (+Gino) dafür bedanken, dass sie meine Promotion zu einer so schönen und unvergesslichen Zeit gemacht haben. Ich möchte mich für den vielen Spaß, den wir immer wieder zusammen haben aber auch die Unterstützung vielmals bedanken. Vielen Dank, dass ich teil dieser großartigen Arbeitsgruppe sein durfte.

Ich möchte mich auch bei meinen Freunden und meiner Familie für die letzten 3 Jahre bedanken. Ich danke meiner Familie für ihre Unterstützung während meines gesamten Studiums. Ohne ihren Rückhalt wäre dieser weg so nicht möglich gewesen. Zuletzt möchte ich mich noch von ganzem Herzen bei Line bedanken dafür, dass sie mich während der gesamten Zeit unterstützt hat, in mich vertraut hat, für die vielen Zusprüche während der letzten Jahre und vor allem für die schöne Zeit. Vielen Dank!